

# Design fundamental technologies self-latching MEMS optical switch with moving polymer waveguides

Liu, Haobing

2007

Liu, H. B. (2007). Design fundamental technologies self-latching MEMS optical switch with moving polymer waveguides. Doctoral thesis, Nanyang Technological University, Singapore.

<https://hdl.handle.net/10356/6052>

<https://doi.org/10.32657/10356/6052>

---

Nanyang Technological University

*Downloaded on 09 Apr 2024 11:58:47 SGT*



**NANYANG  
TECHNOLOGICAL  
UNIVERSITY**

**DESIGN AND FUNDAMENTAL TECHNOLOGIES  
FOR SELF-LATCHING MEMS OPTICAL SWITCH  
WITH MOVING POLYMER WAVEGUIDES**

**LIU HAOBING**

**SCHOOL OF MECHANICAL & AEROSPACE ENGINEERING**

**2007**

DESIGN AND FUNDAMENTAL TECHNOLOGIES FOR SELF-LATCHING  
MEMS OPTICAL SWITCH WITH MOVING POLYMER WAVEGUIDES

LIU HAOBING

2007

# **Design and Fundamental Technologies for Self-latching MEMS Optical Switch with Moving Polymer Waveguides**

**Liu Haobing**

**School of Mechanical & Aerospace Engineering**

A thesis submitted to the Nanyang Technological University  
in fulfilment of the requirement for the degree of  
Doctor of Philosophy

**2007**

## Acknowledgements

I am extremely grateful to my supervisor, A/Prof. Franck Alexis Chollet, School of Mechanical and Aerospace Engineering (MAE), Nanyang Technological University (NTU). His solid knowledge, experience and insight on the MOEMS region have guided me for all these years. He is so warmhearted that every discussion with him benefits me much. And all his helps I won't forget.

My very special thanks give to A/Prof. Miao Jianmin, director of the Micromachines Center (MMC), NTU, and the technicians of the MMC, Mr. Koh Hai Tong, Mr. Hoong Sin Poh, Mr. Wong Kim Chong, Mr. Pan Yih Ke, Mr. Ho Kar Kiat, Mr. Lau Joo Kiang, Mr. Nordin Bin Abdul Kassim, and Mr. Pek Soo Siong. The facilities in the MMC and their help are fundamental for the project.

I am also grateful to the reviewers of this report, and the research fellows of the MMC, Dr. Zhu Hong, Dr. Sun Tietun, Dr. Ciprian Iliescu, Dr. Fu Yongqing, Dr. Chen Longqing, Dr. Li Wenzhong, Mr. Wang Xiaodong and Ms. Deng Liquan, for their unselfish assistance, helpful discussion and valuable suggestions.

I am fortunate to work in the same lab with Mr. Huang Xu, Ms. Zhou Yinghui, Mr. Chen Bangtao, Mr. Sun Jianbo, Mr. Wu Mingjie, Mr. Wu Jie, Mr. Tang Gongyue and Mr. Yuan Yanhui. They are helpful not only in the research, but also the daily life.

Thanks to my family and friends, for their endless support.



## Acknowledgements

---

## Abstract

This research deals with some innovative technologies in MEMS (Micro Electro Mechanical Systems) and a novel optical switch based on them.

A novel micro self-latching bi-stable actuator that can be fabricated by MEMS process with one mask is introduced in this work. This device is based on two key structures: a micro hinge without wear and tear, which is solved by introduction of a novel Fork Hinge structure, and a pre-compressed spring, which is solved by micro assembly of a pair of arch like structures. Driven by electrostatic combdrives and mechanically latched at is two working positions, the bi-stable actuator provides stable performance and ultra small energy consumption, a stage with moving range of 20 $\mu$ m, and switching time within 0.5ms, making it suitable for many MEMS applications.

The recently established guided-wave MOEMS (Micro-Opto-Electro-Mechanical Systems) technology, especially MOEMS with moving waveguides, can combine the merits of integrated optics and conventional free-space MOEMS. A new approach for an optical switch used for optical communication, coined as the Self-latching Waveguides Optical MEMS Switch (SWOMS), is introduced as one of the important applications of these technologies. SWOMS is featured with the newly developed Self-latching MEMS actuator, and a computational optimized configuration of polymer waveguides. By moving the uniquely designed waveguides but not merely bending a straight waveguide as it is done conventionally, the SWOMS provides 2 $\times$ 2 instead of only 1 $\times$ 2 switching capability, and has a gap reduction mechanism between parts of waveguides in which light is channeled to further reduce the coupling losses. Testing of the fabricated prototype device and waveguides indicated a switching speed below 0.5ms, a total loss below 3dB and crosstalk below -36dB. Combining these features with other inherent merits, such as digital accurate control, self-latching and low power consumption, low polarization dependence, low wavelength

## Abstract

---

dependence, high reliability and long lifetime, and potentially low cost, the SWOMS may be a promising alternative to existing candidates.

The fabrication process is an important factor in a successful MEMS and it has to be considered together with the design. Many challenges have been met during the developing of fabrication process for the SWOMS, and some new MEMS process technologies have been invented and are introduced in this work.

One new process technology is a set of mask layout rules that solves the stiction problem that is often met at the release step after the DRIE (Deep reactive ion etching) of SOI (Silicon on insulator) wafer. This technology can lead to structure fabrication and release in one DRIE step without any wet process, or, at least, completely remove the stiction problem during wet release or other further wet processes. Another unique process technology provides a method to build silicon-polymer hybrid structure by silicon-polymer bonding utilizing polymer membrane and capillary force.

This thesis will clarify the basic principle and structure of this novel optical switch, describe the computer aided design of the bi-stable MEMS actuator, depict the simulation & optimization of the polymer waveguides, detail the micro fabrication of the electro-mechanical actuator and the polymer waveguides, and their assembly, and finally report the testing of the device and characterization of the waveguides. The background, content and applications of our new technologies will also be detailed in suitable chapters.

# Table of Contents

<b>Acknowledgement</b> .....	I
<b>Abstract</b> .....	III
<b>Table of Contents</b> .....	V
<b>List of Tables</b> .....	VIII
<b>List of Figures</b> .....	IX
<b>Chapter 1 Introduction</b> .....	<b>1</b>
1.1 Background.....	1
1.1.1 Optical Switches and the SWOMS.....	1
1.1.2 Self-latching Actuator.....	6
1.1.3 MOEMS with Moving Waveguides.....	8
1.2 Objective and Scope .....	11
1.3 Organization.....	12
<b>Chapter 2 Literature Review</b> .....	<b>13</b>
2.1 MEMS and MOEMS .....	13
2.2 Micro Fabrication Technologies.....	16
2.3 Self-latching MEMS Devices .....	18
2.4 Optical Networking and Switching .....	22
2.4.1 Introduction to Optical Networking .....	22
2.4.2 OEO and All-optical Switching .....	24
2.5 All-optical Switches .....	26
2.5.1 3D MEMS Switch .....	27
2.5.2 2D MEMS Switch .....	28
2.5.3 Opto-mechanical Switch .....	30
2.5.4 PLC Switch .....	30
2.5.5 Liquid Crystal Switch .....	31
2.5.6 Moving Waveguide Switch .....	32
2.6 Feature Comparison of All-optical Switches .....	34
<b>Chapter 3 Basic Structure and Principle of SWOMS</b> .....	<b>36</b>
3.1 The Micro Self-latching Bi-stable Structure .....	36
3.1.1 Basic Structure Components .....	36
3.1.2 Bi-stable Self-latching Principle .....	38
3.1.3 Micro Fork Hinge Structure .....	39
3.1.4 Integrated Assembly of the Device .....	43
3.1.5 Principle of the Self-latching Structure .....	47
3.2 Introduction of SWOMS .....	49
3.2.1 Optical Switching Principle .....	49
3.2.2 Gap-reduction mechanism .....	51
<b>Chapter 4 Design of the Bi-stable Micro Actuator</b> .....	<b>52</b>
4.1 Calculation and Simulation Tools .....	52
4.2 Design of the Micro Fork Hinge .....	53

## Table of Contents

4.2.1	Simplification of the Model .....	53
4.2.2	Design Objective.....	55
4.2.3	Analytical Calculation Design .....	56
4.2.3.1	Branch Beam Design .....	59
4.2.3.2	Estimation of Maximum Stress in the Branch Beam .....	62
4.2.3.3	Main Beam Design .....	63
4.2.3.4	Gap Verification .....	64
4.2.3.5	Verification of the Stability of the Beams .....	67
4.2.3.6	P versus $\theta$ .....	68
4.2.4	FEA Simulation of the Fork Hinge Structure .....	69
4.2.5	Summary of the Fork Hinge Design .....	73
4.3	Design of the Latching Spring and Lock Structure .....	74
4.3.1	Design Objective .....	74
4.3.2	Design Using Analytical Model .....	75
4.3.3	FEA Simulation of the Spring .....	79
4.3.4	Summary .....	80
4.4	Design of the Combdrives and Suspensions .....	82
4.4.1	Design Objective .....	83
4.4.2	Combdrive Design .....	83
4.4.3	Folded Flexure Design .....	86
<b>Chapter 5</b>	<b>Design of the Polymer Waveguides .....</b>	<b>88</b>
5.1	Design Objective.....	90
5.2	Calculation of the Parameters .....	90
5.3	BPM Simulation and Optimization of the Waveguides .....	94
5.3.1	2D BPM Simulation .....	94
5.3.2	3D BPM Simulation .....	108
5.4	Summary of Waveguide Design .....	112
<b>Chapter 6</b>	<b>Fabrication of the Optical Switch.....</b>	<b>113</b>
6.1	Basic Fabrication Steps.....	113
6.2	Fabrication Facilities .....	114
6.3	Layout Controlled One-Step Dry Etch & Release and Stiction-free Wet Release of MEMS Using DRIE/SOI .....	117
6.3.1	Introduction.....	118
6.3.2	Patterns and their release properties.....	119
6.3.3	The notching effect of DRIE on SOI wafer.....	121
6.3.4	Layout design rules for one-step release and easy wet release .....	125
6.3.5	Conclusion.....	129
6.4	Design of Masks.....	129
6.5	Fabrication of the Bi-stable Actuator.....	134
6.5.1	Photolithography.....	135
6.5.2	The Tweaked DRIE Process.....	136
6.5.3	Extra DRIE to Form Notches.....	140
6.5.4	Photoresist Removing and HF Wet Release.....	141

## Table of Contents

6.6	Fabrication of the Waveguides.....	142
6.7	Silicon-Polymer Bonding and Final Steps of fabrication.....	146
<b>Chapter 7</b>	<b>Test of the SWOMS.....</b>	<b>149</b>
7.1	Electro-mechanical Test.....	149
7.1.1	Assembly of the Spring Structure.....	149
7.1.2	Bi-stable Latching Functionality.....	150
7.1.3	Switching Speed and Natural Frequency Test .....	151
7.2	Test of the Waveguides and Optical switching.....	153
7.2.1	2x2 Optical Switching functionality of the Waveguides.....	155
7.2.1.1	Test Using Visible Light.....	155
7.2.1.2	Optical Switching Function Test of the Polymer Waveguides Using Infrared Light.....	156
7.2.2	Characterization of the Polymer Waveguides Using Infrared Light.....	159
7.2.2.1	The Propagation Loss of 4x9 $\mu$ m Core Straight Waveguide and Its Coupling Loss with Single Mode Fiber.....	160
7.2.2.2	Effect of the Taper on Fiber Coupling.....	162
7.2.2.3	Loss Due to Intersections.....	163
7.2.2.4	Bending Loss of the Polymer Waveguides.....	165
7.2.2.5	Coupling Loss Between 4x9 $\mu$ m core Waveguides.....	166
7.2.2.6	Propagation Loss and Crosstalk of the Waveguides Used on the SWOMS.....	167
7.2.3	Estimation and Analysis of Total Insertion Loss of the SWOMS..	169
7.3	Summary of the Tests.....	171
<b>Chapter 8</b>	<b>Conclusions.....</b>	<b>173</b>
8.1	Summary of the Report.....	173
8.2	Contributions.....	173
8.3	Directions for Further Developing.....	175
<b>Appendix A:</b>	<b>Calculation Programs for Maple 7.....</b>	<b>176</b>
<b>Appendix B:</b>	<b>Steps and Options of the ANSYS FEA Simulation.....</b>	<b>189</b>
<b>Publication list.....</b>		<b>191</b>
<b>References.....</b>		<b>192</b>

## List of Tables

Table 2.1: MEMS products example.....	14
Table 2.2: MEMS fabrication processes.....	17
Table 2.3: Comparison of all-optical switches .....	35
Table 5.1: Performance specifications of ZP49 and ZP51.....	89
Table 6.1: Result of the pattern release test .....	120
Table 7.1: Losses measured coupling single mode fiber with different lengths of straight waveguides with core size of $4 \times 9 \mu\text{m}$ .....	161
Table 7.2: Loss measurement of $60^\circ$ intersections.....	164
Table 7.3: Coupling loss measured between waveguides with core size of $4 \times 9 \mu\text{m}$ .....	167
Table 7.4: Loss measurement of the waveguides used on the SWOMS.....	168
Table 7.5: Characterization of bending loss of the waveguides used in the SWOMS.....	169
Table 7.6: Loss components and the estimated values.....	171

## List of Figures

Figure 1.1:	Distribution of venture-capital funding went into the optical switch markets in early 2001 (replotted) [11].....	4
Figure 1.2:	construction of 4 x 4 optical switch using 2 x 2 hybrid units (right) greatly reduces unit quantity needed as compare to using purely 1 x 2 switching units (left).....	11
Figure 1.3:	Gap exists between bending waveguide and fixed waveguide (upper image) and Gap reduction or even elimination by using real motion of the waveguide when switching (lower image).....	11
Figure 2.1:	Components of MEMS [38].....	14
Figure 2.2:	MOEMS and relative concepts [40].....	15
Figure 2.3:	Application of MEMS in Lightwave network [44].....	16
Figure 2.4:	A MEMS nonvolatile memory cell [43].....	18
Figure 2.5:	A bistable snapping microactuator [17].....	19
Figure 2.6:	Top and side view of the latching relay [13].....	20
Figure 2.7:	A multi-morph cantilever micro relay (top and cross section views) [16].....	20
Figure 2.8:	A multi-morph cantilever micro relay (latch and unlatching procedures) [16].....	21
Figure 2.9:	Time-division multiplexed (TDM) channel combines slower signals to make faster ones, stepping up a hierarchy defined by standards from a single voice channel to 10 Gbit/s or more [41].....	23
Figure 2.10:	DWDM Optical network elements [68].....	24
Figure 2.11:	Interoperate of all-optical switch (OOO) and OEO switch. [42].....	26
Figure 2.12:	3-D MEMS optical switch architecture [42] .....	27
Figure 2.13:	A mirror cell of the 3-D MEMS switch [44] .....	27
Figure 2.14:	2-D free space MEMS optical switches [3] [49] .....	28
Figure 2.15:	The OLIVE structure of NTT [50] .....	29
Figure 2.16:	Compact Latching-Type Single-Mode-Fiber Switches [53] .....	30
Figure 2.17:	A silica-based thermo-optic switch [54] .....	31
Figure 2.18:	A 2×2 liquid crystal optical switch [9] .....	32
Figure 2.19:	An optical switch based on moving waveguides #1 (by M. Horino et al.) [36] .....	33
Figure 2.20:	An optical switch based on moving waveguides #2 (by E. Ollier et al.) [6] .....	33
Figure 2.21:	An optical switch based on moving waveguides #3 (by T. Bakke et al.) [66] .....	33
Figure 2.22:	Calculated transmission loss as a function of air gap for SOI-based switch with polymeric waveguides [66] .....	34
Figure 3.1:	Schematic drawing of the self-latching device after etching and	



## List of Figures

	release.....	36
Figure 3.2:	Components of the self-latching device .....	37
Figure 3.3:	Self-latching principle .....	38
Figure 3.4:	Self-latching device using hinges .....	39
Figure 3.5:	Fork Hinge structure and flexible beam .....	40
Figure 3.6:	Deformation of flexible beam .....	40
Figure 3.7:	Comparison of deformation of Fork Hinge and flexible beams under the same forces condition .....	41
Figure 3.8:	Comparison of behavior of Fork Hinge and flexible beams under the same deformation $S_x$ .....	42
Figure 3.9:	Structure of a combdrive actuator .....	43
Figure 3.10:	Working principle of combdrive actuator .....	44
Figure 3.11:	The spring structure .....	44
Figure 3.12:	The spring assembly principle .....	45
Figure 2.13:	The situation before assembly .....	45
Figure 3.14:	Assembly step 1: apply voltage on the right combdrive .....	46
Figure 3.15:	Assembly step 2: apply voltage on the left combdrive and finish.....	46
Figure 3.16:	Left latching position .....	47
Figure 3.17:	Unstable middle position .....	48
Figure 3.18:	Right latching position .....	48
Figure 3.19:	The principle of a $1 \times 2$ SWOMS .....	49
Figure 3.20:	$1 \times 2$ SWOMS before assembly .....	50
Figure 3.21:	Switching principle of a $2 \times 2$ SWOMS .....	50
Figure 3.22:	Gap-reduction mechanism .....	51
Figure 4.1:	Fork Hinges used in SWOMS .....	54
Figure 4.2:	Fork Hinge design parameters .....	55
Figure 4.3:	Force analyses of the beams .....	57
Figure 4.4:	Force and moment analysis of the left branch beam .....	58
Figure 4.5:	$\theta_b$ (rad) versus $m_1$ (N·m) and $L_1$ (m) .....	60
Figure 4.6:	$\theta_b$ (rad) versus $m_1$ (N·m) when $L_1 = 400\mu\text{m}$ .....	61
Figure 4.7:	Main beam design .....	63
Figure 4.8:	Composition of the gap .....	65
Figure 4.9:	Calculation of $\Delta L$ .....	65
Figure 4.10:	Relation between $P$ and $\theta$ .....	68
Figure 4.11:	$P$ versus $\theta$ .....	69
Figure 4.12:	Fork Hinge structure for FEM simulation .....	70
Figure 4.13:	Von Mises stress (Pa) of Fork Hinge .....	70
Figure 4.14:	Stress at the beam connection point .....	71
Figure 4.15:	Contour plot of displacement in Y direction .....	72
Figure 4.16:	The displacement of the complete Fork Hinge structure .....	72
Figure 4.17:	Spring design parameters .....	74
Figure 4.18:	Spring deformation analysis .....	75
Figure 4.19:	Spring force analysis .....	76

## List of Figures

Figure 4.20:	The lock structure .....	78
Figure 4.21:	Spring FEA meshing .....	79
Figure 4.22:	Spring displacement ( $\mu\text{m}$ ) .....	79
Figure 4.23:	Spring stress (MPa) .....	80
Figure 4.24:	Reduced-order model of the Fork Hinge structure .....	81
Figure 4.25:	Simplified model (left) and force needed for switching (right) .....	81
Figure 4.26:	The design parameters of combdrive .....	82
Figure 4.27:	Moving range of the combdrives .....	84
Figure 4.28:	Two combdrives connected together. ....	86
Figure 5.1:	Waveguide and its cross-section .....	88
Figure 5.2:	Attenuation per radian for $E_{11}^x$ and $E_{11}^y$ modes if $n_1/n_2 = 1+\Delta$ and $\Delta \ll 1$ [76].....	92
Figure 5.3:	Calculated bending losses per radian at different radius .....	93
Figure 5.4:	2D effective index of a fiber .....	95
Figure 5.5:	structure for coupling simulation with infinite cladding.....	95
Figure 5.6:	Simulated coupling loss for different core sizes .....	96
Figure 5.7:	BPM 2D graph for fibers coupling with $4\mu\text{m}$ core waveguide .....	97
Figure 5.8:	The worst (top) and the best (bottom) coupling condition for $7\mu\text{m}$ core waveguide with varying length.....	97
Figure 5.9:	Coupling for $11\mu\text{m}$ core waveguides with fibers .....	98
Figure 5.10:	Coupling for $14\mu\text{m}$ core waveguides with fibers .....	98
Figure 5.11:	Setting for coupling simulation with finite cladding.....	99
Figure 5.12:	Coupling of fibers with $4\mu\text{m}$ core $20\mu\text{m}$ cladding waveguide .....	100
Figure 5.13:	Coupling of fibers with $11\mu\text{m}$ core $20\mu\text{m}$ cladding waveguide .....	100
Figure 5.14:	Structure for bend and coupling simulation with infinite cladding...	101
Figure 5.15:	Loss of fiber coupled with bent waveguides of different core sizes .....	101
Figure 5.16:	2D BPM intensity of bent waveguide with core size of $3\mu\text{m}$ , $6\mu\text{m}$ , and $11\mu\text{m}$ (top to bottom) .....	102
Figure 5.17:	The hybrid core size setting and 2D field intensity BPM graph of S-bended waveguide core size of $3\mu\text{m}$ , tapered to $12\mu\text{m}$ and couple with fibers .....	103
Figure 5.18:	Change from S-bend to SB-bend .....	104
Figure 5.19:	Simulated total loss VS radius of the SB-bend .....	104
Figure 5.20:	2D BPM coupling and bending simulation using finite cladding ...	105
Figure 5.21:	Size comparison of two curved cross structures with identical radius but different intersection angles.....	105
Figure 5.22:	Structure for simulation of intersecting waveguides .....	106
Figure 5.23:	Simulated Loss and Crosstalk when waveguides intersect at different angles.....	106
Figure 5.24:	2D BPM setting and result for real guide structure .....	107
Figure 5.25:	Waveguide structure for 3D BPM simulation .....	108
Figure 5.26:	The total loss for different waveguide core height in 3D BPM	

## List of Figures

	simulation.....	109
Figure 5.27:	BPM 3D Contour view .....	110
Figure 5.28:	2D field intensity plot at the cross-section $Y = 0$ generated by 3D BPM.....	110
Figure 5.29:	field intensity images at the cross-section of the input fiber (left) and the output fiber (fight) .....	111
Figure 5.30:	field images at cross-sections along axis $Z$ .....	111
Figure 6.1:	The double-sided mask aligner.....	114
Figure 6.2:	The spin coater.....	115
Figure 6.3:	DRIE system.....	115
Figure 6.4:	RIE system.....	115
Figure 6.5:	The e-beam evaporator.....	116
Figure 6.6:	The wet benches.....	116
Figure 6.7:	The optical microscope.....	116
Figure 6.8:	The SEM.....	117
Figure 6.9:	The wire bonding system.....	117
Figure 6.10:	Patterns for release test on 50 $\mu$ m thick SOI wafer.....	119
Figure 6.11:	Release test setting.....	120
Figure 6.12:	Cross-sections of the patterns showing the pattern-dependent notching appearing under the beam.....	121
Figure 6.13:	DRIE of trenches on SOI wafer.....	122
Figure 6.14:	The start and growth of the notching (Some beams disappear after 9mins and because they are completely released and flew away when we cut the sample).....	124
Figure 6.15:	The growth of the notch of trenches with 50 $\mu$ m depth and different widths.....	125
Figure 6.16:	Self-releasing beam (right) obtained by changing layout.....	126
Figure 6.17:	Structure destroyed due to overheating.....	128
Figure 6.18:	A totally dry released patterned structure and the bottom view.....	128
Figure 6.19:	Mask cell for the bi-stable actuator.....	130
Figure 6.20:	Application of the rules for one step etch & release process on the layout.....	130
Figure 6.21:	SEM picture shows the under-etching of the waveguide polymer in RIE process.....	131
Figure 6.22:	Mask layout of the waveguide core.....	131
Figure 6.23:	Mask layout of the waveguide cladding.....	132
Figure 6.24:	Superposition of the 3 masks in a cell.....	132
Figure 6.25:	Enlarged view of the superimposed masks.....	133
Figure 6.26:	The complete mask with multiple cells and all layers superimposed .....	133
Figure 6.27:	The alignment marks.....	134
Figure 6.28:	Fabrication process of the bi-stable actuator.....	135
Figure 6.29:	The RIE lag effect.....	137

## List of Figures

Figure 6.30:	2 $\mu$ m trench and 2 $\mu$ m beam fabricated with a standard recipe.....	137
Figure 6.31:	The dimension change of DRIE.....	138
Figure 6.32:	The beam and trench formed after the tweaked DRIE process.....	140
Figure 6.33:	Structures formed after extra DRIE.....	141
Figure 6.34:	SEM photo of the bi-stable actuator.....	142
Figure 6.35:	fabrication process of the waveguides.....	143
Figure 6.36:	The SEM picture of the waveguides core after RIE for 35mins.....	144
Figure 6.37:	(A) A photo of the waveguides polymer and patterned Au layer on quartz wafer before the final dry etching step. (B) The SEM image of the cladding shape of waveguides made on the quartz wafer.....	146
Figure 6.38:	The polymer-silicon bonding & fabrication.....	147
Figure 6.39:	the prototype of SWOMS.....	148
Figure 7.1:	a narrower gap between the fingers at the end of a combdrive.....	149
Figure 7.2:	The lock structure and the fork hinge before (left) and after assembly (right).....	150
Figure 7.3:	SEM pPhotos of a combdrive and a fork hinge when the actuator at its left (left) and right latching position (right).....	151
Figure 7.4:	The configuration for the electro-mechanical test of the actuator...	152
Figure 7.5:	Electro-mechanical response of the actuator (the drift after the signal edge is due to the capacitive coupling with a low frequency cut-off of 20Hz).....	152
Figure 7.6:	Facilities for waveguide testing.....	154
Figure 7.7:	Photos of a sandwiched waveguide sample.....	154
Figure 7.8:	Observation setting for switching function using visible laser.....	155
Figure 7.9:	Visible laser couples into different waveguides when moving the waveguides.....	156
Figure 7.10:	Infrared laser input from the fiber switches to the two outputs by moving the waveguides. The dashed lines were plotted on the images to indicate the locations of waveguide cores.....	157
Figure 7.11:	Field images recorded from the end of the single mode fiber (left) and the waveguide with 4x9 $\mu$ m core (right).....	158
Figure 7.12:	Setting for characterization of the polymer waveguides with infrared laser.....	159
Figure 7.13:	Setting to measure the reference fiber output power.....	160
Figure 7.14:	Setting for straight waveguide coupling with fiber.....	160
Figure 7.15:	Measured Loss VS Waveguide length when coupling single mode fiber with straight waveguides with core size of 4x9 $\mu$ m.....	162
Figure 7.16:	Setting for tapered core waveguide coupling with fiber.....	163
Figure 7.17:	Setting for measurement of the intersection loss.....	164
Figure 7.18:	Loss measured per intersection at different angles.....	165
Figure 7.19:	Setting for the bending loss measurement.....	166
Figure 7.20:	The bending loss measured for the polymer waveguide bends with different radii.....	166

---

## List of Figures

Figure 7.20:	Setting for measurement of waveguide/waveguide coupling loss....	167
Figure 7.21:	Setting for the test of waveguides used on the SWOMS.....	168

## Chapter 1 Introduction

New needs stimulate new technologies and inventions. New technologies in turn will find more applications.

Motivated by constructing a novel optical switch, we developed a new self-latching MEMS device, improved the technology of MOEMS with moving waveguides, and explored new fabrication processes. These new technologies benefit the optical switch described in this thesis, and more applications are expected to be found for them

### 1.1 Background

#### 1.1.1 Optical Switches and the SWOMS

With the rapid development of modern communication, the bandwidth of existing networks never seems broad enough. By some estimates, bandwidth usage in the Internet alone is doubling every six to twelve months. This growing demand for bandwidth takes its roots from consumers' needs like Internet, real-time video, teleconferencing, etc. Fiber-optic lines have been hailed as the ultimate speedway for information transmission. However, current networks are using only a small fraction of the potentially available bandwidth of fiber-optic transmission lines mostly due to the lack of more efficient networks' elements.

Dense Wavelength Division Multiplexing (DWDM) has been considered as the ultimate solution for the increasing need of bandwidth by most of the optical service providers. To reach this goal, different components for DWDM such as tunable sources and filters, optical switches, variable attenuators, and spectral equalizers are required. Especially, optical switches are key elements to manage the bandwidth capacity that DWDM provide to fulfill the increasing consumer demands. In DWDM

optical networks, optical switches are used for protection and restoration switching, remote provisioning and reconfiguration, wavelength add-drop switching, cross connects and circuit switching.

Optical switching is still a young technology, and both hardware and applications are evolving. Basically, optical switches can be divided into two broad categories. One is transparent or all-optical switch; the other is opaque or optical-electrical-optical (OEO) switch. OEO switches detect the optical signals from the input fibers, transform them into electrical signals, switch the electrical signals using solid-state components, and then convert the signals back to the optical form and send to the output fibers. In contrast, optical signals go straight through an all-optical switch without being converted into any other form.

OEO switches are well-established technology and are currently dominating the market. They have advantages including the ease of pulse reshaping, retiming, re-synchronizing by digital regeneration, and they allow performance monitoring of the stream. However, the OEO conversion is costly and can't keep pace with the rapidly growing demand for bandwidth. When DWDM is used with bit rates higher than 10Gbps (a high rate for electronics), OEO conversion must be eliminated to avoid mismatch and bottleneck problem at the switching and at the add-drop points.

The solution is all-optical switching, which will not only eliminate costly OEO conversion and bottlenecks and create new network service delivery options, but also eliminate costly upgrades by working immediately with new wavelength, increased line rates, and new protocols.

Although all-optical switching is not going to take off immediately, it will come sooner or later. Passed through the boom in 2001 and downturn in the last few years, the All-optical-switch market revives again in the year of 2005 [1].

Based on the different technologies, all-optical switches can be divided into several clans, and we will give more details and examples in the next chapter.

- Opto-mechanical Switches [2]. They are the conventional macro devices available so far, working by moving optical fiber or other bulk optic elements, but they are slow and expensive.
- MEMS Switches.
  - 1) 2-D Free-space MEMS Switches [3]. They have  $N^2$  architecture requiring  $N^2$  mirrors for  $N \times N$  switching, with digital controlled Mirrors that have only 2 positions.
  - 2) 3-D Free-space MEMS Switches [4]. Based on analogue feedback controlled mirrors that rotate freely. They usually use  $2N$  architecture ( $2 \times N$  mirrors) for  $N \times N$  switching.
  - 3) Bubble Switches [5]. Based on change of reflection at waveguide intersection by moving of bubbles in fluid-containing waveguides. It was inspired by the inkjet technology.
  - 4) Guided-wave MOEMS Switches [6]. Will be described in next sections, especially MOEMS switches with moving waveguides.
- Planar Lightwave Circuit (PLC) Switches [7] [8]. Usually based on Mach-Zehnder interferometer built by planar waveguides.
  - 1) Electro-Optic Switches. Based on electro-optic effect.
  - 2) Thermo-Optic Switches. Based on thermo-optic effect.
  - 3) Acoustic-optic Switch. Based on acoustic-optic effect.
- Liquid Crystal Switches [9]. Application of the technology coming from LCD video projector.
- Other types of switches. For example electro-holographic switch for large scale cross-connection [10].



As it is difficult to obtain all the features needed for a “perfect” all optical switch, none of above kinds of optical switches has yet dominated the market. So far, opto-mechanical switches are mature, but they are expensive macro devices and their switch speed is slow. PLC switches are quick, and are solid-state devices with high reliability, yet they have disadvantages such as wavelength dependence, high crosstalk and high insertion loss. From Figure 1.1, MEMS switches are considered as the most promising and are under development or even commercialized by companies and universities all around the world. 3-D free-space MEMS switch is currently the most suitable for large-scale optical cross-connects (OXC) (from  $32 \times 32$  to more than  $1000 \times 1000$  ports) due to their  $2N$  structure, but their complicated feedback loop control method prohibits them to be used for small-scale OXC ( $1 \times 2$ ,  $2 \times 2$ ,  $1 \times N \dots$ ) and other applications. 2-D free-space MEMS switches are becoming mature for small and moderate scale OXC and other applications. However, for 2-D free-space devices, collimators for each optical channel are usually needed, and insertion loss uniformity is a problem because they usually present different collimator-mirror distances for different light channels. MOEMS switches with moving waveguides can combine the merits of free-space MEMS switch and PLC switch, and overcome their shortcomings simultaneously, but existing devices suffer from high insertion loss due to gaps between connected waveguides.

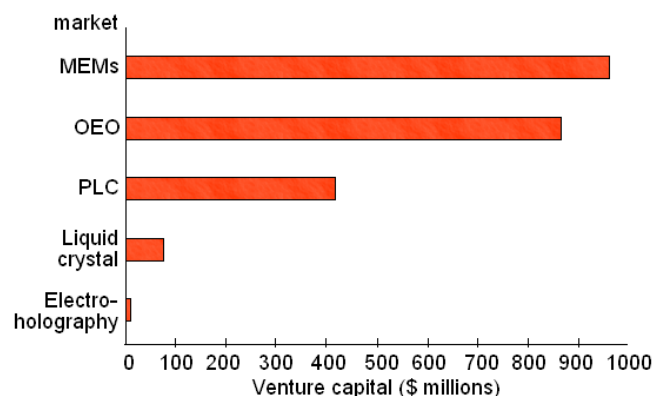


Figure 1.1: Distribution of venture-capital funding went into the optical switch markets in early 2001 (replotted) [11]

A novel optical switch based on MOEMS with moving polymer waveguides technology and the newly developed bi-stable self-latching technology, named as

Self-latching Waveguides Optical MEMS Switch (SWOMS), is introduced in this work. The perfect combination of these two technologies featured SWOMS with waveguide gap reduction to reduce the loss and bi-stable self-latching. Combined with other technologies such as U-groove for fiber attachment, integrated electrostatic comb drive actuator, and digital control, SWOMS shows very promising features including:

- Low insertion loss. This is attributable to alignment precision between waveguides with MEMS fabrication, optimization of the waveguide design, and the allowing reduction of air gap between fixed and moving waveguide sections. An insertion loss below 3dB is estimated.
- Good port-to-port loss uniformity. As the light signal from different ports pass through same length of same sized waveguides, and the propagation loss can be adjusted by changing the waveguide length, the loss can be kept uniform.
- Ultra low power consumption. This is due to the electrostatics actuation method and the self-latching feature.
- Low cost. Low cost comes from the MEMS batch fabrication process, digital control method without complicated control electronic circuit, U-groove for easily fiber attaching, no need of expensive components such as collimators, and a reduced assembly cost.
- Good switching speed. This is due to the simple switching method and the electrostatic actuator with speed below 0.5 milliseconds, which is fast enough for different applications.
- Low crosstalk. Crosstalk is the interference between different channels, which can be easily controlled in our moving waveguides structure to below -36dB.
- Maintain connection without power. A latching switch retains its state in the event of power failure, allowing the connection through the switch to remain unaffected.

- Low polarization dependence. Polarization dependence exists in some optical switches such as liquid crystal switches, PLC electro-optic switches, and some guided-wave active components. Switching by moving waveguides will show extremely low polarization dependence.
- Negligible wavelength dependence. This is also due to the moving waveguides switching method.
- High reliability. As the light signal is constrained in the waveguides, and the waveguides are latched in their work position, the connection is highly reliable. Because of the pure mechanical self-latching, SWOMS should be robust to EMI (electromagnetic interference) and vibration exposure.
- Long lifetime. MEMS devices with no friction have shown very long lifetime, e.g. 100,000 hours for DMD (Digital Micromirror Device) [12].
- Scalability. Unlike other moving waveguide switches that have only 1x2 basic units, the basic units of SWOMS can appear as 2x2 and 1x2. It is expandable to 1x4, to 1xN, and 4x4, to NxN due to its digital control method. And the introduction of 2x2 unit greatly reduces the unit quantity needed for NxN switch.

One of the identified problems of SWOMS is that it has  $N^2$  architecture for  $N \times N$  switching. Like 2-D MEMS switches, it is not suitable for large scale OXCs. However, SWOMS will easily find a role in optical communication applications such as small-scale OXCs, add-drop switch, or for protection, restoration, and provisioning.

### 1.1.2 Self-latching Actuator

Self-latching MEMS devices are micro actuators that can be latched at two or more of their working positions. As electronic devices become more and more digital, self-latching improves the performance of devices by being inherently stable without drift or change induced by the environment. It is a very useful feature for many MEMS applications such as switches, relay, and valves.

Perhaps the most important advantage of self-latching device is that it consumes very small energy. This is a critical feature in applications such as RF communication, portable electronics and aerospace, where power consumption must be minimized; and it also benefits most applications by the reduction of heat dissipation.

In addition, such devices inherently possess a memory function, thus can be utilized as memory cells, logic elements, or configuration elements.

Although common in macro devices, self-latching is not easy to realize in the micro world because of the limitation of the material, restriction of MEMS fabrication method, and some other special problems of micro-scale like very quick wear out of working surface. Thus most of the existing latching macro mechanisms cannot work with MEMS. To date, a few approaches have been proposed in other labs. One approach utilizes the operation of an electromagnet to actuate a soft magnetic armature and a permanent magnet to latch [13-15]. This is not a suitable mechanism in MEMS domain because relatively higher working electric current and the need for magnets makes such device not so compatible with MEMS fabrication process and presumably expensive. Another approach uses thermal actuator to bend a beam and utilizes a block or spring to latch [16-17]. Such devices perform quite well. Yet the thermal actuator method means relatively slower response, large power consumption and heat generation during operation, which cancel out some merits of the self-latching. Other early approaches for limited applications include buckled bridge based on residual-compressive-stress [18], position holding using static friction [19], and shape-memory-alloy devices. It seems the most attractive solutions are those utilizing pure mechanical properties of spring like structures based on sophisticated calculation to predict their behavior. E. g. a spring system for a bi-stable switch [87].

A novel self-latching MEMS device is introduced in this work. The device has only one structural layer and can be easily fabricated with MEMS process. It uses electrostatic combdrives as actuators and has a purely mechanical latching mechanism without friction between components. These features assure low power consumption,

high speed, long lifetime, and stable performance as it is essentially immune to EMI and temperature variation. Furthermore, because the movable components of the device move in the wafer plane in both x and y direction, the structure is flexible enough to be used as an actuating element for many applications.

### 1.1.3 MOEMS with Moving Waveguides

Micro-Opto-Electro-Mechanical Systems (MOEMS), or optical MEMS, are often considered as optical application of MEMS. During the past years, many MOEMS architectures, including micromirrors, microlenses, modulators and switches, microchoppers, microplatforms for optics, scanners, integrated optical sensors and other devices with optical functions have been developed. The application areas of MOEMS demonstrated by numerous prototypes include optical communications, digital image acquisition, presentation and processing, IT peripherals, automotive, astronomy, environment, biomedical devices, and industrial maintenance.

Many MOEMS that have reached high performance level are based on deforming micromembranes or moving micromirrors that can be easily fabricated by MEMS process. Examples of deforming membranes include spectral equalizers [20], reflection modulators [21], tunable sources and filters based on Fabry-Perot interferometers [22], or adaptive optics [23]. In the case of moving micro mirrors, Examples include DMD (Digital Micromirror Device) by Texas Instrument [24], two-dimensional (2-D) optical cross-connect matrix or three-dimensional (3-D) optical cross-connect matrix [25], optical switches and attenuators [26].

In all these structures, light propagates in free space, so that they belong to the category of free-space MOEMS. The rapid progress of MEMS technology, integrated optoelectronics, and micro-optic technologies in the past 10 years enables the combination of photonic components to activate and power conventional MOEMS structures. In the recent years, another category of MOEMS devices, named as guided-wave MOEMS, has been attracting interest. In such devices light propagates in waveguides instead of free-space.

Guided-wave MOEMS is the integration of planar waveguides with micromachined structures for optical application. This combination of waveguides and MEMS structure can take advantage of both technologies. On one hand, light can be guided better and in a more flexible way in waveguides than in conventional free-space MOEMS, and for example, it eliminates the expensive collimators often used in free-space MOEMS. On the other hand, MEMS structures provide new methods to control waveguides other than electro-optic or thermo-optic effect used in conventional planar lightwave circuit, in which special materials like lithium niobate ( $\text{LiNbO}_3$ ) are needed.

Some operation mechanism and application of guided-wave MOEMS have already been demonstrated. For instance, optical switches with moving waveguides [6], devices with moveable microstructure placed above the waveguide to spoil the waveguiding action [28], optical modulators based on Mach-Zehnder interferometer and evanescent interaction [29], optical pressure sensor based on evanescent interaction or elasto-optic effect [30], vibration sensor [31], distance sensor [32], chemical or biosensors [33], and nanoprobe for near-field optical microscopy [34].

Here we concentrate on MOEMS with moving waveguides. This mechanism can be applied as optical switch [6, 36], sensor [31] and scanner [35]. MOEMS with moving waveguides are especially attractive for optical switching because they are characterized by low insertion loss, low wavelength and polarization sensitivity, high extinction ratio, low power consumption and are suitable for mass production. Ollier et al. in LETI [6] and M. Horino et al. [36] have demonstrated their optical switches with moving waveguides separately with different actuation method. LETI even has commercialized their design through a start-up company.

In these previous approaches, the waveguides are simply bent but no translation occurs, therefore, there has to be a gap between the bent waveguide and the fixed waveguide all the time (Figure 1.3). This gap is one of the main sources of the insertion loss of such devices, and the insertion loss limits the scalability of the switch.

In addition, existing devices with bending waveguide can provide only  $1 \times 2$  basic switching units. When constructing them to an  $N \times N$  architecture, a large amount of units and many layers of cascading are needed, which increases the complexity, cost and optical loss.

In this report, the waveguides will not only be bent, but also really move in the plane. Polymer waveguides that can be easily processed and added to microstructure by postprocessing before the release of the microstructure are introduced in our approach.

The SWOMS can be configured as  $2 \times 2$  and also  $1 \times 2$  units. Our  $2 \times 2$  capability is first seen in the category of optical switches by moving waveguides, which greatly reduces the quantity of units needed to construct larger scale OXCs. Thanks to the connection in planar waveguides circuit, the larger scale OXC switch may be built without assembly of the units. In a broadcast & select (B&S) architecture [27] used for larger scale OXCs, 24 units cascaded in 4 layers are needed for a  $4 \times 4$  switch if using pure  $1 \times 2$  units. By using hybrid  $1 \times 2$  and  $2 \times 2$  units, only 12 units (four  $2 \times 2$  units and eight  $1 \times 2$  units) cascaded in 3 layers are needed, as shown in figure 1.2. In the case of  $8 \times 8$  OXC, a configuration using only  $1 \times 2$  switches needs 112 units in 6 layers, while 64 units (16  $2 \times 2$  units and 48  $1 \times 2$  units) in 5 layers are needed for a hybrid configuration. The above configurations are strict-sense nonblocking connector. If using rearrangeable non-blocking connector, even smaller amount of units is needed. E.g. the Benes network uses 20  $2 \times 2$  units in 5 layers to form an  $8 \times 8$  cross-connection.

As the polymer has Young's modulus 2 orders of magnitude smaller than the structural material like silicon, polymer waveguides can be easily deformed without influencing the actuating structure. The deformation and moving of the polymer waveguides provide much more flexibility to design MOEMS with moving waveguides, and the gap between movable and fixed waveguides can be reduced to nearly zero (Figure 1.3).

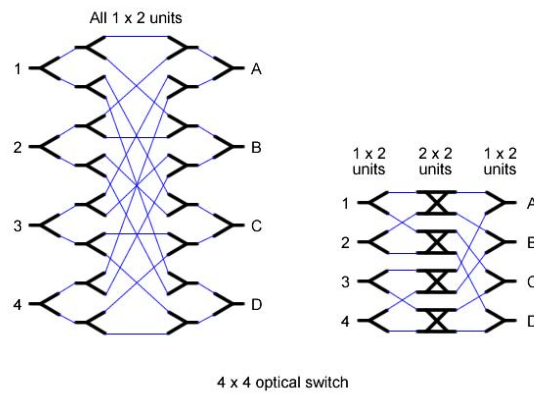


Figure 1.2: construction of 4 x 4 optical switch using 2 x 2 hybrid units (right) greatly reduces unit quantity needed as compare to using purely 1 x 2 switching units (left)

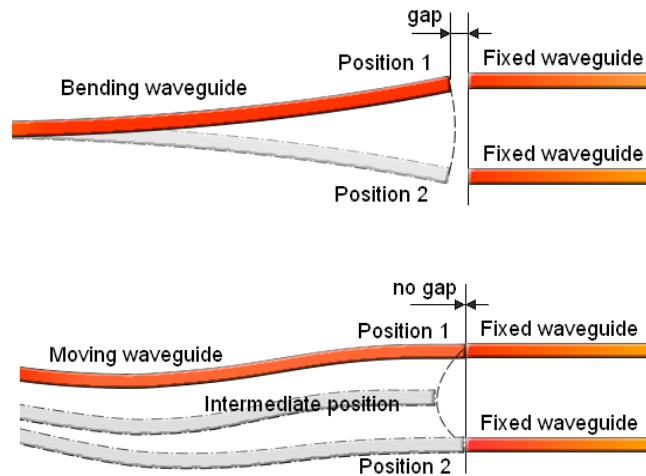


Figure 1.3: Gap exists between bending waveguide and fixed waveguide (upper image) and Gap reduction or even elimination by using real motion of the waveguide when switching (lower image)

## 1.2 Objective and Scope

The main objective of this project is to develop a novel self-latching MEMS optical switch named the Self-latching Waveguides Optical MEMS Switch (SWOMS) and exploit its application in optical communication.

To reach the objectives, the research scope covers the following topics:

- Develop a bi-stable self-latching actuator that is suitable for MEMS applications. Develop some novel components for the actuator, e.g. the Micro Fork Hinge and the pre-compressed micro spring.



- Design, simulation and optimization of the waveguides for a 2x2 switching unit. Try to establish rules for the design of waveguides coupled with fibers.
- Develop the 2x2 SWOMS featuring with self-latching and gap-reduction, and study its applications
- Study the new process technologies for the fabrication of SWOMS, e.g. some layout design rules lead to one-step release and stiction-free release of device built by DRIE on SOI wafer, and new technology for polymer-silicon bonding
- Fabricate and test the SWOMS

### 1.3 Organization

The report is divided into seven chapters. After this first introduction chapter, we will proceed to chapter 2 with the literature review. It will give some background knowledge on MEMS, MOEMS, self-latching devices, optical networks, and optical switches, helping readers to understand the concepts used in this work. Chapter 3 describes the basic structure and working principle of the switch. This chapter comprehensively depicts how the 2×2 switch works and how all the features of the switch i.e. self-latching, self-assembly and gap reduction can be obtained by the novel structures. Then, in chapter 4 the analytical calculation, digital simulation and design of the actuator are presented. Chapter 5 clarifies the optical simulation and optimization of the polymer waveguides. Chapter 6 describes the fabrication and testing of the switch. The fabrication process along with the new technologies developed, the masks used for photolithography, the fabrication result, and the testing results will be described and analyzed in detail. Finally, in chapter 7 we give the conclusion of this thesis and a look in the future of the project.

## Chapter 2 Literature Review

This Chapter will introduce the concepts of MEMS, MOEMS, and micro fabrication technologies, present some existing self-latching devices, and discuss the necessity of all-optical switch by depicting the development of fiber-optical telecommunication. Then different kinds of existing all-optical switches or that are under development will be described. Finally, a feature comparison of SWOMS with other all-optical switches will be presented.

### 2.1 MEMS and MOEMS

Micro Electro Mechanical Systems or MEMS is a term coined around 1989 by Prof. R. Howe and others [37] to describe an emerging research field, where mechanical elements, like cantilevers or membranes, had been manufactured at a scale more akin to microelectronic circuit than to lathe machining. But MEMS is not the only term used to describe this field and from its multicultural origin it is also known as Micromachines, a term often used in Japan, or as Microsystem Technology (MST), in Europe. MEMS is the integration of mechanical elements, sensors, actuators, and electronics through the utilization of microfabrication technology. MEMS makes the realization of complete systems-on-a-chip possible by bringing together silicon-based microelectronics with micromachining technology (see Fig. 2.1), and promises to revolutionize nearly every product category.

MEMS is a diverse, fertile and enabling technology which allows the development of smart products by augmenting the computational ability of microelectronics with the perception and control capabilities of microsensors and microactuators. The information of environment can be gathered by the microsensors including mechanical, thermal, optical, biological, chemical, and magnetic phenomena. And the microactuators respond to the quest of microelectronic by moving, positioning, regulating, pumping, motoring, and switching etc.

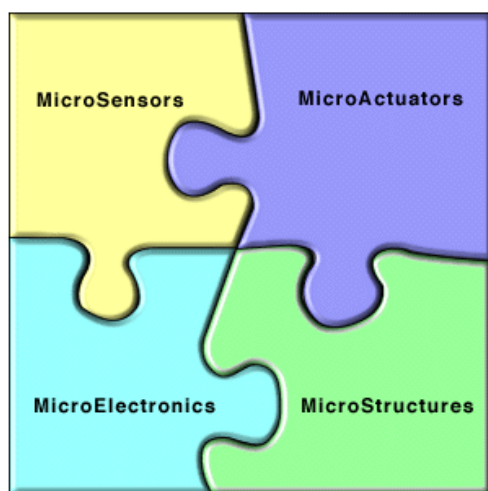


Figure 2.1: Components of MEMS [38]

The MEMS components currently on the market can be broadly divided in six categories (Table 2.1), the most well-known is pressure and inertia sensors produced by different manufacturer like Motorola, Analog Devices, Sensoror or Delphi we have many other products. The micro-fluidic application are best known for the inkjet printer head popularized by Hewlett Packard, but they also include the burgeoning bioMEMS market with micro analysis system like the capillary electrophoresis system from Agilent or the DNA chips. In 2002 these products represented a market of about 3.2B\$, with roughly one third in inkjet printer nozzle, one third in pressure sensor and the rest split between inertia sensors, RF MEMS, optical MEMS, projection display chip and bioMEMS [55].

Product category	Example
Pressure sensor	Manifold pressure (MAP), tire pressure, blood pressure...
Inertia sensor	Accelerometer, gyroscope, crash sensor...
Microfluidics / bioMEMS	Inkjet printer nozzle, micro-bio-analysis systems, DNA chips...
Optical MEMS / MOEMS	Micro-mirror array for projection (DLP), micro-grating array for projection (GLV), optical fiber switch, adaptive optics...
RF MEMS	High Q-inductor, switches, antenna, filter...
Others	Relays, microphone, data storage, toys...

Table 2.1: MEMS products example

Micro-Opto-Electro-Mechanical systems (MOEMS) can be defined as devices providing simultaneously mechanical, electrical, and optical functions, collectively fabricated by batch-process techniques coming from microelectronic fabrication [39]. The concepts relation to MOEMS is shown in Figure 2.2 [40]. MOEMS are also often called optical MEMS. By looking at the examples presented before, we see that many devices considered as MOEMS are, in fact, MEMS structures with optical applications.

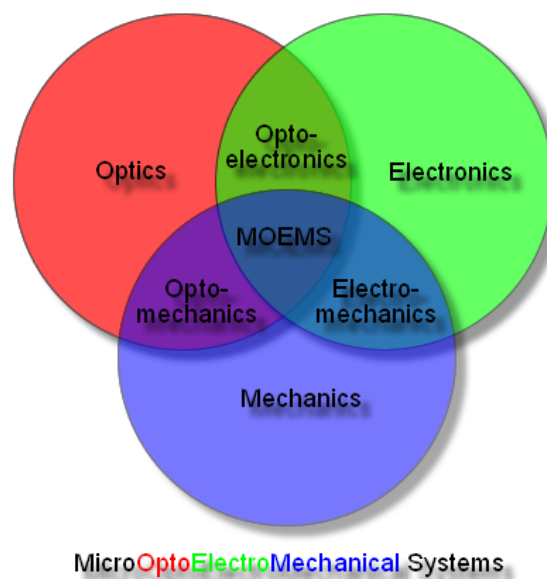


Figure 2.2: MOEMS and relative concepts [40]

Optical MEMS includes the component for the fiber optic telecommunication like the switch based on a moving mirror produced by Sercalo. They also include the optical switch matrix that is now waiting for the recovery of the telecommunication industry. This component consists of 100s of micro-mirror that can redirect the light from one input fiber to one output fiber, when the fibers are arranged either along a line (proposed by the now defunct Optical Micro Machines) or in a 2D configuration (Lambda router from Lucent). Moreover MOEMS deals with the now rather successful optical projection system that is competing with the LCD projector. The MEMS products are based either on an array of torsional micro-mirror in the Texas Instrument Digital Light Processor (DLP) system or on an array of controllable grating as in the Grating Light Valve (GLV) from Silicon Light Machines.

MOEMS become a big and important branch of MEMS because light can be easily deflected with nearly no force needed, which meet the force range of micro actuators, and the dimensions of microstructures range from fraction of wavelength to thousands of wavelength, which provide adequate methods to control light. The numerous demonstrations already existing highlight the following various potential application areas of MOEMS: optical communications, digital image acquisition, presentation and processing, IT peripherals, environment, automotive, astronomy, biomedical devices, industrial maintenance, and military. Figure 2.3 shows in lightwave systems where MEMS devices will be the technology solution of choice for network architects.

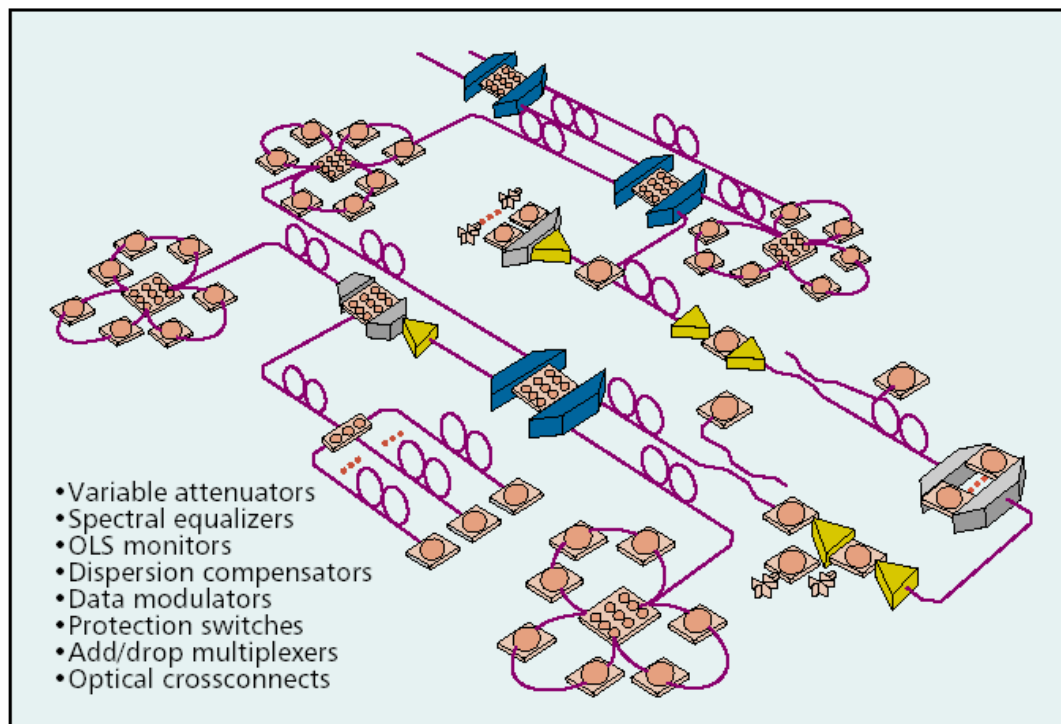


Figure 2.3: Application of MEMS in Lightwave network [44]

## 2.2 Micro Fabrication Technologies

Micro-fabrication is the set of technologies used to manufacture micro-sized mechanical devices. This task can unfortunately not rely on the traditional mechanical fabrication techniques such as milling, drilling, turning, forging and casting because of the small features needed. The fabrication techniques had thus to come from another source [77]. As MEMS devices have about the same feature size as integrated

circuits, MEMS fabrication technology quickly took logical inspiration from microelectronics. Techniques like photolithography, thin film deposition by chemical vapor deposition (CVD) or physical vapor deposition (PVD), thin film growth by oxidation and epitaxy, doping by ion implantation or diffusion, wet etching, dry etching, etc. have all been adopted by the MEMS technologists. However, as MEMS and IC fabrication are different, these techniques have often evolved as they were applied to MEMS and have developed new capabilities (Table 2.2). Moreover, MEMS has spurred many unique fabrication techniques like bulk micromachining, surface micromachining, deep RIE, LIGA, etc [62].

<b>MEMS Processes</b>	
<b>IC Processes</b>	<b>Micromachining Processes</b>
Oxidation	Bulk Micromachining
Diffusion	Surface Micromachining
LPCVD	Wafer Bonding
Photolithography	Deep Silicon RIE
Epitaxy	LIGA
Sputtering, etc.	Micro-molding, etc.

Table 2.2: MEMS fabrication processes

MEMS technology is not only about size although MEMS devices are extremely small. Furthermore, MEMS is not about making things out of silicon, even though silicon possesses excellent materials properties making it an attractive choice for many high-performance mechanical applications. Instead, MEMS is a new way of making complex electro mechanical systems using batch fabrication techniques similar to the way integrated circuits are made and making these electromechanical elements along with electronics. Historically, sensors and actuators are the most costly and unreliable part of a macroscale sensory-actuator-electronics system. In comparison, MEMS technology allows these complex electromechanical systems to be manufactured using batch fabrication techniques allowing the cost and reliability of the sensors and actuators to be put into parity with that of integrated circuits.

MEMS fabrication often tries to be a batch process to benefit from the same potential

low cost as IC. As such it often starts with a wafer (silicon, polymer, glass...) that may play an active role in the final device or may only be a substrate on which the MEMS is built. The wafer is processed with a succession of thin film deposition, doping, photolithography and wet/dry etching steps to form the device. The devices have then to pass through a special step to free the moveable mechanical parts called 'release step' which can be done before or after the dicing. Finally the components are assembled, packaged and tested.

## 2.3 Self-latching MEMS Devices

Bi-stable Self-latching is a very useful feature for many MEMS applications such as switches, valves, sensors, memory cells, logic elements, or configuration elements. However, self-latching is not easy to obtain in the micro world because of the limitation of the material, very quick wear out, and restriction of MEMS fabrication method.

An integrated nonvolatile memory cell based on MEMS technology developed by Beat Halg is shown in Figure 2.4 [43]. It consists of a thin micromachined bridge under compressive stress that buckle and it has two stable mechanical states to which the logical levels "0" and "1" are assigned. The state of the bridge can be changed using electrostatic forces and it may be read out by sensing the corresponding capacitance. Switching voltage around 30 V have been achieved and a huge number of write cycles with low read/write time are expected.

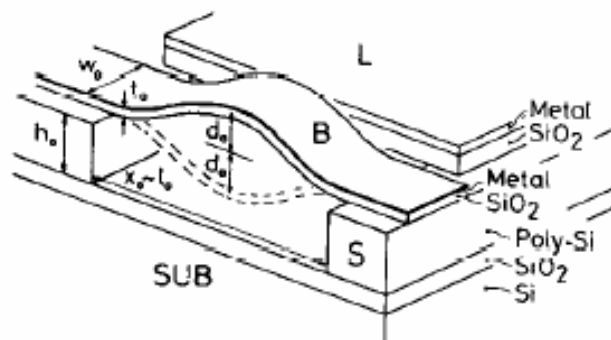


Figure 2.4: A MEMS nonvolatile memory cell [43]

Hirotsugu Matoba et al. reported a mechanical bistable switching device actuated by the interactive forces of a buckling cantilever and a tension band connected to its end (Figure 2.5) [17]. The device has been built using a combination of surface and bulk micromachining on materials familiar in IC fabrication: a silicon substrate, LPCVD poly-silicon, silicon nitride, and silicon dioxide. The switching element is a cantilever formed from three thin-film layers: polysilicon, silicon dioxide, and polysilicon. The cantilever is made to buckle as a result of strong axial force from a built-in tension band. The device is operated by heating the cantilever asymmetrically with a current of 7 mA at 24V for 12  $\mu$ s. The Joule heating in one of the two polysilicon layers gives rise to a snapping action that moves the cantilever end  $\pm 6 \mu$ m in a direction perpendicular to the underlying silicon substrate.

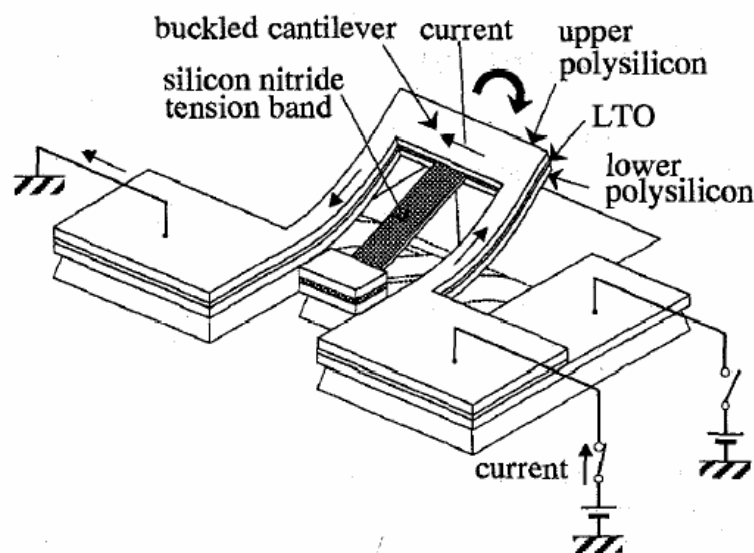


Figure 2.5: A bistable snapping microactuator [17]

M. Ruan et al. demonstrated a latching micro magnetic relay (Figure 2.6) [13]. The device is based on preferential magnetization of a permalloy cantilever in a permanent external magnetic field. Switching between two stable states is accomplished by short current pulse through an integrated coil underneath the cantilever.



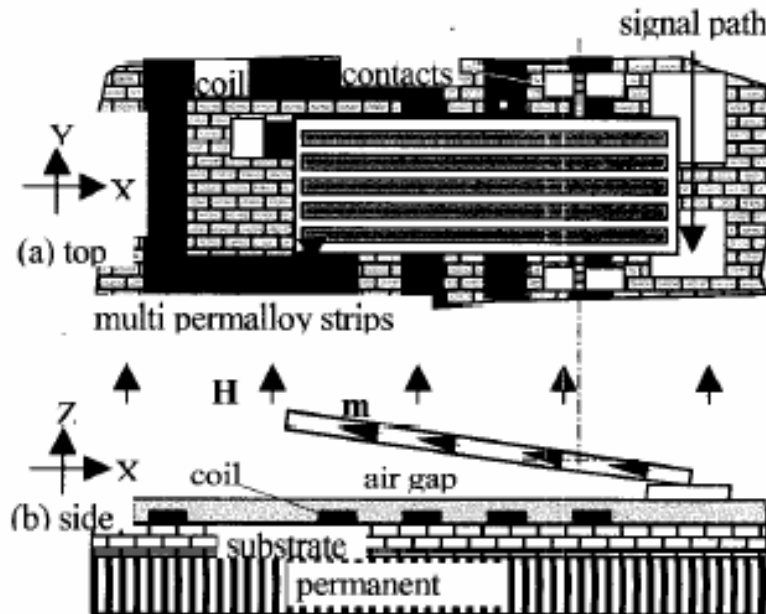


Figure 2.6: Top and side view of the latching relay [13]

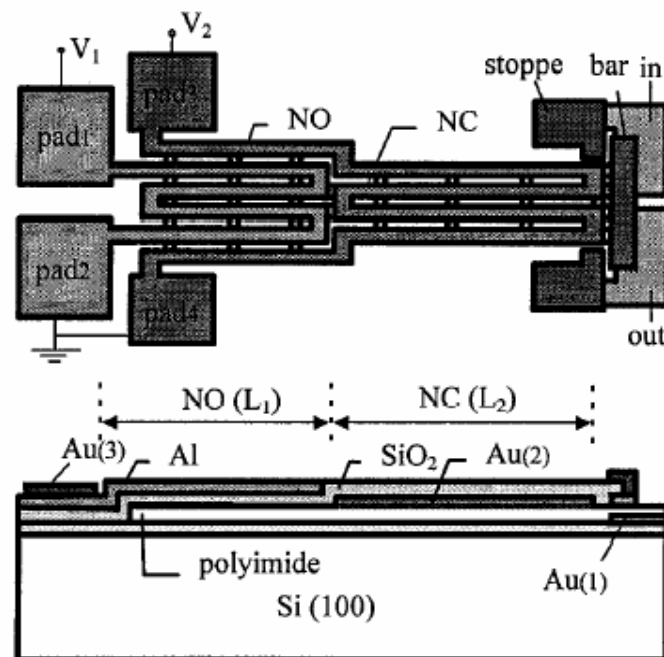


Figure 2.7: A multi-morph cantilever micro relay (top and cross section views) [16]

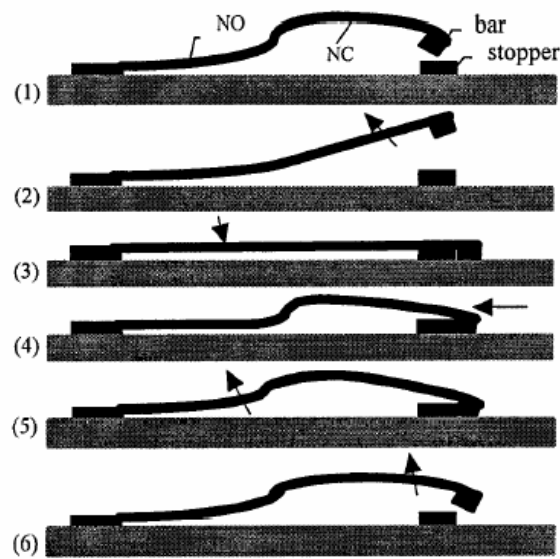


Figure 2.8: A multi-morph cantilever micro relay (latch and unlatching procedures) [16]

Figure 2.7 and 2.8 illustrate a surface micromachined bi-stable microrelay based on the latching of a two-segment multimorph cantilever actuator presented by Xi-Qing Sun et al [16]. The two-segment multimorph actuator is composed of two bimorph segment actuators that are connected with each other, one is normally open and the other is normally closed. The two bimorph segments can be actuated independently in such a way that the device has two stable mechanical latching states, namely, “on” and “off”, which can be electrically read out with large off/on resistance ratios. This bistable relay is operated by two separate thermal power pulse of 12 mW and 10 mW respectively.

Studying the above devices and others, there are four categories of bistable mechanisms that have been reported so far in MEMS: magnetic latching mechanism [13-15], latching by groove or block [16] [45], multi-segment mechanisms [46] [47], and residual-compressive-stress buckled-beam mechanisms [17] [18] [43]. As there is friction inside the latching by the groove or block mechanisms and multi-segment mechanisms, their short lifetime make such micro devices hardly practical for demanding applications. Magnetic latching mechanism is complicated to fabricate with MEMS fabrication process, and for buckled-beam mechanisms the residual stress in it is hard to precisely control.

Considering these problems, it seems that a better bi-stable self-latching mechanism should be purely mechanical, monolithic, without friction, no using residual stress and easy to fabricate. A novel bi-stable self-latching device with these features will be introduced in the next chapter.

## **2.4 Optical Networking and Switching**

### **2.4.1 Introduction to Optical Networking**

Optical networks are based on optical technologies and components that provide switching, routing, grooming, and restoration for high capacity telecommunication. Optical communications used to involve little more than the transmission of signals between points over an optical fiber. However, as customers demand new and different types of data traffic, more services and options, a new paradigm was needed for the network. Recently, this field has evolved to the point that not only can optical networks transmit signals optically, but they can also organize and process them in optical form. Optical networking is thought to provide the required bandwidth and flexibility to meet these demands, and the benefits include networks with increased capacity, speed, and versatility. Optical networking marks a fundamental shift in the architecture of fiber communications. The ultimate goal of optical networking is the so called all-optical network, in which signals stay in optical form throughout the network.

Telecommunication began in 1960s, when telephone planners set up a hierarchy of standard data rates based on time-division multiplexing of digitized signals. A digitized voice channels needs 56 or 64 kbit/s, As the volume of telephone traffic increased, planners added a family of higher data rates (see Fig. 2.9)., The advent of single-mode fiberoptics allowed much faster data rates, leading to the family of synchronous optical network (SONET), or synchronous digital hierarchy (SDH). The top data rates of SONET in practical use are 2.5 or 10 Gbit/s.

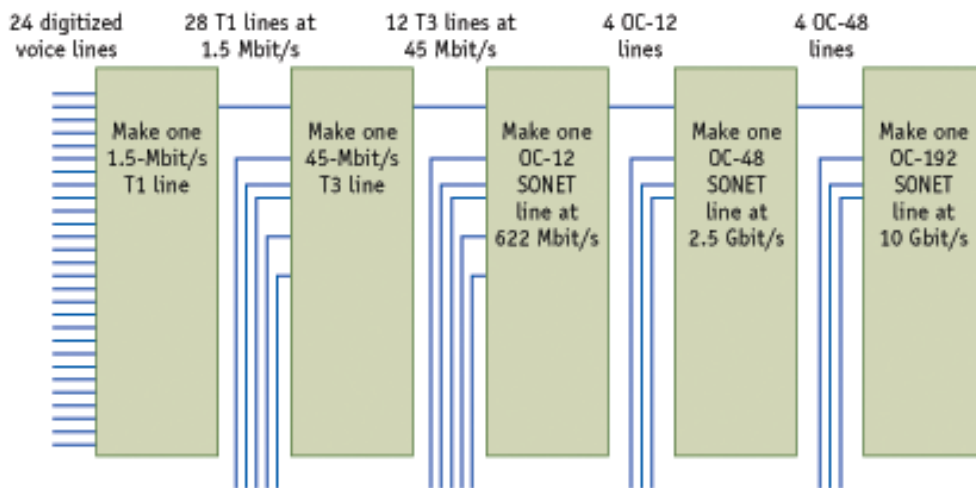


Figure 2.9: Time-division multiplexed (TDM) channel combines slower signals to make faster ones, stepping up a hierarchy defined by standards from a single voice channel to 10 Gbit/s or more [41].

The advent of wavelength-division multiplexing (WDM) in late 1970s was the first big step toward optical networking, when engineers realized that optical fibers could carry separate signals at different wavelengths. After the development of erbium-doped fiber amplifiers which could simultaneously amplify signals at multiple wavelengths, WDM was practically applied.

WDM is attractive because it multiplies the capacity of a single fiber by carrying 4, 8, 16, 32, 40 or more optical channels at different wavelengths. However, such a high capacity sets severe challenge to the traditional TDM system because the need to keep track of all the different components of the combined signal and demultiplex them when they reach their destination requires expensive electronic TDM multiplexer, corresponding receiver and demultiplexers to pick out the signals to process. A WDM system handles the optical traffic using a different, easy and better method. Optical components can separate one optical channel from the combined signal without electronics thus increased the signal granularity for telecommunications carrier. The optical channels become separate information pipelines through the same fiber, which the network operator can manage regardless of content.

Dense Wavelength Division Multiplexing (DWDM) is an extension of WDM which has the ability to combine hundreds of wavelength signals on a fiber as optical filters and laser technology improved, the DWDM optical network (Fig. 2.10)

promises carriers a better way to manage their growing volume of traffic. However, some serious challenges appeared when implementing optical networking. Fiber optic "pipes" are well-developed, but optical switching and signal management is in its infancy and further developments are needed.

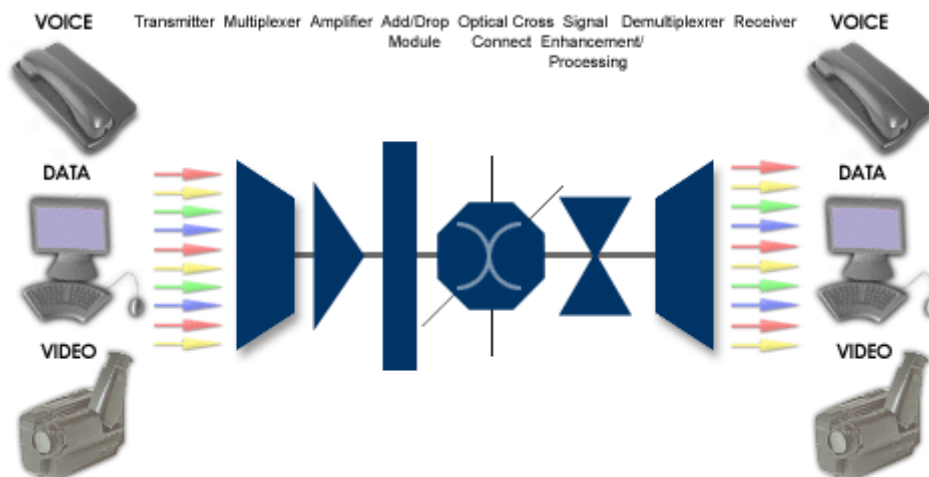


Figure 2.10: DWDM Optical network elements [68]

### 2.4.2 OEO and All-optical Switching

DWDM have been embraced by carriers for quickly respond to an increasing need for bandwidth, particularly in the long-haul core network. And it is also the foundation for the new-generation optical network. However, as DWDM delivers only raw capacity, service providers currently need to implement a solution to manage the bandwidth that DWDM provide. Optical switches present the answer. To guarantee a lower cost, and secure efficiency with new revenue-generating services, service providers have two choices of optical switches: the electronic-based OEO switches and the photonic-based, all-optical switch.

Basically, an optical switch maps wavelength from an input port to the appropriate output based on their destination. Let's look at some functions the optical switches can serve.

- Protection and restoration Switching. Protection switching is a simple but vital function. It redirects signals along a different path in case of cable break or equipment failure.
- Remote Provisioning and Reconfiguration. Provisioning is the changing of network configuration to alter the services delivered to customers, or to provide new services. The remote provisioning is used to save money and help telecommunications companies manage their networks more efficiently.
- Wavelength Add-Drop Switching. DWDM provides inexpensive bandwidth but can sacrifice routing flexibility, because diverting part of the traffic in a simple DWDM line system to an intermediate destination requires that all the remaining wavelength signals must be detected and regenerated. As the number of wavelength signals increases to 40 or more, the cost of providing DWDM repeaters on the transmitted channels becomes prohibitive. These repeaters can be eliminated using wavelength add-drop: a transparent optical component to divert selected wavelength signals out of a DWDM transmission line and also add new signals to rescue the dropped wavelength.
- Cross-Connects and circuit Switching. Cross-connects direct signals from any of N possible inputs to any of M possible outputs. It is the basic and most important function of optical switches.

An OEO switch is an optical switch that route information based on using electrical components. The input and output modules are optical, but receivers turn the photons to electrons for their journey over an electronic back-plane. At the output module, the electrons are converted back into photons to follow their path through a fiber transmission link. This is a flexible architecture which has the benefit of performing regeneration of the signal and allows SONET level performance monitoring of the stream. Other advantages of OEO switches including they are well-established technology, and as part of the optical/electrical conversion it is possible to get full digital regeneration including reshaping, retiming, and re-synchronizing the signals. However, this architecture has a higher price resulting from all the optical to electrical

conversions especially when keeping pace with the growth in capacity of optics in the near future and the rapid growing customer demand for bandwidth.

As optical layer and all-optical switch are emerging to meet the need for cost-effective bandwidth, delivering and managing this new layer and the services running on it has created the need for new, all-optical network elements and technologies. However in practice, the true promise of optical networking, including improved flexibility, manageability, scalability and the dynamic delivery of new revenue-generating services is best accomplished through the optimized deployment of intelligent OEO switches combined with the appropriate future integration of all-optical switches, as shown in Figure 2.11.

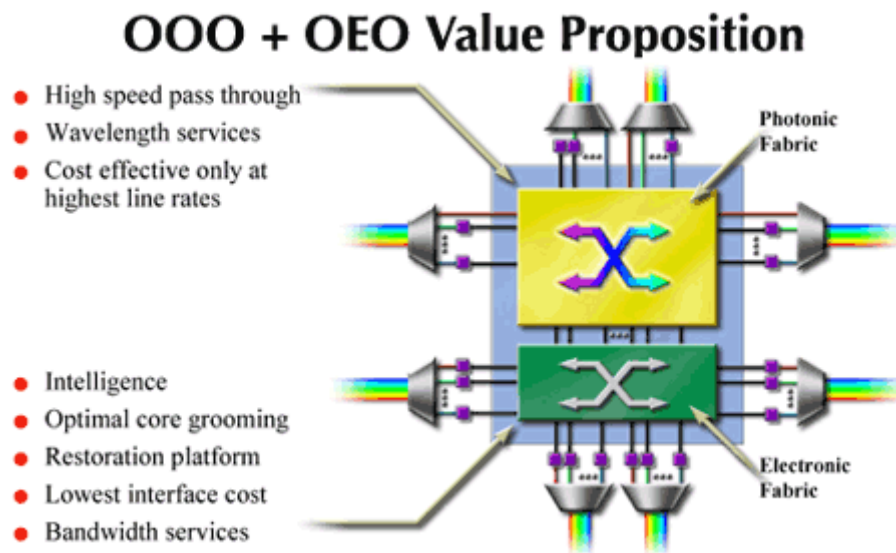


Figure 2.11: Interoperate of all-optical switch (OOO) and OEO switch. [42]

## 2.5 All-optical Switches

We have introduced in chapter 1 that depending on the technology involved, there are different kinds of all-optical switch. Some examples of all-optical switch will be presented in this section.



### 2.5.1 3D MEMS Switch

Figure 2.12 [42] and Figure 2.13 [44] show the architecture and a single mirror cell of a 3-D MEMS optical switch developed by Lucent. A 3-D MEMS switch has mirrors that can rotate about two axes. Light can be redirected precisely in free-space to multiple angles, at least as many as the number of inputs. This approach result in only  $N$  or  $2N$  mirrors needed for  $N \times N$  optical cross-connects switch. In this commercialized design,  $2N$  mirrors are used to minimize the insertion loss [48]. 3-D MEMS switches are considered as the leading candidates for building large-scale photonic cross-connects due to their  $2N$  architecture, yet they are not suitable for other applications because they use a complex feedback loop analog control method.

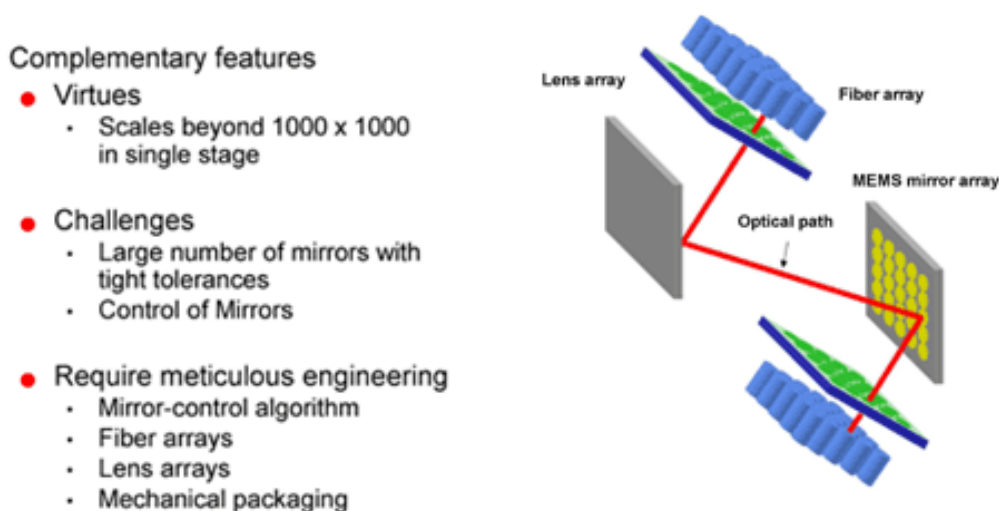


Figure 2.12: 3-D MEMS optical switch architecture [42]

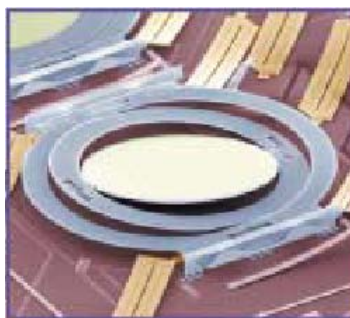


Figure 2.13: A mirror cell of the 3-D MEMS switch [44]



### 2.5.2 2D MEMS Switch

Toshiyoshi et al and Lin et al demonstrated typical 2-D free-space MEMS optical switches (see Figure 2.14) [3] [49]. Lightwave passes through a collimator, is reflected by a digitally controlled mirror or directly pass through to the receiver ports. The advantage of such design is that although  $N^2$  mirrors are needed for  $N \times N$  switching, lightwave is reflected only once, which avoids the stack up of the insertion loss. However, costly collimators are still needed, and as the light lines from different ports travel different distances in free-space, the uniformity of the insertion loss is a problem.

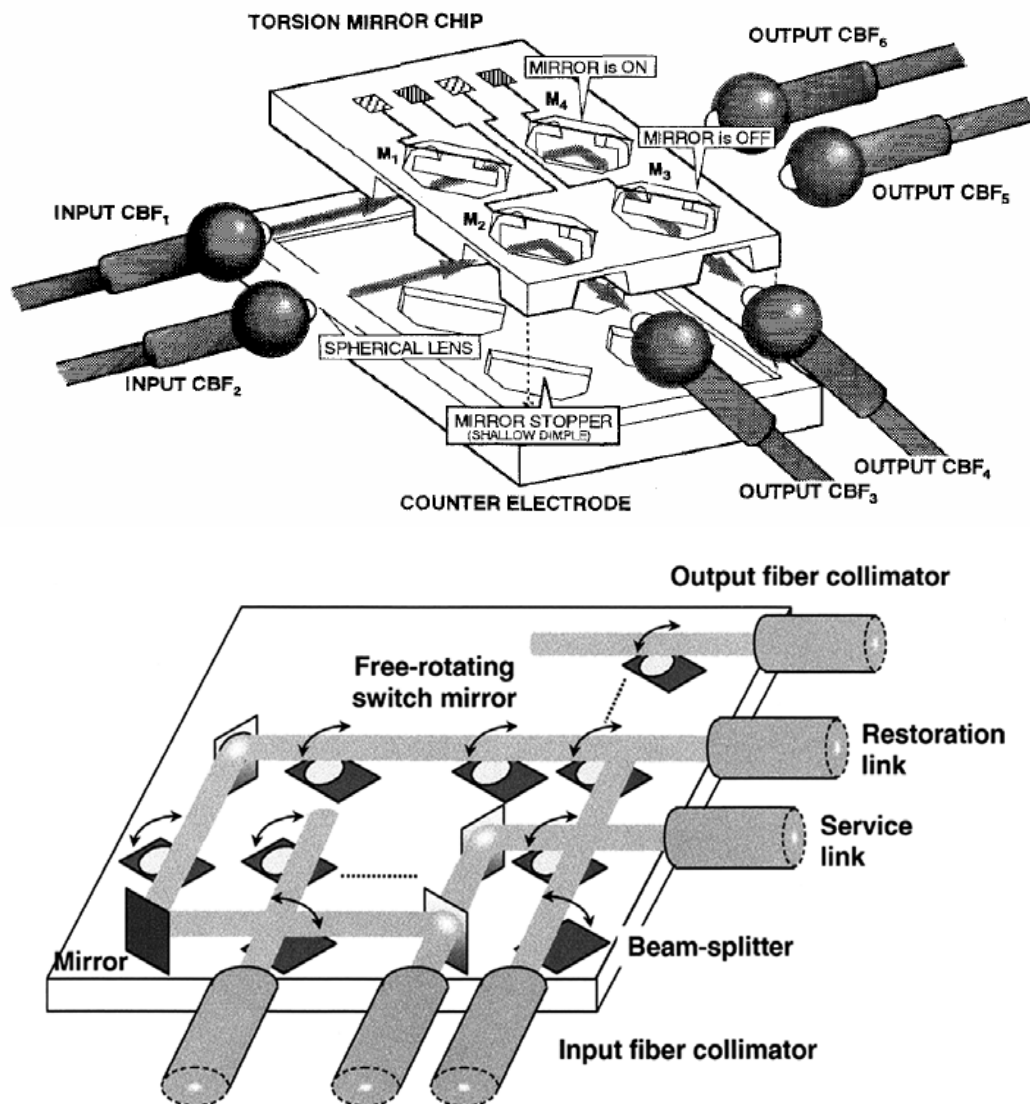


Figure 2.14: 2-D free space MEMS optical switches [3] [49]

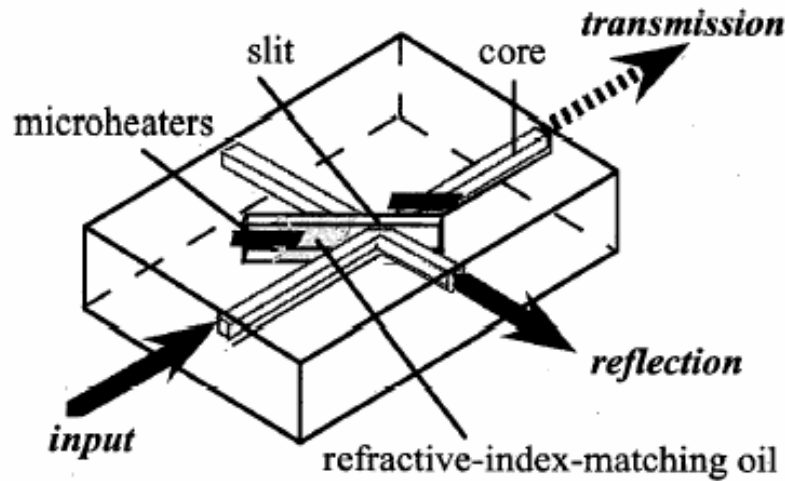


Figure 2.15: The OLIVE structure of NTT [50]

Makihara et al at NTT Opto-electronics Laboratories demonstrated a bubble MEMS optical switch called the oil-latching interfacial-tension variation effect switch (OLIVE) (see Figure 2.15) [50]. They have also proposed a multiarrayed  $2 \times 2$  switch and a  $16 \times 16$  matrix switch [51] that use OLIVEs. An OLIVE consists of a crossing waveguide substrate that has a groove at each crossing point and a pair of microheaters. The groove is partially filled with the refractive-index-matching liquid and is completely sealed by an upper lid. The microheaters are positioned so that they produce a thermal gradient along the groove. In the practical switch structure, the optical inputs and outputs will be connected to single-mode optical fiber arrays. The fundamental concept of the optical switching is as follows. The refractive-index-matching liquid in the groove is driven due to surface-tension variation caused by heating (thermocapillarity). When the liquid is present at the crossing point of waveguides, the optical signals pass straight through the groove; however, when the liquid moves away from the crossing point, the signals are switched into the crossing waveguide by total internal reflection (TIR) on the groove wall, i.e., at the silica–air interface. Agilent Laboratories [52] also commercialized a similar structure based on their inkjet printer technology but without self-latching function.

### 2.5.3 Opto-mechanical Switch

Figure 2.16 shows a compact latching-type single-mode-fiber switch developed by Shinji Nagaoka et al also at NTT [53]. Although some micromachining technologies are adopted during fabrication, it is indeed an opto-mechanical switch. In the developed switches, the magnetic attraction force produced between permanent magnets and a micromagnetic-alloy pipe fixed around the fiber actuate a movable fiber. The ultralight micropipes were successfully mass-produced by a fiber-micromachining technique based on metallizing and etching of sacrificial fibers. They used refractive-index-matching oil in the switches to reduce insertion loss and reflected light. A similar device is the fiber-optic switch demonstrated by Hoffmann et al. which uses thermo-mechanical actuator to move optical fibers [45].

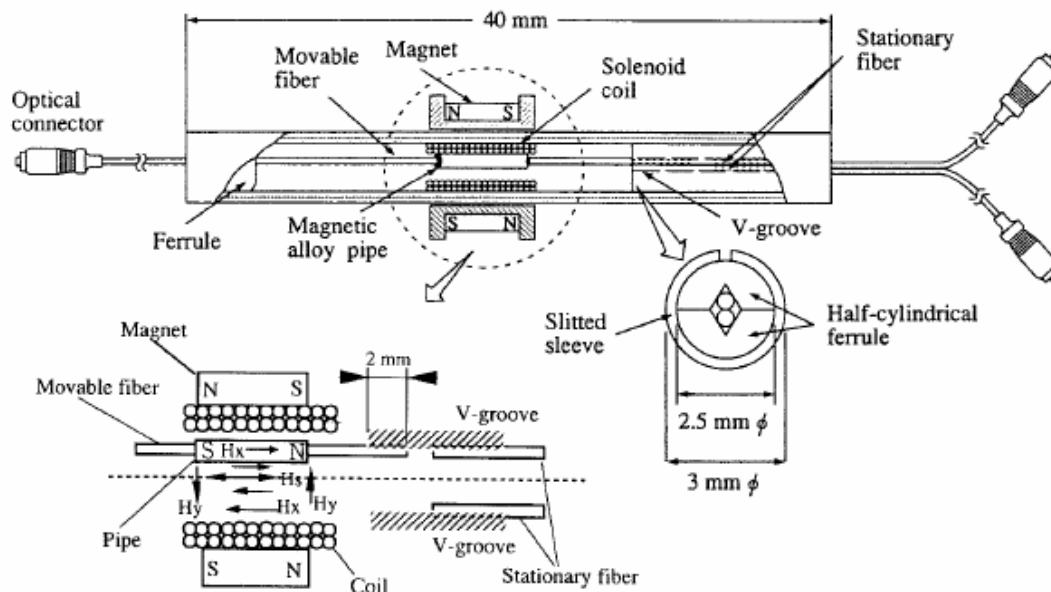


Figure 2.16: Compact Latching-Type Single-Mode-Fiber Switches [53]

### 2.5.4 PLC Switch

A planar lightwave circuit (PLC) thermo-optic switch is demonstrated in Figure 2.17 [54]. S. Sohma et al. developed this silica-based thermo-optic switch (TOSW) using PLC technology. The basic element of the TOSW is a  $2 \times 2$  switch with a Mach-Zehnder interferometer (MZI) configuration, and it operates by employing the

thermo-optic effect. The index of refraction change induced by heater changes the phase of one arm and interference with the signal from the other arm at the output. The power needed by this demonstrator has been optimized and reduced to much less than the 450mW that usually needed by a conventional TOSW.

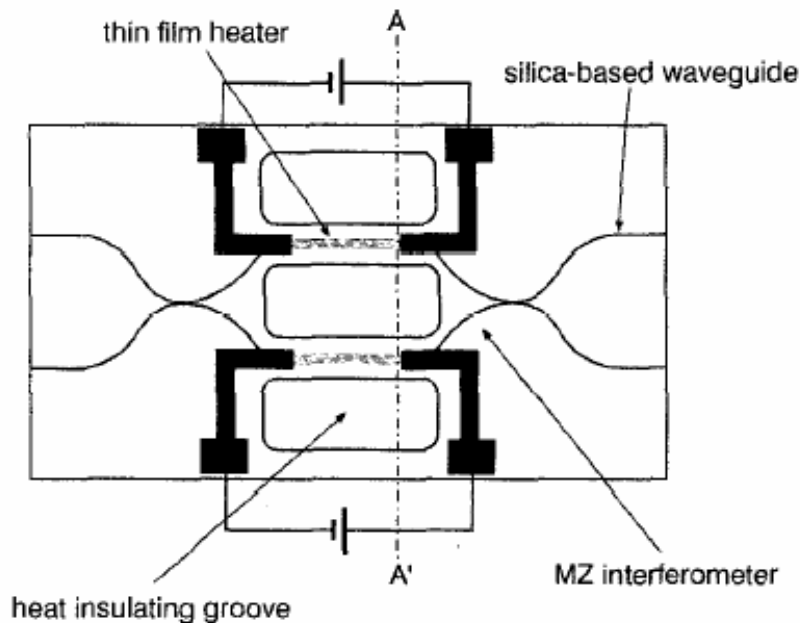
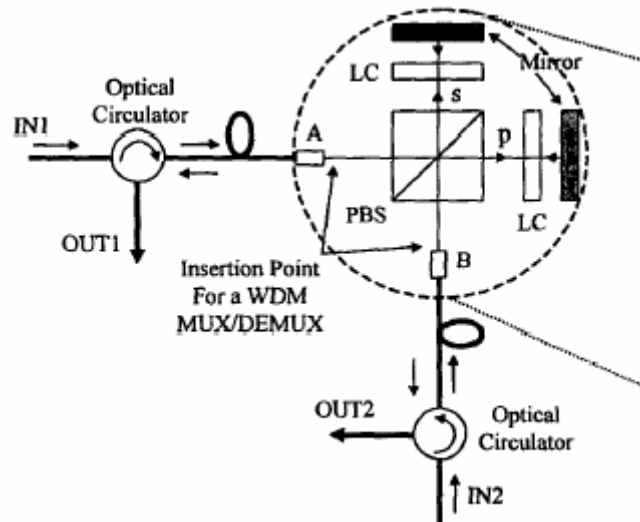


Figure 2.17: A silica-based thermo-optic switch [54]

### 2.5.5 Liquid Crystal Switch

Sarun Sumriddetchkajorn et al. demonstrated a  $2 \times 2$  optical switch based on ferroelectric liquid crystals (FLCs) (see Figure 2.18) [9]. It uses not only the FLC but also the cube polarization splitting optics to provide self-aligning and low polarization sensitivity via a reflective architecture. A  $2 \times 2$  switching element routes optical signals from two input ports to two output ports and has two states: straight state and exchange state. A pair of fiber collimators is used as the input and output. The other optical elements include a polarization beam splitter (PBS), and the two optical circulators. A crosstalk of  $-19.52\text{dB}$  and a loss performance of  $7.53\text{dB}$  have been reported.

Figure 2.18: A  $2 \times 2$  liquid crystal optical switch [9]

### 2.5.6 Moving Waveguide Switch

Figure 2.19 [36], Figure 2.20 [6], and Figure 2.21 [66] demonstrated three currently existing optical switches based on moving waveguides. In Figure 2.19 the device is actuated by electromagnetic force and has a latching function. In Figure 2.20 it is actuated by electrostatic combdrive and using silica-on-silicon waveguides. And in Figure 2.21 the device uses polymer waveguides and it is built on a SOI (silicon on insulator) wafer. Such structures combine the merits of free-space MEMS switch and PLC switch, characterized by low insertion loss, low wavelength and polarization sensitivity, high extinction ratio, low power consumption and are suitable to mass production. But all of them still suffer from insertion loss due to the gap existing between the moving waveguides and the fixed waveguides. This gap not only causes insertion loss, but also causes the problem of bad loss uniformity because the loss is very sensitive to the width of the gap (see Figure 2.22) [66]. The accumulation of these losses and the bad loss-uniformity limited the scalability of such devices. In addition, the basic switching unit is  $1 \times 2$ , which can be easily cascaded as a  $1 \times N$  switch, but will need many units to form an  $N \times N$  switch.

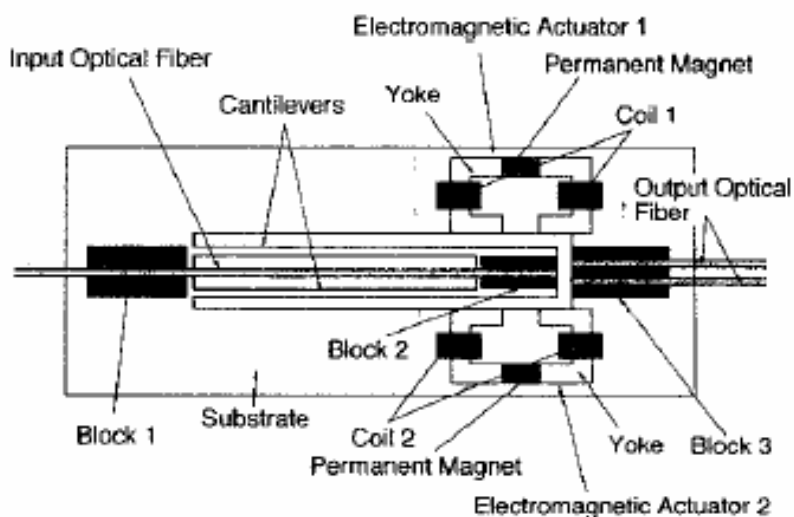


Figure 2.19: An optical switch based on moving waveguides #1 (by M. Horino et al.) [36]

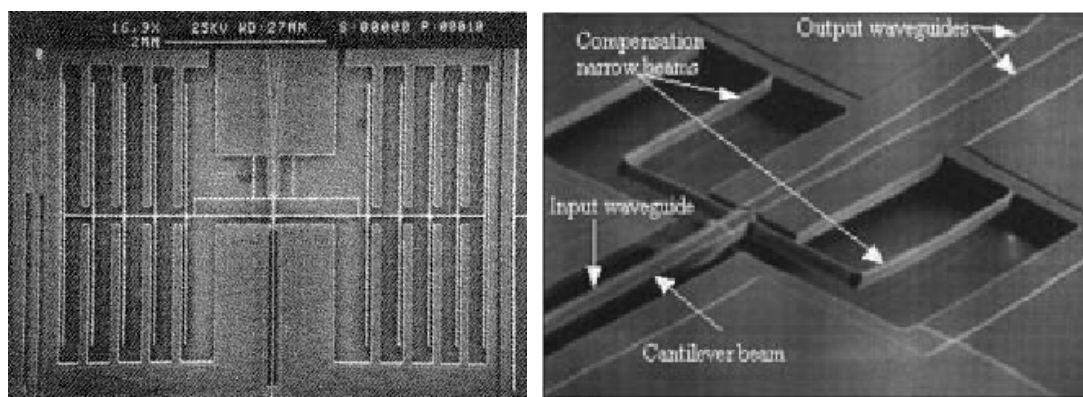


Figure 2.20: An optical switch based on moving waveguides #2 (by E. Ollier et al.) [6]

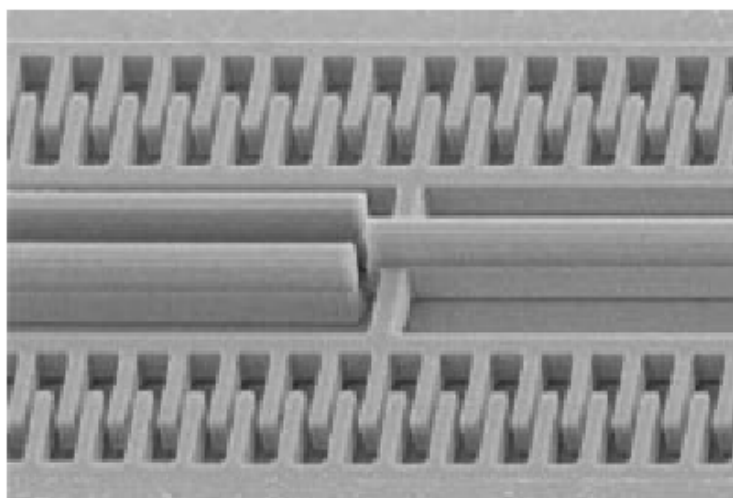


Figure 2.21: An optical switch based on moving waveguides #3 (by T. Bakke et al.) [66]

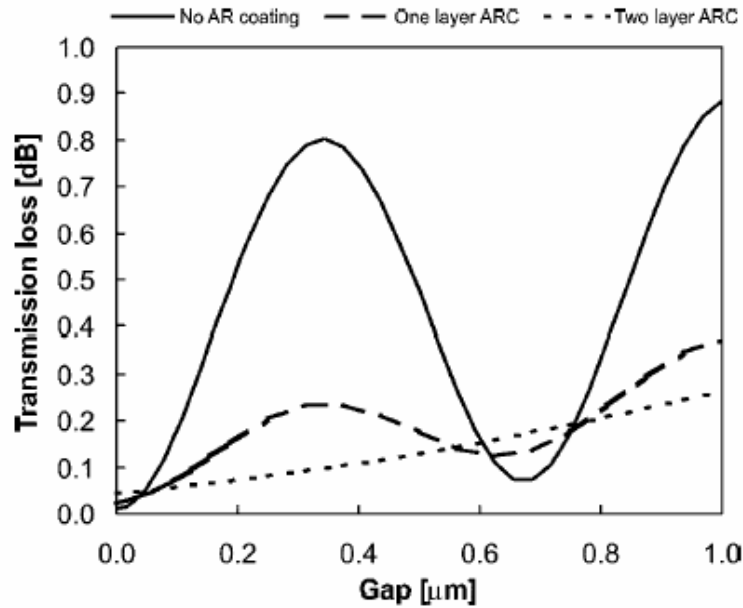


Figure 2.22: Calculated transmission loss as a function of air gap for SOI-based switch with polymeric waveguides [66]

## 2.6 Feature Comparison of All-optical Switches

After introduction of all these existing optical switches, the Self-latching Waveguide Optical MEMS Switch (SWOMS) will be introduced in chapter 3, which is also based on moving waveguides. By using the newly developed self-latching structure and really moving the waveguides instead of only bending them, the annoying gap can be reduced. And the basic unit of SWOMS can be  $1 \times 2$  or  $2 \times 2$ , which gives more flexibility to apply the technology for different applications. Table 2.3 compares all kinds of all-optical switches, the comments refer to [42], [56], and [57], and the values of SWOMS are estimated. From the table, we can easily find the advantages of the SWOMS. The structure and detailed description of the SWOMS will be given in the next chapter.



	3-D MEMS	2-D MEMS	PLC	Thermo-Optic PLC	Electro-Optic	Bubble MEMS	Liquid Crystal	Opto-Mechanical	Existing Moving waveguides	SWOMS
Insertion loss (dB)	3~10	1~4	3.5~6	4~10	3.5~5	3~8	0.3~1	1.5~5	1~3	
Switching time (ms)	10~20	0.2~10	5~10	<0.01	10~100	0.3~1	2~10	0.5~1	0.5~2	
Cross talk (dB)	-30~-50	-60	-25~-45	-15~-35	-20~-50	-20	-30~-60	-30~-50	-30~-55	
Loss uniformity	✓	?	✗	?	?	✓	✓	?	✓	
Polarization effects	✓	✓	✓	?	?	?	✓	✓	✓	
Wavelength independence	✓	✓	✗	✗	✓	✓	✓	✓	✓	
Power consumption	✓	✓	✗	✓	✗	✓	✗	✓	✓	
Scalability	✓	?	✗	✗	✗	✗	✗	✗	?	
Digital control	✗	✓	✗	✓	✓	✗	✓	✓	✓	
Integrated actuator	✓	✓	✓	✓	✓	✓	✗	✓	✓	
No collimator	✗	✗	✓	✓	✓	✗	?	✓	✓	
Self-latching	✗	?	✗	✗	✓	✗	✓	?	✓	
Low cost	?	?	✓	✓	✓	✗	✗	✓	✓	

Legend:    ✓ = good    ✗ = poor    ? = problematic

Table 2.3: Comparison of all-optical switches



## Chapter 3 Basic Structure and Principle of SWOMS

### 3.1 The Micro Self-latching Bi-stable Structure

#### 3.1.1 Basic Structure Components

The bi-stable MEMS device we developed has only one layer of structure. Typically, it can be fabricated on a SOI (silicon on insulator) wafer with one mask. After deep reactive ion etching (DRIE) and structure release by chemical etching of the insulator, the basic structure appears. Figure 3.1 shows the schematic drawing of the structure.

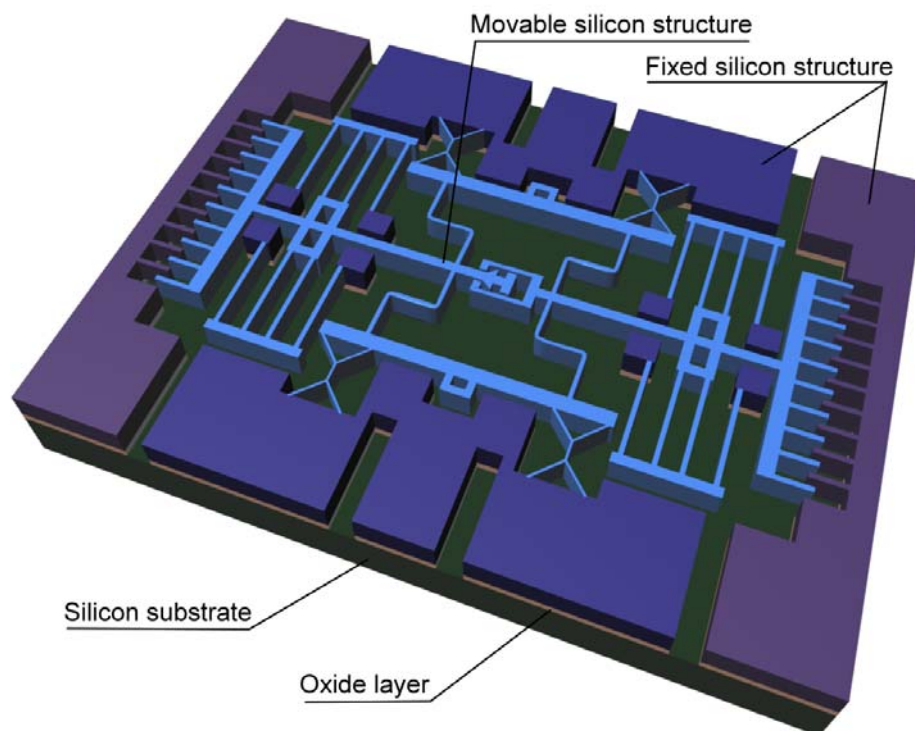


Figure 3.1: Schematic drawing of the self-latching device after etching and release

There are three layers of material in Figure 3.1: The silicon top layer, the intermediate oxide layer, and the silicon substrate. The top layer has been patterned to the desired shape. The fixed parts of this layer are bonded to the silicon substrate by intermediate oxide, yet the oxide under the movable parts has been etched away so that they can move freely.

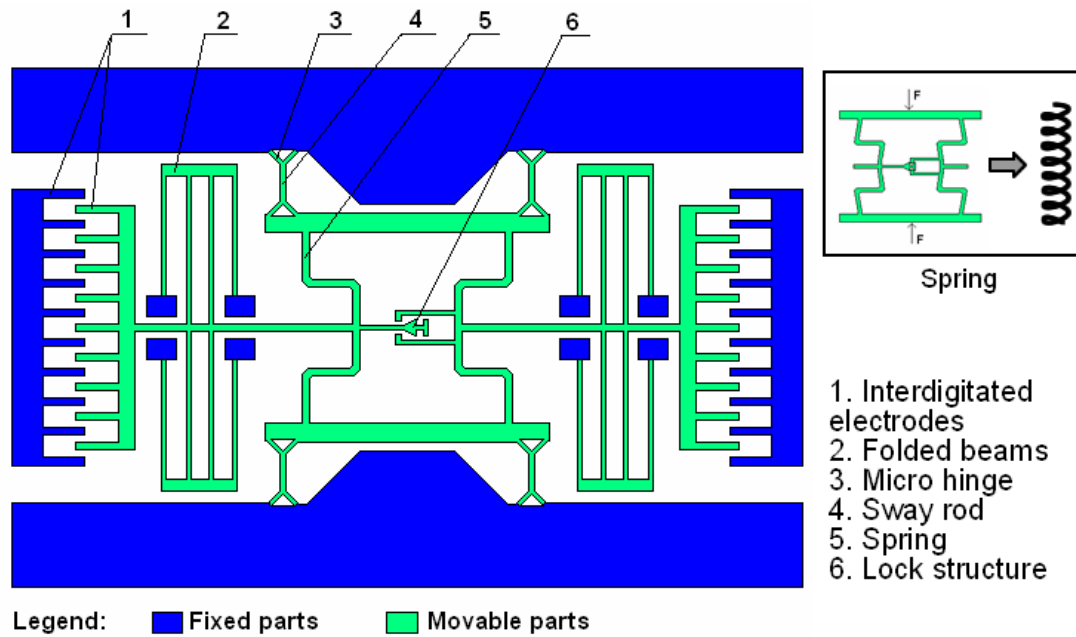


Figure 3.2: Components of the self-latching device.

The components of the self-latching device, as shown in Figure 3.2, include:

- Interdigitated electrodes. Also known as combdrives, they act as the actuators to move the device between its two stable positions. They also provide the force needed for assembly.
- Folded beams. These beams are used to keep the combdrives in their position and move in only one direction.
- Micro hinges. A newly developed Fork Hinge structure is used here to provide quasi-hinge function.
- Sway rods. The sway rods are important components for the self-latching. They sway left and right between the two latching positions.
- Spring. The spring is the component that store energy to keep the device in its stable positions. It looks like two bows facing each other. After assembly, the two bows act as a compressed spring.
- Lock structure. The lock structure will lock together after assembly, which can keep the spring in its compressed state.

### 3.1.2 Bi-stable Self-latching Principle

The basic self-latching principle is similar to a simple structure with two sway rods and a compressed spring, as illustrated in Figure 3.3.

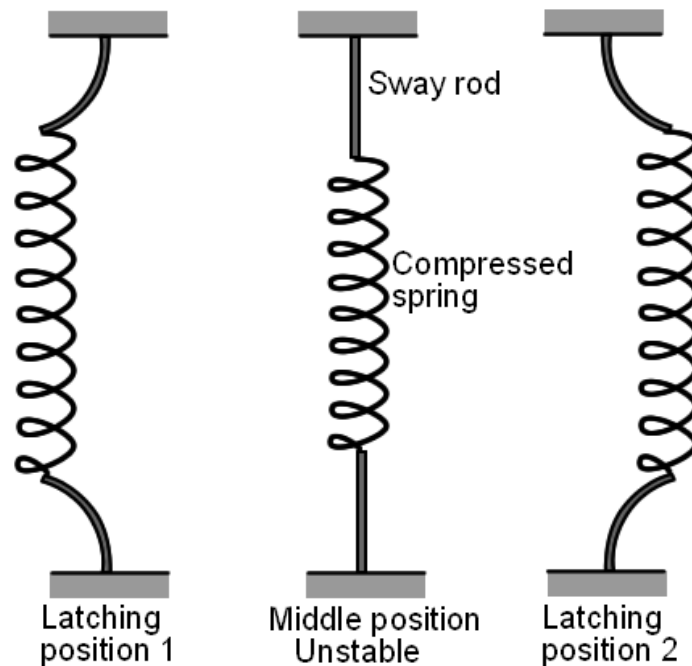


Figure 3.3: Self-latching principle

In the above structure, when the sway rod is at its middle position, the spring is compressed. This situation is unstable because the system is in the state of higher potential energy. Whenever the rods sway left or right, the potential energy will drop. Thus with any disturbance, the system will leave the unstable position and keep latching at lower potential energy position 1 or position 2.

The structure we designed also has the sway rods and spring. However, because the device is fabricated using micromachining technology, there is a special factor. Usually, when we fabricate a spring, it cannot be pre-compressed in the working position. In the macro world, we can compress a spring and assemble it on the working position manually or by robots. Yet in the micro batch fabrication process, this is impossible or very costly.

In order to keep the device symmetric at its two latching position, the sway rods are at their middle position after DRIE and release. In the same time, the spring is in its

original state without any compression. However, an original compression is needed to make the spring store energy. An assembly process is used to accomplish this goal.

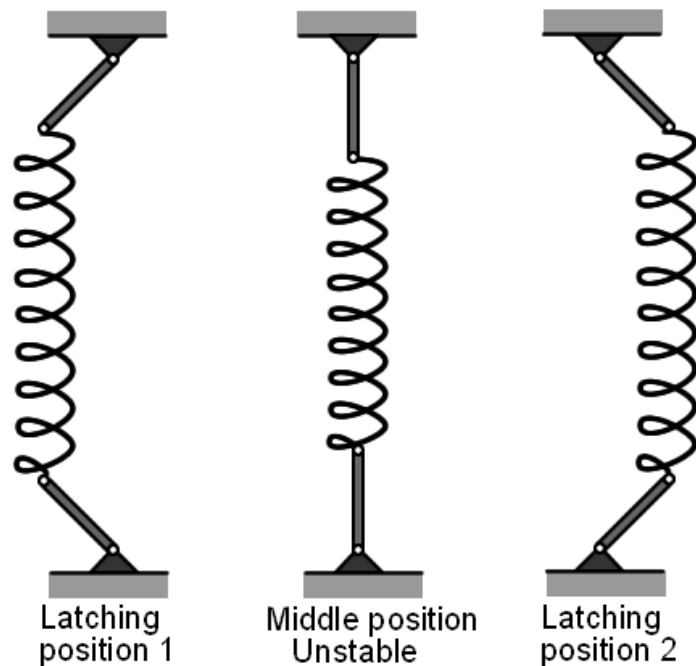


Figure 3.4: Self-latching device using hinges

Another difficulty is the design of the sway rods. The rods should be flexible enough so that they can be bent by the spring to the desired moving range. On the other hand, the rods should be strong enough that they can keep straight at the middle position under the pressure of the spring. These demands are hard to satisfy by just changing the dimensions of the rods, especially for hard and brittle materials such as silicon. In the macro world, we can easily solve this problem by using hinges, as shown in Figure 3.4. Yet in the micro world, hinges are usually prohibited because the friction between parts of the hinge gives the device a very short lifetime. A newly developed quasi-hinge structure, namely the Fork Hinge, is used to solve this problem.

### 3.1.3 Micro Fork Hinge Structure

The structure of the Fork Hinge is shown in figure 3.5. A simple flexible beam is put on right for comparison.

In MEMS design, simple flexible beams are usually used as substitution for hinges to avoid the friction problem of real hinge when only small rotation angle is needed. In

the beginning, we also hoped to use this simple flexible beam as a sway rod in the latching structure. There are three design factors for the flexible beam: the depth  $d$ , the thickness  $t$ , and the length  $L$ . the depth  $d$  doesn't matter much because all the other structures have the same depth decided by the SOI wafer. The thickness  $t$  of the beam is a very sensitive factor because the deformation of the beam is proportional to the cube of  $t$ . As crystal silicon is a high modulus material (i.e. Young's modulus  $E \approx 130\text{Gpa}$  along  $\langle 100 \rangle$  direction), the beam looks like it is never flexible enough to satisfy the demand of deformation  $s = 10\mu\text{m}$  (this value is chosen to get  $2s = 20\mu\text{m}$  distance between two parallel waveguide, which is large enough that the crosstalk caused by coupling between them is negligible, and not too large to be out of the moving range of combdrive) and rotation angle  $a = 0.1\text{rad}$  (see Figure 3.6). So that it seems the smaller the thickness  $t$ , the better. However, the smallest  $t$  we can reach is limited by the fabrication process. For DRIE process, a feature size below  $2\mu\text{m}$  is hard to achieve. So we choose  $2\mu\text{m}$  as the thickness all along the beam to ensure the largest deformation.

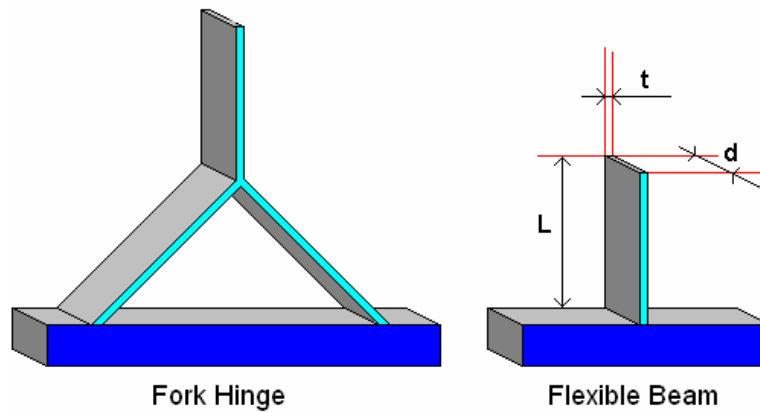


Figure 3.5: Fork Hinge structure and flexible beam

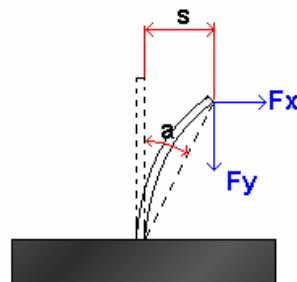


Figure 3.6: Deformation of flexible beam

So there is only one parameter can be changed: the length  $L$  of the beam. However, no suitable  $L$  can be found to satisfy our demand of  $s$  and  $a$ . If  $L$  is small, the forces  $F_x$  and  $F_y$  needed to deform the beam to  $s$  will be too large and out of range of most micro actuators. Or even if we can provide so large forces, the beam will break under the internal stress. If  $L$  is large, it is easier to reach the requirement for  $s$ , but the angle  $a$  is then too small to reach our demand. And the larger the  $L$ , the more risk that the beam be unstable and buckle in the middle position.

In order to solve this problem, a Fork Hinge structure has been developed. Figure 3.7 compares the deformation of a Fork Hinge with flexible beams under the same forces  $F_x$  and  $F_y$ . And Figure 3.8 compares their deformation behavior if we impose the same deformation along the  $x$  direction.

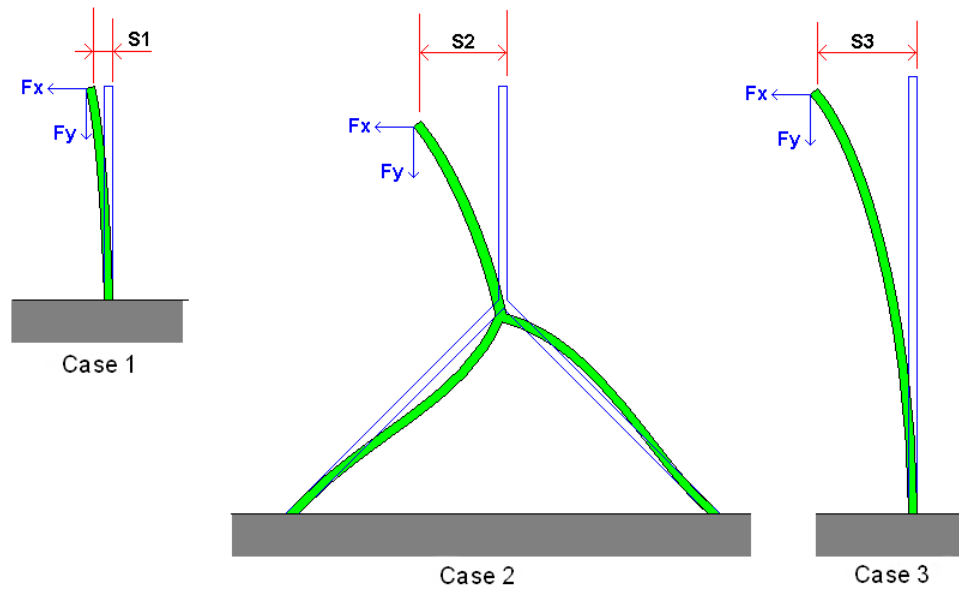


Figure 3.7: Comparison of deformation of Fork Hinge and flexible beams under the same forces condition

Under the same forces, the Fork Hinge (Figure 3.7 case 2) deforms much more than the short flexible beam (case1). Whether its deformation  $S_2$  is larger or smaller than the deformation  $S_3$  of the long flexible beam depends on the ratio of  $F_y$  and  $F_x$ . If  $F_y$  is much larger than  $F_x$ ,  $S_2$  will be larger than  $S_3$ , and if  $F_y$  is smaller than  $F_x$ ,  $S_3$  will be the larger one. This phenomenon stems from that the deformation of the Fork Hinge is more sensitive to  $F_y$  than the flexible beam. Besides providing deformation

comparable with the long flexible beam, the Fork Hinge has an obvious advantage as it can remain stable under a much larger axial pressure force simply because all the beams of the Fork Hinge are much shorter than the long flexible beam.

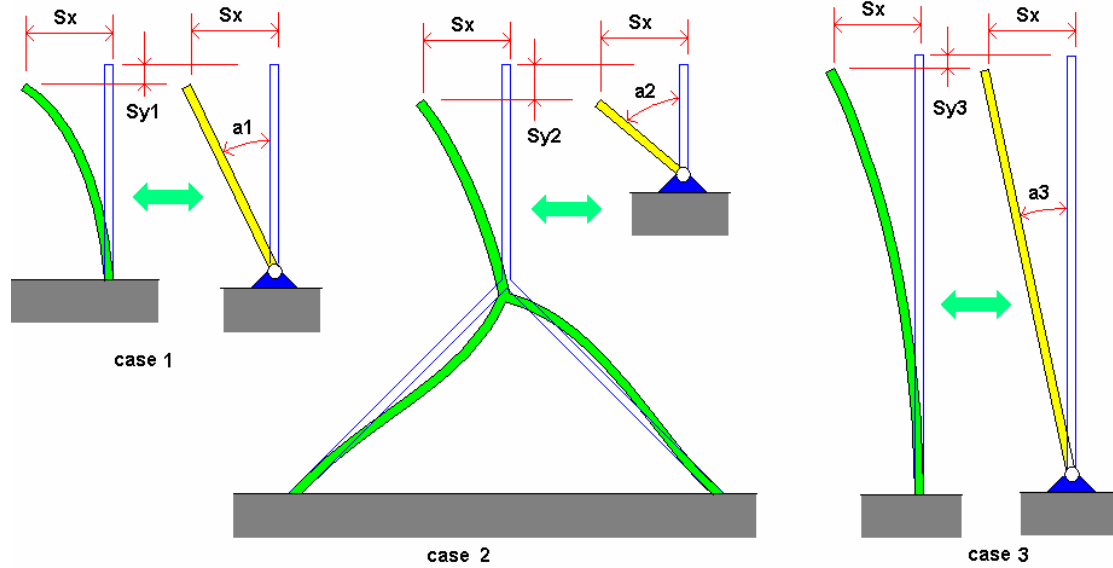


Figure 3.8: Comparison of behavior of Fork Hinge and flexible beams under the same deformation  $S_x$

Figure 3.8 illustrates the behavior of the structures when their deformations along the  $x$  direction have the same value  $S_x$ . From the Figure, it is easy to find that the Fork Hinge is the best, and the long flexible beam the worst. As we can see,  $S_{y2} > S_{y1} > S_{y3}$ , which means, if we compare them to a real hinge and rod system, the Fork Hinge behaves like the one that have the largest rotation angle because  $a_2 > a_1 > a_3$ . It is easy to understand why  $S_{y1} > S_{y3}$ , but why  $S_{y2}$  should be larger than  $S_{y1}$ ? It is because the special bending of the two branch beams causes their joint point to move down. The upper beam of the Fork Hinge will not only tilt as the short flexible beam in case 1, but also move down with the joint point.

With such good performance of large deformation and large rotation angle, the Fork Hinge can find its application not only in this project, but also in other MEMS devices when quasi-hinge structures are needed. As a substitution for hinges, the Fork Hinge is as simple as the flexible beam, but acts much more like a real hinge.

### 3.1.4 Integrated Assembly of the Device

The forces needed for the assembly are provided by integrated combdrives. Combdrive is an electrostatic device that has been used as standard MEMS actuators since its invention in 1989. It is widely adopted because it has the features such as a low energy consumption due to the absence of current flow, an acceptable moving range (up to  $40\mu\text{m}$ ), an acceptable actuation force (up to hundreds  $\mu\text{N}$ ) which remains nearly constant within its moving range. Moreover, it is relatively easy to design and fabricate. The structure of the combdrive is shown in Figure 3.9. A typical combdrive actuator has two combs, one is fixed and the other is movable. Usually, a combdrive works together with a folded flexure (also shown in Figure 3.9) which keeps the position of the movable comb and constrains its motion along only one direction.

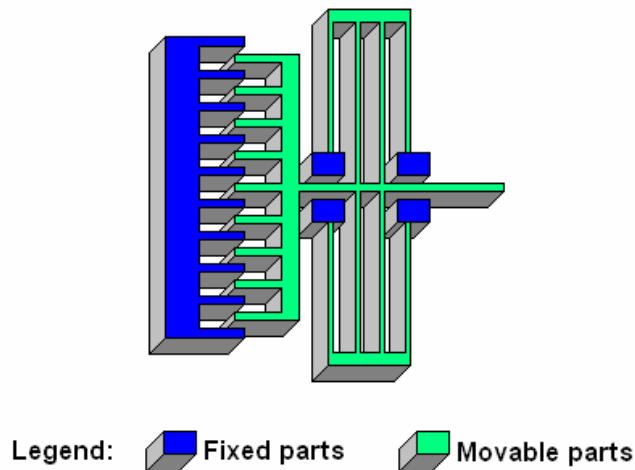


Figure 3.9: Structure of a combdrive actuator

The working principle of the combdrive actuator is illustrated in Figure 3.10. When there is no electric potential difference between the fixed comb and the movable comb, the movable comb stays in its original position defined by the folded flexure. If a voltage is applied between the fixed comb and the movable comb, the two parts will attract each other due to Coulomb's force. The movable comb cannot stay in its original position and will move toward the fixed comb, until other forces, i.e. the restoring force of the folded flexure, balance the electrostatic attraction force.



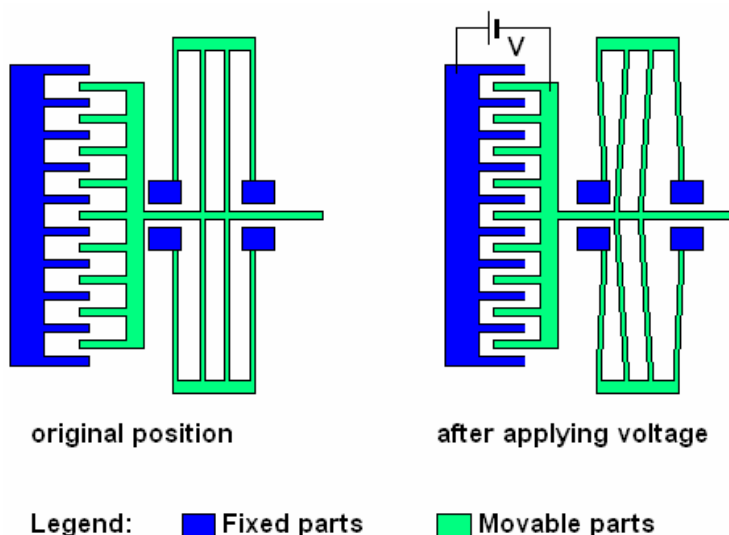


Figure 3.10: Working principle of combdrive actuator

The spring used in this device is a combination of two bows, as shown in Figure 3.11. The lock structure for assembly is also shown.

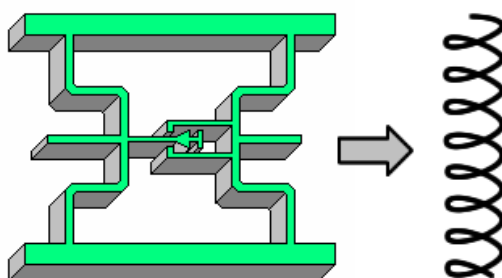


Figure 3.11: The spring structure

The principle of the spring assembly is illustrated in Figure 3.12. In situation A, the spring is in its original relaxed state after etching and release. In situation B, two forces are applied on the left and right bow. The bows are moved apart by the forces until the notch and hook of the lock structure locks together. Then we stop applying the force, the bows cannot return to their original positions. In this situation, if there is no force and the structure is balanced, the original length of the spring is longer than in situation A because of the bow geometry. Situation C shows that if the length of the spring cannot increase freely, the spring is pre-compressed.

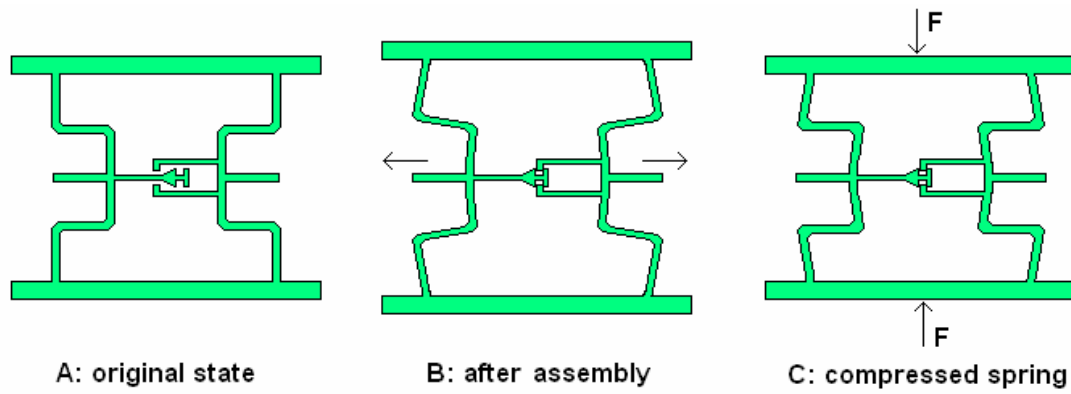


Figure 3.12: The spring assembly principle

After all these introduction of structure and principle of the Fork Hinge, the combdrive actuator, and the assembly of spring, let's have a look at the assembly process of the self-latching device (see Figure 3.13, 3.14, 3.15).

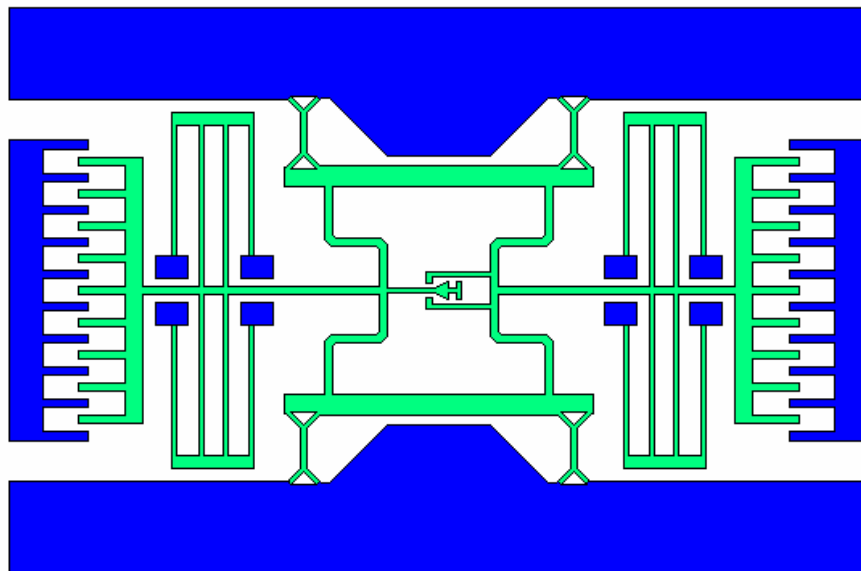


Figure 3.13: The situation before assembly

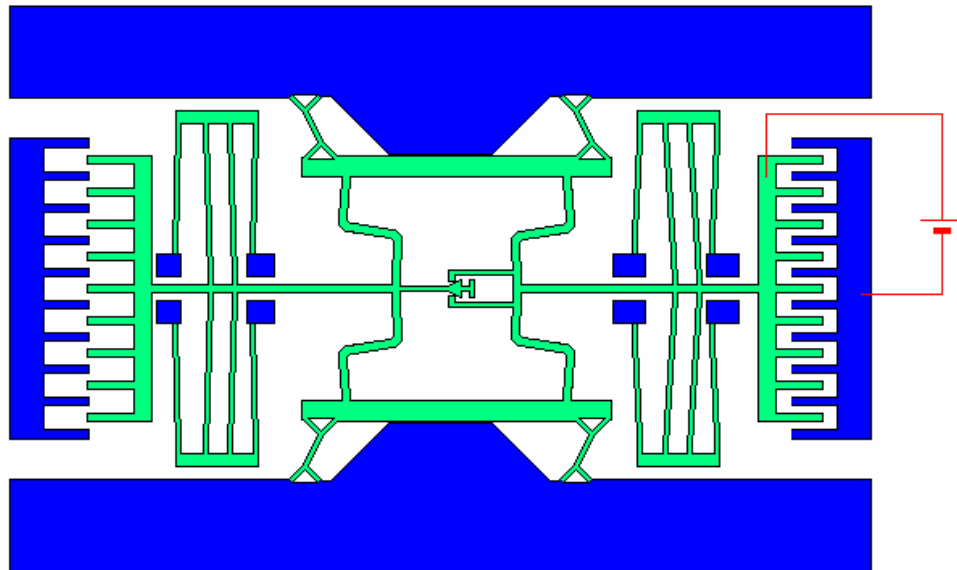


Figure 3.14: Assembly step 1: apply voltage on the right combdrive

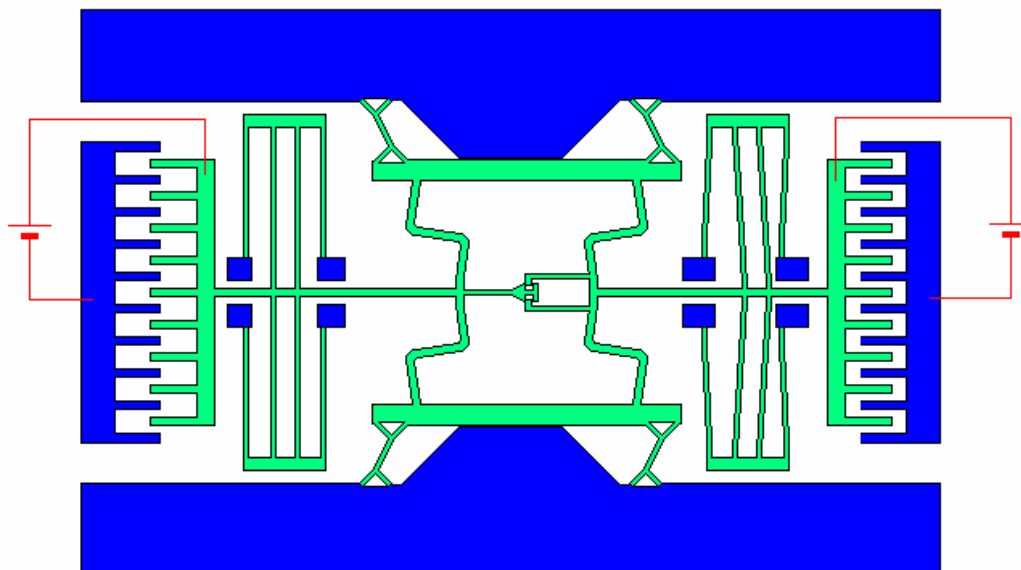


Figure 3.15: Assembly step 2: apply voltage on the left combdrive and finish

The assembly process is obtained in two steps: first, apply voltage on the right combdrive, and then maintain this voltage and apply a voltage on the left combdrive. After these two steps, the lock structures will interlock together. Removing both of the voltages, the device will stay in the right position due to the self-latching.

### 3.1.5 Principle of the Self-latching Structure

After the assembly, the device is latched on the right position and ready to work. If we want to shift it to the left latching position, all we need is to apply a voltage on the left combdrive. A pulling force will be provided by the left combdrive. If this force is larger than the latching force, the spring will move toward left and the sway rods sway left. After passing through the middle position, the device will move to the left latching position automatically. Then the voltage can be removed and the device will stay in the left latching position. Now, by applying a voltage on the right combdrive, the device will shift to the right. Thus the device can switch between the left and the right latching positions. Figure 3.16 to Figure 3.18 demonstrated three positions of the device: the left latching position, the middle unstable position, and the right latching position.

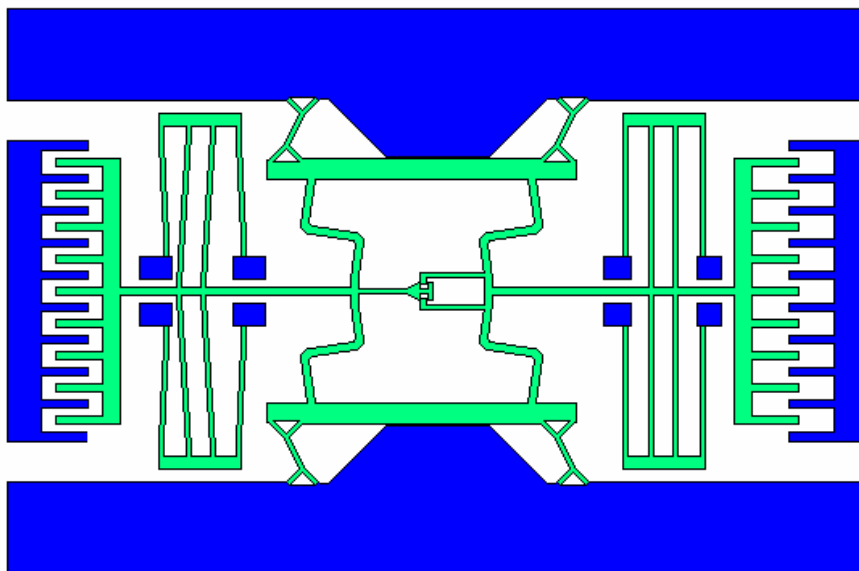


Figure 3.16: Left latching position

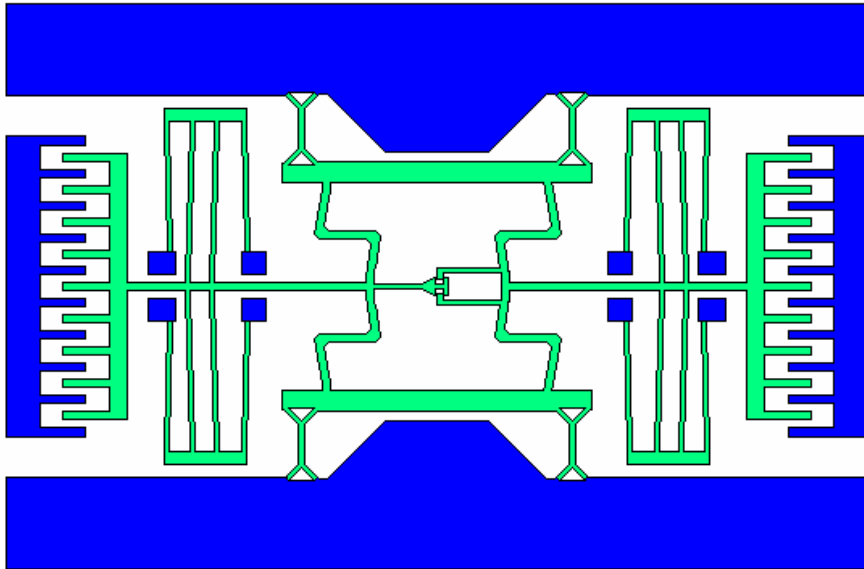


Figure 3.17: Unstable middle position

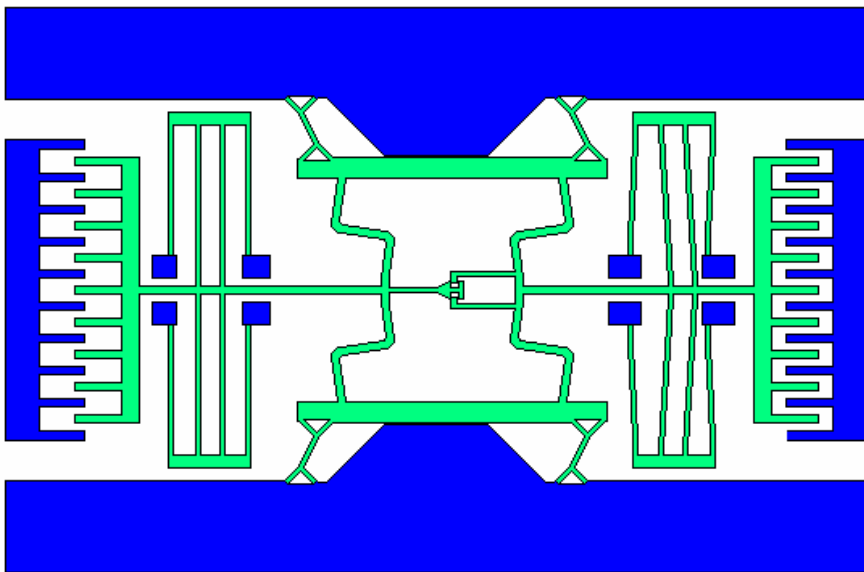


Figure 3.18: Right latching position

## 3.2 Introduction of SWOMS

### 3.2.1 Optical Switching Principle

The self-latching waveguides optical MEMS switch (SWOMS) is the combination of the formerly introduced self-latching device with waveguide technology. Observing Figure 3.1, we can find that the spring structure of the self-latching device can be looked as a movable stage that can move left and right. If we attach optical waveguides on this stage, the waveguides can move together with it. Thus an optical switch based on moving waveguides can be formed.

Figure 3.19 demonstrates the principle of a  $1 \times 2$  SWOMS. Lightwave comes from the input fiber (the lower fiber) and then propagate along the input waveguide. There are two output waveguides connected to two output fibers. The output waveguides are attached to the fixed parts of the device and cannot move. The input waveguide has one end attached to the fixed substrate and connected to the input fiber, while the other end is attached to the movable stage. Before assembly of the device, the input waveguide is at the middle position between the two outputs and it cannot transmit signal (see Figure 3.20). After assembly, the input waveguide will be connected to one of the two outputs. Thus when the stage moves left and right, the optical signal is switched between the two outputs.

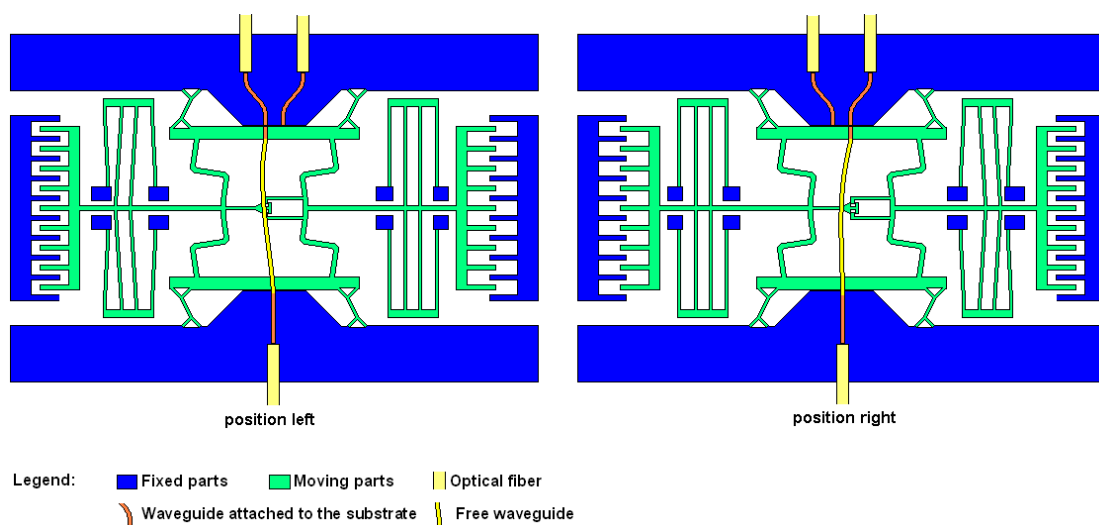


Figure 3.19: The principle of a  $1 \times 2$  SWOMS

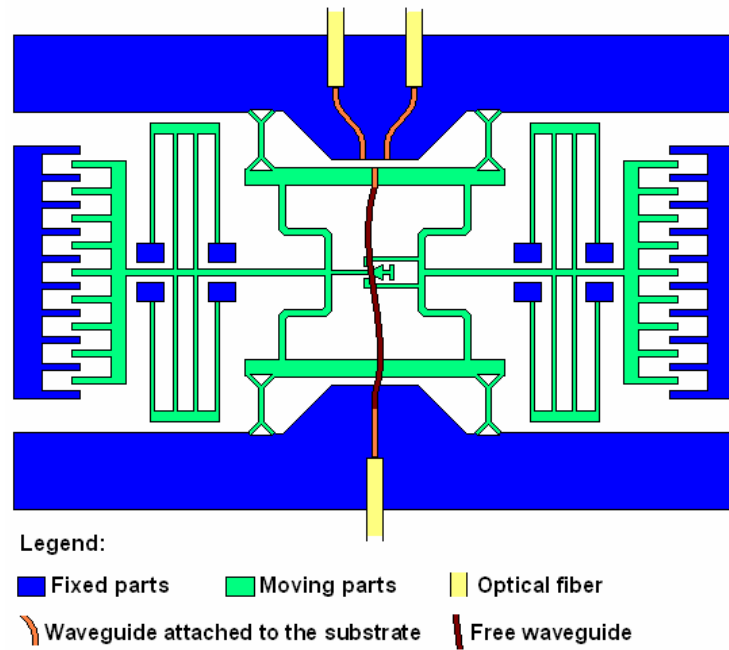


Figure 3.20: 1×2 SWOMS before assembly

Unlike other optical switch based on moving waveguides, the SWOMS can provide not only 1×2 switch unit, but also 2×2 switch unit. Figure 3.21 shows the principle of a 2×2 SWOMS. The 2×2 SWOMS has two input fibers and two output fibers. The lightwave is transmitted by two waveguides in each position, so there are actually four waveguides with their ends attached on the stage of the spring structure. This architecture is original and unique to our SWOMS

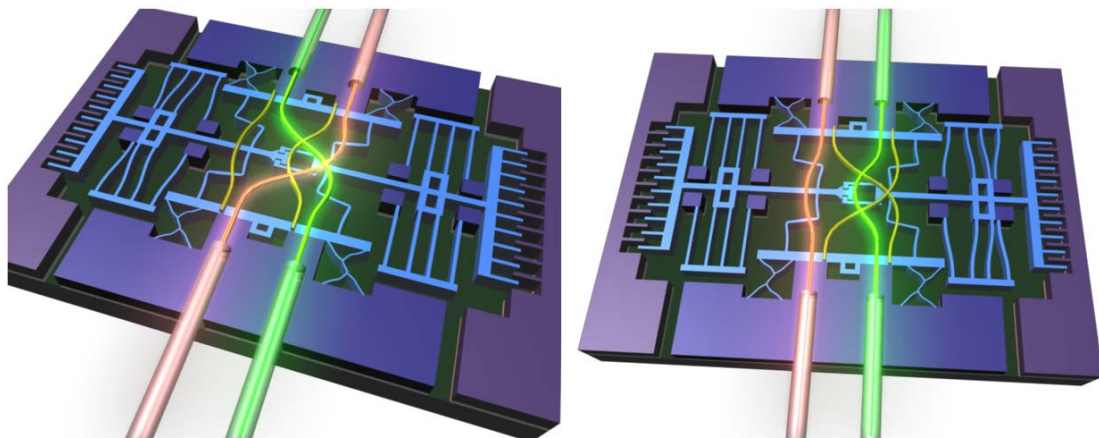


Figure 3.21: Switching principle of a 2×2 SWOMS

### 3.2.2 Gap-reduction Mechanism

We have mentioned in the chapter 2 that the SWOMS has a very important feature: gap-reduction. For optical switch based on moving waveguides, a gap between the movable waveguide and the fixed waveguide is needed during switching to avoid friction. When the switch reaches its working position, this gap causes insertion loss as shown in Figure 2.22. The SWOMS has a mechanism to reduce the gap when the device is at its working position. By observing the behavior of the waveguides during the switching process of the SWOMS (see Figure 3.22), we can understand this mechanism. The gap exists during switching and the gap reduces to nearly zero when the SWOMS is at its latching positions. That's exactly what we want. The key component to realize this mechanism is the sway rod, which also acts as a key component for self-latching.

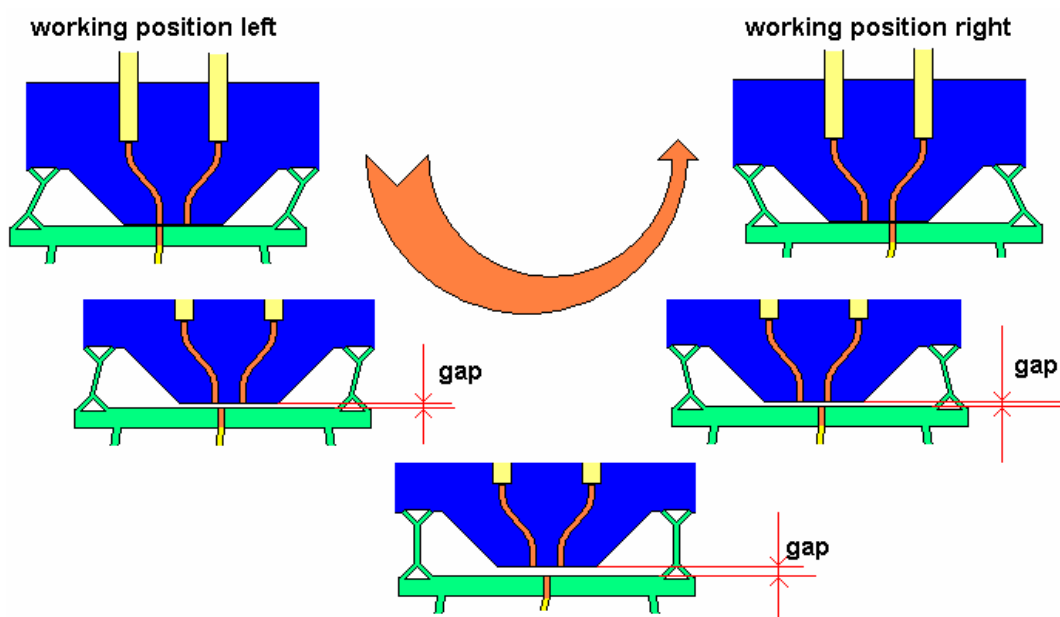


Figure 3.22: Gap-reduction mechanism



## Chapter 4 Design of the Bi-stable Micro Actuator

In order to design this new device, analytical models for the structures are built and the values of the design parameters are chosen according to calculations and diagrams. Then computational simulation methods are used for verification and optimization.

### 4.1 Calculation and Simulation Tools

Four computer software tools have been used in the design of SWOMS.

- MAPLE 7 for mathematical calculation;
- CoventorWare for MEMS simulation;
- ANSYS for FEA simulation of the mechanical structure;
- OlympIOs for simulation and optimization of the waveguides.

MAPLE 7 is a comprehensive computer system for advanced mathematics. It includes facilities for interactive algebra, calculus, discrete mathematics, graphics, numerical computation and many other areas of mathematics. It also provides a unique environment for rapid development of mathematical programs using its vast library of built-in functions and operations [58]. In this project, MAPLE 7 is mainly used to do calculus, solve differential equation, and provide plots as the basis of parameter choice.

CoventorWare is an integrated suite of tools designed to produce an accurately modeled MEMS design. Coventor's Designer tool enables the user to design, specify, and model MEMS structures. The Coventor solvers create solutions for these designs. Output results can be analyzed, graphed, and iterated to assist user in completing the design process. This versatile software is process-independent and features capabilities such as 2-D layout creation and editing, process emulation, 3-D generation of solid models from 2-D masks, electrostatic simulation (BEM), mechanical simulation (FEM), coupled electromechanical simulation, etc. [59]

ANSYS is a widely used finite element analysis software which enables engineers to Build computer models or transfer CAD models of structures, products, components, or systems, apply operating loads or other design performance conditions, study physical responses, such as stress levels, temperature distributions, or electromagnetic fields, optimize a design early in the development process to reduce production costs, do prototype testing in environments where it otherwise would be undesirable or impossible (for example, biomedical applications). The ANSYS program has a comprehensive graphical user interface (GUI) that gives users easy, interactive access to program functions, commands, documentation, and reference material. [73]

OlympIOs is a platform for design, simulation and mask layout in Integrated Optics. The modular approach of the software strategy offers the advantages of a tailor-made (user-defined) software package and unmatched flexibility in meeting every individual's specific design and simulation requirements. [74]

## 4.2 Design of the Micro Fork Hinge

In the structure of SWOMS, two micro Fork Hinges are connected together to form the sway rod, which is one of the key components of the self-latching structure. We begin the design of SWOMS from the Fork Hinge because it is the most critical and most difficult part of the self-latching structure, and the result is the base of the design of other structures.

### 4.2.1 Simplification of the Model

The Fork Hinge structures used in SWOMS can be modeled as Figure 4.1.

Two pairs of Fork Hinges work together in SWOMS. Each pair consists of two Fork Hinges facing each other. In order to simplify the analytical design, from the forces analyze of Figure 4.1, we can write down the following equations:

$$\begin{cases} F_1 + F_2 = F \\ m_a + m_b + F_2 \times L = F \times \left(\frac{L}{2} + x\right) \\ m_a + m_b + F \times \frac{L}{2} = F_2 \times L \end{cases} \quad (4.1)$$

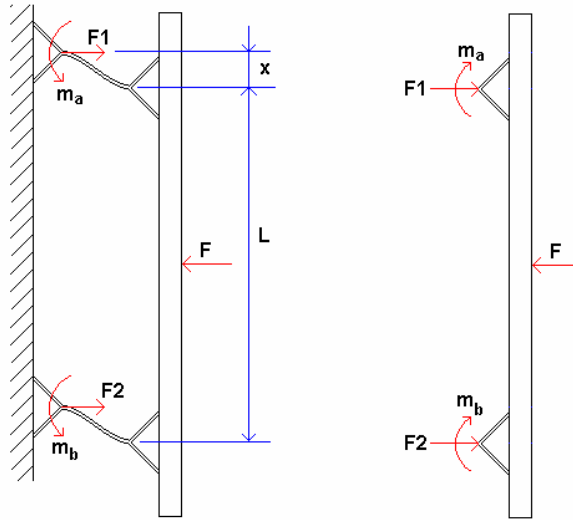


Figure 4.1: Fork Hinges used in SWOMS

So that,

$$\begin{cases} F_2 = \left(\frac{1}{2} + \frac{x}{2L}\right)F \\ m_a + m_b = \frac{x}{2}F \end{cases} \quad (4.2)$$

Because  $x \ll L$ , we can get that

$$F_2 \approx F_1 = F/2 \quad (4.3)$$

$$\text{And } m_a \approx m_b = \frac{x}{4}F \quad (4.4)$$

Equation 4.3 and 4.4 mean that we can concentrate on only one pair of Fork Hinges during design because the other pair sustains nearly the same forces and moments, as shown in Figure 4.2.

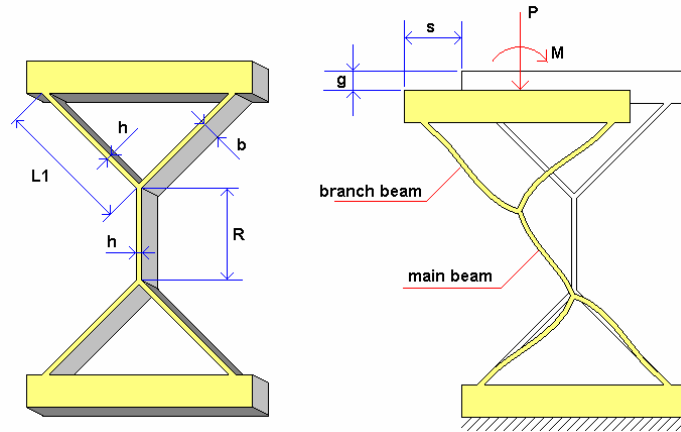


Figure 4.2: Fork Hinge design parameters

### 4.2.2 Design Objective

The dimension parameters shown in Figure 4.2 need to be decided by design. Among these parameters, the thickness of the beams  $h$  is a parameter fixed by the available fabrication method. As we mentioned in the last chapter,  $h$  should be as small as possible, here we choose  $h = 2\mu\text{m}$  so that it is not too difficult to be fabricated with micromachining. The choice of depth of the beam  $b$  is limited by the aspect ratio and etching depth of the DRIE method, and also the thickness of the surface silicon layer of the SOI wafer available. The DRIE can routinely fabricate structure with aspect ratio up to 30, which allows  $b$  to be chosen up to  $60\mu\text{m}$ . For higher out of plane stiffness of the structure,  $b$  needs to be large, but a smaller value makes fabrication easier. For the calculation of in plane properties of the structure,  $b$  is not a critical parameter because all the properties are varying linearly to it. Considering these we choose  $b = 30\mu\text{m}$  here for the calculation.

Therefore, the objective of the Fork Hinge design is:

When  $b = 30\mu\text{m}$  and  $h = 2\mu\text{m}$ , choose suitable branch beam length  $L_1$  and main beam length  $R$  that satisfy the following conditions:

- Under reasonably small force  $P$  that can be provided by a combdrive actuator, the structure can move to the position where  $s = 10\mu\text{m}$ , as shown in Figure 4.2. The value of  $s$  is determined by the function and limitation of the whole device.

Here  $s = 10\mu\text{m}$  is chosen to get  $2s = 20\mu\text{m}$  distance between two parallel waveguides. This distance is large enough so that the crosstalk caused by coupling between them is negligible, and not too large to be out of the moving range of the combdrive actuator.

- When  $s = 10\mu\text{m}$ ,  $g \geq 2\mu\text{m}$ . This demand is used to ensure that a gap exists between the movable parts and the fixed parts during switching.
- When under force  $P$  and moment  $M$ , and in the situation of the deformation as large as  $s = 10\mu\text{m}$ , the maximum stress  $\sigma_{\text{max}}$  inside the structure should be much smaller than the yield strength of silicon (7Gpa). Considering the alternative loading and the stress concentration due to the roughness of the etched surface, it is reasonable to demand  $\sigma_{\text{max}} < 0.5\text{GPa}$ .
- All the beams should keep their stability (no failure by buckling) even under axial compressive force as large as  $2P$ . This demand limits the length of the beams.

### 4.2.3 Analytical Calculation Design

The forces that the beams sustained have been analyzed in Figure 4.3. Only half of the structure shown in Figure 4.2 has been analyzed because the upper half bears same forces as the lower half, which is due to the geometric symmetry of the structure. From the force analyses of the main beam:

$$\begin{cases} (F_{1b} - F_{2a}) \times \cos 45^\circ = (F_{1a} + F_{2b}) \times \cos 45^\circ \\ (F_{1b} - F_{2a}) \times \sin 45^\circ + (F_{1a} + F_{2b}) \times \sin 45^\circ = P \\ P \times \frac{s}{2} = m_1 + m_2 \end{cases} \quad (4.5)$$

In the equations  $m_1$  is the moment applied on the left branch beam.  $F_{1a}$  and  $F_{1b}$  are the forces applied on the joint point of the left branch beam in two vertical directions. While  $m_2$ ,  $F_{2a}$  and  $F_{2b}$  are moment and forces applied on the joint point of the right branch beam.

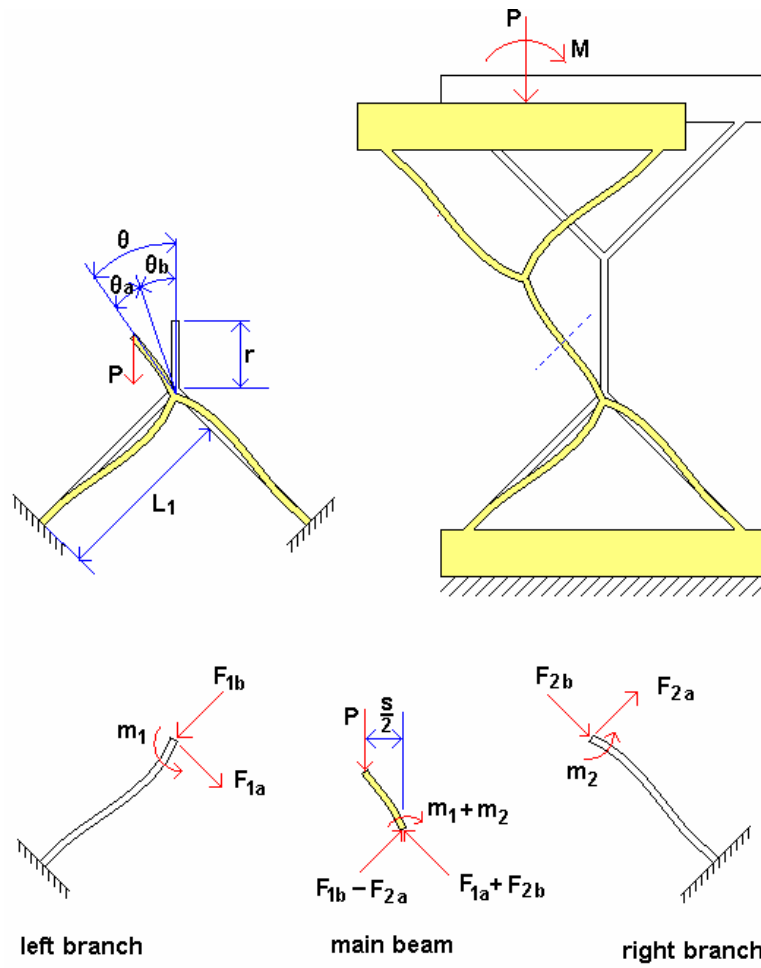


Figure 4.3: Force analyses of the beams

Analyzing the forces and deformation of the left and right branch, we can find that  $m_1 \approx m_2$ ,  $F_{1a} \ll F_{1b}$ , and  $F_{2a} \ll F_{2b}$ . Combining these conditions with equation 4.5, we can get:

$$F_{1b} \approx F_{2b} = \frac{\sqrt{2}}{2} P \quad (4.6)$$

$$\text{And } m_1 \approx m_2 = \frac{s}{4} P \quad (4.7)$$

$$\text{And } F_{1b} = \frac{2\sqrt{2}}{s} m_1 \quad (4.8)$$

$$\text{Where } s = 10 \mu\text{m} \quad (4.9)$$

### 4.2.3.1 Branch Beam Design

We begin our design from branch beams. Because the left branch and right branch deform nearly the same way, here we only analyze the left branch. From the moment and deformation analysis in Figure 4.4, and according to the differential equation for small bending [60],

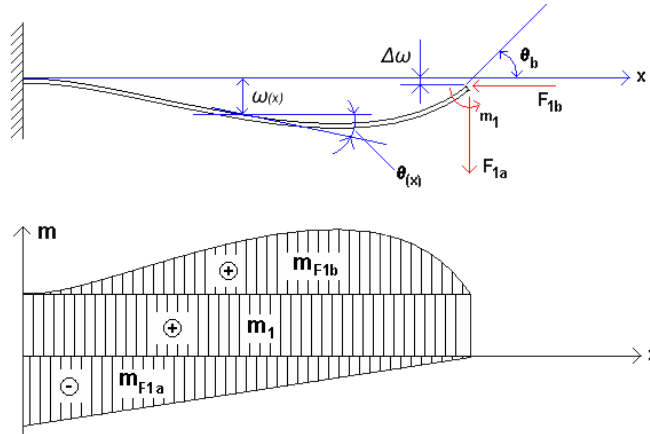


Figure 4.4: Force and moment analysis of the left branch beam

$$\left\{ \begin{array}{l} \frac{d^2 \omega_{(x)}}{dx^2} = \frac{M_{(x)}}{E_{45} I} \\ M_{(x)} = m_1 - F_{1a} \times (L_1 - x) + F_{1b} \times (-\omega_{(x)}) \\ \theta_{(x)} = \frac{d\omega_{(x)}}{dx} \\ \omega_{(0)} = 0 \\ \frac{d\omega_{(0)}}{dx} = 0 \\ \omega_{(L_1)} = \Delta\omega \approx 0 \end{array} \right. \quad (4.10)$$

In equation 4.10,  $M_{(x)}$  is the moment acting on the beam at the position  $x$ ;  $\omega_{(x)}$  is the deformation in  $Y$  direction;  $\theta_{(x)}$  is the angle between the beam and the  $X$ -axis;  $L_1$  is the length of the beam; and  $I$  is the moment of inertia of the beam, which is,

$$I = \frac{b \times h^3}{12} = \frac{30 \times 10^{-6} \times (2 \times 10^{-6})^3}{12} = 0.2 \times 10^{-22} (m^4) \quad (4.11)$$

Due to the type and orientation of the silicon wafer we use, here  $E_{45}$  is the Young's

## Chapter 4

## Design of the Bi-stable Micro Actuator

modulus on the directions of the  $\{100\}$  crystal planes. The Young's moduli of crystalline silicon along two directions are used in this design, one is  $E_{45}$ , and the other is  $E_0$ .  $E_0$  is the Young's modulus of single crystal silicon along the  $\langle 110 \rangle$  direction ( $45^\circ$  angle to the  $\{100\}$  planes), and  $E_{45}$  is the Young's modulus along the  $\langle 100 \rangle$  direction. The magnitude of  $E_0$  and  $E_{45}$  of crystalline silicon are not equal because it is an anisotropic material [61]. Their values are,

$$E_{45} = 130 \text{ GPa} \quad (4.12)$$

$$E_0 = 168 \text{ GPa} \quad (4.13)$$

Equation 4.10 can be solved using Laplace Transform, or by using the software Maple 7. Anyhow, the result is,

$$\omega_{(x)} = \frac{F_{1a}}{F_{1b}} x + \frac{m_1 - F_{1a}L_1}{F_{1b}} - \frac{F_{1a}\sqrt{E_{45}I}}{F_{1b}^{\frac{3}{2}}} \sin\left(\sqrt{\frac{F_{1b}}{E_{45}I}} \cdot x\right) - \frac{m_1 - F_{1a}L_1}{F_{1b}} \cos\left(\sqrt{\frac{F_{1b}}{E_{45}I}} \cdot x\right) \quad (4.14)$$

$$\theta_{(x)} = \frac{F_{1a}}{F_{1b}} - \frac{F_{1a}}{F_{1b}} \cos\left(\sqrt{\frac{F_{1b}}{E_{45}I}} \cdot x\right) + \frac{m_1 - F_{1a}L_1}{\sqrt{F_{1b}E_{45}I}} \sin\left(\sqrt{\frac{F_{1b}}{E_{45}I}} \cdot x\right) \quad (4.15)$$

A condition  $\omega_{(L1)} = \Delta\omega \approx 0$  can be added to Equation 4.14. It comes from the fact that the deformation of this point on the left branch beam is limited by the length change of the right branch beam. In fact from the calculation that will be described later in Eq. 4.42, the value is  $0.528 \times 10^{-6} \text{ m}$  that is very close to 0 for the calculation here. Combining this condition with the equation 4.8, 4.12, 4.9, and 4.11,  $F_{1a}$  can be calculated as,

$$F_{1a} = -0.894 \times 10^8 m_1 (\sqrt{2}m_1)^{(\frac{3}{2})} \cdot (\cos(0.279 \times 10^9 \cdot \sqrt{\sqrt{2}m_1} \cdot L_1) - 1) / (0.322 \sin(0.278 \times 10^9 \cdot \sqrt{\sqrt{2}m_1} \cdot L_1) \cdot \sqrt{2}m_1 - 0.894 \times 10^8 \cos(0.198 \times 10^9 \cdot \sqrt{\sqrt{2}m_1} \cdot L_1) \cdot (\sqrt{2}m_1)^{(\frac{3}{2})} \cdot L_1) \quad (4.16)$$



Equation 4.16 shows that  $F_{1a}$  can be expressed as function of  $m_1$  and  $L_1$ . Inserting equation 4.16 into equation 4.15, combining with the equation 4.8, 4.9, 4.11, 4.12, and taking the value  $x = L_1$ , we can also express the rotation angle at the tip of the beam

$\theta_b$  as function of  $m_1$  and  $L_1$ :

$$\theta_b = \theta_{(x=L_1)} = f(m_1, L_1) \quad (4.17)$$

The details of this function aren't given here because it has a very complicated form (refer to the appendix for the complete calculation program using Maple 7), and instead, we plot it in Figure 4.5.

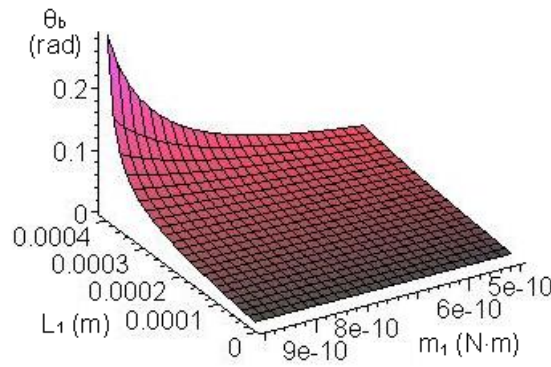


Figure 4.5:  $\theta_b$  (rad) versus  $m_1$  (N·m) and  $L_1$  (m)

Because  $\theta_b$  depends only on  $m_1$  and  $L_1$ , and also because the force  $P$  is proportional to  $m_1$ , the objective of the branch beam design can be expressed as follows: choose a suitable  $m_1$  (the smaller the better) and  $L_1$  (the shorter the better) to get a suitable  $\theta_b$  that satisfy the deformation character of the Fork Hinge structure. Another consideration is the maximum stress in the branch beam, which should match the maximum stress in the main beam so that the whole Fork Hinge get the highest efficiency, and of course, both values should be very small.

From Figure 4.5, we find that the increase of  $\theta_b$  is not linear with the increase of  $m_1$  and  $L_1$ . When the values of  $m_1$  and  $L_1$  become bigger,  $\theta_b$  increases more quickly. When the combination of  $m_1$  and  $L_1$  reaches a certain value,  $\theta_b$  will increase so rapidly that the beam lose its stability. Therefore, we should choose  $m_1$  and  $L_1$  from

the area where we can best benefit from the nonlinearity of the structure, while still keeping its stability. Figure 4.6 illustrated the nonlinear relation between  $\theta_b$  and  $m_1$  when  $L_1$  has been fixed to  $400\mu\text{m}$ .

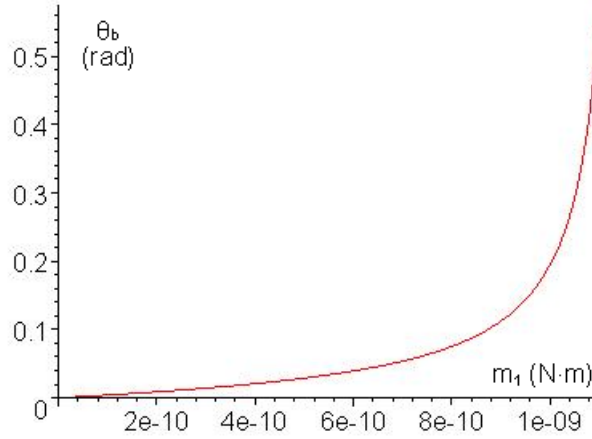


Figure 4.6:  $\theta_b$  (rad) versus  $m_1$  (N·m) when  $L_1 = 400\mu\text{m}$ .

In order to satisfy all the above demands, different combinations of  $m_1$  and  $L_1$  have been chosen for calculation of the forces, the stress, the angle  $\theta$ , the  $r$ , and the gap  $g$ . Finally, an optimized combination of  $m_1$  and  $L_1$  has been chosen as follows:

$$L_1 = 400 \mu\text{m} \quad (4.18)$$

$$m_1 = 0.88 \times 10^{-9} \text{ N}\cdot\text{m} \quad (4.19)$$

$$\theta_b = 0.1 \text{ rad} \quad (4.20)$$

Inserting the value of  $m_1$  and  $L_1$  into equation 4.7, 4.8, and 4.16, we can get:

$$F_{1a} = 7.08 \mu\text{N} \quad (4.21)$$

$$F_{1b} = 248.9 \mu\text{N} \quad (4.22)$$

$$P = 352 \mu\text{N} \quad (4.23)$$

From the value of  $F_{1a}$  and  $F_{1b}$ , we can verify that the assumption  $F_{1a} \ll F_{1b}$  is indeed reasonable.

### 4.2.3.2 Estimation of Maximum Stress in the Branch Beam

We must ensure that the stress inside the branch beam is small enough to meet our requirement. The maximum stress happens where the moment on the branch reach its largest value because for bending beams, the normal stress is the main factor leading to catastrophic failure. For a certain value of moment  $M$ , the maximum normal stress on the cross-section of the beam is:

$$\sigma = \frac{M \cdot h}{2I} \quad (4.24)$$

Where  $h$  is the thickness of the beam, and  $I$  the moment of inertia of the beam.

From Figure 4.4, the moments along the length of the branch beam are not the same, and the maximum stress happens where the maximum moment exists. In order to find the value of  $x$  where  $M$  reaches its maximum value, the following equations need to be solved:

$$\begin{cases} \frac{dM_{(x)}}{dx} = 0 \\ M_{(x)} = m_1 - F_{1a} \times (L_1 - x) + F_{1b} \times (-\omega_{(x)}) \\ \omega_{(x)} = \frac{F_{1a}}{F_{1b}}x + \frac{m_1 - F_{1a}L_1}{F_{1b}} - \frac{F_{1a}\sqrt{E_{45}I}}{F_{1b}^{\frac{3}{2}}} \sin\left(\sqrt{\frac{F_{1b}}{E_{45}I}} \cdot x\right) - \frac{m_1 - F_{1a}L_1}{F_{1b}} \cos\left(\sqrt{\frac{F_{1b}}{E_{45}I}} \cdot x\right) \end{cases} \quad (4.25)$$

Using the known values from former calculation and Maple 7, we can get,

$$x = 284 \text{ } \mu\text{m} \quad (4.26)$$

So that, the maximum moment in the branch

$$M_{b\max} = M_{(x=284)} = 2.08 \times 10^{-9} \text{ N}\cdot\text{m} \quad (4.27)$$

And the maximum stress in the branch:

$$\sigma_{b\max} = \frac{M_{b\max} \cdot h}{2I} = 0.104 \text{ GPa} \quad (4.28)$$

So that the maximum stress is much smaller than the yield strength of silicon (7GPa) and it is also smaller than our more stringent goal of 0.5GPa.

#### 4.2.3.3 Main Beam Design

The objective of the main beam design is to choose a suitable beam length ( $r$  is half of the beam length  $R$ ) where under the force  $P$ , the middle point of the beam (the point where the force  $P$  is acting in Figure 4.7) will move a distance of  $s/2$  in the horizontal direction. The beam should also satisfy other requests, for example, not exceeding the yield strength. Analyzing Figure 4.7, we can write the following equations:

$$\begin{cases} \theta = \theta_a + \theta_b \\ r \cdot \sin \theta = s/2 \\ \theta_a = \frac{\omega_a}{r} \\ \omega_a = \frac{P \cdot \sin \theta \cdot r^3}{3E_0 \cdot I} \end{cases} \quad (4.29)$$

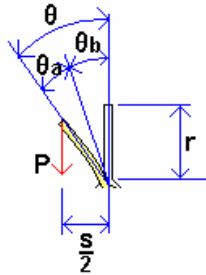


Figure 4.7: Main beam design

Using the conditions:

$$\theta_b = 0.1 \text{ rad}$$

$$s = 10 \times 10^{-6} \text{ m}$$

$$P = 352 \times 10^{-6} \text{ N}$$

$$E_0 = 168 \times 10^9 \text{ Pa}$$

$$I = 2 \times 10^{-23} \text{ m}^4$$

We solve the equations 4.29, and we get,

$$\theta = 0.11 \text{ rad} \quad (4.30)$$

$$r = 45.3 \text{ } \mu\text{m} \quad (4.31)$$

Therefore the length of the main beam can be  $R = 2r = 90.6 \text{ } \mu\text{m}$ . In practice, we can choose the length as:

$$R = 91 \text{ } \mu\text{m} \quad (4.32)$$

The maximum moment on the main beam:

$$m_{m \max} = P \cdot \frac{s}{2} = 1.76 \times 10^{-9} \text{ N}\cdot\text{m} \quad (4.33)$$

The maximum stress in the main beam:

$$\sigma_{m \max} = m_{m \max} \cdot \frac{h}{2I} = 0.088 \text{ GPa} \quad (4.34)$$

Comparing equation 4.34 and 4.28,  $\sigma_{m \max}$  is a bit smaller than  $\sigma_{b \max}$ , and very safe.

The maximum stress of the whole Fork Hinge structure is,

$$\sigma_{\max} = \max(\sigma_{m \max}, \sigma_{b \max}) = 0.104 \text{ GPa} \quad (4.35)$$

#### 4.2.3.4 Gap Verification

So far, we have chosen that  $L_1 = 400 \mu\text{m}$  and  $R = 91 \text{ } \mu\text{m}$  for the Fork Hinge structure, and under the force  $P = 352 \text{ } \mu\text{N}$ , the structure can move its full range as  $s = 10 \text{ } \mu\text{m}$  in the horizontal direction. Now, we will verify if this move will generate a vertical gap  $g$  larger than  $2 \text{ } \mu\text{m}$ .

From Figure 4.8, the gap  $g$  comprises two parts,  $g_1$  comes from the rotation of the main beam, and  $g_2$  comes from the length change of the branch beam,

$$g = g_1 + 2g_2 \quad (4.36)$$

The gap  $g_1$  can be calculated by supposing that the main beam doesn't bend too much,

$$g_1 = R(1 - \cos \theta_1) = 0.558 \text{ } \mu\text{m} \quad (4.37)$$

## Chapter 4

## Design of the Bi-stable Micro Actuator

In order to calculate  $g_2$ , we should get the length change of the branch beam  $\Delta L$ , as shown in Figure 4.9.  $\Delta L$  can be calculated by simplifying the bending curve of the beam as three segments of arc. The position  $x = x_m$  is where the beam reaches its maximum deformation  $w_{\max}$ , and we noticed that the first two arc segments are symmetrical and each has a length of  $x_m/2$

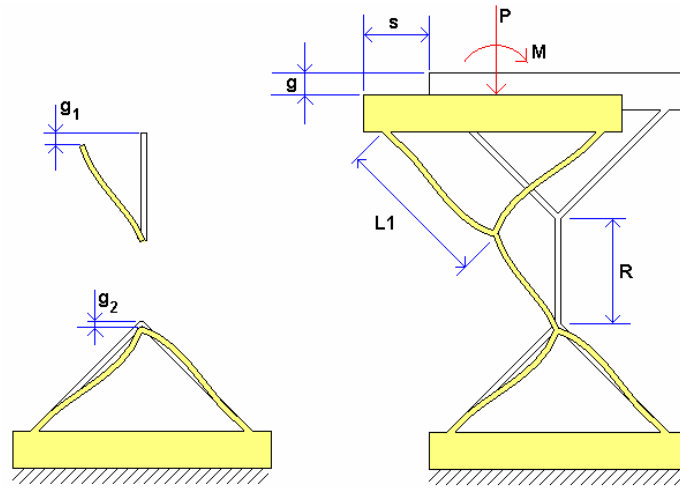
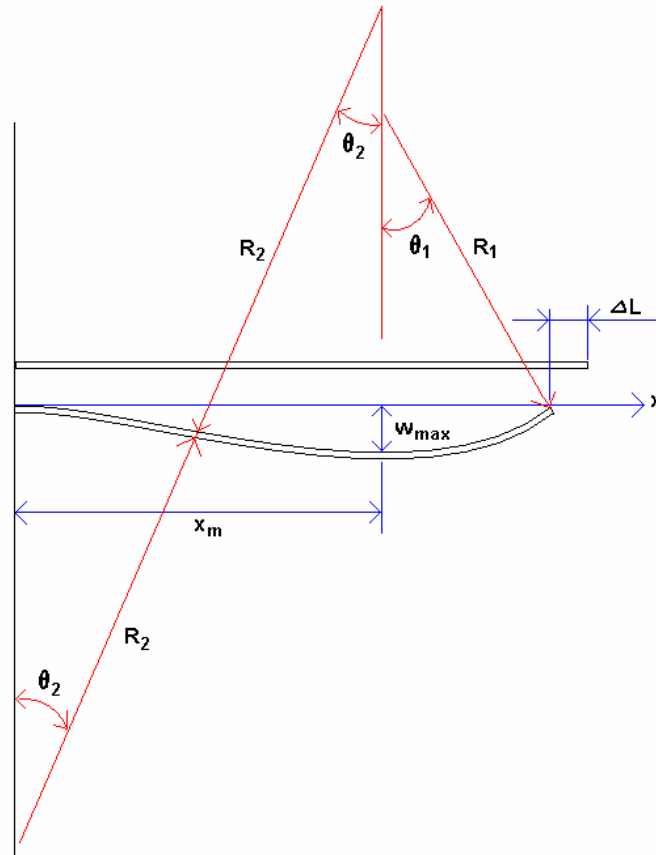


Figure 4.8: Composition of the gap

Figure 4.9: Calculation of  $\Delta L$

## Chapter 4

## Design of the Bi-stable Micro Actuator

$$\begin{cases} \frac{d\omega_{(x)}}{dx} = 0 \\ \omega_{(x)} = \frac{F_{1a}}{F_{1b}}x + \frac{m_1 - F_{1a}L_1}{F_{1b}} - \frac{F_{1a}\sqrt{E_{45}I}}{F_{1b}^{\frac{3}{2}}} \sin\left(\sqrt{\frac{F_{1b}}{E_{45}I}} \cdot x\right) - \frac{m_1 - F_{1a}L_1}{F_{1b}} \cos\left(\sqrt{\frac{F_{1b}}{E_{45}I}} \cdot x\right) \end{cases} \quad (4.38)$$

Giving the known conditions and solve these equations, we can get that,

$$x_m = 248.2 \text{ } \mu\text{m} \quad (4.39)$$

And

$$\omega_{\max} = \omega_{(x_m)} = -8.62 \text{ } \mu\text{m} \quad (4.40)$$

Then the following equations are used to calculate the  $\Delta L$ ,

$$\begin{cases} \Delta L = (L_1 - x_m) - R_1 \cdot \sin \theta_1 + 2\left(\frac{x_m}{2} - R_2 \cdot \sin \theta_2\right) \\ R_1 \cdot \theta_1 = L_1 - x_m \\ R_1 \cdot (1 - \cos \theta_1) = \omega_{\max} \\ R_2 \cdot \theta_2 = \frac{x_m}{2} \\ R_2 \cdot (1 - \cos \theta_2) = \frac{\omega_{\max}}{2} \end{cases} \quad (4.41)$$

Solving equations set 4.41 (for detailed solving process, the reader is referred to the appendix), we get,

$$\Delta L = 0.528 \text{ } \mu\text{m} \quad (4.42)$$

Thus,

$$g_2 = \sqrt{2}\Delta L = 0.746 \text{ } \mu\text{m} \quad (4.43)$$

And by inserting this value in equation 4.36, the value of the gap is,

$$g = 2.05 \text{ } \mu\text{m} \quad (4.44)$$

Which means that the value of the gap fits the demand of  $g \geq 2 \mu\text{m}$  under the force  $P=352\mu\text{N}$ . In practice, the force from the spring is larger than  $475\mu\text{N}$ , which will make the value of  $g$  even larger, and the result is thus satisfactory.

#### 4.2.3.5 Verification of the Stability of the Beams

There are two kinds of beams in the Fork Hinge structure, one is the branch beam, and the other is the main beam. As the branch beam is much longer than the main beam, it seems easier to lose its stability than the main beam. Thus only the branch beam needs to be tested for stability.

The slenderness of the branch [60] beam is given by,

$$\lambda = \frac{u \cdot L_1}{\sqrt{\frac{I}{A}}} \quad (4.45)$$

Where the values of  $L_1$  and  $I$  are already known from the former calculation.  $A$  is the area of the cross section of the beam. Because both ends of the beam are fixed, the coefficient of length  $u$  should be 0.5. Thus,

$$u = 0.5$$

$$A = b \cdot h = 6 \times 10^{-11} \text{ m}^2$$

Therefore the slenderness:

$$\lambda = 346.6 > \lambda_p = 132$$

So the beam is a long beam, and the critical load of the beam is:

$$P_{cr} = \frac{\pi^2 \cdot E_{45}}{\lambda^2} A = 641 \mu\text{N} \quad (4.46)$$

When the Fork Hinge is under load  $P = 352\mu\text{N}$ , the axial load on the branch beam is

$$F_{1b} = 248.9 \mu\text{N}. \text{ Thus, the structure is stable and safe as } P_{cr} \gg F_{1b}.$$



#### 4.2.3.6 P versus $\theta$

In this section, we will calculate the vertical load  $P$  needed to balance the restoring force of the Fork Hinge structure at different angles of the full range of it. The result will be used as condition for the spring design and combdrive design. Analyzing Figure 4.10, the relation between  $P$  and  $\theta$  (between  $-0.11$  rad and  $+0.11$  rad) is given by:

$$\left\{ \begin{array}{l} \theta = \theta_a + \theta_b \\ \theta_a = \frac{P \sin \theta \cdot r^2}{3E_0 I} \\ \theta_b = \frac{F_{1a}}{F_{1b}} - \frac{F_{1a}}{F_{1b}} \cos\left(\sqrt{\frac{F_{1b}}{E_{45} I}} \cdot L_1\right) + \frac{m_1 - F_{1a} L_1}{\sqrt{F_{1b} E_{45} I}} \sin\left(\sqrt{\frac{F_{1b}}{E_{45} I}} \cdot L_1\right) \\ m_1 = \frac{P \cdot r \cdot \sin \theta}{2} \\ F_{1b} = \frac{\sqrt{2}}{2} p \\ 0 = \omega_{(L_1)} = \frac{F_{1a}}{F_{1b}} L_1 + \frac{m_1 - F_{1a} L_1}{F_{1b}} - \frac{F_{1a} \sqrt{E_{45} I}}{F_{1b}^{\frac{3}{2}}} \sin\left(\sqrt{\frac{F_{1b}}{E_{45} I}} \cdot L_1\right) - \frac{m_1 - F_{1a} L_1}{F_{1b}} \cos\left(\sqrt{\frac{F_{1b}}{E_{45} I}} \cdot L_1\right) \end{array} \right. \quad (4.47)$$

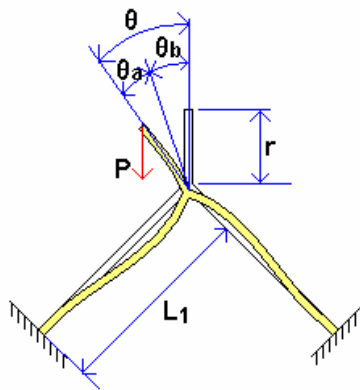


Figure 4.10: Relation between  $P$  and  $\theta$

The above equations cannot be solved using algebraic solution. However, using numerical solution with Maple 7, we can plot the relation between  $P$  and  $\theta$ , as shown

in Figure 4.11. From which we see that the vertical load  $P$  needed to balance the restoring force remains nearly constant as  $352 \pm 0.2\% \mu\text{N}$ .

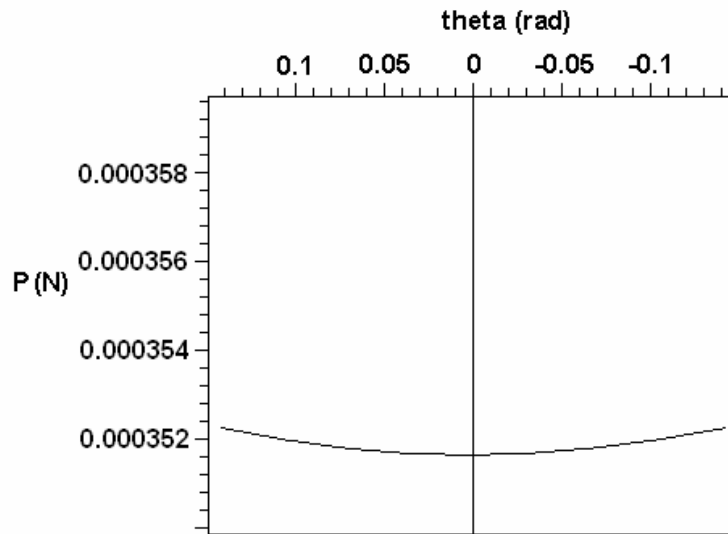


Figure 4.11:  $P$  versus  $\theta$

#### 4.2.4 FEA Simulation of the Fork Hinge Structure

So far we have finished the analytical calculation of the Fork Hinge structure, and have chosen the dimensions of the structure as follows:

$$b = 30 \mu\text{m}$$

$$h = 2 \mu\text{m}$$

$$L_1 = 400 \mu\text{m}$$

$$R = 91 \mu\text{m}$$

In order to verify the calculation, the FEA tool ANSYS has been used to simulate the structure with these dimensions and forces. The basic settings of the structure are shown in Figure 4.12. At point B and point C, all DOF are fixed. At point A, we impose a displacement  $U_x = 5 \mu\text{m}$  and a force  $F_y = 352 \mu\text{N}$ .

The steps and options of the ANSYS FEA simulation are referred to appendix B. Figure 4.13 shows the von Mises stresses of the structure under the given load conditions. It also shows the deformation shapes of the beams, which are exactly as the analytical prediction before. The maximum stress is 0.119 GPa, which is just a

little larger than the calculated value  $\sigma_{\max} = \max(\sigma_{m\max}, \sigma_{b\max}) = 0.104$  Gpa (equation 4.35) due to stress concentration at the connection point of the main beam and branch beams.

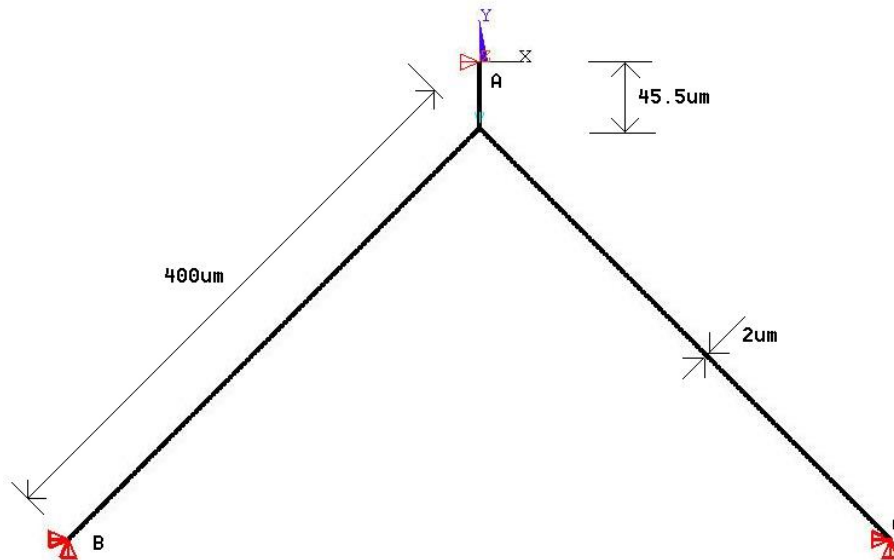


Figure 4.12: Fork Hinge structure for FEM simulation

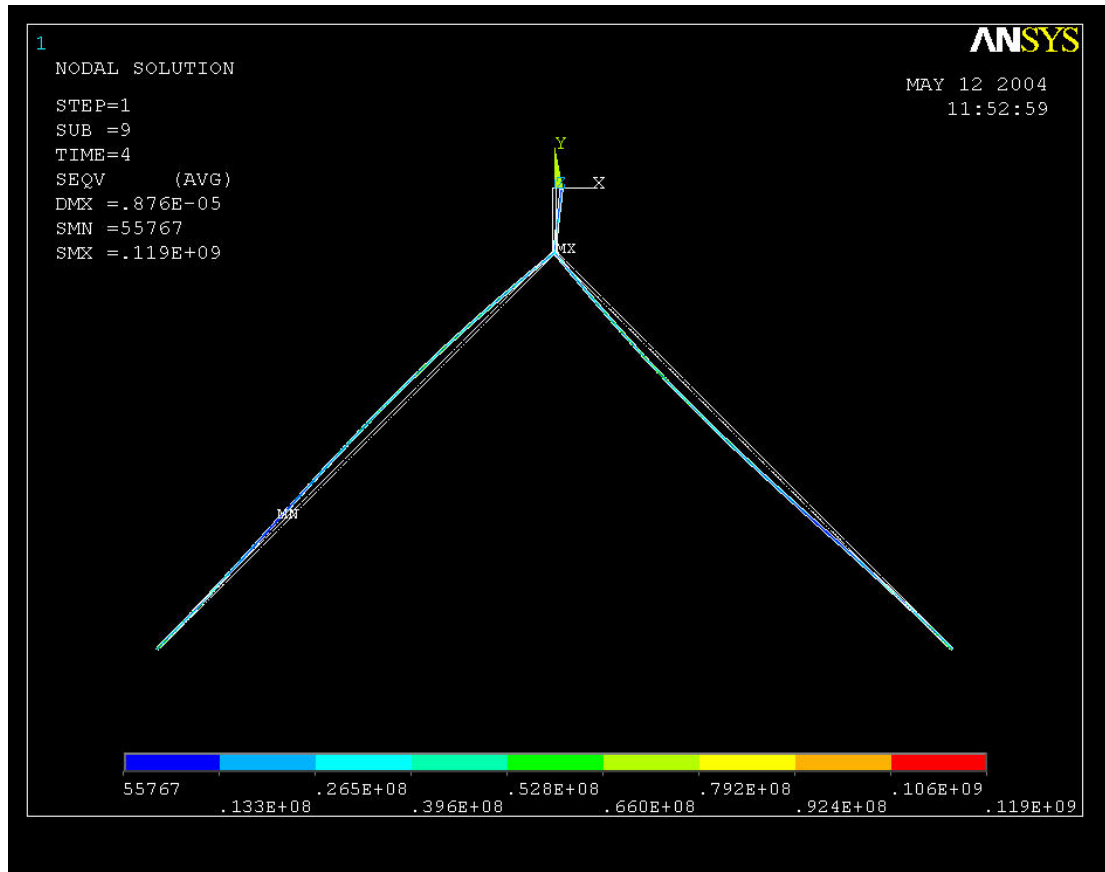


Figure 4.13: Von Mises stress (Pa) of Fork Hinge

Figure 4.14 is a zoom of Figure 4.13. It clearly shows the distribution of the stresses and the point on which maximum stress happens.

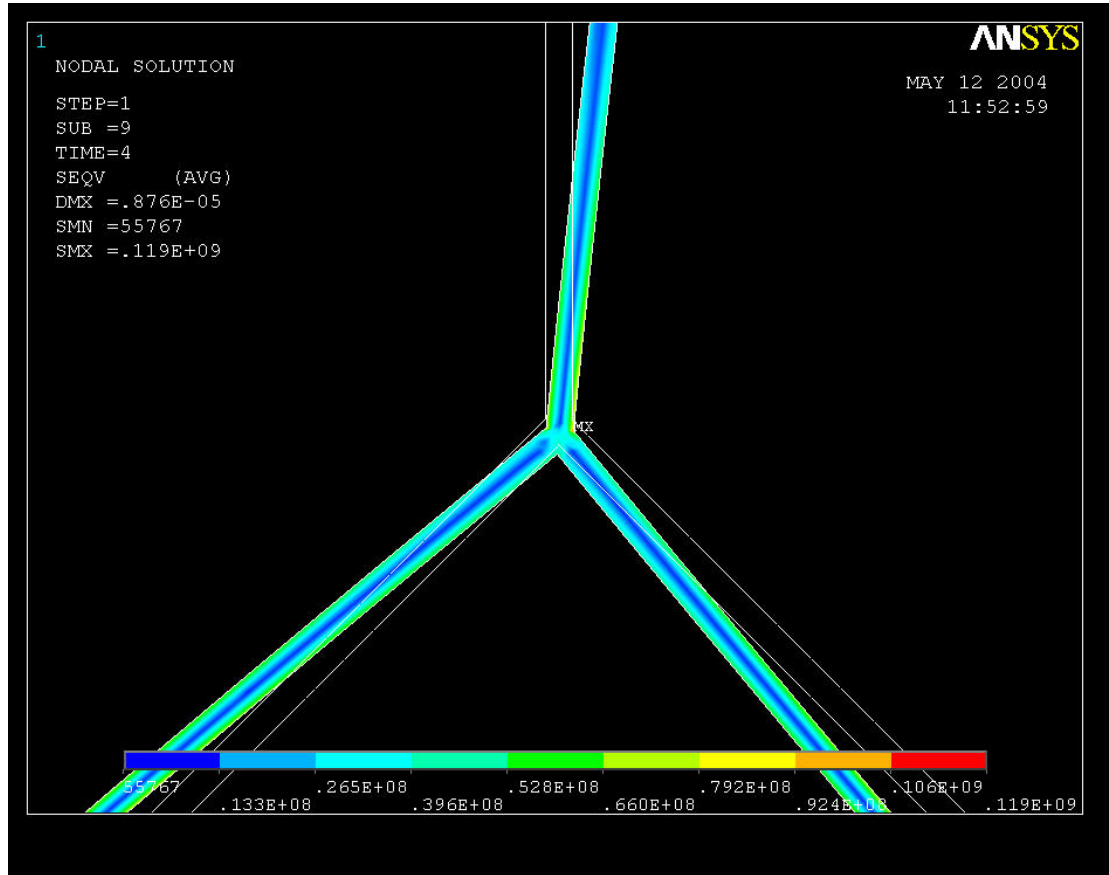


Figure 4.14: Stress at the beam connection point

ANSYS simulation has also been used to verify the gap  $g = 2.05 \mu\text{m}$  (equation 4.44).

Figure 4.15 is the contour plot of the displacement of the structure in the Y direction. By querying the value at the top center node of the main beam, a value of  $-0.955 \mu\text{m}$  is obtained, and the FEA simulation value of the gap is  $2 \times 0.955 = 1.91 \mu\text{m}$ . Thus the difference between the analytical calculation and the FEA simulation is  $(2.05 - 1.91) / 2.05 \approx 6.8\%$ . For such a complicated calculation, this result is another proof of the correctness of our analytical model.

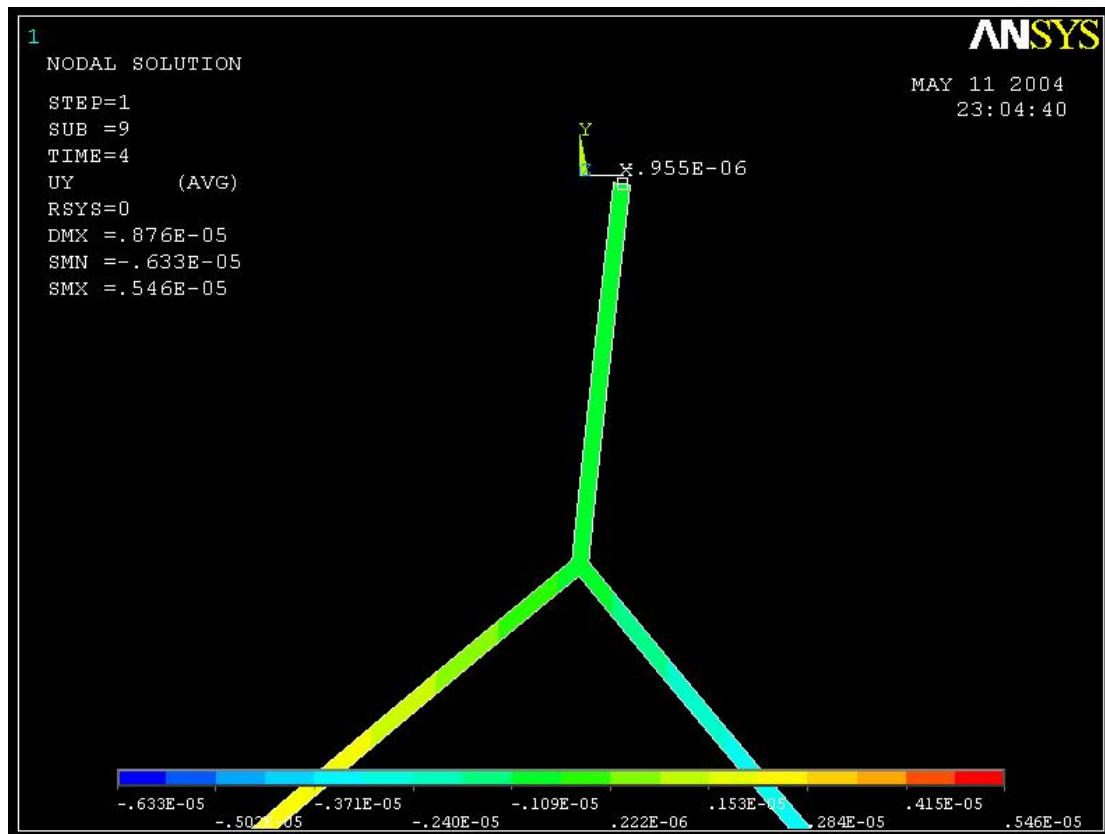
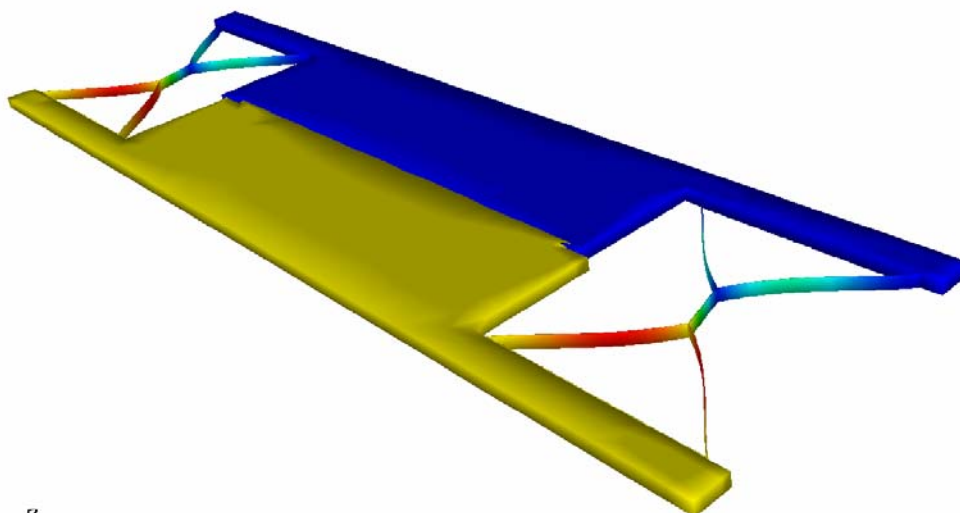


Figure 4.15: Contour plot of displacement in Y direction

In the application of SWOMS, two Fork Hinges are connected together and their main beams form a sway rod. Two sway rods work together to move the stage parallel. Figure 4.16 is the simulation of the movement when the hinges work together. This simulation was conducted by CoventorWare.



7

Figure 4.16: The displacement of the complete Fork Hinge structure

### 4.2.5 Summary of the Fork Hinge Design

Referring to Figure 4.2, we have designed the Fork Hinge structure with the following dimensions:

$$h = 2 \text{ } \mu\text{m}$$

$$b = 30 \text{ } \mu\text{m}$$

$$R = 91 \text{ } \mu\text{m}$$

$$L_1 = 400 \text{ } \mu\text{m}$$

These dimensions were optimized when the structure is under a vertical load of

$$P = 352 \text{ } \mu\text{N}$$

The deformation of the structure can be:

$$s = 10 \text{ } \mu\text{m}$$

$$g = 2.05 \text{ } \mu\text{m}$$

The maximum stress

$$\sigma_{\max} = 0.104 \text{ GPa}$$

The long beam is stable at axial compressive force as large as

$$P_{cr} = 641 \text{ } \mu\text{N}$$

And the vertical force  $P$  needed to balance the restoring force of the structure at the whole moving range of the structure remains nearly constant as  $352 \pm 0.2\% \text{ } \mu\text{N}$ , as shown in Figure 4.11.

### 4.3 Design of the Latching Spring and Lock Structure

The structure of the spring has been shown in Figure 3.11. Because the left and right arches of the structure are symmetric, we concentrate only on its right arch.

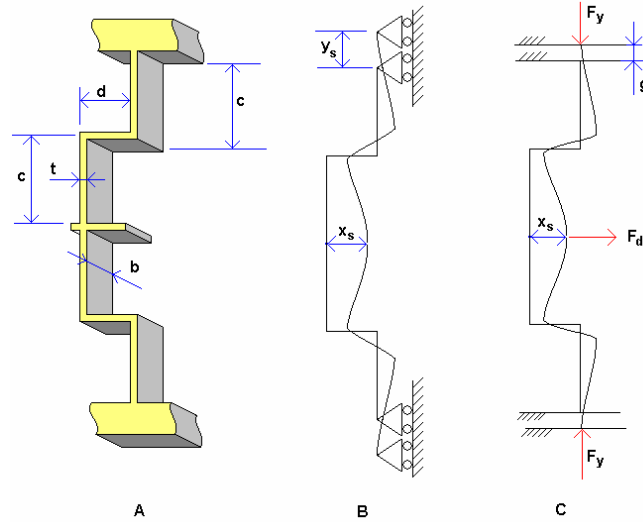


Figure 4.17: Spring design parameters

#### 4.3.1 Design Objective

The objective of the spring design is to choose its dimensions. As shown in Figure 4.17 A, the values of  $b$ ,  $c$ ,  $d$ , and  $t$  need to satisfy the following requirements:

- During assembly of the two archs, if the middle point of the arch moves a distance of  $x_s = 10\mu\text{m}$  horizontally, as shown in Figure 4.17 B, both ends of the arch should then move a distance of  $y_s = 8\mu\text{m}$  vertically if there is no limitation in the  $y$  direction. These values are carefully chosen considering the force and range of combdrive, and the force needed for latching. “ $x_s = 10\mu\text{m}$ ” is the distance the middle point of the arc moved in reference to the end points of the arc in horizontal direction during assembly of the spring structure. The  $y_s = 8\mu\text{m}$  is chosen to provide suitable spring force. Thus after assembly, the length of the spring will be  $16\mu\text{m}$  longer than the value before assembly. And at the middle position of the switch, the spring will be compressed by  $16\mu\text{m}$ .

- If the expansion of the assembled spring is constrained and it can only change by  $g = 2\mu\text{m}$  at both ends, as shown in Figure 4.17 C. Then the SWOMS is at its latching position, the spring will be compressed by  $16 - 2 \times 2 = 12\mu\text{m}$ . In this case, the vertical force  $F_y$  generated by the spring should be larger than the force needed from the spring to balance the restoring force of the fork hinge structure, which is  $352\mu\text{N}$  from the calculation in section 4.2.3.6. Here we choose  $450\mu\text{N}$  as the design objective to ensure reliable self-latching at the latching position.
- The force  $F_d$  needed for assembly should not be too large, or it may exceed the maximum force of the combdrive actuator.
- The stress inside the spring should be very small, i.e. smaller than  $0.5\text{GPa}$  to ensure long lifetime.

### 4.3.2 Design Using Analytical Model

In order to satisfy the first requirement, let's observe the deformation relation in the vertical and horizontal direction. Because of the geometry and the force symmetry, only one fourth of the arch needs to be studied, as shown in Figure 4.18.

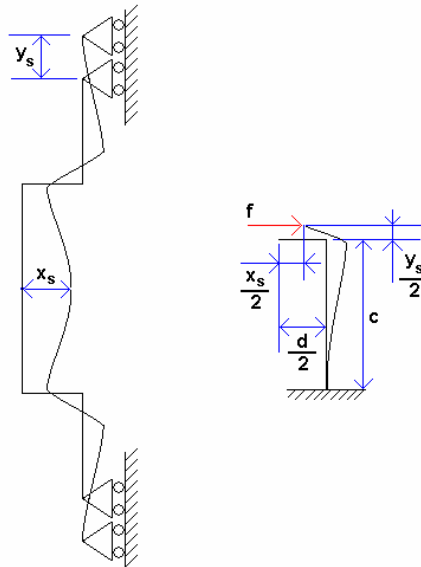


Figure 4.18: Spring deformation analysis

Analyzing the geometry, we have,



$$\begin{cases} \frac{x_s}{2} = \frac{f \cdot c^3}{3EI} \\ \frac{y_s}{2} = \frac{f \cdot c^2 \cdot \frac{d}{2}}{2EI} \\ \frac{x_s}{y_s} = \frac{10}{8} \end{cases} \quad (4.48)$$

Then we get,

$$d = \frac{16}{15} c \quad (4.49)$$

In order to satisfy the second requirement and calculate  $F_d$ , we can also analyze one quarter of the arch of the spring that have already been compressed by  $12\mu\text{m}$  (see Figure 4.19).

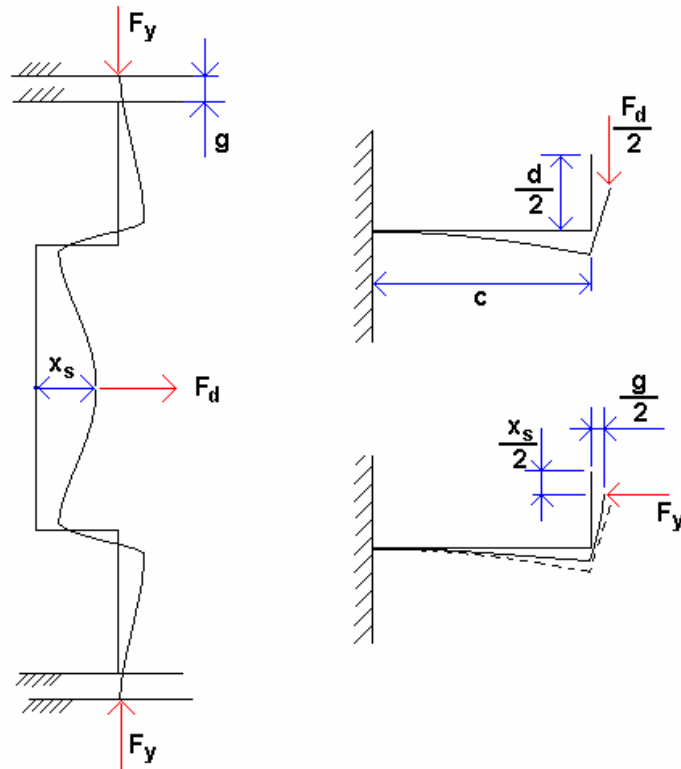


Figure 4.19: Spring force analysis

Here we have,

## Chapter 4

## Design of the Bi-stable Micro Actuator

$$\begin{cases} \frac{x_s}{2} = \frac{\frac{F_d}{2} \cdot c^3}{3EI} - \frac{F_y \cdot \frac{d}{2} \cdot c^2}{2EI} \\ \frac{g}{2} = \frac{\frac{F_d}{2} \cdot c^2}{2EI} \cdot \frac{d}{2} - \left( \left( \frac{F_y \cdot \frac{d}{2} \cdot c}{EI} \right) \cdot \frac{d}{2} + \frac{F_y \cdot \left( \frac{d}{2} \right)^3}{3EI} \right) \end{cases} \quad (4.50)$$

Using the conditions that

$$x_s = 10 \text{ } \mu\text{m}$$

$$g = 2.0 \text{ } \mu\text{m}$$

$$F_y = 450 \text{ } \mu\text{N}$$

$$d = \frac{16}{15}c$$

$$E = 168 \text{ GPa}$$

$$I = \frac{b \cdot t^3}{12}$$

$$b = 30 \text{ } \mu\text{m}$$

Equation 4.50 can be solved as:

$$F_d = 1268 \text{ } \mu\text{N}$$

$$t = 0.03517c$$

with  $c = 295 \text{ } \mu\text{m}$ , then

$$t = 10.4 \text{ } \mu\text{m}$$

$$d = 315 \text{ } \mu\text{m}$$

Thus, the dimensions for the spring can be chosen as,

$$b = 30 \text{ } \mu\text{m} \quad (4.51)$$

$$c = 300 \text{ } \mu\text{m} \quad (4.52)$$

$$d = 325 \text{ } \mu\text{m} \quad (4.53)$$

## Chapter 4

## Design of the Bi-stable Micro Actuator

$$t = 10.4\mu\text{m} \quad (4.54)$$

And,

$$F_y = 450 \mu\text{N} \quad (4.55)$$

$$F_d = 1268 \mu\text{N} \quad (4.56)$$

This force is achievable with a combdrive actuator, thus fulfilled the third requirement of the design.

The maximum moment and maximum stress on the spring:

$$M_{\max} = \frac{F_d}{2} \cdot c - F_y \cdot \frac{d}{2} = 1.17 \times 10^{-7} \text{ N}\cdot\text{m} \quad (4.57)$$

$$\sigma_{\max} = \frac{M_{\max} \cdot \frac{t}{2}}{I} = 0.217 \text{ GPa} \quad (4.58)$$

This stress is below the requirement of 0.5GPa, and the fourth requirement is also satisfied.

The lock structure is used to lock the assembly when the spring is pre-stressed. It is a relatively easy task to design thus we just give the result as Figure 4.20.

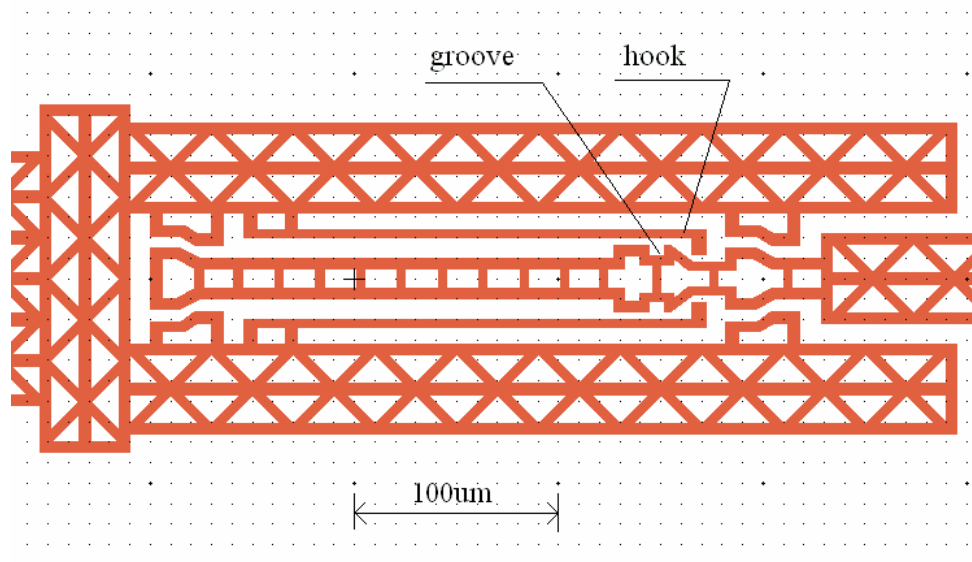


Figure 4.20: The lock structure

### 4.3.3 FEA Simulation of the Spring

Figure 4.21 shows the FEA mesh of the spring structure by CoventorWare. Figure 4.22 is the simulation of displacement relation between  $x_s$  and  $y_s$ , and Figure 4.23 shows the stress distribution, which agrees with our analysis well.

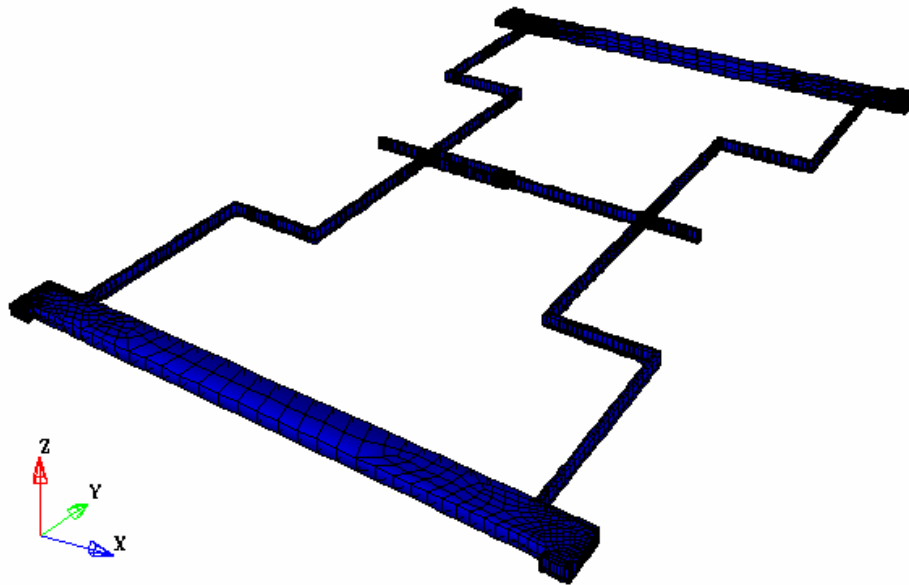


Figure 4.21: Spring FEA meshing

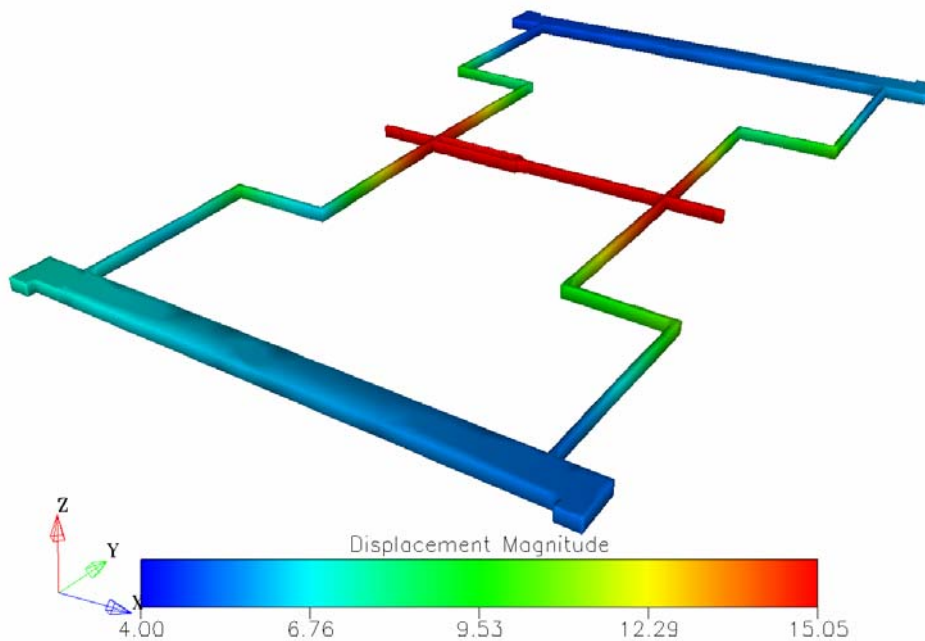


Figure 4.22: Spring displacement ( $\mu\text{m}$ )

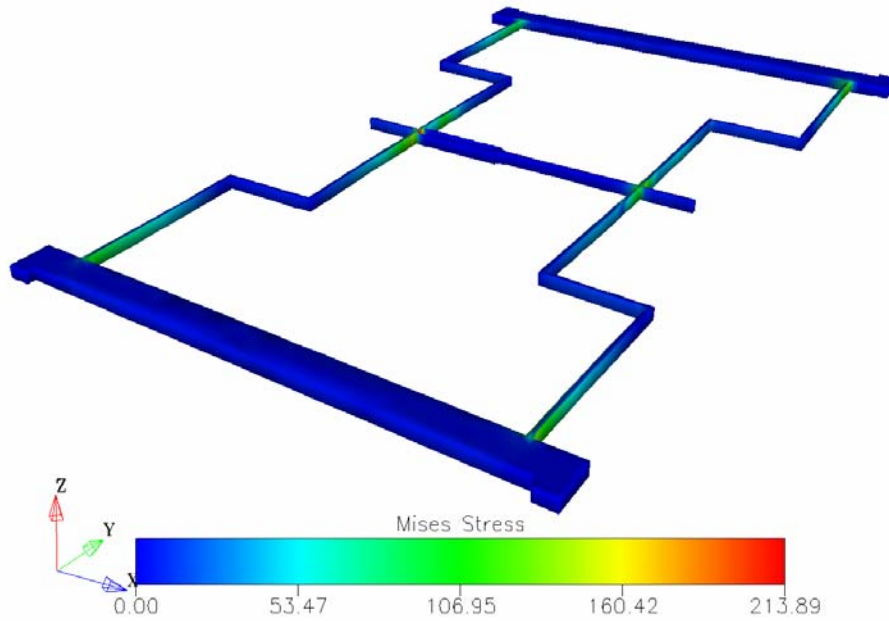


Figure 4.23: Spring stress (MPa)

#### 4.3.4 Summary

So far we have finished the design of the spring and the Fork Hinge structure. The combination of them formed the bi-stable latching system. Here we discuss some feature of this system.

A main concern is how much force needed to switch such system from one latching position to the other. This can be analyzed by simplifying the spring structure and Fork Hinge structure using a reduced- order model.

According to the displacement of point A, the Fork Hinge structure can be simplified as a sway rod as in Figure 4.24. The only difference is that there is always a vertical force  $P = 352\mu\text{N}$  needed to balance the restoring force.

Although the spring structure is not strictly linear, considering its small working range ( $2\mu\text{m}$ ) in the actuator, it can be looked as linear and we can define a spring constant. When the spring is at the latching position of the actuator, considering upper half of the spring, the force  $F_y$  provide by the spring is calculated to be  $450\mu\text{N}$  according to Eq. 4.55, and the top of the spring is compressed by  $6\mu\text{m}$ . Thus the spring constant is:

$$k_s = \frac{450 \times 10^{-6}}{6 \times 10^{-6}} = 75 \text{ N/m} \quad (4.59)$$

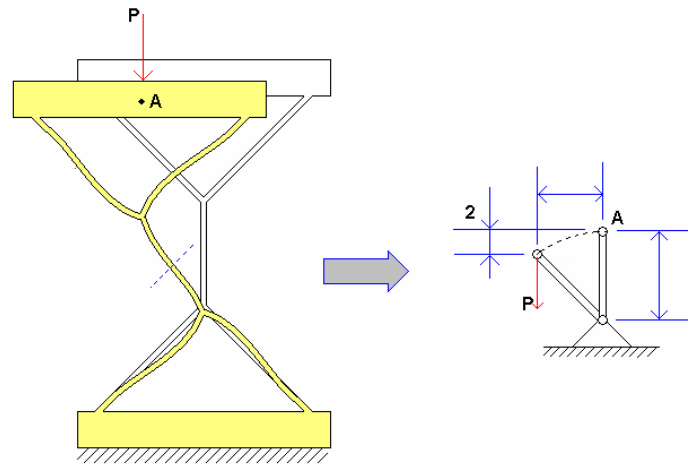


Figure 4.24: Reduce-order model of the Fork Hinge structure

The difference between the spring structure and a simple 1 DOF spring is that the spring structure produces forces not only in the vertical direction, but also in the transverse direction.

With these simplifications and the known parameters of the system, we can calculate the force needed to switch the bi-stable structure from one position to the other (see Figure 4.25). The detailed calculation process can be found in the appendix Maple 7 calculation program. Because this force will be provided by the actuator, this analysis is the basis of the design of the combdrive actuator.

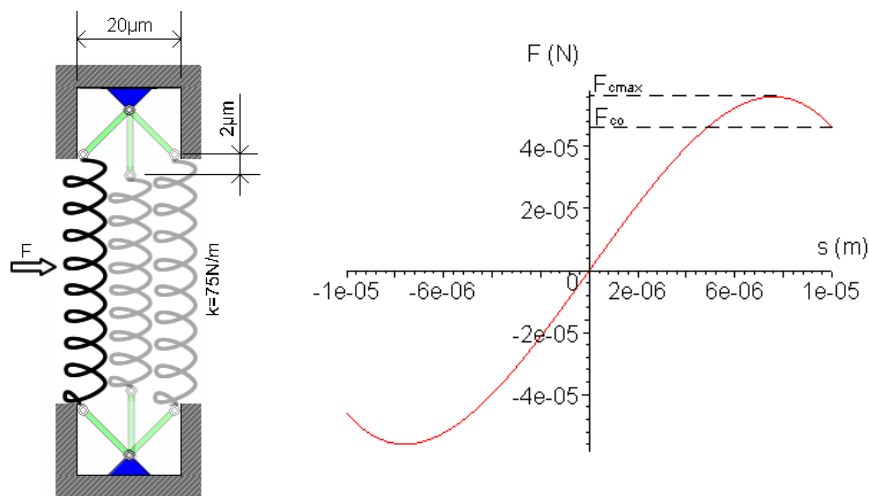


Figure 4.25: Simplified model (left) and force needed for switching (right)

From the calculation, the force needed to overcome the latching effect of the spring/sway-rod system at the latching position is,

$$F_{co} = 45 \text{ } \mu\text{N} \quad (4.60)$$

And the actuator force needed to change the structure from one latching position to the other is given by the maximum value of the  $F$  in Figure 4.25,

$$F_{c\max} = 56 \text{ } \mu\text{N} \quad (4.61)$$

#### 4.4 Design of the Combdriives and Suspensions

The combdrive and its suspension always work together. The combdrive provide the electrostatic attraction force. The suspension provides the restoring force and limits the motion vertically (Figure 4.26), preventing the fingers of the combdrive from sticking together. Combdriive structures leave little freedom to design, but suspensions can have different structure such as fixed-fixed beams, crab-leg flexure, and folded-beam flexure. The folded-beam flexure shown in the Figure here is considered to be the best because it moves in a straight line and has very high ratio between the spring constants in the vertical and the horizontal direction.

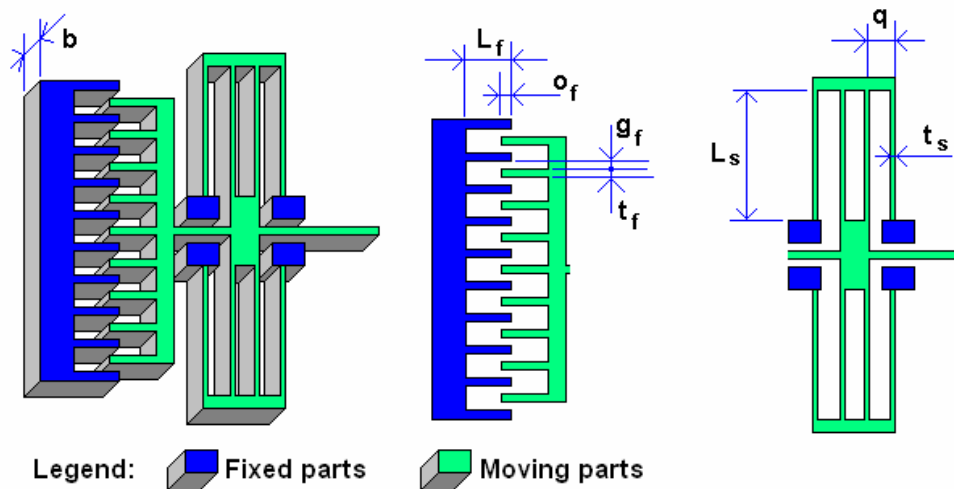


Figure 4.26: The design parameters of combdrive

### 4.4.1 Design Objective

In the Figure 4.26, the value of  $b$  is already fixed as  $30\mu\text{m}$ . So the design objective is to choose the suitable values of  $L_f$ ,  $O_f$ ,  $g_f$ ,  $t_f$ , the voltage  $V_a$  used to assemble the spring, the voltage  $V_s$  used for switching, the finger number of the moving comb  $N$ , and the suitable values of  $L_s$ ,  $t_s$ , and  $q$  for the folded flexure to meet the following requirements:

- The combdrive should be able to provide  $1268\mu\text{N}$  (see Equ. 4.56) for latch-assembly when we apply the voltage  $V_a$ , and can reliably provide  $56\mu\text{N}$  (see Equ. 4.61) frequently for switching under the  $V_s$ .
- The length of the finger  $L_f$  and the overlap  $O_f$  of the fixed and moving comb should meet the moving range of the whole structure.
- The fingers of the combdrive should be stiff enough that it won't bend much and tend to stick together.
- The supporting beams should be very compliant in the moving direction of the comb to ensure the large displacement, while be very stiff in the orthogonal direction to keep side stability.

### 4.4.2 Combdrive Design

For a combdrive, the gap  $g_f$  between the fingers should be as small as possible to ensure larger actuating force. In this situation,  $g_f$  is limited by the fabrication process. So

$$g_f = 2\mu\text{m} \quad (4.62)$$

is chosen due to the critical feature size of fabrication. The finger length  $L_f$  and the finger overlap  $O_f$  need to be chosen according to the moving range of the structure



## Chapter 4

## Design of the Bi-stable Micro Actuator

Figure 4.27 shows the moving track of the fingertip of the left and right moving comb due to the motion of the spring structure. Where 1 is the original position, 2 is the position when the whole structure has moved right but before the latch-assembly, 3 is the position of the fingertips after assembly, and 4 is the structure switching from right to left. According to the analyses in Figure 4.27, the finger length should be longer than  $27.5\mu\text{m}$ , and the overlap should be larger than  $10\mu\text{m}$ . Considering fabrication tolerance, we can choose,

$$L_f = 31 \mu\text{m} \quad (4.63)$$

$$O_f = 10 \mu\text{m} \quad (4.64)$$

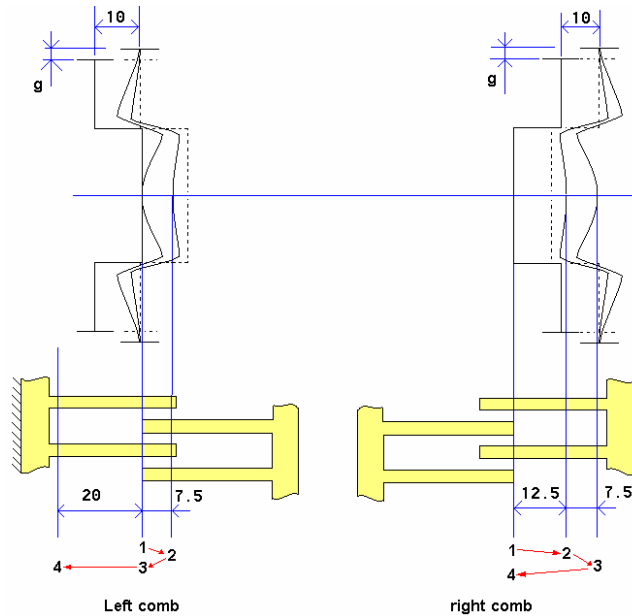


Figure 4.27: Moving range of the combdrives

The force provided by a combdrive can be roughly calculated by [62]:

$$F = \frac{\varepsilon \cdot b \cdot V^2 \cdot N}{g_f} \quad (4.65)$$

Here  $\varepsilon$  is the dielectric constant of air, which equals to  $8.854 \times 10^{-12} \text{ N/V}^2$ . The value of  $b$  and  $g_f$  are known, Thus we need to choose suitable voltage and finger number to get desired force. It is often preferred to choose as small as possible number of fingers in order to reduce the volume and failure risk of the device, which means we

## Chapter 4

## Design of the Bi-stable Micro Actuator

need to choose a higher voltage. However, the breakdown voltage of air limits the maximum voltage value, as when the voltage is too high, a spark will form between the fingers and destroy the combdrive.

The electrical breakdown field of air is quoted as  $3 \times 10^6$  V/m in the macro world. However, this value is not applicable for our design because when the gap between electrodes is below  $5 \mu\text{m}$ , the electrical breakdown field will increase significantly and follow the Paschen's law. For  $2 \mu\text{m}$  air gap, the breakdown field has been measured as  $1.7 \times 10^8$  V/m [63]. So that for a  $2 \mu\text{m}$  gap, the breakdown voltage is about,

$$V_{break} = 1.7 \times 10^8 \times 2 \times 10^{-6} = 340 \text{ V}$$

Therefore, we can choose 110V as the assembly voltage and 25V as the switching voltage of the device for safety concern, and 800 fingers in each comb. Choosing the number of fingers of the combdrive requires considering many aspects including: actuation force, fabrication easiness, wafer area occupied, maximum voltage that can be applied, stiffness of the structure, and stability of the supporting flexure. The number of 800 is chosen to balance all this requirements and resulted from an optimization obtained after many rounds of calculation.

$$V_a = 110 \text{ V} \quad (4.66)$$

$$V_s = 25 \text{ V} \quad (4.67)$$

$$N = 800 \quad (4.68)$$

The assembly force provided by the combdrive, according to equation 4.65, will be,

$$F_a = \frac{\varepsilon \cdot b \cdot V_a^2 \cdot N}{g_f} = 1285 \mu\text{N} > F_d = 1268 \mu\text{N} \quad (4.69)$$

And the switching force

$$F_s = \frac{\varepsilon \cdot b \cdot V_s^2 \cdot N}{g_f} = 66.4 \mu\text{N} > F_{cmax} = 56 \mu\text{N} \quad (4.70)$$

### 4.4.3 Folded Flexure Design.

It is difficult to arrange 800 fingers on a single comb. In order to get a more stable structure, we arranged the fingers in two combs. Thus for each side of the SWOMS, there are two combdrives and two folded flexures, as shown in Figure 4.28, and every comb has 400 fingers. The two comb electrodes are connected so that they can work together.

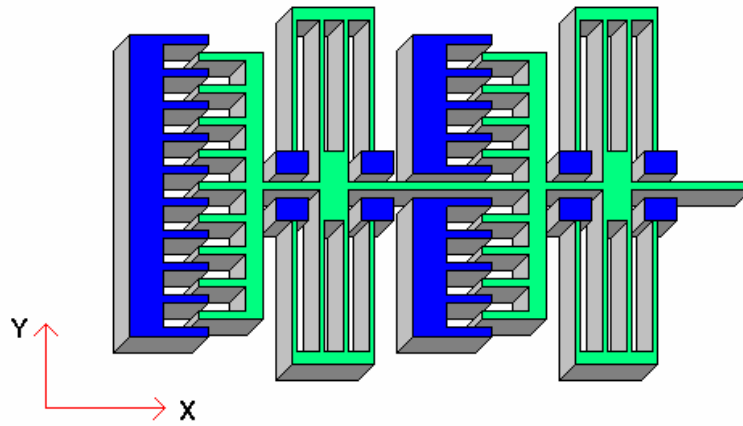


Figure 4.28: Two combdrives connected together.

The suspensions are used to make the structure flexible enough in the X direction and very stiff in the Y direction to keep side stability. For a folded beam flexure, the condition is that the spring constant in Y direction [64]:

$$k_y > K_{y0} = \frac{2 \cdot n \cdot \varepsilon \cdot b \cdot X_m \cdot V^2}{g_f^3} \quad (4.71)$$

Here  $n = 400$  is the number of fingers for one comb;  $\varepsilon$ ,  $b$ , and  $g_f$  are known;  $X_m$  is the maximum overlap of the fingers, here the value is  $31\mu\text{m}$ ; and  $V$  is the voltage 110V. Applying these values on equation 4.71, we get

$$K_{y0} = 9963 \text{ N/m} \quad (4.72)$$

In order to satisfy this demand and get the maximum flexibility in the X direction, we chose the following dimensions:

## Chapter 4

## Design of the Bi-stable Micro Actuator

$$L_s = 1800 \mu\text{m} \quad (4.72)$$

$$t_s = 6.4 \mu\text{m} \quad (4.73)$$

Thus, the spring constant in the Y direction is [64]:

$$k_y = \frac{200EI}{3L_s(\Delta x)^2} = \frac{200E \cdot \frac{b \cdot t_s^3}{12}}{3L_s(20 \times 10^{-6})^2} = 10194 \text{ N/m} > K_{y0} \quad (4.74)$$

The spring constant in X direction is:

$$k_x = \frac{2E \cdot b \cdot h^3}{L^3} = 0.453 \text{ N/m} \quad (4.75)$$

Thus the restoring force caused by the folded flexures when the SWOMS at its one latching position is:

$$F_{xr} = 2k_x \cdot \Delta x = 19.2 \mu\text{N}$$

This value is smaller than the latching force  $45\mu\text{N}$  provided by the spring/sway-rod system, thus won't influence the latching effect of the SWOMS. Moreover, because the mass of the movable parts of the SWOMS is below  $100\mu\text{g}$ , the latching force remained as  $45\mu\text{N} - 19.2\mu\text{N} = 25.8\mu\text{N}$  means the structure can keep its latching place even under impact of acceleration as large as  $25g$ .

Finally, a last parameter  $q$  needs to be chosen. Because its value is not critical for our design, a value of  $200\mu\text{m}$  looks suitable. It won't occupy much space and is large enough to prevent the beams from touching each other.

## Chapter 5 Design of the Polymer Waveguides

Figure 5.1 shows the waveguides used for a  $2 \times 2$  SWOMS and the cross-section of the waveguide. A  $1 \times 2$  SWOMS unit is much simpler than this one and has been shown in Figure 3.19. Lightwave coming from the fiber will be coupled into the fixed waveguide, then coupled into the movable waveguides, and be transmitted to the desired output fixed waveguide and the output fiber. The switching is achieved by shifting the movable waveguides to the left or to the right. As the polymer has a Young's modulus about two orders of magnitude smaller than silicon, its influence on the mechanical performance is negligible.

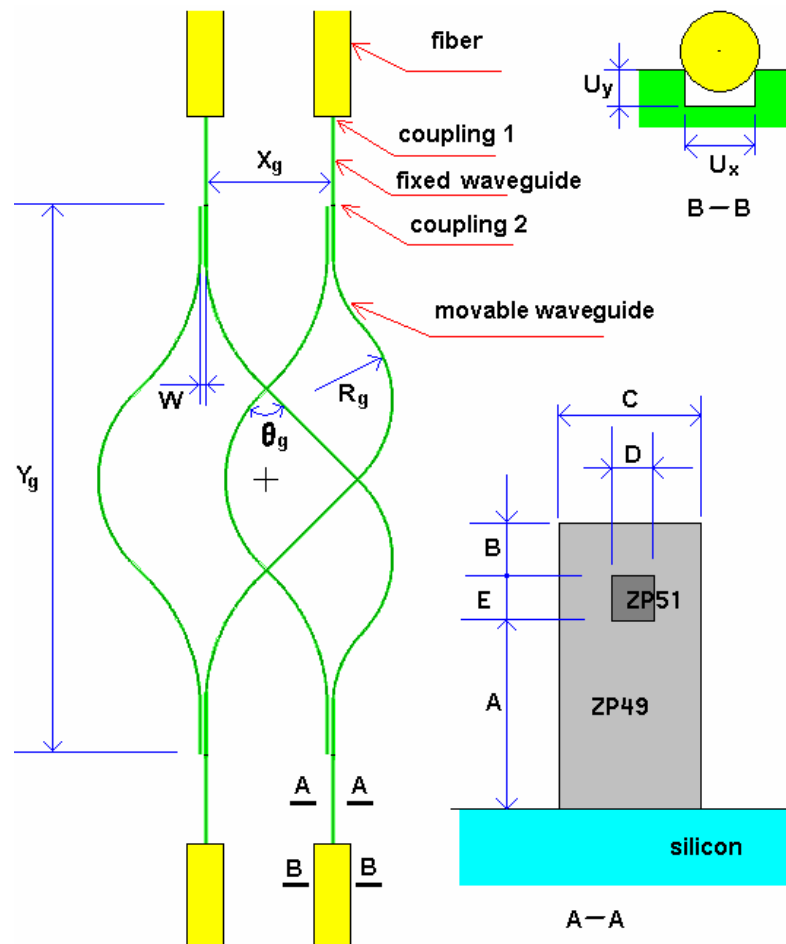


Figure 5.1: Waveguide and its cross-section

Polymers are promising candidates for constructing of waveguide devices with adjustable refractive indices, low optical propagation loss, and good thermal and environmental stability. Several polymeric films have been investigated, including

polymethyl methacrylate (PMMA), polystyrene, polyimide, polycarbonate, and polysiloxane [65]. Many of them can be processed very simply by a spin-coating method on a silicon substrate [66].

ZP49 and ZP51 are the two polymers chosen to build the waveguides of SWOMS. They are thermally curable polymers based on highly fluorinated polyether. Here ZP51 ( $n = 1.5100$ ) is used as the core material and ZP49 ( $n = 1.4900$ ) as the cladding material. ZP51 and ZP49 are available from ZEN Photonics in Korea. They are useful for optical waveguides and optical thin film applications due to the low optical loss, high thermal and environmental stability. Their performance specifications are listed in table 5.1 [75].

	Items	ZP49	ZP51
Liquid	Viscosity ( cps @ 25°C)	240~300	260~320
	Filtration	0.1~0.2 $\mu$ m absolute PTFE filter	
	Curing Temp./Time	250°C for 2 hr.	
Film	Propagation loss (measured from slab waveguide)	0.3dB/cm @ 1.55 $\mu$ m wavelength	
		0.15dB/cm @ 1.3 $\mu$ m wavelength	
	Refractive index @ 1.55 $\mu$ m	1.490	1.510
	Birefringence ( $n_{TE}-n_{TM}$ )	0.004 $\pm$ 0.001	
	Refractive index uniformity	<0.00002	
	Thermo-optic coefficient	$-0.7\sim-1.2\times 10^{-4}/^{\circ}\text{C}$	
	CTE (ppm/ $^{\circ}\text{C}$ , by TMA)	93	78
	Glass transition temp. ( $T_g$ )	146°C	206°C
	Degradation temp. (1% wt loss)	392°C	444°C
	Surface roughness (AFM)	<0.3nm at 8 $\mu$ m thickness	
	Film thickness	< 10 $\mu$ m/coating (multi-coating available)	

Table 5.1: Performance specifications of ZP49 and ZP51

## 5.1 Design Objective

The design objective includes:

- Choose suitable values of  $A$ ,  $B$ ,  $C$ ,  $D$ ,  $E$  for the cross-section of the waveguides. These values must ensure that the light propagates with best coupling and smallest loss, the core and cladding must contain almost all the energy, and the energy leaked to the silicon substrate should be negligible.
- Choose suitable values of  $R_g$ ,  $\theta_g$ ,  $X_g$ ,  $Y_g$ , and  $W$  to define the shape of the waveguides. The objective is to get the lowest insertion loss and the lowest crosstalk.
- Choose suitable values of  $U_x$  and  $U_y$  for the U groove to ensure good alignment of the fiber core and the waveguide core.

## 5.2 Calculation of the Parameters.

The parameters are selected upon theoretical calculations. Thereafter, BPM (beam propagation method) is used to simulate and optimize the waveguides.

The condition for single mode operation of a square-core ( $D=E$ ) waveguide is [67]:

$$D < \frac{2.13\lambda}{\pi\sqrt{n_0^2 - n_1^2}} \quad (5.1)$$

Where  $D$  is shown in Figure 5.1,  $n_0$  is the refractive index of the core, and  $n_1$  is the refractive index of the cladding. In our case, the values are 1.51 and 1.49.  $\lambda$  is the wavelength (1.55 $\mu\text{m}$  or 1.31 $\mu\text{m}$  for telecommunication). Applying these values to equation 5.1 we get,

$$D < 3.63 \text{ } \mu\text{m} \quad (5.2)$$

Thus we can choose

$$D = E = 3.5 \text{ } \mu\text{m} \quad (5.3)$$

So that the normalized frequency in the waveguide is:

$$V = \frac{\pi \cdot D \cdot \sqrt{(n_0^2 - n_1^2)}}{\lambda} \approx 2 \quad (5.4)$$

For such a waveguide, about 79% of the mode power is propagating in the core, and a cladding with thickness  $2D$  is enough to contain most of the power. Thus we can choose  $B = 4 \text{ } \mu\text{m}$ ,  $C = 10 \text{ } \mu\text{m}$  for better adhesion of the polymer to the silicon substrate, and  $A = 14 \text{ } \mu\text{m}$  for stronger mechanical property.

The value of  $W$  is  $20 \mu\text{m}$ , which has been designed as the moving range of the self-latching device. This value is large enough to ensure that the crosstalk caused by coupling between the two parallel waveguides is negligible.

$R_g$  is the radius of the bending, which should be larger than a critical value to ensure small bending loss. The calculation method and Figure 5.2 shown here for the bending loss were extracted from a paper of E. A. J. Marcatili [76].

According to the parameters formerly chosen, the refractive index of the waveguide's core is  $n_1 = 1.51$ , and the refractive index of the cladding is  $n_2 = 1.49$ . The core is a single square core with a size of  $a = 3.5 \text{ } \mu\text{m}$ . The wavelengths are  $\lambda = 1.55 \text{ } \mu\text{m}$  and  $1.31 \text{ } \mu\text{m}$ .

$$\Delta = \frac{n_1}{n_2} - 1 = 0.0134 \ll 1$$

The vertical coordinates of Figure 5.2 shows the value of  $(2\Delta)^{1/2} \alpha_c R$ , where the value of  $\alpha_c R$  is the attenuation per radian of bending. The unit of the vertical coordinates is neper (1 neper = 8.686 dB). The lateral coordinates of the plot is  $a/A$ , where  $A$  is a length used as a normalizing dimension.

$$A = \frac{\lambda}{2(n_1^2 - n_2^2)^{\frac{1}{2}}}$$



## Chapter 5

## Design of the Polymer Waveguides

For  $\lambda = 1.55 \mu\text{m}$ ,

$$\frac{a}{A} = \frac{2a}{\lambda} (n_1^2 - n_2^2)^{\frac{1}{2}} = 1.106$$

In order to reach a low attenuation as  $0.001 \text{ neper/rad}$ ,

$$(2\Delta)^{1/2} \alpha_c R = 1.6 \times 10^{-4} \text{ nepers}$$

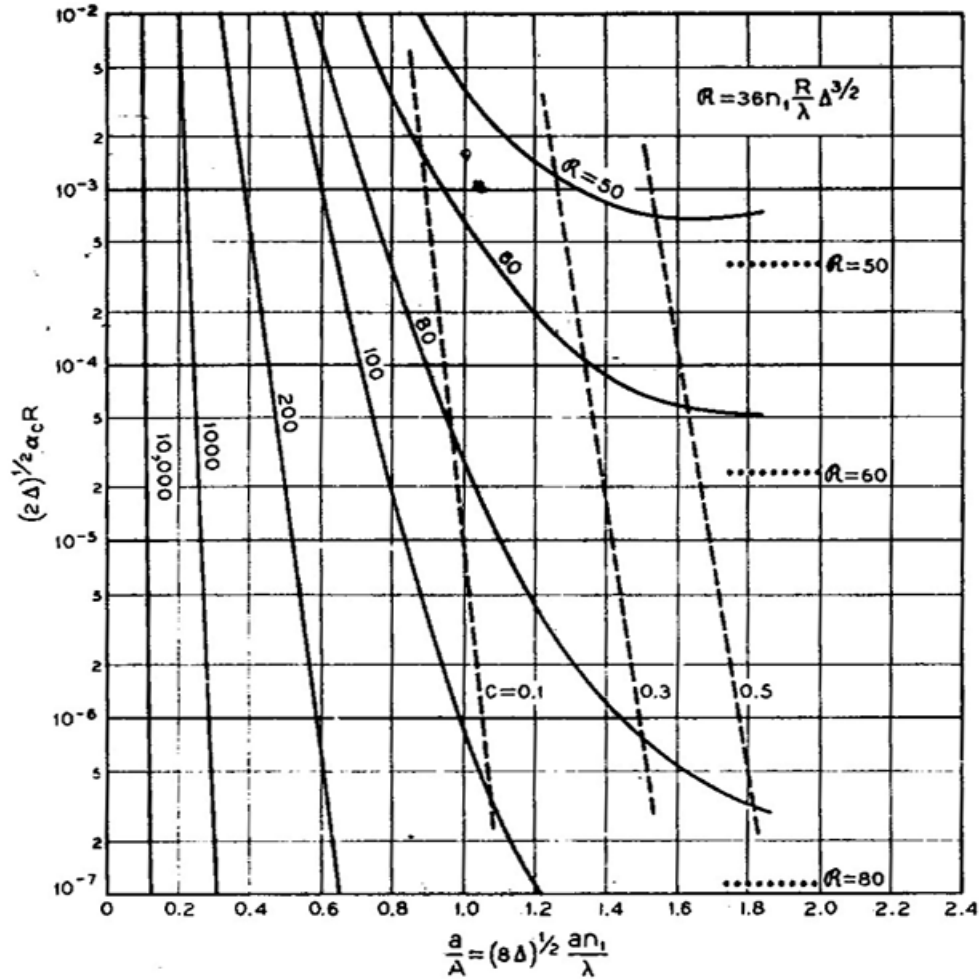


Figure 5.2: Attenuation per radian for  $E_{11}^x$  and  $E_{11}^y$  modes if  $n_1/n_2 = 1+\Delta$  and  $\Delta \ll 1$  [76]

Applying these two values with Figure 5.2, we obtain that  $R \geq 70$ . Then the radius of curvature  $R$  can be solved by:

$$R = 36n_1 \frac{R}{\lambda} \Delta^{3/2} = 36 \times 1.51 \times \frac{R}{1.55} \times 0.0134^{3/2} \geq 70$$

And the result is

$$R \geq 1286 \mu\text{m}$$

Repeating above process, a relation between the bending loss per radian and radius of curvature can be plotted as in Figure 5.3. Two curves are in the plot for both  $\lambda=1.55 \mu\text{m}$  and  $1.31 \mu\text{m}$ . In our case, radii larger than  $1500 \mu\text{m}$  have been chosen for all the bent waveguides to keep the bending loss below  $0.1 \text{dB}$ .  $\theta_g$  is the angle between two intersecting waveguides, a value of  $60^\circ$  to  $90^\circ$  is good enough to keep the loss below  $0.04 \text{dB}$  [69] and obtain negligible crosstalk.  $\theta_g = 60^\circ$  is chosen in our case to reduce the total length and size of the waveguides.

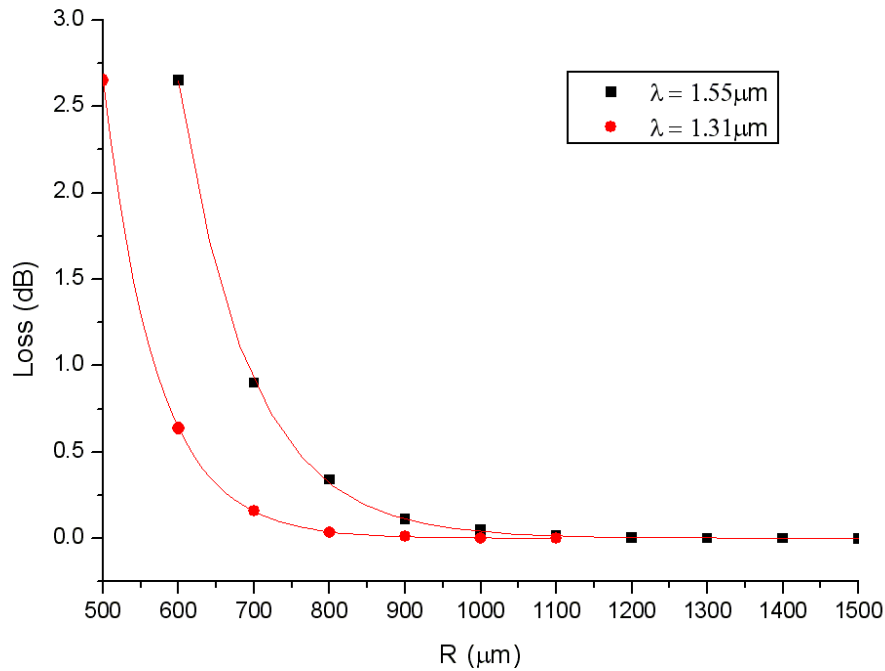


Figure 5.3: Calculated bending losses per radian at different radius

Satisfying above values, we calculated and choose the value of  $X_g$  and  $Y_g$  as,

$$X_g = 740 \mu\text{m}$$

$$Y_g = 4660 \mu\text{m}$$

For the optical fiber holding structure, the value of  $U_x$  is obtained from geometry using the  $125 \mu\text{m}$  diameter of the optical fiber.  $U_y$  is  $30 \mu\text{m}$ , as it is the value of the

thickness of the top silicon layer.

The above analytical calculation only determined the basic shape of the waveguides, and gave basic dimensions for single-mode cross-section. However, the cross-section of the waveguides may vary at different locations to optimize the total performance, and the influence of coupling loss has not been calculated. The Beam Propagation Method (BPM) simulation conducted with OlympIOs software is used here to optimize and define the detailed dimensions of the waveguides.

### 5.3 BPM Simulation and Optimization of the Waveguides

A waveguide device can be simulated using the Beam Propagation Method (BPM). The BPM is based on that if an optical field distribution is known at the beginning of the waveguide, the propagated field can be calculated at a certain distance in the propagation direction. An approximation of Maxwell equations and numerical techniques are used to solve the boundary conditions [74]. In our case, we use a 2D-BPM algorithm to find the basic characteristic of the waveguides, and a 3D-BPM algorithm to verify and finally adjust the parameters. The object of the optimization is to obtain the smallest losses combination of coupling loss, bending loss and intersection loss for the complete waveguide structure.

#### 5.3.1 2D BPM Simulation

A straight polymer waveguide coupled with single mode optical fibers at the input and output is used here to find how to get smallest coupling loss. The fiber has a core of diameter  $9\mu\text{m}$ , refractive index 1.46526, and a cladding of diameter  $125\mu\text{m}$ , refractive index 1.46. The waveguide uses ZP51 ( $N=1.51$ ) as the core and ZP49 ( $N=1.49$ ) as the cladding. The cross-sectional shape of the waveguide core and cladding is rectangular as imposed by the fabrication technology, while their dimensions need to be determined.

The Effective Index Method (EIM) is used to transform the real 3D refractive index problem into a 2D problem that the 2D BPM can handle. The third dimension is

reduced to an effective index that can be put into the structure definition for the 2D BPM. The effective index is calculated by putting the vertical refractive index profile, the layer heights, and wavelength into a 1D mode solver or slab solver. In our case for the optical fiber, the 3D cylinder structure is reduced to a 2D structure with core refractive index  $N_{\text{effCo}} = 1.46431$ , and cladding index  $N_{\text{effCl}} = 1.46$ , as shown in Figure 5.4. For the waveguides, we use  $N_{\text{effWcl}} = 1.49$  for the cladding refractive index, and  $N_{\text{effWco}} = 1.50486$  for the core. These values will vary with the waveguide layer structure.

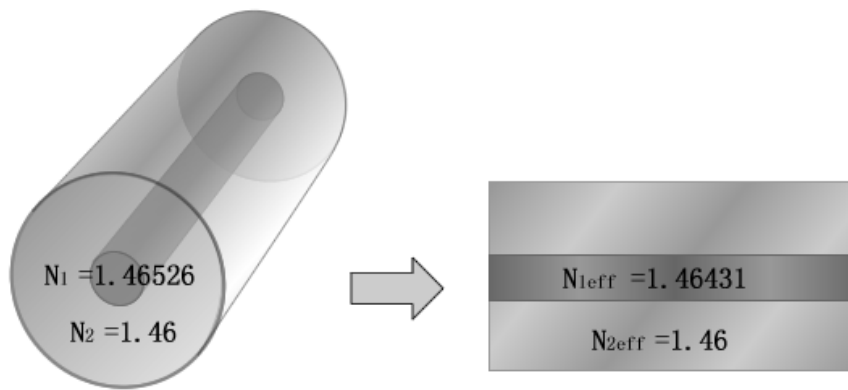


Figure 5.4: 2D effective index of a fiber

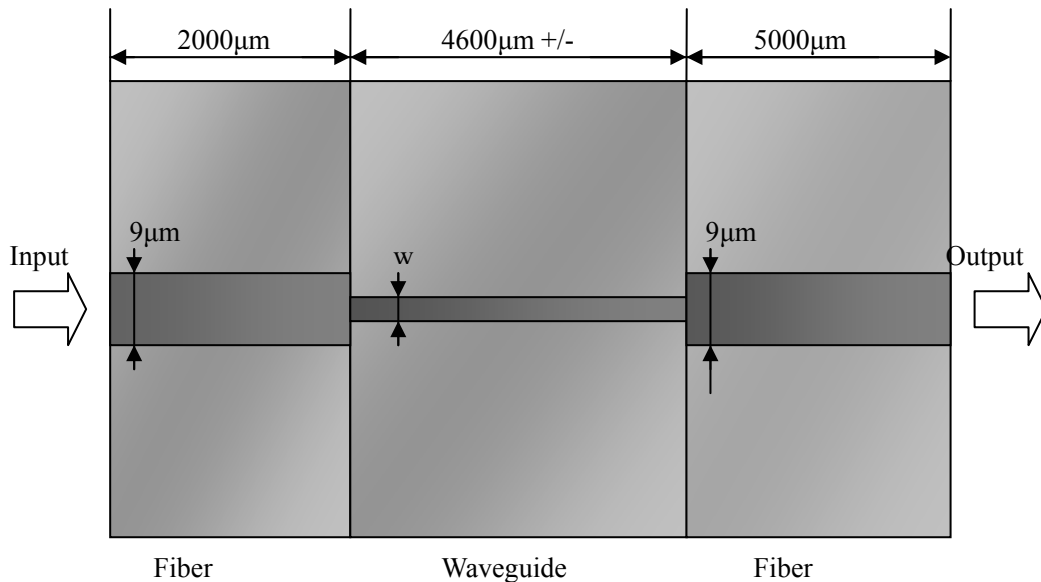


Figure 5.5: Structure for coupling simulation with infinite cladding

With these effective refractive indices, we simulate the propagation in the guide with infinite cladding to find the core size for best coupling between waveguide and fiber. The simulated structure is shown in Figure 5.5. The input field at the left side is

Gaussian with waist  $5\mu\text{m}$ , wavelength  $1.32\mu\text{m}$  and power  $1\text{W}$ , and the output is measured at the right end to calculate the loss.

The parameter for the simulation is  $w$ , the width of the waveguide core, and we changed it between  $3\mu\text{m}$  and  $13\mu\text{m}$  and observed the coupling loss. The result is shown in Figure 5.6. For the core width from  $3\mu\text{m}$  to  $6\mu\text{m}$ , the coupling loss decreases as the core is getting wider. For example, the loss is  $2.36\text{dB}$  for a  $3\mu\text{m}$  core and  $1.65\text{dB}$  for a  $5\mu\text{m}$  core. The field propagation for  $4\mu\text{m}$  core is shown in Figure 5.7 with 2D field intensity and 3D solid graph. When the core size increases to  $7\mu\text{m}$ , a new phenomenon happens and the coupling loss varies, showing a periodicity with the waveguide length, and ranging from  $0.11\text{dB}$  to  $1.33\text{dB}$ . This periodicity comes from the interference between the multiple modes existing in the waveguide when the core size is getting bigger. Figure 5.8 compares the maximum loss and minimum loss situations of the  $7\mu\text{m}$  core waveguide coupling.

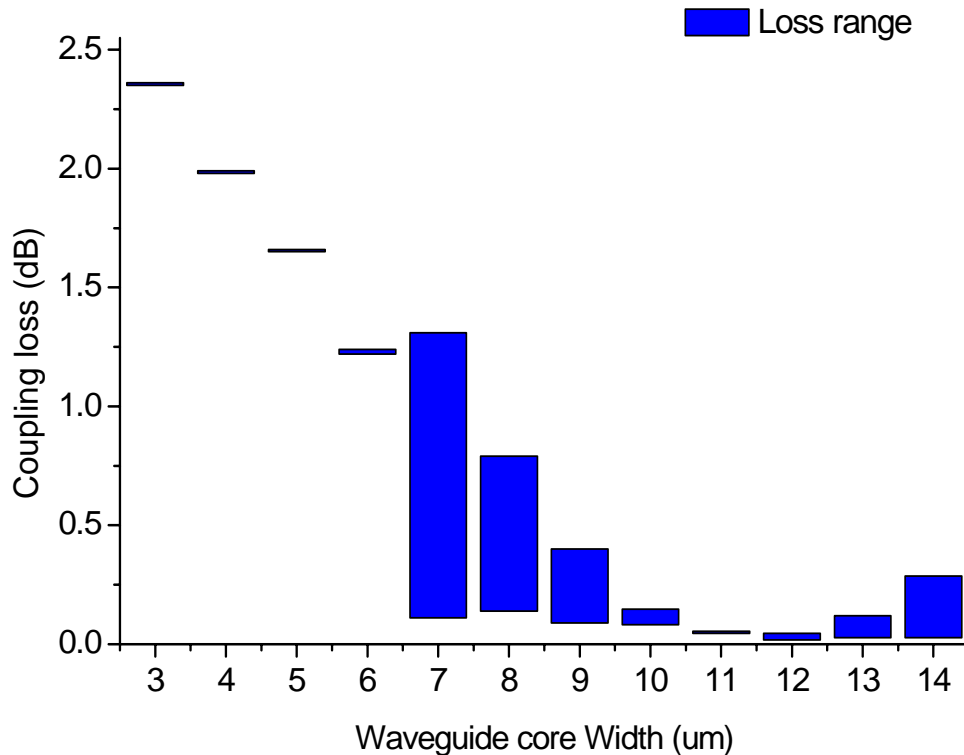


Figure 5.6: Simulated coupling loss for different core sizes

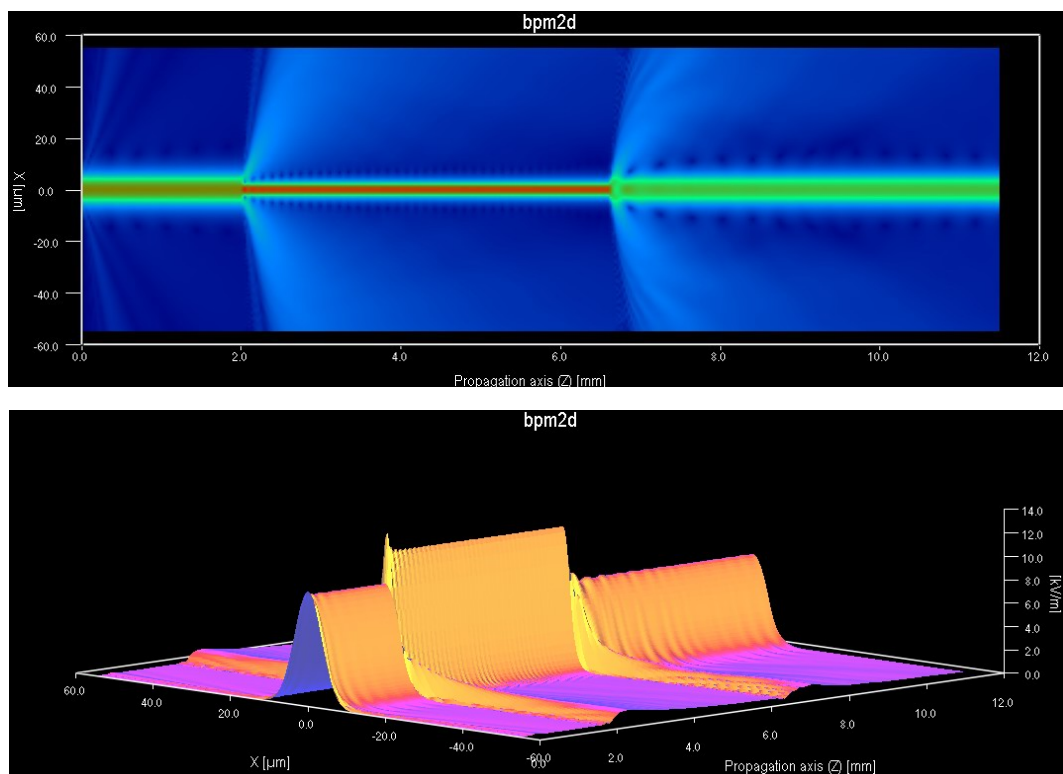


Figure 5.7: BPM 2D graph for fibers coupling with 4 $\mu$ m core waveguide

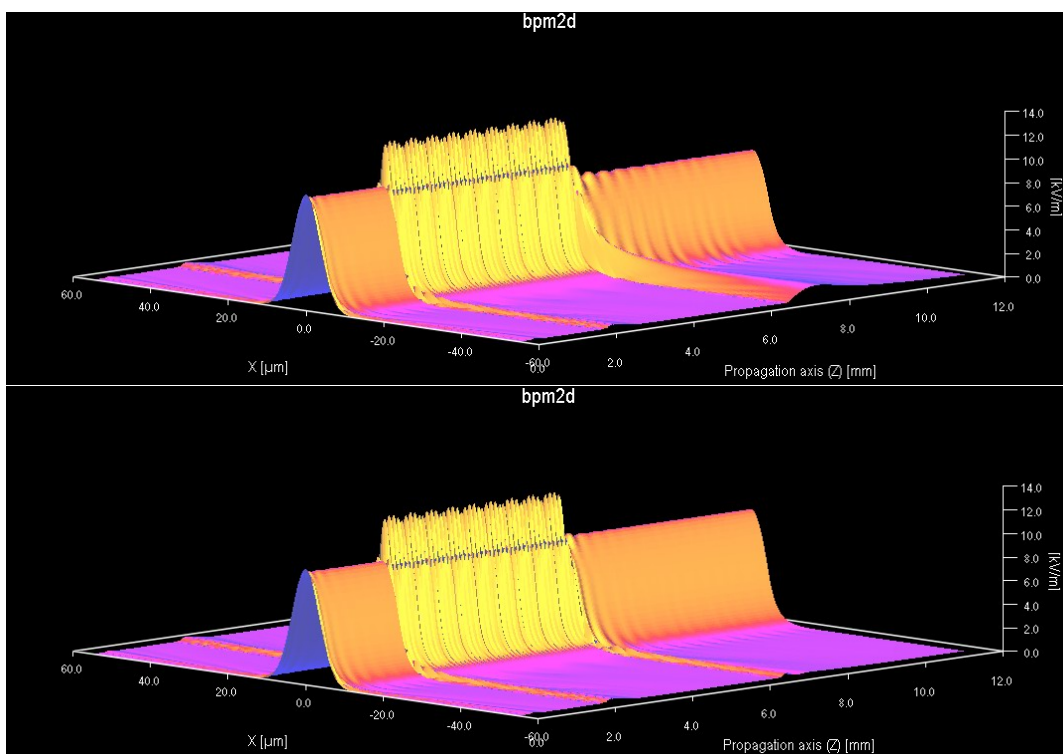


Figure 5.8: The worst (top) and the best (bottom) coupling condition for 7 $\mu$ m core waveguide with varying length

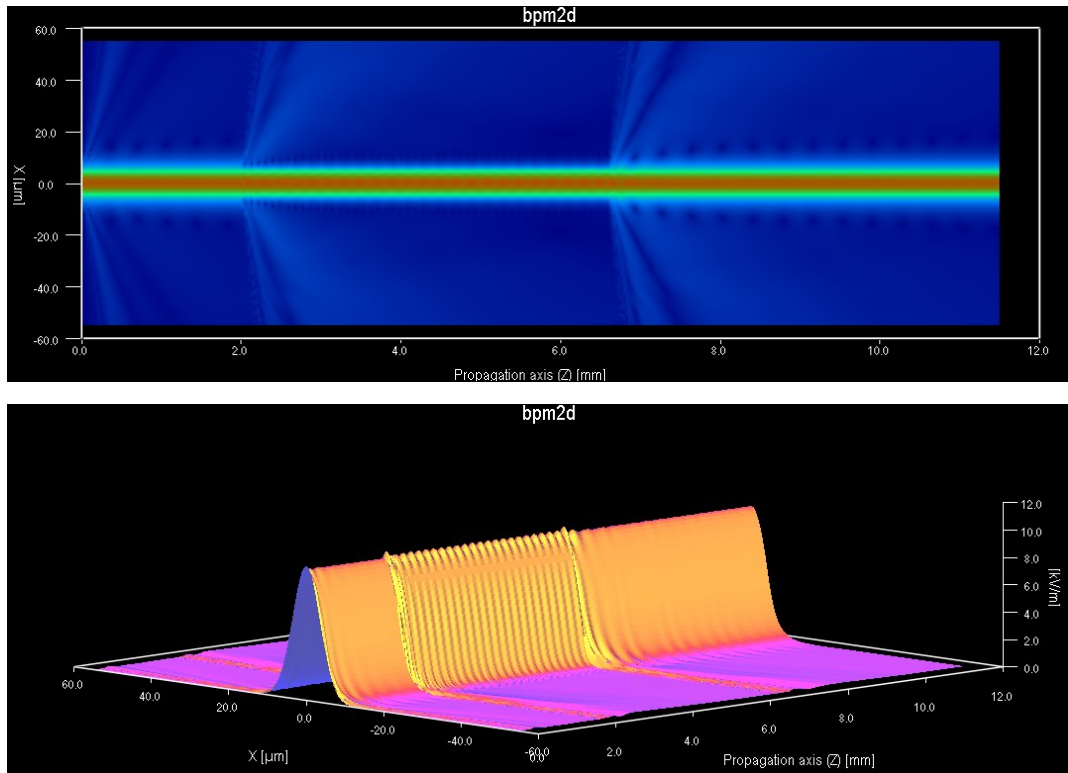


Figure 5.9: Coupling for 11 $\mu$ m core waveguides with fibers

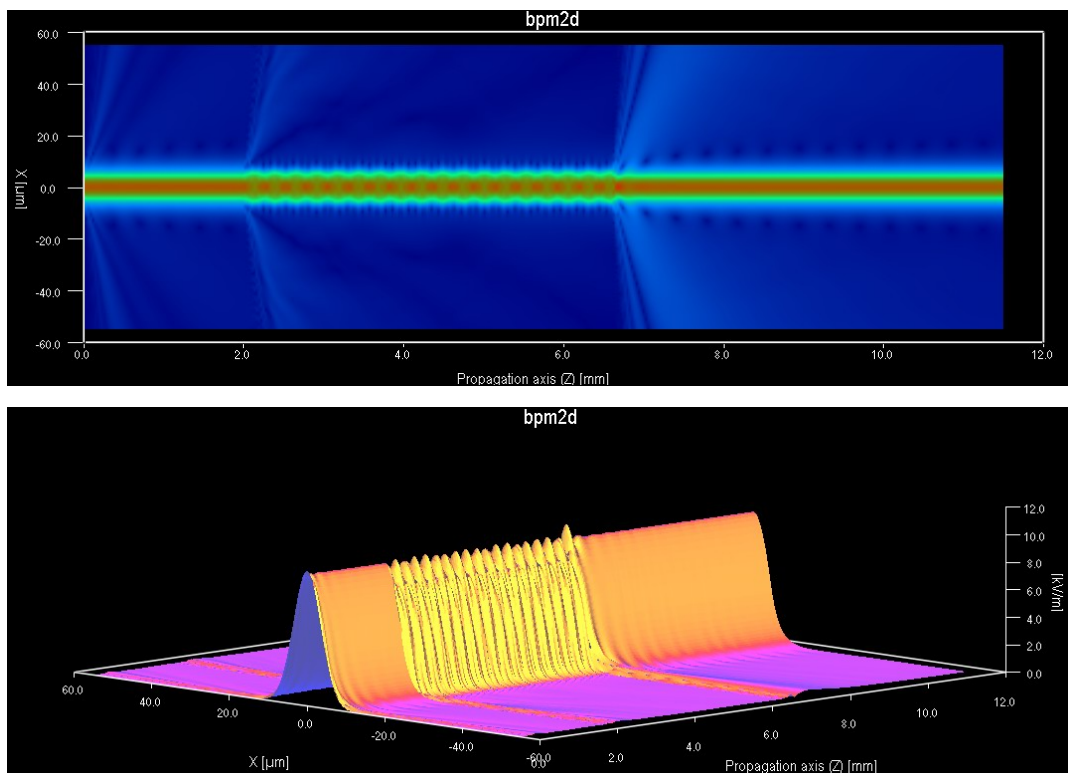


Figure 5.10: Coupling for 14 $\mu$ m core waveguides with fibers

Fortunately, this periodicity and loss range decrease as we keep increasing the core size. When the core size reaches at 11-12 $\mu\text{m}$ , both the loss and loss range reach a minimum value, which is exactly what we want (Figure 5.9). And when the core size increases above this value, the oscillation in the field appears again (Figure 5.10). Thus, with an infinite cladding, for the set refractive index and wavelength, a core size of 11 to 12 $\mu\text{m}$  give the lowest coupling loss.

In a second step, we simulate the effect of the cladding width as Figure 5.11. We have tried different combinations of cladding and core size. For small sized core, part of the input energy couples into the cladding and is transited inside the cladding. As the cladding is multimode we observe again an oscillation in the coupling loss, which varies with the cladding size and the waveguide length. Figure 5.12 is an example with core size 4 $\mu\text{m}$  and a cladding size 20 $\mu\text{m}$ . Once again, the core sizes of 11 to 12 $\mu\text{m}$  give best result, as shown in Figure 5.13. For the waveguide with core 12 $\mu\text{m}$  and cladding 20 $\mu\text{m}$ , the simulated coupling loss is only 0.009dB. Another merit of this core size is that the loss is not sensitive to the cladding size when the cladding size is above 20 $\mu\text{m}$ . When the core size increases above 12 $\mu\text{m}$ , the coupling loss increases and the periodicity appears again.

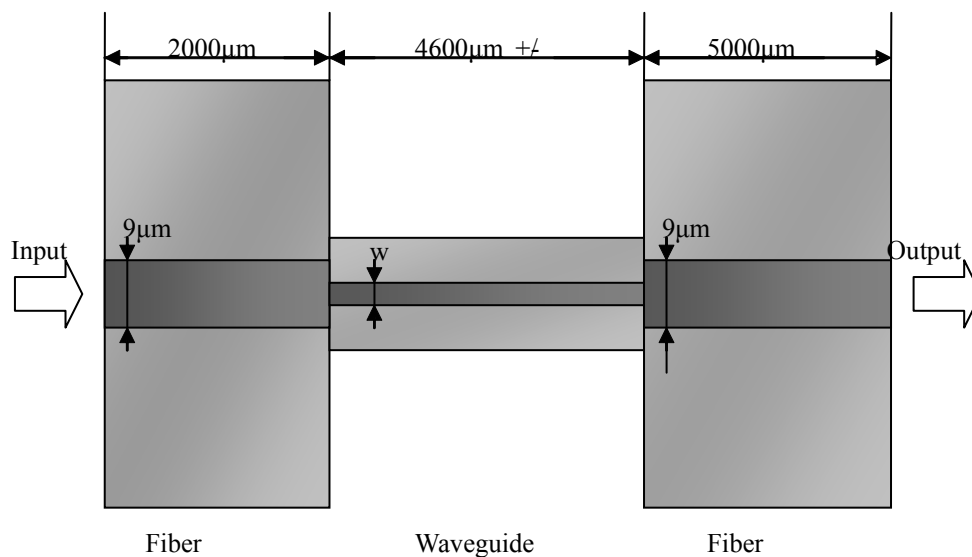


Figure 5.11: Setting for coupling simulation with finite cladding



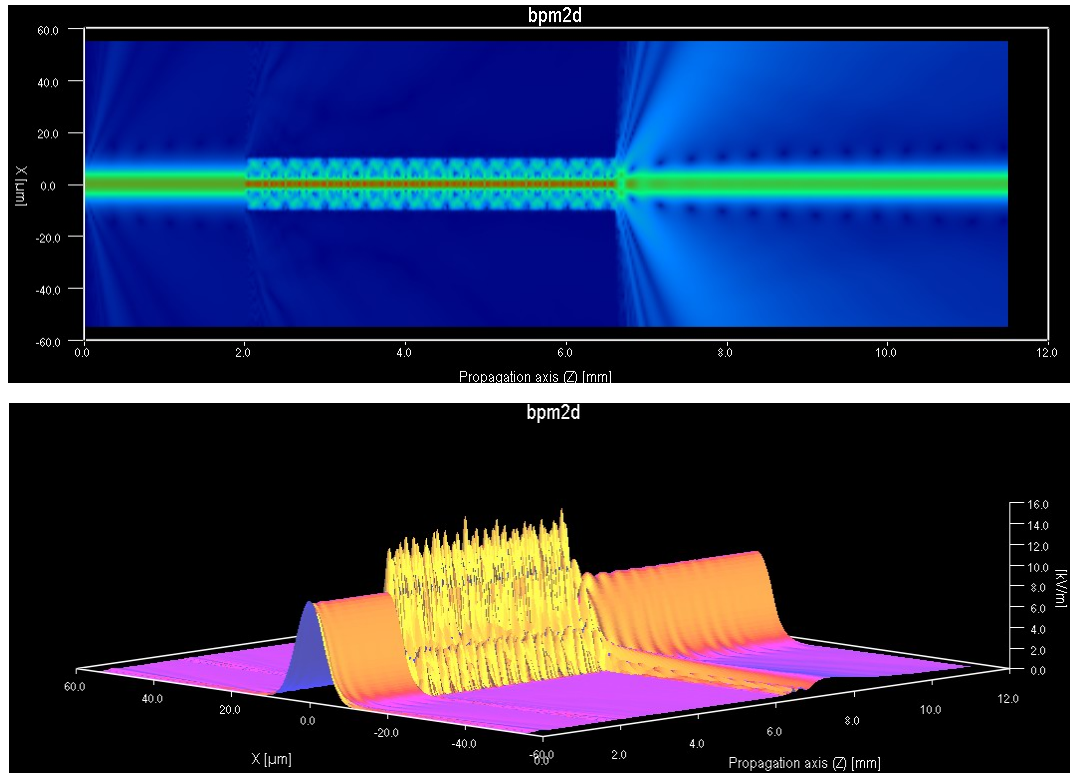


Figure 5.12: Coupling of fibers with  $4\mu\text{m}$  core  $20\mu\text{m}$  cladding waveguide

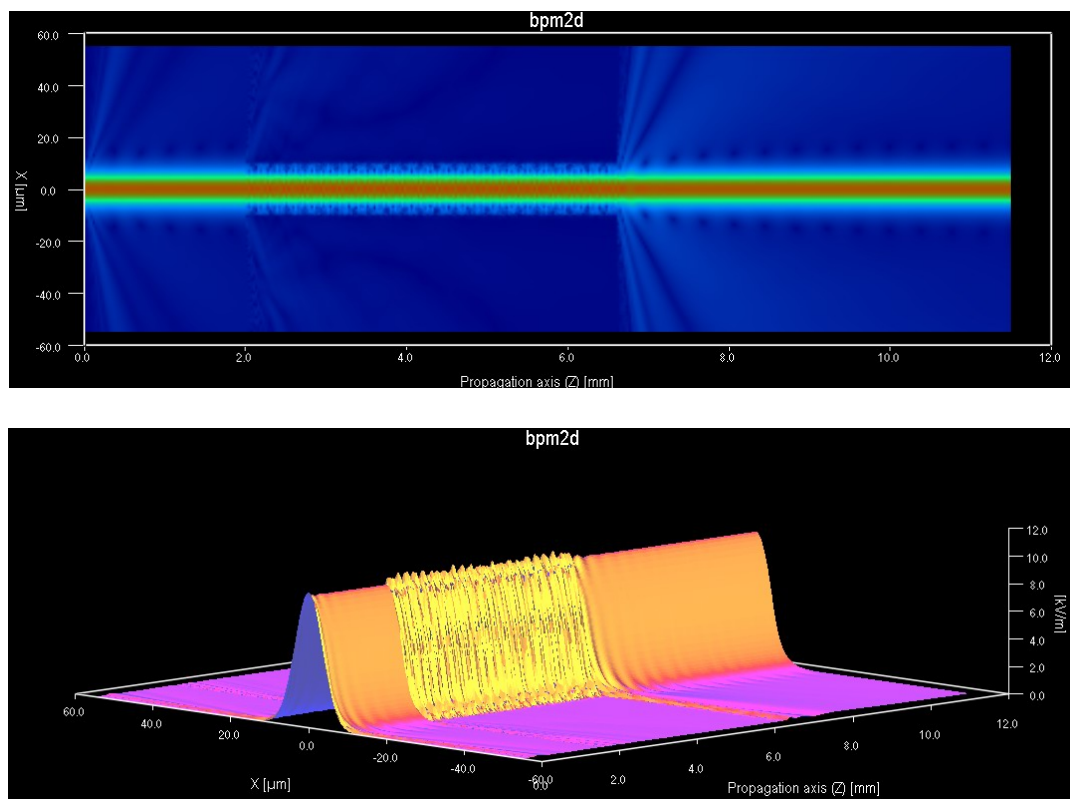


Figure 5.13: Coupling of fibers with  $11\mu\text{m}$  core  $20\mu\text{m}$  cladding waveguide

From the above simulation and analysis, for our refractive index and wavelength setting, the core size of 11 to 12  $\mu\text{m}$  is the best for reducing coupling loss for both infinite and finite cladding situations.

In the third step of simulation, we add bends to the waveguide core (Figure 5.14). Two S-bends connected together with two straight parts coupling with the fiber at both ends. The S-bends have a radius of 1500  $\mu\text{m}$  and an offset of 100  $\mu\text{m}$ . To simplify the simulation, we use an infinite cladding and set the same as in step one.

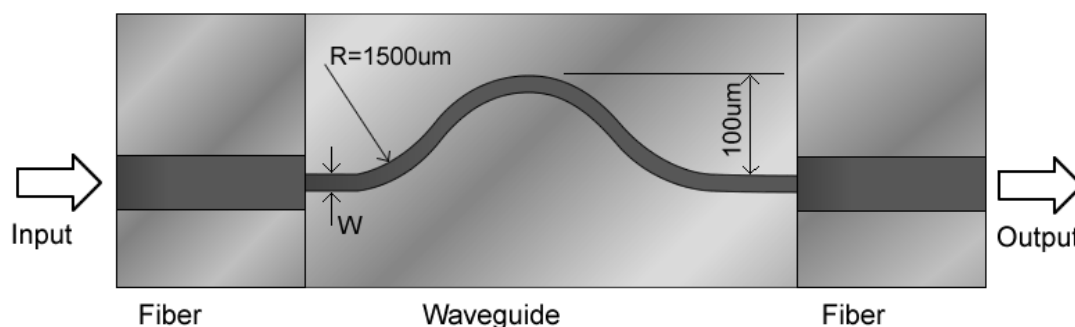


Figure 5.14: Structure for bend and coupling simulation with infinite cladding

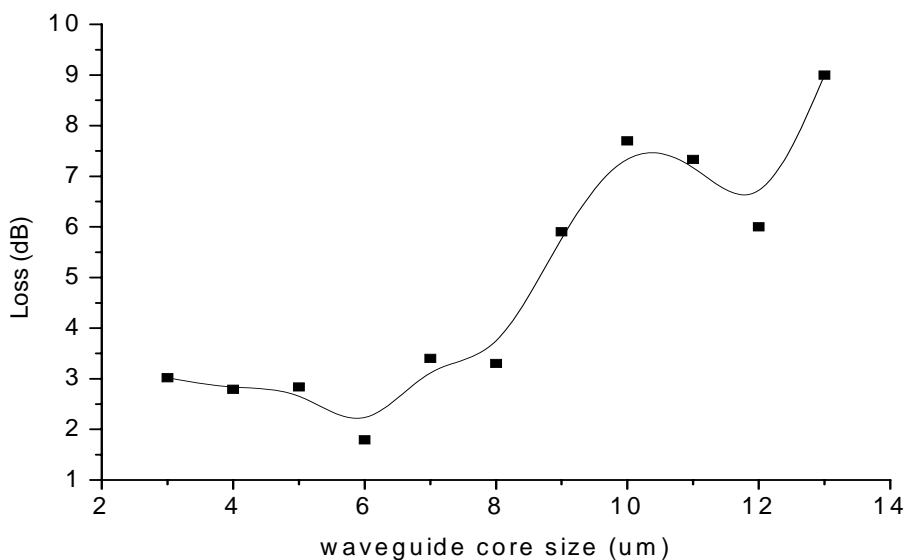


Figure 5.15: Loss of fiber coupled with bent waveguides of different core sizes

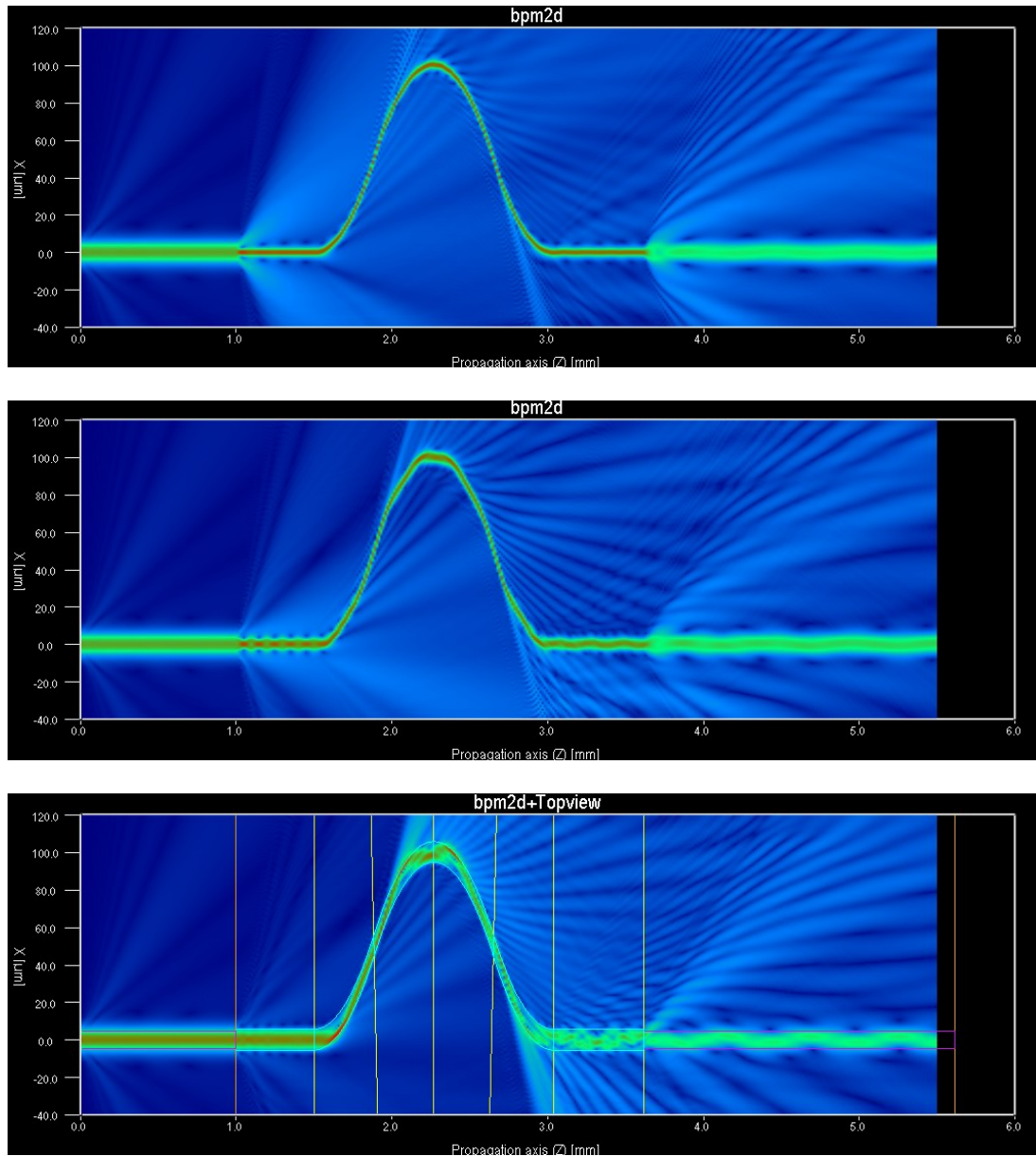


Figure 5.16: 2D BPM field intensity of bent waveguide with core size of  $3\mu\text{m}$ ,  $6\mu\text{m}$ , and  $11\mu\text{m}$  (top to bottom)

We have tried different waveguide core sizes with this setting and computed the overall loss due to the coupling and the bend. The result is shown in Figure 5.15. From the plot, the smallest loss happens with  $6\mu\text{m}$  core, which have the best combination of coupling loss and bending loss. Below this value the coupling loss is dominant. While above this size the bending loss is dominant and increases rapidly with the core size. Figure 5.16 compares the 2D BPM field intensity with the bent waveguide core size of  $3\mu\text{m}$ ,  $6\mu\text{m}$ , and  $11\mu\text{m}$ .

These results are not satisfactory as the lowest combined loss is as large as 2dB, while

individually coupling loss and bending loss can be very small (below 0.1dB). One solution would be to increase the radius of the s-bend of the wider core waveguide to reduce the bending loss. However, this will make the size of the waveguide too large for an acceptable layout and largely increase the scattering loss.

We propose another solution, which uses an 11~12 $\mu\text{m}$  core to couple with fibers, a 3~4 $\mu\text{m}$  core at bending parts, and connect these two cores with a tapered section, as shown in Figure 5.17. With this hybrid core size setting, the total loss drops to 0.495dB immediately.

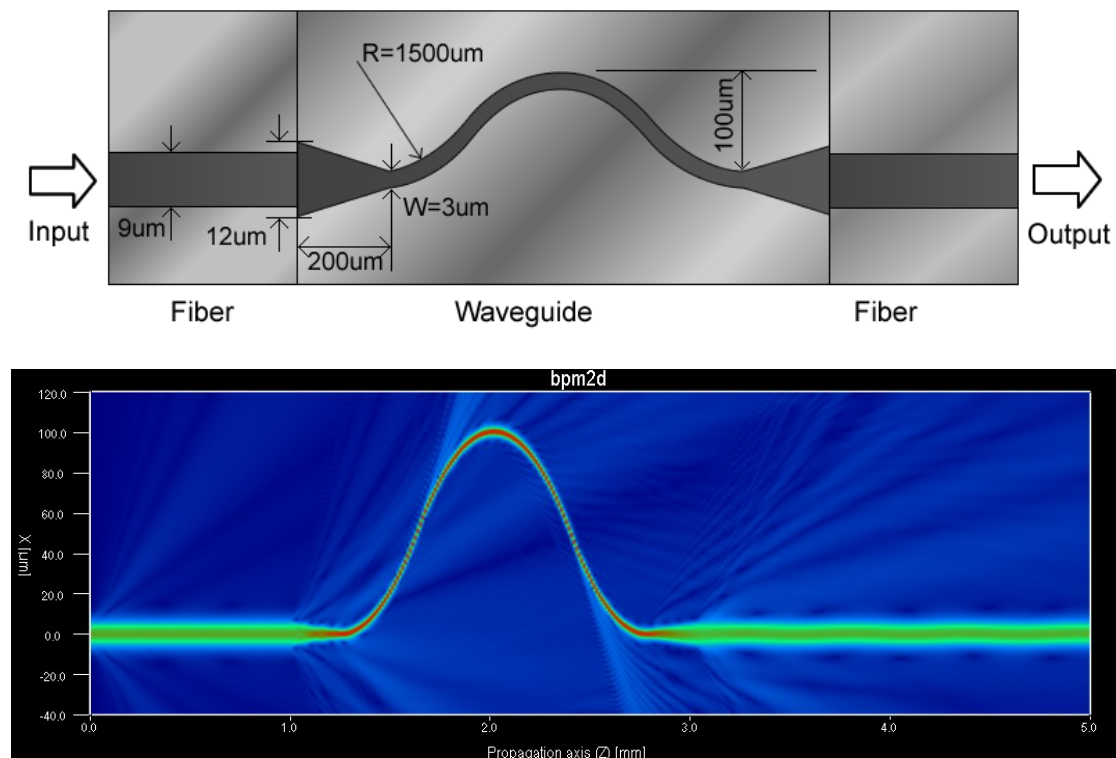


Figure 5.17: The hybrid core size setting and 2D field intensity BPM graph of S-bended waveguide core size of 3 $\mu\text{m}$ , tapered to 12 $\mu\text{m}$  and couple with fibers

This 0.495dB loss can be further decreased by some minor structure changes. E.g. change the S-bend to an SB-bend, which has a short straight between two arcs (Figure 5.18). Another change is to add a short straight part between the bend and the taper.

With these changes, the total loss has been reduced to 0.238 dB when  $R = 1500\mu\text{m}$ . Different values of  $R$  have been simulated for the same offset of 100 $\mu\text{m}$ . The result is shown in Figure 5.19. From the plot we can see that when the bending radius is

smaller than  $1000\mu\text{m}$ , the loss is large and it decreases as radius increases. The loss reaches a low value when  $R \approx 1500\mu\text{m}$ . Further increasing the radius of the bend does not reduce it further because in this case, the loss comes mainly from the coupling and the taper instead of the bend. This final loss value matches with the former calculation and our expectation. Thus we choose  $1600\mu\text{m}$  as the smallest radius for our waveguide bends.

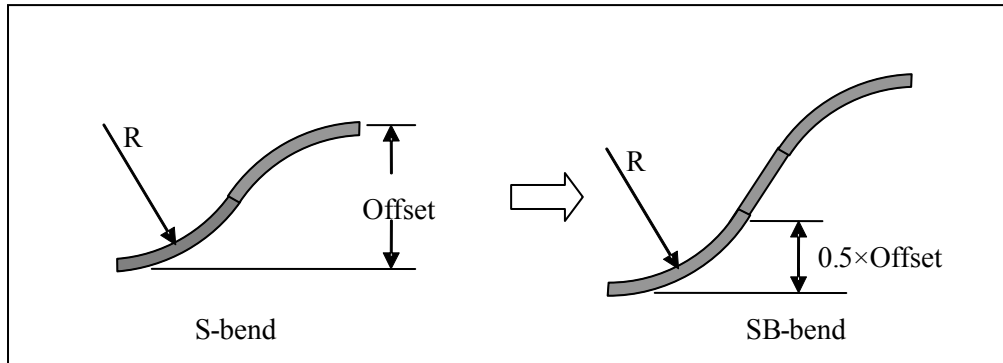


Figure 5.18: Change from S-bend to SB-bend

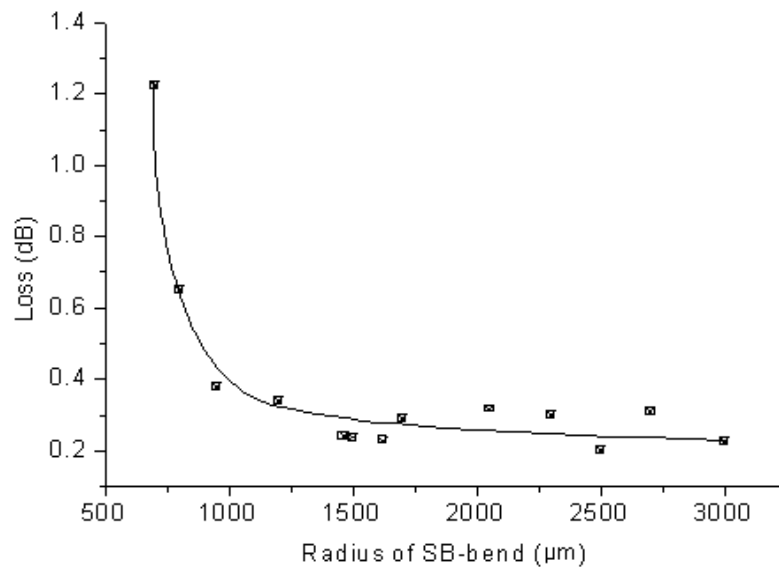


Figure 5.19: Simulated total loss VS radius of the SB-bend

In the next step of simulation we use a finite cladding for the waveguide. After some minor adjustment and optimization, the final sizes of waveguides are decided. A straight waveguide length of  $300\mu\text{m}$  with  $11\mu\text{m}/18\mu\text{m}$  for core/cladding is inserted between fiber and taper. The taper is  $11\mu\text{m}/18\mu\text{m}$  at one end and  $3\mu\text{m}/12\mu\text{m}$  at the other end, and  $200\mu\text{m}$  long. The SB-bends have a core/cladding dimension of

$3\mu\text{m}/12\mu\text{m}$ , radius of  $1600\mu\text{m}$ , and offset  $340\mu\text{m}$ .  $50\mu\text{m}$  of straight waveguide with the same size connects the bend to the taper (see Figure 5.20). With this setting, the simulated total loss is very low at  $0.077\text{dB}$ .

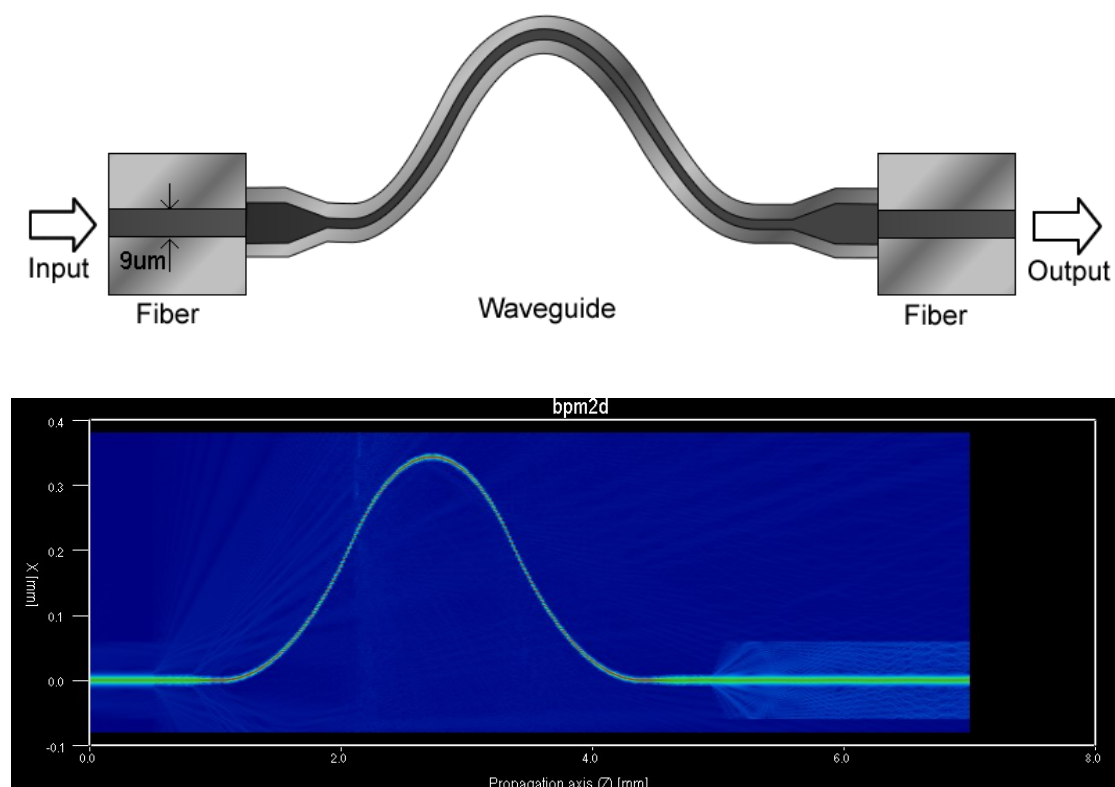


Figure 5.20: 2D BPM coupling and bending simulation using finite cladding

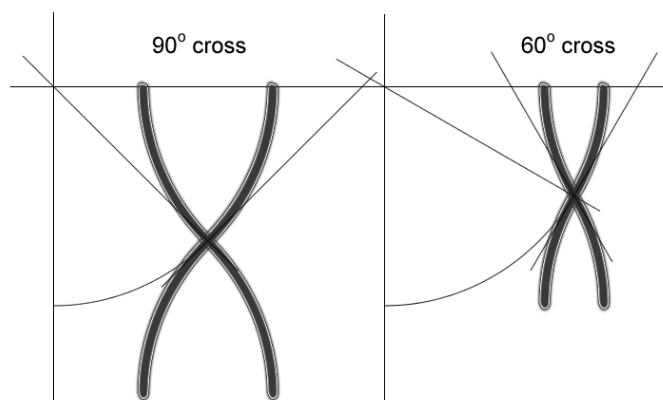


Figure 5.21: Size comparison of two curved cross structures with identical radius but different intersection angles.

In addition to the radius, another important factor that influences the layout of the waveguides is the angle between the intersecting waveguides. It is obvious that smaller intersection angle allows smaller total size waveguide structure thus has much



benefit for the design of waveguide devices (see Figure 5.21 for comparison of the sizes of cross structures with  $90^\circ$  and  $60^\circ$  intersection angles). However, smaller intersection angle causes more loss and more crosstalk. There has to be a compromise that obtains a relatively small intersection angle while keeping the loss and crosstalk acceptable.

We have simulated the crosstalk and loss of two waveguides with core size  $3\mu\text{m}$  and cladding size  $12\mu\text{m}$  which intersect at different angles (Figure 5.22). The result is shown in Figure 5.23. From  $30^\circ$  to  $90^\circ$ , the loss is very low below  $0.05\text{dB}$ . Below  $30^\circ$  the loss increases rapidly. Considering together with the crosstalk and the size of the waveguides, we have chosen a  $60^\circ$  intersection for our structure, which has a loss of  $0.028\text{dB}$  and a crosstalk of  $-45\text{dB}$

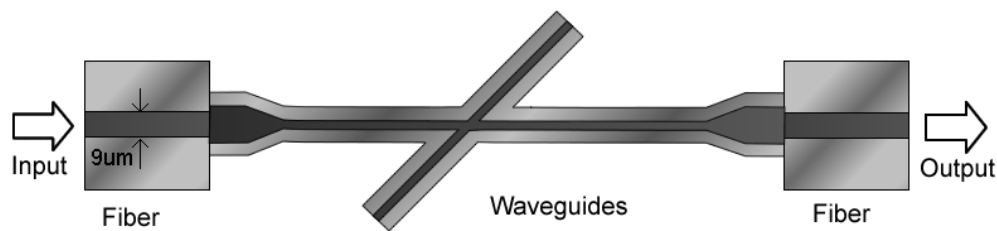


Figure 5.22: Structure for simulation of intersecting waveguides

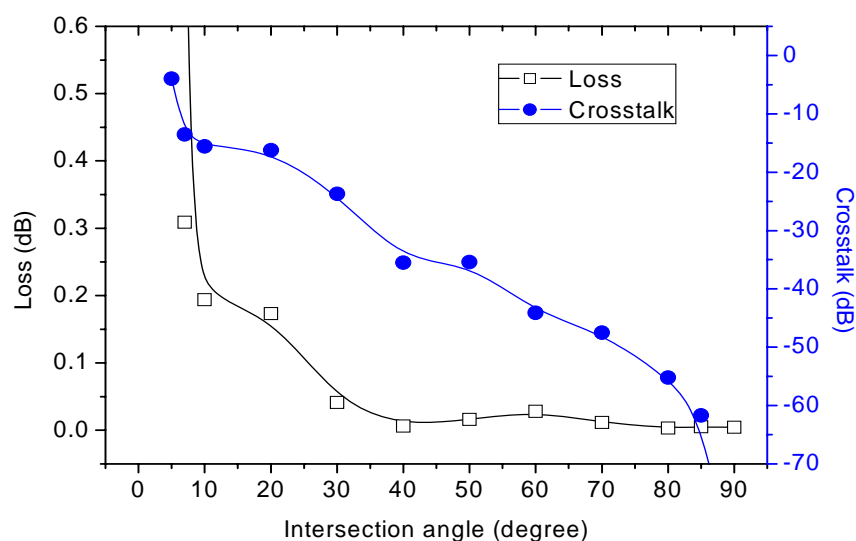


Figure 5.23: Simulated Loss and Crosstalk when waveguides intersect at different angles

In the last step of 2D BPM simulation, we use waveguide with designed size, radius, angle and length, those are: 11 $\mu\text{m}$  core size straight for coupling with fibers, taper to 4 $\mu\text{m}$  with length 200 $\mu\text{m}$ , the 4 $\mu\text{m}$  core guide bend with radius larger than 1600 $\mu\text{m}$ , two intersecting guides crossing at angle 60°, and all the waveguides have finite cladding. Figure 5.24 shows the structure and the BPM result graph. The values of the total loss and crosstalk are:

$$\text{Loss} = -10 \times \log \frac{P_{out}}{P_{in}} = -10 \times \log \frac{1.14751}{1.18032} = 0.1224 \text{ dB}$$

$$\text{Crosstalk} = 10 \times \log \frac{P_{cross}}{P_{in}} = 10 \times \log \frac{1.43327 \times 10^{-5}}{1.18032} = -49.16 \text{ dB}$$

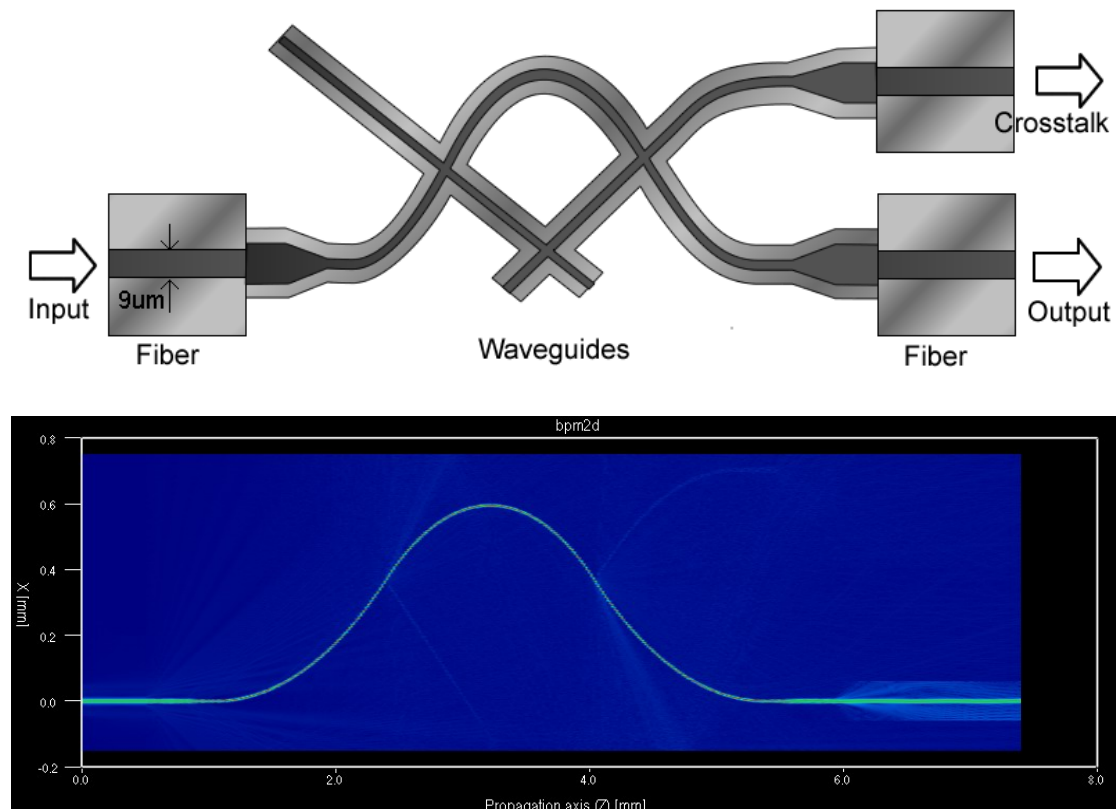


Figure 5.24: 2D BPM setting and result for real guide structure

In addition to studying the loss and crosstalk in the above ideal situation, we also simulated the influence of some practical problems. One is the influence of the silicon structure supporting some part of the waveguide cladding. Silicon has a refractive index about 3.45 for 1.31 $\mu\text{m}$  wavelength at room temperature [78], which will absorb



some wave energy reach the margin of the cladding. We simulated this situation and the result is that the influence is very small and can be neglected, e.g. 0.043dB for the waveguide with core  $11\mu\text{m}$  / cladding  $20\mu\text{m}$ .

Another problem is the misalignment between fiber and waveguide, as the center of the waveguide and the center of the fiber may not be aligned exactly. For  $1\mu\text{m}$  misalignment of  $12\mu\text{m}$  core and  $20\mu\text{m}$  cladding sized waveguide, the loss due to the misalignment is estimated to 0.12dB by simulation.

### 5.3.2 3D BPM Simulation

Finally, we go to the exciting 3D world of BPM simulation, which as anticipated, necessitated a very long computing time to commit.

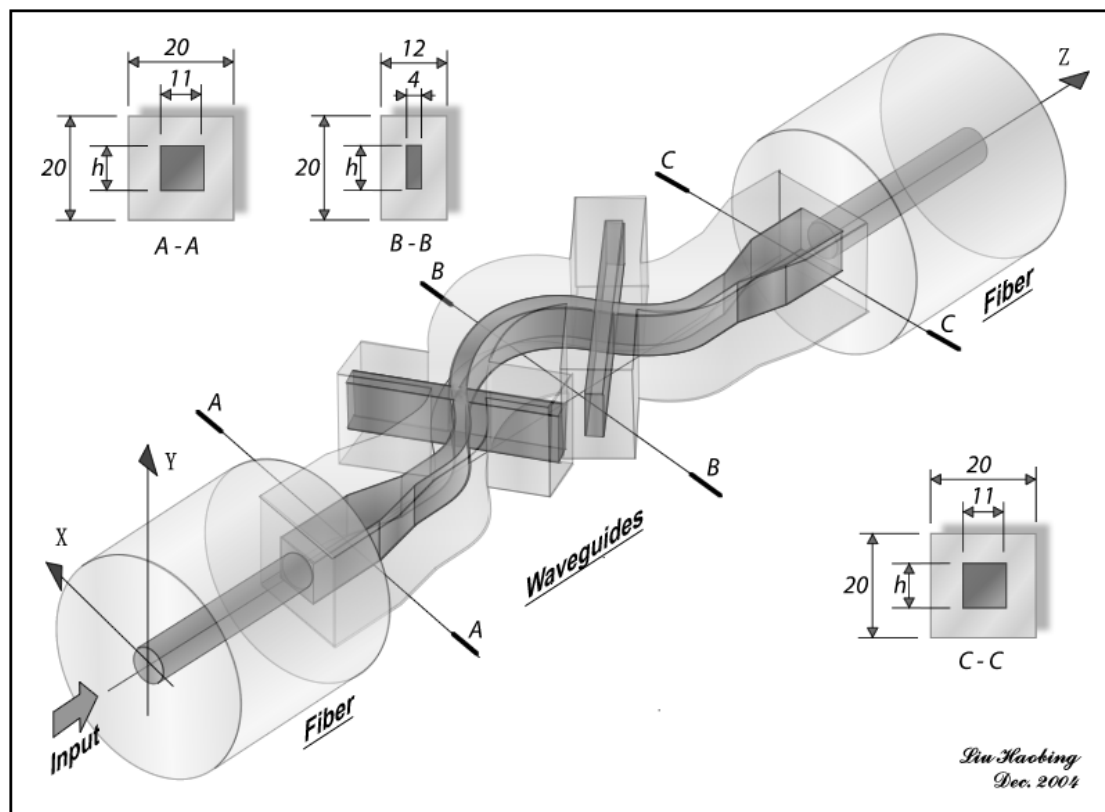


Figure 5.25: Waveguide structure for 3D BPM simulation

The waveguide structure for 3D BPM simulation is illustrated in Figure 5.25. The fibers use standard size and index e.g.  $9\mu\text{m}$  diameter core and  $120\mu\text{m}$  diameter cladding with refractive indices of 1.46526 and 1.46 respectively. For the waveguides, the 3D structure has a rectangular cross-section, which has one more parameter than

the 2d structure: the height of the core  $h$ . The cores of waveguides have a unique height because of the limitation of the fabrication method. The width of the waveguide is varying as established with the previous 2D simulation, that is,  $11\mu\text{m}$  width for coupling with fiber, and  $4\mu\text{m}$  for the bent parts to reduce the bending loss. Figure 5.25 also shows the cross-section dimensions of the waveguide. The refractive indices of the waveguide are 1.51 and 1.49 for the core and the cladding corresponding to the materials used. The radius of bending is  $1600\mu\text{m}$ , and the angle of the two intersections is  $60^\circ$ .

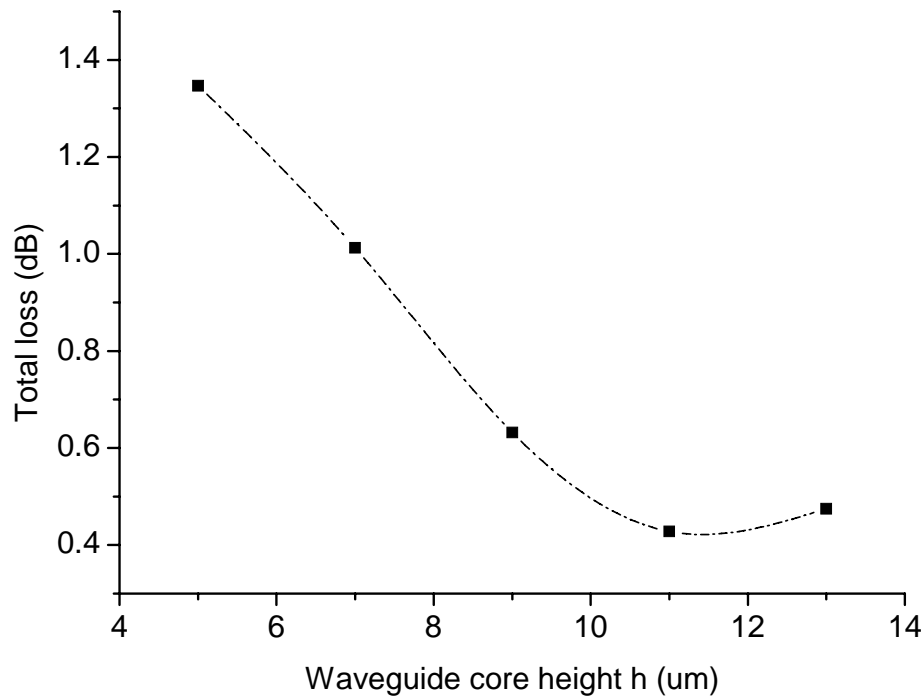


Figure 5.26: The total loss for different waveguide core height in 3D BPM simulation

With the above settings, we have simulated the structure for different core height value  $h$ . Figure 5.26 gives the relation between the loss and the height. Here  $h = 11\mu\text{m}$  gets the best coupling again. The simulated total loss in this situation is 0.428dB, and the crosstalk of the intersection is about -40dB. The 3D BPM simulation resulted a significantly larger loss than the value obtained by 2D BPM simulation because coupling and scattering losses in more directions are included, and the granularity or grid of the 3D BPM is not as fine as 2D BPM due to limited computational power of a

PC. More detailed simulation information is provided bellow.

Figure 5.27 is the BPM 3D field intensity contour view generated by simulation. Figure 5.28 is a planar field intensity plot at the cross-section  $Y = 0$ . It looks very similar to the field intensity image obtained by 2D BPM. Figure 5.29 is the field images on the cross-section  $Z = 0.3\text{mm}$  (the left image) and  $Z = 4.0\text{mm}$  (the right image), which are fields on the input fiber and output fiber respectively. The images show that after passing through the waveguide, the field keeps its shape in the output fiber as in the input fiber, and with a little loss that the highest intensity drops from  $14\text{kA/m}$  to  $12\text{kA/m}$ .

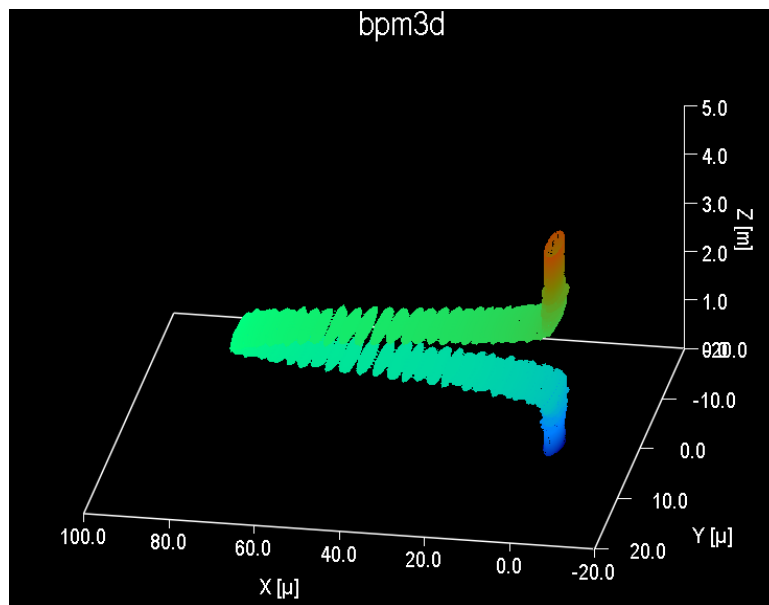


Figure 5.27: BPM 3D Contour view

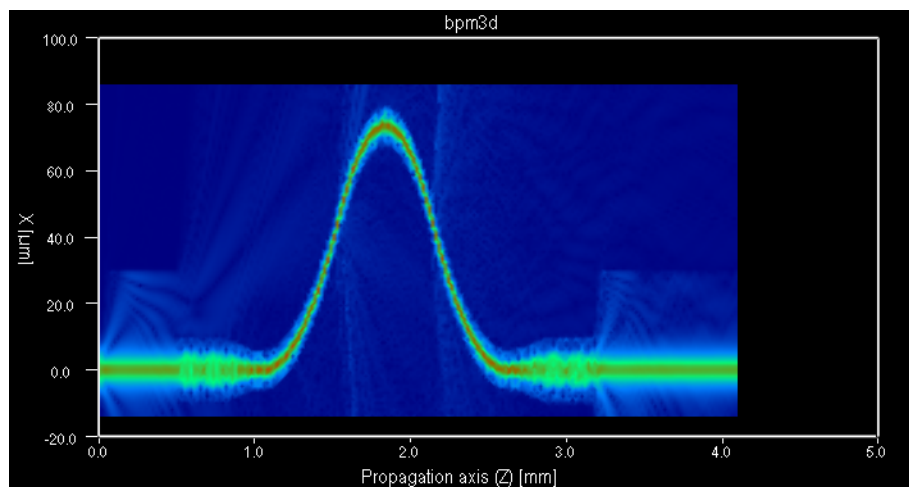


Figure 5.28: 2D field intensity plot at the cross-section  $Y = 0$  generated by 3D BPM

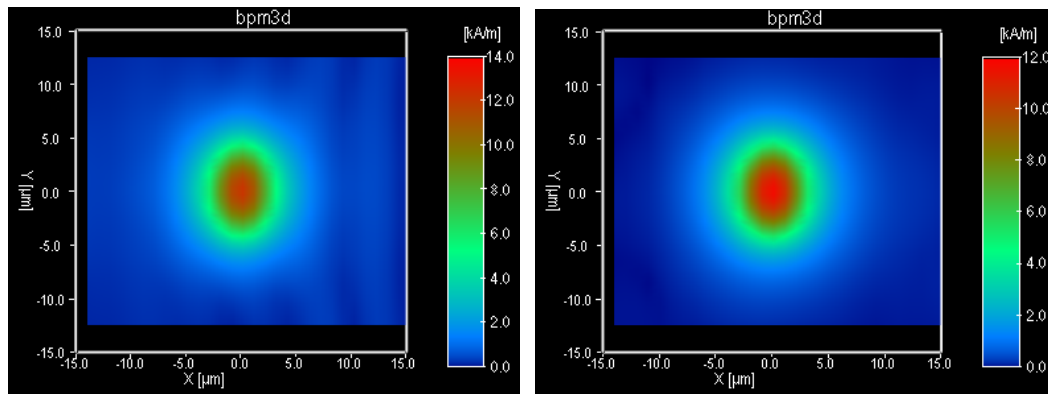


Figure 5.29: field intensity images at the cross-section of the input fiber (left) and output fiber (right)

Figure 5.30 illustrates some field images on some cross-sections along the fiber and waveguide. We can see the field change its shape according to the shape of the waveguide core, e.g. a rectangular shape at the C-C cross-section. And nearly all the field energy is well trapped inside the core of the waveguide.

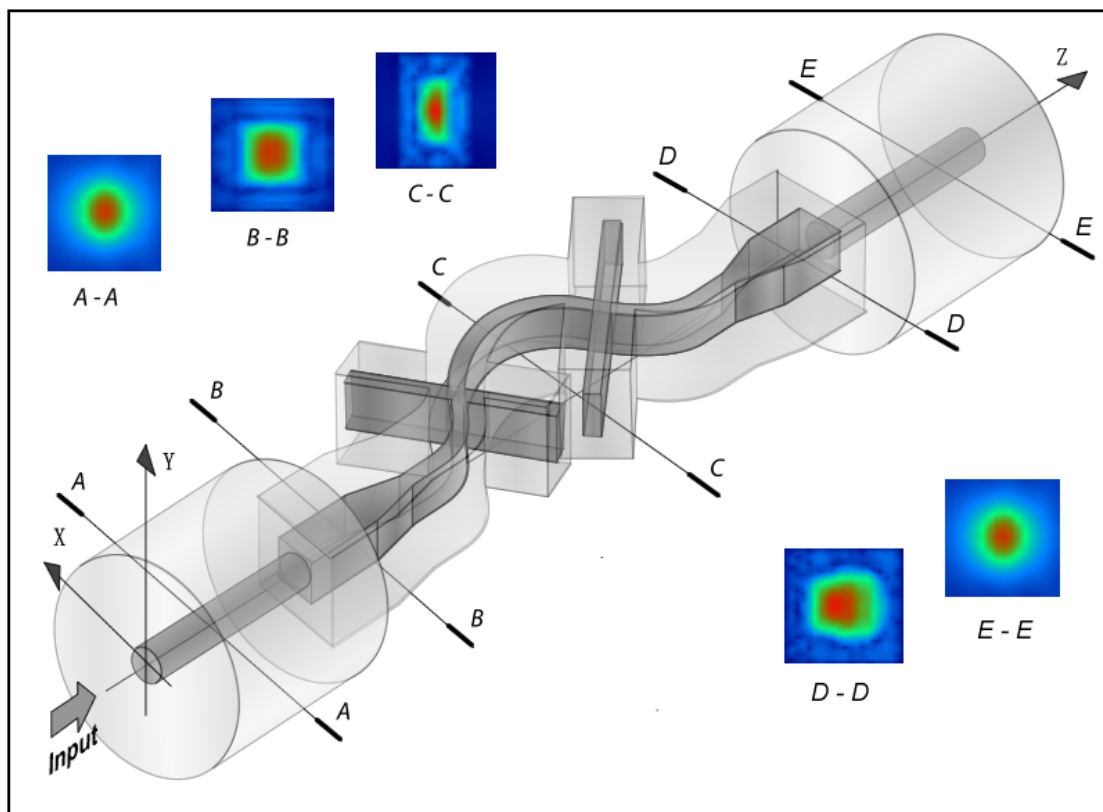


Figure 5.30: field images at cross-sections along axis Z

## 5.4 Summary of Waveguide Design

In this section we introduced the basic concepts of waveguide design, analyzed the parameters, and estimated the insertion loss of the 2×2 SWOMS. We also gave the detailed calculation and simulation, and the structure of the waveguides has been optimized with the simulation.

Although this design is dedicated to our special optical switch, some valuable common suggestions can be distilled from the calculation and simulation for design of optical waveguide devices. A typical waveguide device has bends and intersections. In order to limit the size and bending loss, the waveguides should have core-cladding index difference  $\Delta$  much bigger than the single mode fiber. This larger  $\Delta$  leads to smaller core size of the waveguide for single mode operation, and coupling the waveguide to the fiber result in large coupling loss above 2dB because of their core size difference. A method provided here has solved this problem: the waveguides for coupling with single mode fibers are not necessarily single mode, instead, we use larger waveguide core to couple light with the fiber, and use tapers to shrink the core size when a bend is needed. With such a configuration, the bending loss, coupling loss and size of the waveguide device can be well controlled according to our simulation, e.g. radius of bending below 1.6mm and total loss below 0.5dB. The simulation also gives relations between loss, crosstalk and the angle of intersection.

## CHAPTER 6 Fabrication of the Optical Switch

This chapter will detail the fabrication process of SWOMS. We will introduce new process technologies, and discuss their application. One technology allows building and releasing micro structure in one-step by applying some rules at mask layout for DRIE on SOI wafer, the other is a new polymer-silicon bonding technology that can be used to fabricate hybrid structure that needs alignment.

### 6.1 Basic Fabrication Steps

The fabrication of SWOMS begins from well designed masks for photolithography, a 4 inch SOI wafer, a 4 inch quartz wafer, and the ZP-49 and ZP-51 polymer to form waveguides. The 4 inch SOI wafer has a 500 $\mu$ m silicon substrate layer, a 30 $\mu$ m top silicon layer to form the bi-stable actuator, and a 2 $\mu$ m silicon dioxide layer between them. The quartz wafer has a thickness of 400 $\mu$ m and acts as the base for waveguides fabrication.

There are five major steps to fabricate the SWOMS, and each major step has many sub-steps. We introduce first the five major steps, and the details will be described in latter sections.

Step 1: Fabrication of the bi-stable actuator. With a proper designed mask, the top layer of SOI wafer is pattern by photoresist using photolithography. Then the top layer is anisotropically etched to reach the buried oxide layer by DRIE. After that, the structures formed on the top silicon layer are released by combination of dry and wet release steps.

Step 2: Fabrication of waveguides. Three layers of polymers are spun on the quartz wafer and cured successively to form the under cladding, core, and over cladding layer of the waveguides. The core layer is patterned with a gold mask and etched to form the core of waveguides by RIE before it is covered by the over cladding layer. The cladding layer is patterned later to form the shape of the cladding.

Step 3: Bonding of waveguides with the bi-stable actuator. The waveguide polymer membrane is peeled off from the quartz wafer. It is then floated on the SOI structure using DI water. The waveguides are adjusted to the correct position under microscope. After the liquid dries, the polymer membrane is bonded to the silicon structure by capillary forces.

Step 4: Final etch of waveguide cladding. The polymer membrane of the bonded structure is dry etched to form the shape of the waveguide cladding.

Step 5: The assembly and packaging of the SWOMS. The spring of the actuator is assembled. The fibers are attached, and the whole device is packaged.

## 6.2 Fabrication Facilities

The Micro Machines Center (MMC) of MAE, NTU has a 10k/100 clean room furnished with state of the art equipment for the manufacturing of MEMS, including deposition, photolithography, etching, and characterization systems [72]. With some DIY tools and by cooperation with other labs in NTU, we have all the facilities for the fabrication of SWOMS. We describe here some important facilities in this project.

1. Spin coater, baker, HMDS coater, and mask aligner for photolithography.

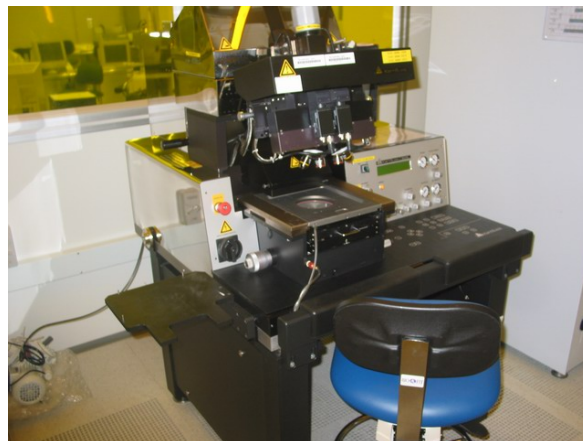


Figure 6.1: The double-sided mask aligner





Figure 6.2: The spin coater

2. STS ICP RIE Deep Si etching system, for etching and releasing the actuator on SOI wafer.

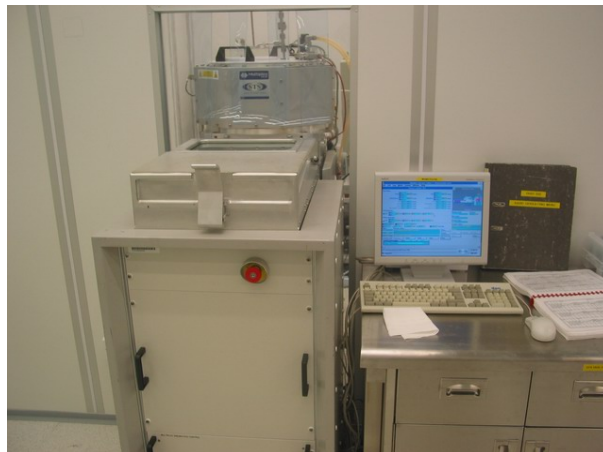


Figure 6.3: DRIE system

3. Reactive ion etching system, for polymer etching.



Figure 6.4: RIE system



4. Electron-beam and magnetron sputter for metal deposition.



Figure 6.5: The e-beam evaporator

5. Wet bench and spin dryer for different wet chemical processes.



Figure 6.6: The wet benches

6. Scanning electron microscope, optical microscopes, Ellipsometer, gold sputter coater, stylus profiler etc. for characterization.



Figure 6.7: The optical microscope



Figure 6.8: The SEM

7. Wafer bonding, wafer dicing, wire bonding system etc. for packaging



Figure 6.9: The wire bonding system

### 6.3 Layout Controlled One-Step Dry Etch & Release and Stiction-free Wet Release of MEMS Using DRIE/SOI

DRIE (Deep reactive ion etching) of SOI (Silicon on insulator) wafer is a popular method to build MEMS because it is versatile and simple. Yet when the devices using this technology become large in size or have compliant beams, the stiction occurring during the HF wet release is a serious problem. Stiction is the killer of many excellent MEMS designs and it can not be easily overcome. However, it was observed that some structure patterns could be wet released more easily than others. Here we discuss the relations between structure patterns and their stiction property, and describe the notching effect, which is found to be the mechanism behind this

phenomenon. We also provide simple mask layout design rules to utilize this effect to our advantage. These rules allow etching the structure and releasing it with the same DRIE step, without any wet process. Alternatively, this method completely removes the stiction problem during wet release or other further wet processes.

### 6.3.1 Introduction

DRIE/SOI technology is usually considered as one of the easiest ways to build high aspect ratio MEMS devices. Its effectivity has been established by commercial products and many MEMS researches which have used it recently [87~90]. With only one mask, high aspect ratio structure can be formed by DRIE. After wet etching of the oxide layer in an HF solution, the device structures are released and can move freely. This process is easy when the structure is simple, small, and very stiff in the vertical direction. However, MEMS devices built on SOI wafer tend to be more complicated and larger (e.g. several millimeters). For such devices, stiction problem during release is still a concern. Stiction happens when the wafer dries [91]. Microstructures are pulled to the substrate by surface tension or capillary forces of the rinse liquid. Then a combination of forces between the structure and substrate, e.g. van der Waals forces and hydrogen bonding, keeps them attached firmly. The stiction is so strong that a force large enough to detach them usually destroys the microstructure [92].

Many efforts have been used to reduce the stiction and increase the release yield [93]. Mechanical approaches include creating bumps on the underside of the structure layer [94], temporarily stiffening the microstructure with polysilicon links [95], or building polymer supporting columns that can be dry etched after the wet release [96]. Other chemical or physical approaches include avoiding wet process by trying HF vapor [97], reducing surface tension by replacing water with methanol before drying, using hydrophobic coating layer [98], avoiding liquid drying process by freeze-drying or supercritical drying [99], or using charge controlled overetching [100].

Although some of the existing approaches have reported high microstructure release yield, they often need complicated process or facility (e.g. CO<sub>2</sub> supercritical drying),

and the easier methods do not achieve good results [93]. In this paper, we will introduce a method that is simple but effective for release of microstructures built on SOI wafers.

### 6.3.2 Patterns and their release properties

During the fabrication of actuators with the DRIE process, we observed that some mesh patterns seldom experience stiction while others almost always did. In order to investigate this phenomenon thoroughly, we designed mesh patterns with different line width, pattern size and pattern shape on a mask. Figure 6.10 shows the 9 patterns used for the test. Pattern 1 has square unit with  $12\mu\text{m}$  line width and  $50\mu\text{m}$  line distance. Pattern 2 changes the beam width to  $6\mu\text{m}$ , and pattern 3 changes the line distance to  $25\mu\text{m}$ . Patterns 4 to pattern 7 adopt different shapes. Pattern 8 adds some so called anti-stiction tips on one side, and pattern 9 reduces the area to half of pattern 1.

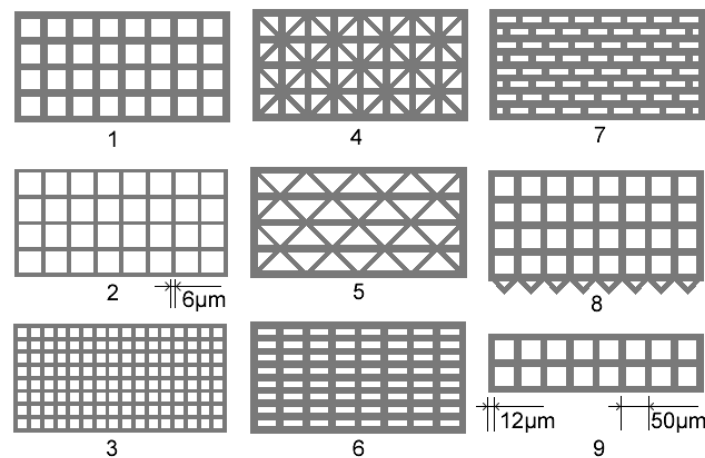


Figure 6.10: Patterns for release test on  $50\mu\text{m}$  thick SOI wafer

Each pattern is connected to a fixed anchor by four  $4\mu\text{m}$  width beams with lengths ranging from  $200\mu\text{m}$  to  $6800\mu\text{m}$ . Figure 6.11 shows the mask designed for testing of one type of pattern and the SEM of the structure after DRIE. After photolithography, deep RIE, and a HF release step using methanol rinsing, we recorded for each set the maximum beam length that could be released (table 6.1).

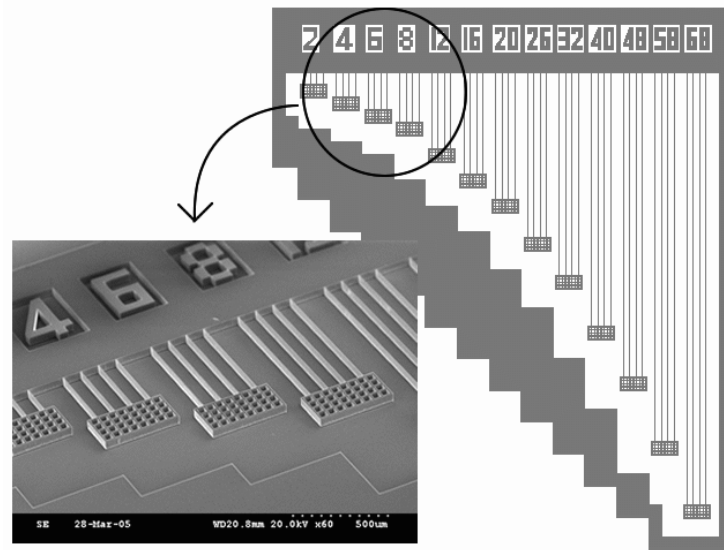


Figure 6.11: Release test setting

Pattern	Maximum released beam length( $\mu\text{m}$ )		
	Sample1	Sample2	Sample3
1	800	200	200
2	1200	400	200
3	6800	6800	6800
4	6800	6800	6800
5	6800	6800	6800
6	5800	6800	5800
7	5800	5800	6800
8	400	200	200
9	200	200	400

Table 6.1: Result of the pattern release test

The result shows a clear contrast. Pattern 1, 2, 8 and pattern 9 stick easily to the substrate. Beams longer than  $200\mu\text{m}$  can not surely resist the stiction. On the other hand, pattern 3, 4, 5, 6 and 7 look invulnerable to stiction. The pattern really matters!

By analyzing closely the result we found that there are 3 factors influencing the release outcome: the pattern density or line distance, the pattern unit shape, and the

line width.

### 6.3.3 The notching effect of DRIE on SOI wafer.

We found that a pattern-dependent notching effect [101~103] is the mechanism for the phenomenon after investigating the samples in SEM. Figure 6.12 compares the cross-sections of pattern 1 and 4 after deep RIE and before wet release. The lower surface of pattern 1 remains flat, and vulnerable to capillary forces that pull the structure down and stick it to the substrate. In contrast, the lower surface of pattern 4 is rough and has micro bumps which effectively inhibit the stiction mechanism during wet release. These bumps are formed by a special type of under-etching called notching, typically occurring during DRIE on SOI wafers. The notching effect is the opening of a narrow horizontal groove (the “notch”) in a conductive material at the interface with an underlying insulator [101], which is greatly related to the trench aspect ratio and shape of the pattern.

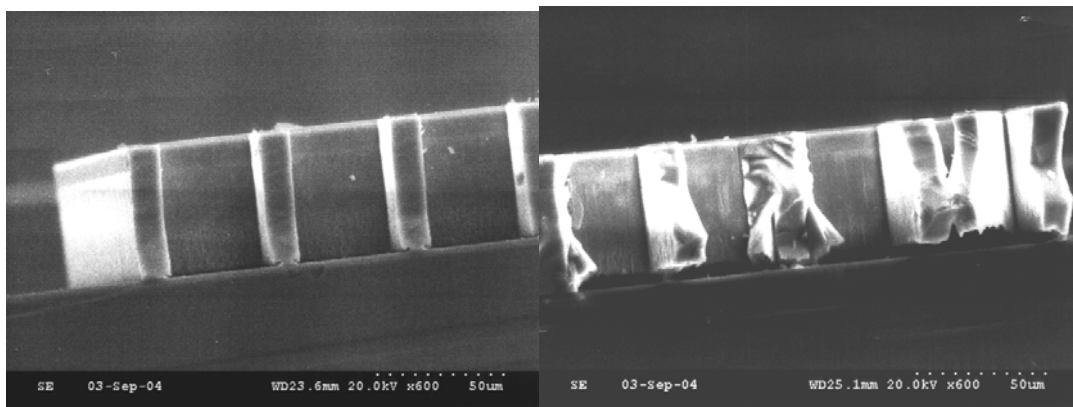


Figure 6.12: Cross-sections of the patterns showing the pattern-dependent notching appearing under the beam.

Notching effect has been observed and usually considered as a kind of charging damage during the plasma etching process of IC fabrication on SOI wafers [103]. Generally, the micro charging is brought out by the directionality difference between ions and electrons in the plasma sheath at the wafer surface. Actually, electrons have much wider angular distribution than ions, and when we etch high aspect ratio trenches, electron shadowing happens and more ions can reach the trench bottom than electrons. If there is an insulator (e.g.  $\text{SiO}_2$ ) instead of conductor (e.g. doped silicon)



at the trench bottom, the insulator will be charged locally, causing potential difference in the trench which deflects the injecting ions to bombard the lower corner sidewall, and initiate the notch. However, there are two major differences between the notching effect in MEMS DRIE fabrication and IC fabrication. First, a typical Bosch [104] DRIE process for MEMS differs strongly from other plasma etching process because DRIE alternates etching ( $\text{SF}_6$  plasma) and passivation ( $\text{C}_4\text{F}_8$  plasma for polymerization). And secondly, the SOI wafers used in MEMS have silicon device layer much thicker than for IC process, usually between  $10\mu\text{m}$  to  $100\mu\text{m}$ . We try here to give an explanation of the phenomenon considering these specificities.

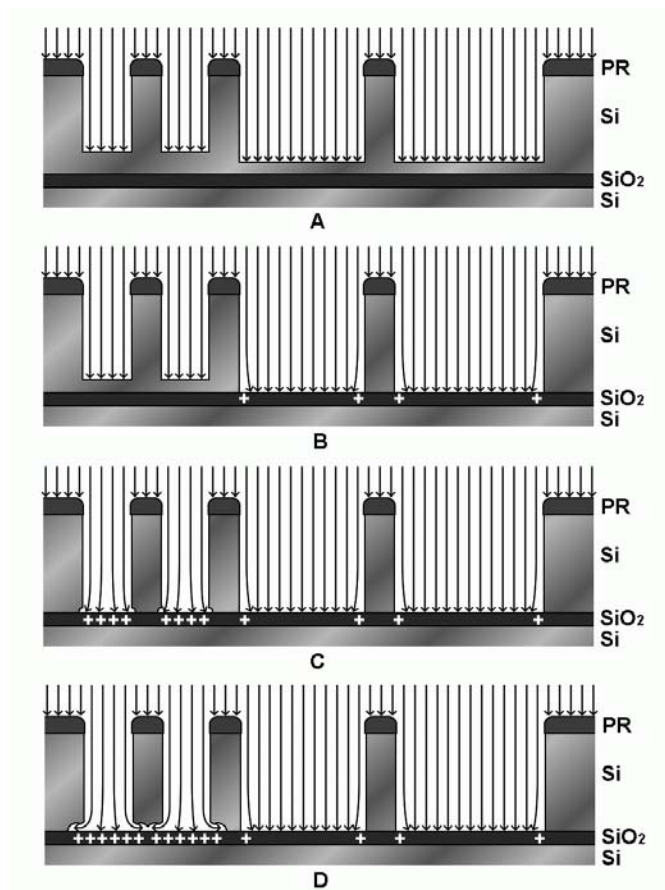


Figure 6.13: DRIE of trenches on SOI wafer

The DRIE process on SOI wafer is illustrated in Figure 6.13. The SOI wafer is patterned by photo resist to form narrow and wide trenches. The arrows represent the direction of ions in the plasma sheath due to the DC bias and the local electrical field. As we've mentioned, Bosch process alternates etching and passivation cycles. After passivation, a thin layer of polymer covers all the trench surfaces. Then in the

following etching step, the ions sputter the polymer selectively at the trench bottom due to their direction, and the unprotected silicon is chemically etched by F radicals. In summary, silicon etching happens where ions sputter away the protecting polymer.

Step A is the normal silicon DRIE process. The wide trenches etch quicker than the narrow ones because of the “RIE lag” [105]. In step B, the wide trenches have reached the oxide layer. Because of electron shadowing, the oxide areas near the side walls are charged by the more directional ions. The resulting potential difference deflects the ions a little reducing the ions that reach this area, preventing the potential difference to go higher, and the process soon reaches a balance. The sidewalls near the wide gaps are barely attacked except by some ions reflected and scattered by the oxide. Step C is a few minutes later, the narrow trenches have also reached the oxide layer, and micro notches started to form. Unlike in the situation with the wide trenches, the electron shadowing is dominant in the narrow trenches, and all the bottom oxide area is charged. The injected ions are then deflected to the bottom edge of the trench, destroying the protective polymer on the lowest part of the silicon sidewall and initiating the micro notches.

Step D shows the growth of the notches. Once a notch has been initiated, the notched area can not be protected effectively by the following passivation cycle. The oxide under the notch gets charged deflecting further the ions, and the micro notches form tunnels in a few cycles. After that, the notch growth will slow down because ions lose their energy when they go through the notch.

The growth of the notch is shown in Figure 6.14 and summarized in Figure 6.15. The trenches with different widths are fabricated on a 50 $\mu\text{m}$  SOI wafer. After the wide trenches have reached the oxide layer, we continue etching the wafer for 15mins, and observe the cross-section of the trenches every 3mins. The curves in Figure 6.15 show that once the notch is initiated, its depth increases quickly in the first few minutes of overetching, and then the growth slows down and finally stops. The final depth of notch has an interesting linear relation to the width of the trench. Actually in our case, 6 $\mu\text{m}$  wide trench reaches a final notch depth about 6 $\mu\text{m}$ , 10 $\mu\text{m}$  wide trench reaches



## Chapter 6

## Fabrication of the Optical Switch

10 $\mu$ m, and 20 $\mu$ m wide trench ends with 20 $\mu$ m deep notch. This linear relation exists when the trench width is below 20 $\mu$ m. For wider trenches (30 $\mu$ m and above), no notch happens because there is a threshold value between 20 $\mu$ m and 30 $\mu$ m, above that the notch is never initiated and thus won't grow. This growth dynamic is a good aspect of the notching effect, for it means that the notch size is mainly determined by the trench width (the design) instead of the overetching time (the process), making it easy to control.

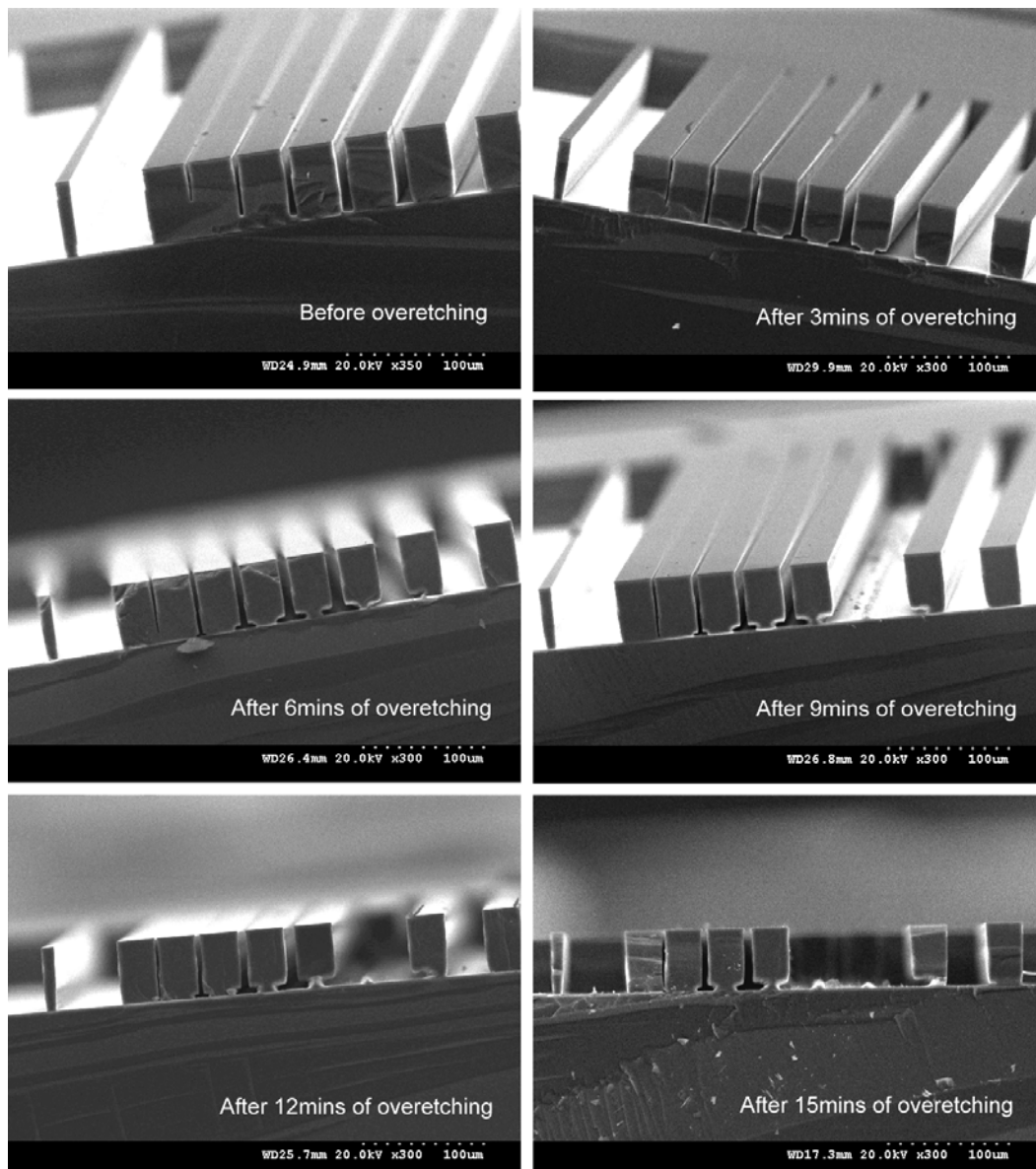


Figure 6.14: The start and growth of the notching (Some beams disappear after 9mins and because they are completely released and flew away when we cut the sample)

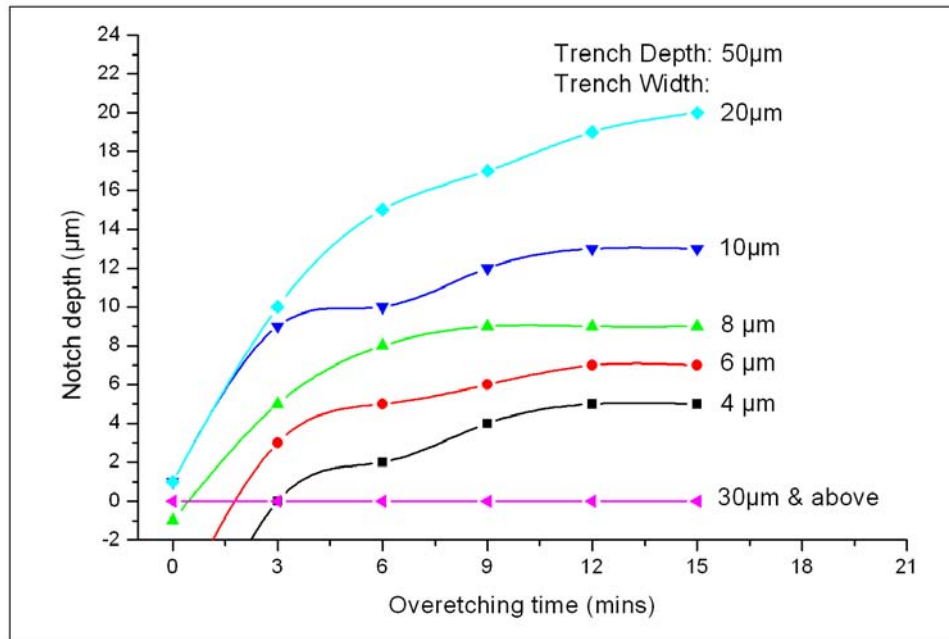


Figure 6.15: The growth of the notch of trenches with 50μm depth and different widths

We can now explain the 3 factors influencing the release result that we've mentioned in section 2 by the notching mechanism. Pattern density or line distance influences the trench width or aspect ratio. Pattern shape also influences the trench width, e. g. the triangular shape can be viewed as having trench widths varying from 0 to a certain value. And the corners of pattern shape have specific effects, e.g. the sharp 45° angle of the triangular pattern can initiate the notch more easily than the 90° corner of the square pattern. For the third factor, it is obvious that thinner beams are released more easily than wider ones, especially as we know that the growth of the notch is limited.

#### 6.3.4 Layout design rules for one-step release and easy wet release.

From the above analysis, in ideal situation, the structures formed on SOI wafer by DRIE can be released without HF oxide etching step if the layout is properly designed. In the case that you don't want to use the one-step dry etch & release, the following rules will still be useful to reduce the chance of stiction dramatically during the wet release process.

**A) For wide releasable structure, use triangular pattern or other dense patterns that make trench aspect ratio above 2 and with proper line width.** The triangular pattern is recommended here because not only does it initiate notching more easily, but also it is much stronger mechanically than other patterns. Pay attention to the line distance and line width. From our experiment in a STS ICP deep RIE system with standard program, for 50 $\mu\text{m}$  SOI wafer, the gap between lines should be below 25 $\mu\text{m}$  to initiate notching (see Figure 6.14). Another source found that for 20 $\mu\text{m}$  thick SOI wafers the critical trench width to initiate nothing is 14 $\mu\text{m}$  [106]. Although the notching effect also depends on the etching system and etching parameters such as RF power, DC bias voltage, gas flow rate, chamber pressure etc, it is mostly aspect ratio dependent because its source is electron shadowing. We give an aspect ratio of 2 as the general guide for initiating the notch, but it probably needs to be adjusted according to the system used.

**B) Avoid wide trench adjacent to moving structure or try to create narrow trench.** Here wide trench means its aspect ratio below 2 according to rule A. Wide trenches can be covered with dummy patterns to avoid it. If some wide trenches are really needed, try to modify the structures between them, and introduce narrow trenches or dense patterns. For example, the left of Figure 6.16 shows a beam between two wide trenches. It can be changed to the right pattern, which has the same function but is much easier to release.

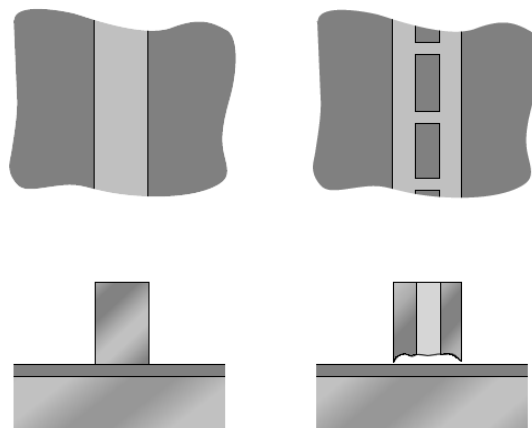


Figure 6.16: Self-releasing beam (right) obtained by changing layout.

**C) Avoid wide beams or try to split them into narrow beams.** Beams wider than the notches under it can not be released properly because growth of the notch has its limit. When a wide beam is needed in our structure, we split it into 2 narrow beams, as the example in Figure 6.16 show.

**D) Pay attention to the heat dissipation problem or take advantage of it.** The back side of the SOI wafer is contacted with helium gas to cool down the whole wafer and keep it below 70°C during the etching process. Before the structure is released, the heat generated on the structure surfaces is dissipated away through the underlying oxide and silicon base. However, once the thin beams have been release by notching, this heat dissipation route is disrupted. The heat has to dissipate to the silicon base through the anchors of the beams. If this alternative heat dissipation route is not effective enough, the released structure may overheat to above 100°C locally, causing insufficient polymerization [107] and PR burning, risking to destroy the structure in a few minutes (see Figure 6.17). Careful design of the anchor can reduce the risk, but this method is difficult to master and may put some limits to the design. **An easy way to solve the heat dissipation problem is to break-down overetching time into short etching steps and allow the structure to cool down in between.** For example, if 5mins of overetching is needed, use five 1min etching steps, with 3mins interval in between. However, on the other hand, the heat dissipation problem can be used advantageously. A group has shown “waffle structure” [100], which consists only of patterns that are released by notching but without anchor for sinking the heat. The structure will be totally etched away in the process and can be used if necessary to open large area of empty space.

The above 4 rules are easy to follow, and the following of them do not set any obstacle for designers to realize their device function.

All the layout rules have been proved effective. Figure 6.18 shows a totally dry released structure and its bottom view. We can see that the bottom surface is roughed according to the mesh pattern. This roughness effectively prohibits the stiction mechanism of an eventual wet process.

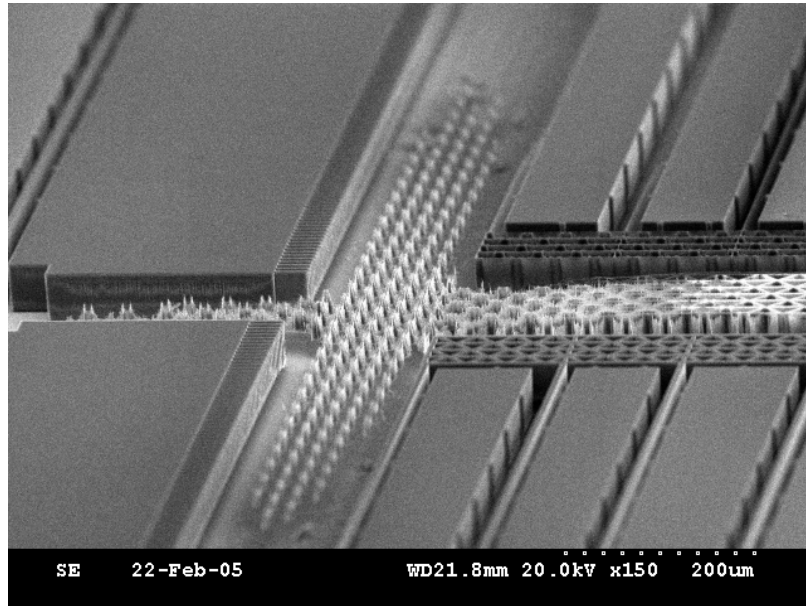


Figure 6.17: Structure destroyed due to overheating

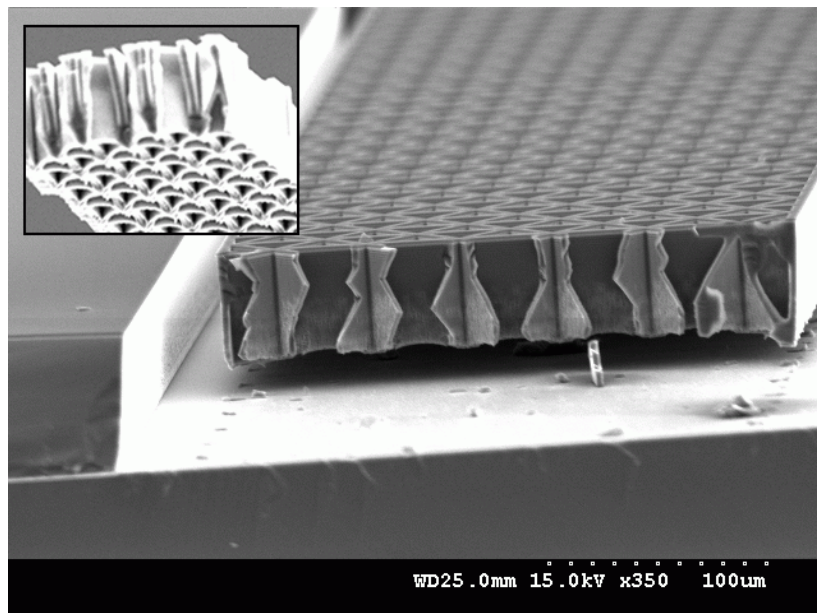


Figure 6.18: A totally dry released patterned structure and the bottom view.

### 6.3.5 Conclusion

When the DRIE process reaches the oxide layer of a SOI wafer, notching may happen depending on the trench aspect ratio and pattern shape. Notching effect is a result of the topography-dependent charging of plasma etching, which causes potential



difference deflecting ions that bombard the lower corners of the trenches. Although notching is a harmful effect in many cases, we show here that we can take advantage of it. With proper layout according to simple rules, micro devices can be fabricated and released in a single step, or at least, can be easily wet released. By removing the stiction problem, this technology allowed to design complicated micro devices with relatively large size.

## 6.4 Design of Masks

Masks are essential to define the desired pattern on photoresist during photolithography. Masks are fabricated separately before the fabrication of the device. The substrate of the mask is a transparent quartz plate with a layer of chromium. The chromium is patterned so that part of the mask is transparent and part is opaque. In our case, three masks are needed, one for patterning the bi-stable actuator structure, the second for patterning the core of the polymer waveguides, and the third for patterning the cladding of the waveguides. Tanner L-edit layout software is used here to design the masks.

The layout design rules described in the last section were established during the fabrication of the bi-stable actuator, and they have been utilized successfully to solve the stiction problem we have met. Figure 6.19 is the mask of an actuator cell. The total size of the cell is 9mm×9mm. Figure 6.20 is an enlarged view of the mask layout.

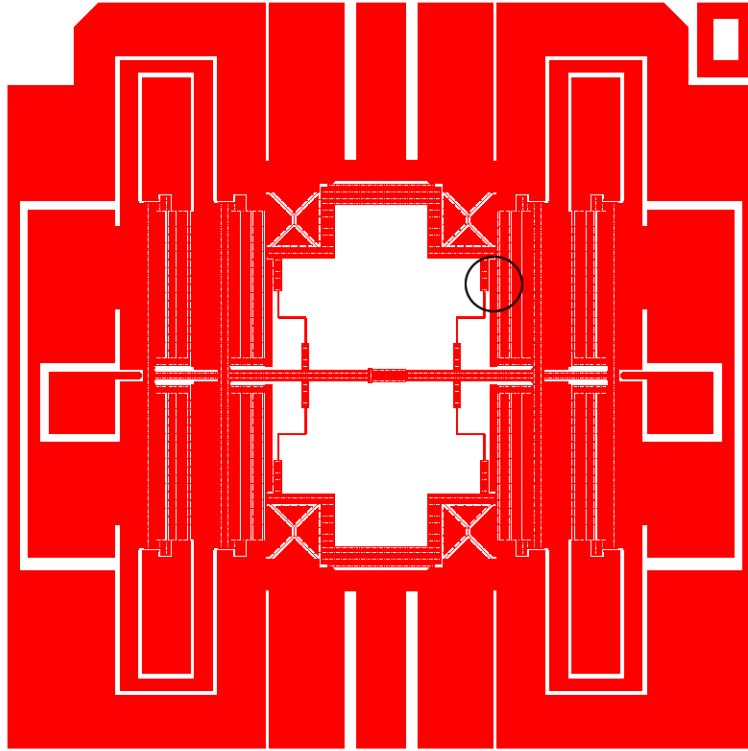
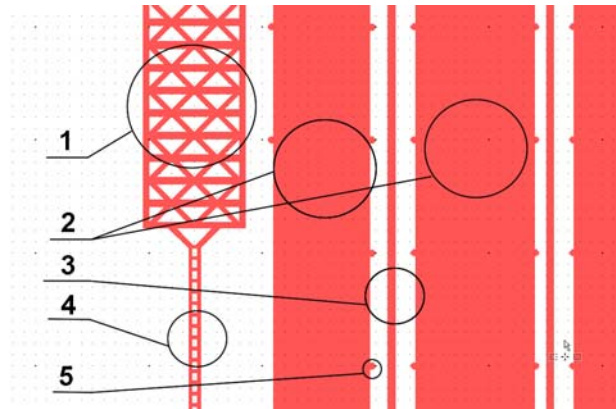


Figure 6.19: Mask cell for the bi-stable actuator



1. Dense triangular pattern for structure release. Rule A
2. Dummy patterns to cover wide gaps. Rule B
3. Narrow beam accompany with narrow trenches. Rule B
4. Split one beam to two and create narrow trench between. Rule C
5. Small pins to avoid lateral stiction.

Figure 6.20: Application of the rules for one step etch &amp; release process on the layout

The mask for the waveguide core is drawn according to the optimized dimensions we obtained in the last chapter. However, considering the under-etching happening in the RIE process of the polymer (Figure 6.21), the mask is designed  $1\mu\text{m}$  larger to compensate this offset. Figure 6.22 is the layout of the waveguide core.

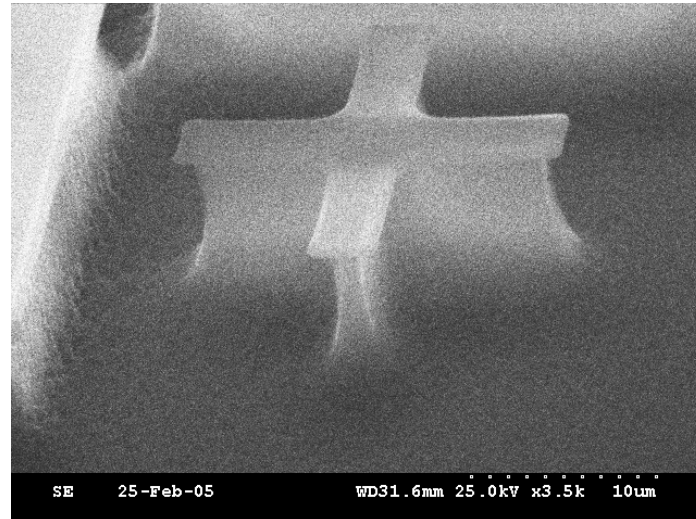


Figure 6.21: SEM picture shows the under-etching of the waveguide polymer in RIE process

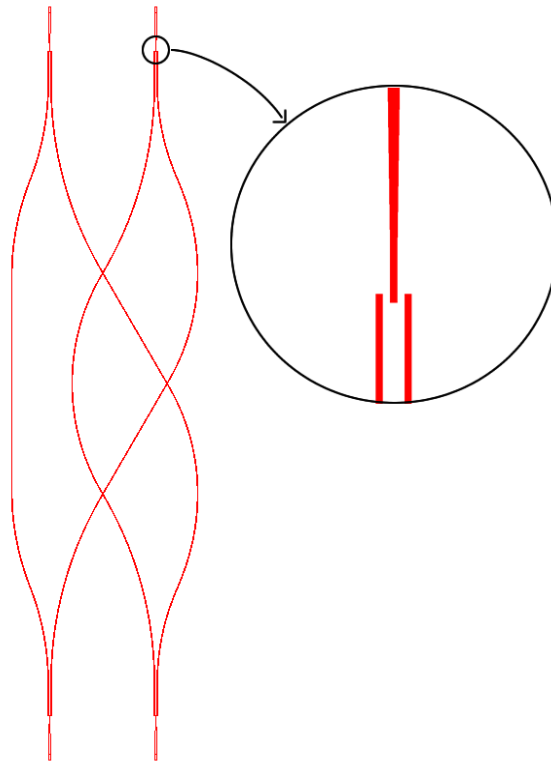


Figure 6.22: Mask layout of the waveguide core

The layout of the waveguide cladding needs to consider not only the compensation for the under-etching that's less critical here than for the core, but also the bonding of the polymer with silicon. Large meshed areas are designed to increase the contact surface of silicon and polymer, as shown in Figure 6.23.



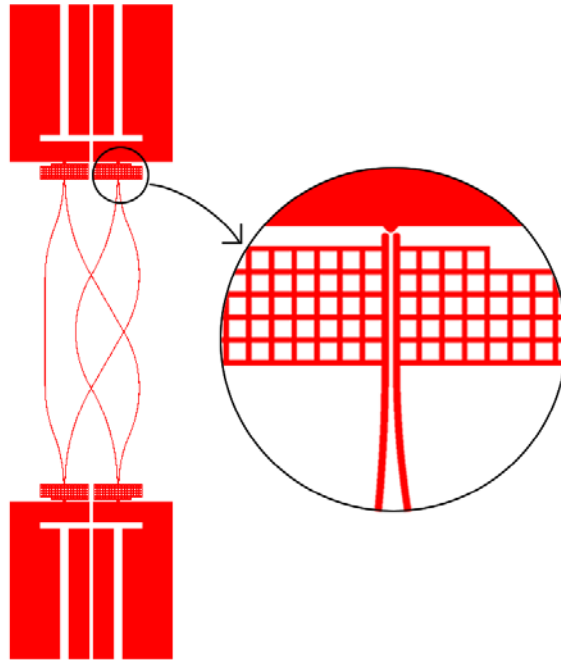


Figure 6.23: Mask layout of the waveguide cladding

These three layers of mask work together as a mask set. They must have correct relative positions, shown in Figure 6.24. The three layers are illustrated with different colors. Figure 6.25 is an enlarged view of the set of masks.

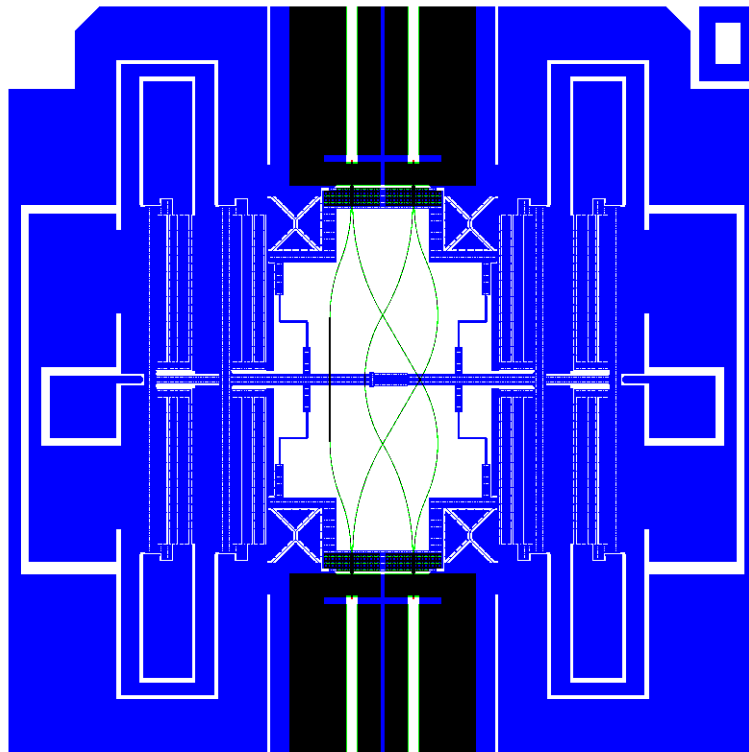


Figure 6.24: Superposition of the 3 masks in a cell

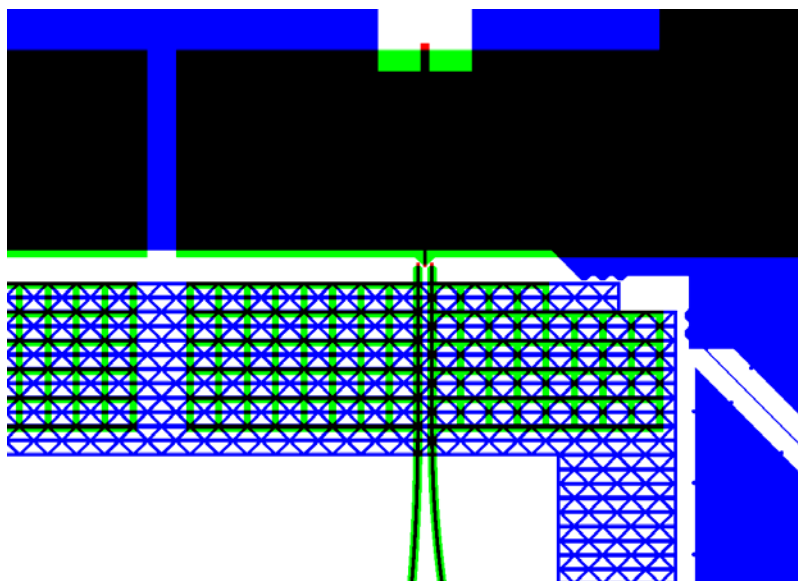


Figure 6.25: Enlarged view of the superimposed masks

The masks are made for 4 inch wafers. One wafer can hold many cells, and each cell will be a SWOMS after fabrication. Figure 6.26 shows the arrangement of the cells on the masks. All the three layers are illustrated on the figure, and at the bottom there are also some structures other than the SWOMS for testing.

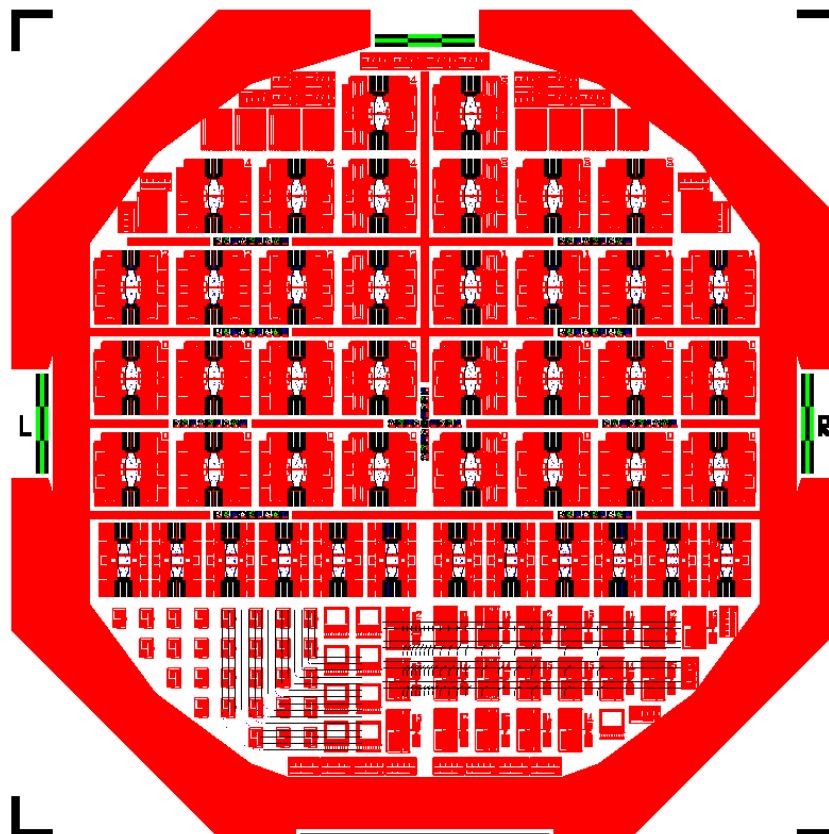


Figure 6.26: The complete mask with multiple cells and all layers superimposed

During the fabrication of micro structure using multiple masks, the alignment of the mask with the structures already existing on the wafer is a concern. The alignment marks are designed for this purpose. We can observe these marks with a microscope and adjust the wafer position on the mask aligner. This adjustment can align different layers to an accuracy of  $1\mu\text{m}$ . Figure 6.27 shows the alignment marks we've designed. The real size of one square is  $1\text{mm}\times 1\text{mm}$ .



Figure 6.27: The alignment marks

## 6.5 Fabrication of the Bi-stable Actuator

The hardest nut to crack in the fabrication of the bi-stable actuator is the stiction problem when wet release, which is solved by the technology described in section 6.3, and the layout design rules has been applied to the mask design. Thus the fabrication of the bi-stable actuator is a good demonstration of the effectiveness of the technology. Beside this, there are some other specific problems met because of the high aspect ratio, high precision and small critical feature size the device requires, i.e. long beams with  $2\pm 0.2\mu\text{m}$  width and  $50\mu\text{m}$  thickness, and grooves with  $2\mu\text{m}$  width and  $50\mu\text{m}$  depth. The problems and their solutions are detailed in this section.

The simplified fabrication process of the bi-stable actuator is illustrated in Figure 6.28

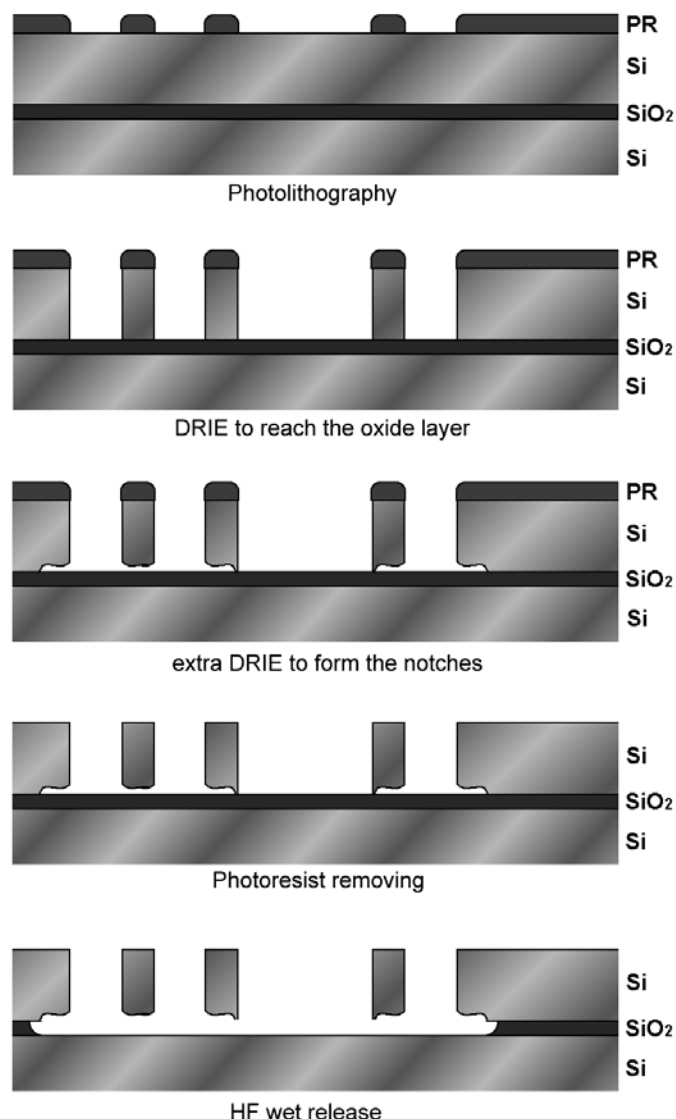


Figure 6.28: Fabrication process of the bi-stable actuator

### 6.5.1 Photolithography

The photoresist used here is AZ7220. The photolithography process consists of the following steps:

1. SOI wafer cleaning in  $\text{H}_2\text{SO}_4 + \text{H}_2\text{O}_2$  at  $120^\circ\text{C}$  for 20mins, DI water rinsing, spin drying, and hot oven drying.
2. Apply HMDS as PR (photoresist) adhesion promoter on the wafer at  $100^\circ\text{C}$  with vacuum for 20secs.

3. Spin AZ7220 on the wafer with Karl Suss spinner at 500rpm for 10secs + 1500rpm for 30secs.
4. Pre-bake on hotplate at 100°C for 90secs, and natural cool down.
5. Mask alignment, and expose with UV for 3.6secs on Karl Suss mask aligner.
6. Post-bake on hotplate at 110°C for 60secs, and natural cool down.
7. Develop with AZ300MIF developer for 3mins, DI water rinse, and spin dry immediately.
8. Hard-bake on hotplate at 100°C for 5mins and 110°C for 1.5mins, and natural cool down.

This photolithography process is optimized for our mask, chemicals and facilities by repeated experiments. The final thickness of the photoresist is 2.15 $\mu$ m.

### 6.5.2 The Tweaked DRIE Process

The DRIE process to reach the oxide layer looks simple and straight, but in fact it is not. DRIE is not a flawless technology, and our device with high aspect ratio, high precision and small critical feature size has pushed this technology to its limit. Many innate problems of DRIE have been met in our fabrication, and we've solved them by tweaking the recipe and process.

1. RIE lag. As shown in Figure 6.29, wider trenches etch down more quickly than narrow ones because more gaseous species can reach their bottom. The etch rate difference makes it difficult to decide the etching time. After wide trenches reached the oxide layer, additional time is needed for the narrow trenches to complete. However, the silicon surface exposed to the etchant has decrease much, thus the etch condition has changed, and the sidewall etching may happen destroying the sensitive thin beams.

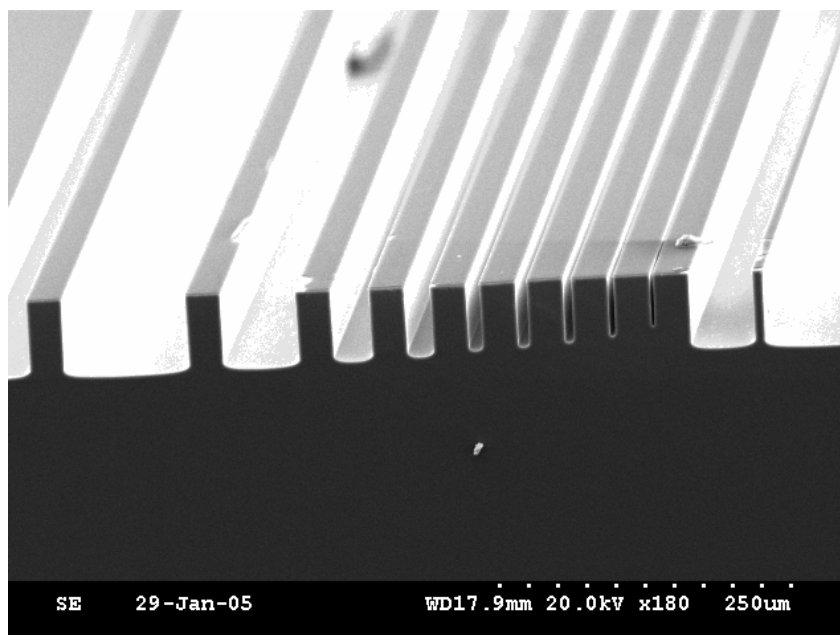


Figure 6.29: The RIE lag effect.

2. Sloping sidewall. The sidewalls of trenches and beams are supposed to be vertical, and the parameters and recipe of the DRIE system have been optimized for this purpose. However, it is impossible to have the sidewalls of narrow and wide trenches vertical simultaneously. The result is, if the narrow trenches are etched down vertically, the thin beam between wide trenches will form a V shape (see Figure 6.30). Or if optimized the recipe to make the thin beam straight down, the narrow trench will form a V shape. The slope is very small ( $<0.5^\circ$ ) and not obvious for wide structures, but it changes strongly the narrower beams and trenches.

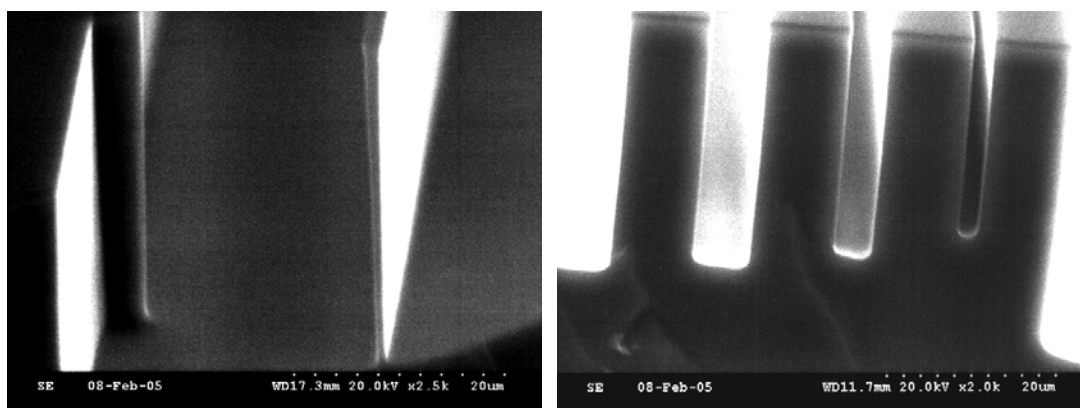


Figure 6.30: 2μm trench and 2μm beam fabricated with a standard recipe.

3. Dimension change. This problem can also be seen in Figure 6.30. The beam and the smallest trench are both designed to be 2μm in width, but the resulting width of the

trench is larger than  $2\mu\text{m}$  and the width of the beam is smaller than  $2\mu\text{m}$ . Figure 6.31 illustrates this phenomenon more clearly. After DRIE, all the trenches are, e.g.  $1\mu\text{m}$  wider than the gaps on the photoresist mask, and the beams are  $1\mu\text{m}$  thinner than supposed. The amount of the change depends on the system and recipe. Whatever, this dimension change makes it difficult to fabricate thin beams precisely. There are some beams with a width of  $2\mu\text{m}$  designed in the bi-stable actuator, if they are fabricated without any compensation, the resulting width is  $1\mu\text{m}$ , which is totally unacceptable.

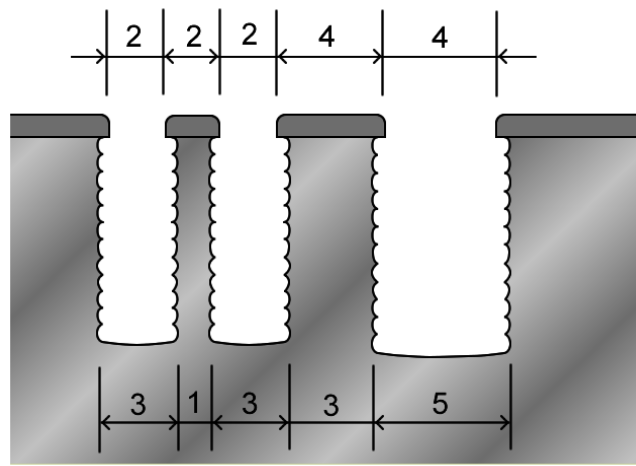


Figure 6.31: The dimension change of DRIE

The dimension change can be compensated in two ways. One way is to change the dimensions of the photoresist before DRIE. The dimensions of photoresist can be changed by two methods: redesigning the mask, or tweaking the photolithography process, e.g. reduce the exposure time. However, when there are  $2\mu\text{m}$  gaps in the design, both methods will face an actual  $1\mu\text{m}$  critical feature size, which can hardly be obtained with contact UV photolithography.

The other way to compensate the dimension change is to tweak the DRIE process. There are also two methods: one is to use a slower recipe, the other is to introduce a slope on the sidewall to shrink the gap. There are two standard recipes in our DRIE system provided by the vendor. One recipe uses 14secs etching and 8secs passivation as a cycle, and its etching rate is about  $2\sim 3\mu\text{m}/\text{min}$ . Let's mark it as recipe Q. The other recipe uses 8secs etching and 5secs passivation, and has etching rate around  $1\mu\text{m}/\text{min}$ . We mark it as recipe S. The recipe Q introduces dimension change of about

1 $\mu\text{m}$ , while recipe S has a dimension change about 0.5 $\mu\text{m}$ . A slower recipe has a smaller dimension change. However, using the slower recipe still can't eliminate the dimension change, and the slower recipe has severer problems of RIE lag and creates sloppier sidewalls than the quicker recipe.

The problems are solved by a combination of all the principles described above. The UV exposure time is reduced to add 0.5 $\mu\text{m}$  to the line widths of photoresist. We use three steps of DRIE to etch down to the oxide of the SOI wafer.

Step 1: 4mins 23secs of DRIE using recipe S<sub>1</sub>, which is a tweaked version of recipe S. Recipe S<sub>1</sub> has etching/passivation time of 7secs/5secs. It can shrink trench width when etching down.

Step 2: 25mins of DRIE using recipe S<sub>2</sub>, which is also a tweaked version of recipe S. Recipe S<sub>2</sub> has etching/passivation time of 9secs/6secs. Unlike recipe S that result in straight down trench and V shaped beam, the recipe S<sub>2</sub> balances the slope of trench and beam, and its etch rate is quicker. After this step, the wide trenches have reached the oxide layer.

Step 3: 3mins of DRIE using recipe Q<sub>1</sub>, which is a tweaked version of recipe Q. Recipe Q<sub>1</sub> has etching/passivation time of 12secs/8secs. The etching time is shorter than the standard recipe Q to avoid sidewall attack problem that we have described in problem 1. A quick recipe is used in this step for two reasons. One is that the RIE lag in the quick recipe is not as severe as in the slow recipe, and the other is that the quick recipe consumes photoresist much less than the slow recipe.

After these three steps, most trenches reached the oxide layer except those that have a width below 6 $\mu\text{m}$ . Figure 6.32 shows a 2 $\mu\text{m}$  beam and a 2 $\mu\text{m}$  trench after these. Comparing it with the Figure 6.30, the improvement is obvious. Both the trench and the beam are nearly straight down. The final average width of the beam is about 1.8 $\mu\text{m}$ , and the final width of the trench is about 1.7 $\mu\text{m}$ .



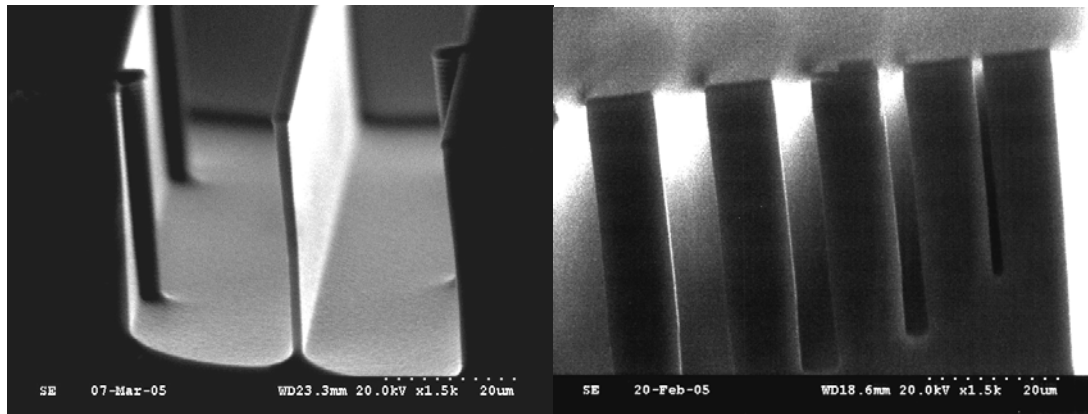


Figure 6.32: The beam and trench formed after the tweaked DRIE process.

### 6.5.3 Extra DRIE to Form Notches

Some extra DRIE time is used to compensate for the RIE lag effect and to form notches. Here, two points must be taken care of: the sidewall attack and the overheating.

We use the recipe  $Q_2$  for this process. Recipe  $Q_2$  is another tweaked version of recipe  $Q$ . It has etching/passivation time of 11secs/9secs, which significantly decreased the etching time and increased the passivation time to avoid sidewall attack. The total extra time is 12mins, and it is split into 3+2+2+1+1+1+1+1mins steps. 3mins of pause is used between each step of the DRIE to allow the sample to cool down, preventing overheating. This method has been described in Rule D of the layout design rules for one step etch and release in section 6.3.

Figure 6.33 shows some portions of the bi-stable actuator after this step. We can see that the structures are all nearly dry-released by notching, and the smallest features are formed correctly.

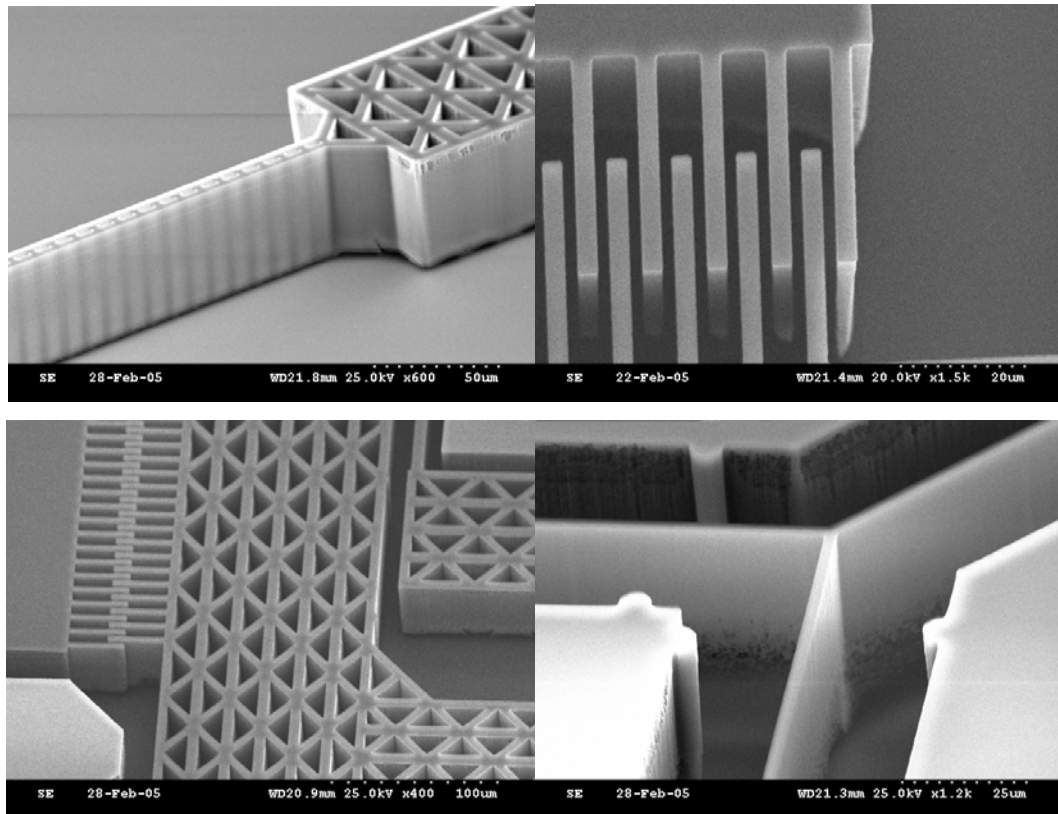


Figure 6.33: Structures formed after extra DRIE

#### 6.5.4 Photoresist Removing and HF Wet Release

After DRIE, the photoresist remained on the SOI wafer is eliminated by RIE with  $O_2$  RF plasma at power 300W, gas flow 10sccm, and vacuum pressure 70mTorr for 20mins.

Although the device is designed to be totally dry-released by notching, a combination of dry and wet release is adopted for two reasons. One is that it is not necessary to totally dry because the stiction problem of wet release is removed when the notches have developed sufficiently. The second reason is that the complexity and non-uniformity of the patterns of our device cause non-uniformity of the notch growth. If we rely only on dry release, the notch non-uniformity causes the height difference of the structures, and also increases the risk of photoresist burning.

The wet release process consists of 4 steps:

1. Sink in 49% HF for 4mins.
2. DI wafer rinsing for 15mins to clean the HF remaining.
3. Methanol rinsing for 10mins
4. Natural drying.

The fabricated bi-stable actuator is shown in Figure 6.34.

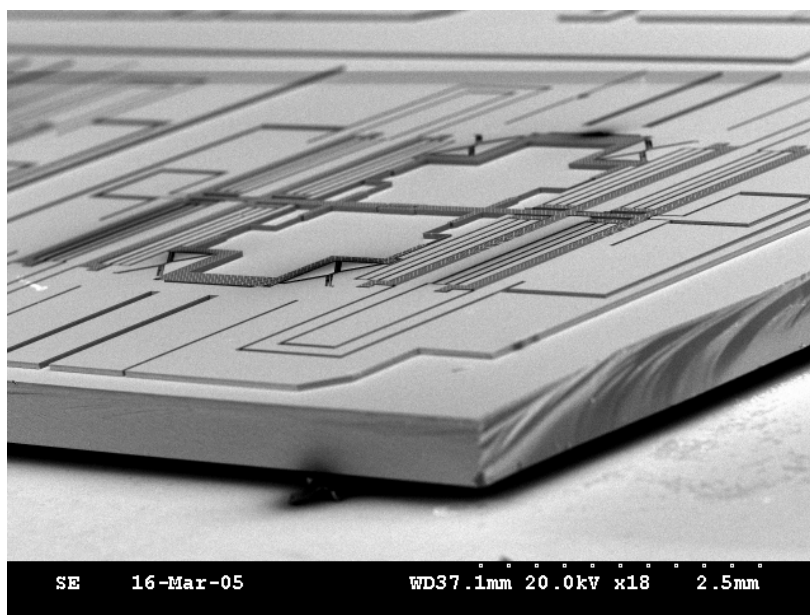


Figure 6.34: SEM photo of the bi-stable actuator

## 6.6 Fabrication of the Waveguides

The waveguides fabrication begins from a 4 inch quartz wafer. Here a quartz wafer instead of a silicon wafer is chosen because quartz is optically transparent and easier for alignment of the cladding mask with the core, and also because it is easier for the later step when we strip the polymer from the wafer.

Figure 6.35 illustrates the process to fabricate the waveguides. The detailed steps are:

1. Apply ZAP1010 on the wafer surface at 2500rpm for 30secs, and bake on hotplate for 3mins at 110°C. The ZAP1010 is an adhesion promoter provided together with ZP49 and ZP51 by Zen Photonics.

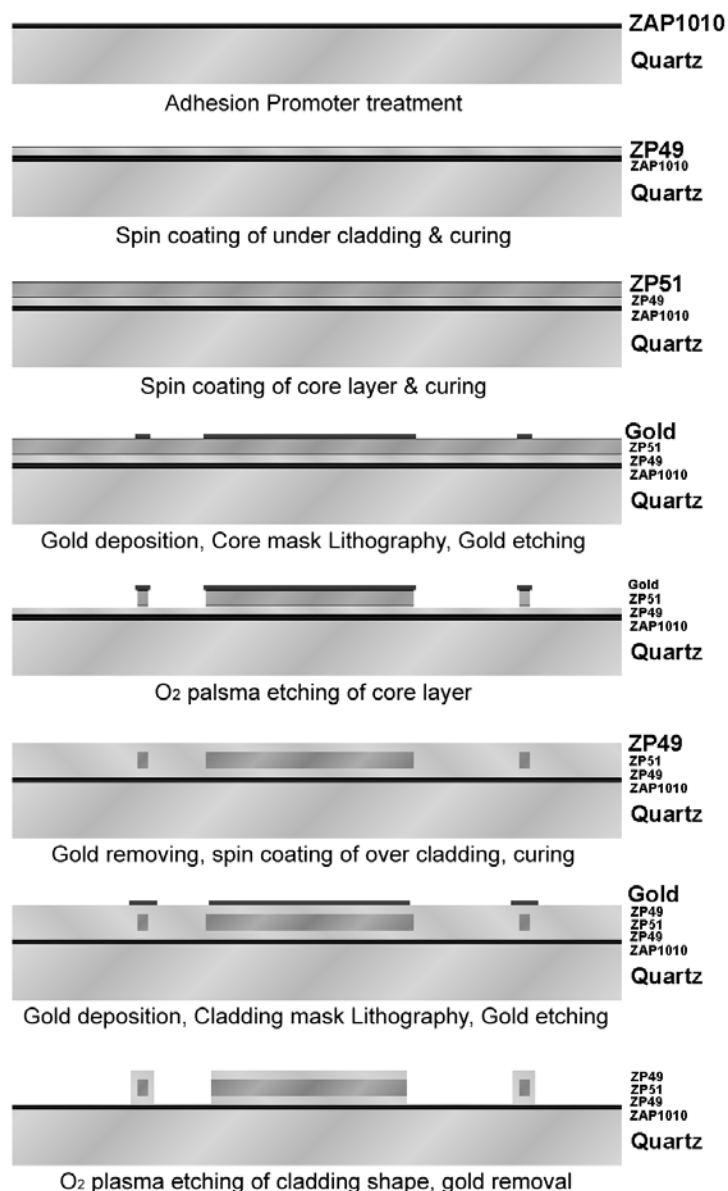


Figure 6.35: fabrication process of the waveguides

2. Spin on ZP49 at 2000rpm for 30secs as the under cladding layer, and then thermally cure with a hotplate. The curing process includes 5 steps:

- 1) 3mins stay at room temperature.
- 2) 5mins ramp to 90°C, and then keep for 10mins.
- 3) 5mins ramp to 150°C, and then keep for 10mins.
- 4) 10mins ramp to 250°C, and then keep for 2hours.
- 5) Natural cool down.

3. Spin on ZP51 at 1000rpm for 30secs as the core layer, and then thermally cure with a hotplate. The thickness of the ZP51 layer is 9 $\mu$ m. The curing process is the same as ZP49 layer.
4. E-beam evaporation of gold (Au) on the surface of the ZP51 layer. At  $5.0 \times 10^{-5}$  torr, 5KV, 130mA, for 30mins. The thickness of the Au is 70nm.
5. Photolithography using the core mask. The photolithography includes the following steps:
  - 1) Spin on AZ7220 at 2000rpm for 30secs, and then pre-bake at 100°C for 90secs.
  - 2) Mask alignment, soft contact, UV exposure for 3.2secs, and then post-bake at 110°C for 60secs.
  - 3) Develop in AZ300MIF for 3mins, DI water rinse, and then spin dry at 1200rpm for 90secs.
  - 4) Hard-bake at 100°C for 3mins and 110°C for 1min30secs.
6. Au etching with Au etchant for 1mins while stirring back and forth. The ingredients of the etchant are KI: I<sub>2</sub>: H<sub>2</sub>O at 4g: 1g: 180ml.
7. RIE of the polymer with O<sub>2</sub> plasma at 8sccm, 80mTorr, 300W RF, for 35mins. The etching depth is 9 $\mu$ m. Figure 6.36 shows the core shape after this step.

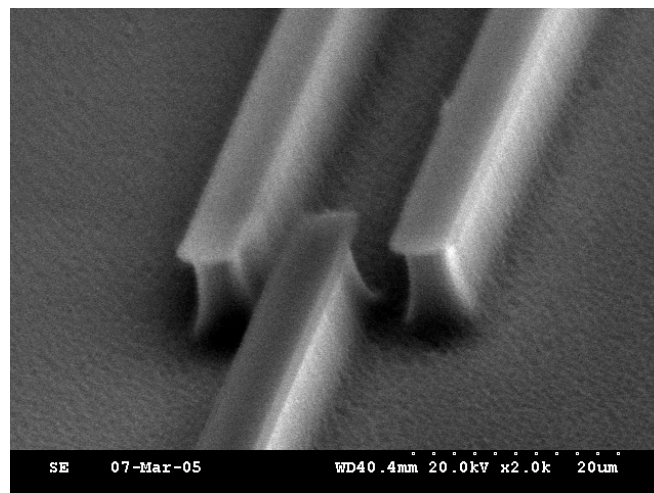
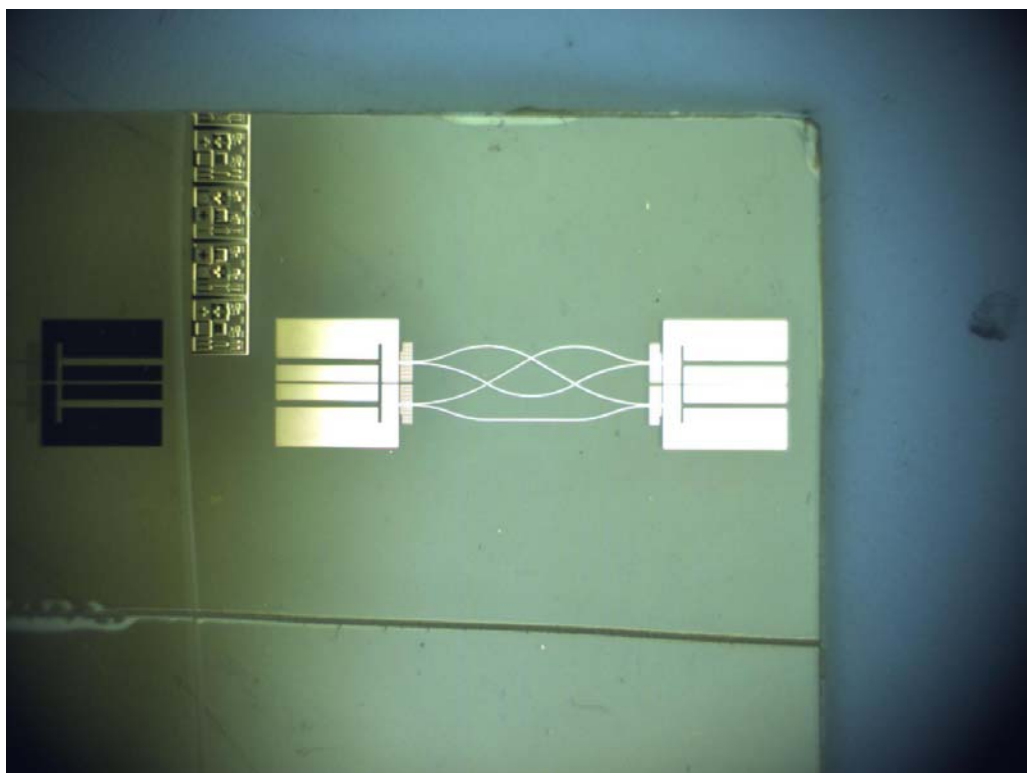


Figure 6.36: The SEM picture of the waveguides core after RIE for 35mins

8. Etch the remaining Au in the Au etchant, and then rinse and dry.

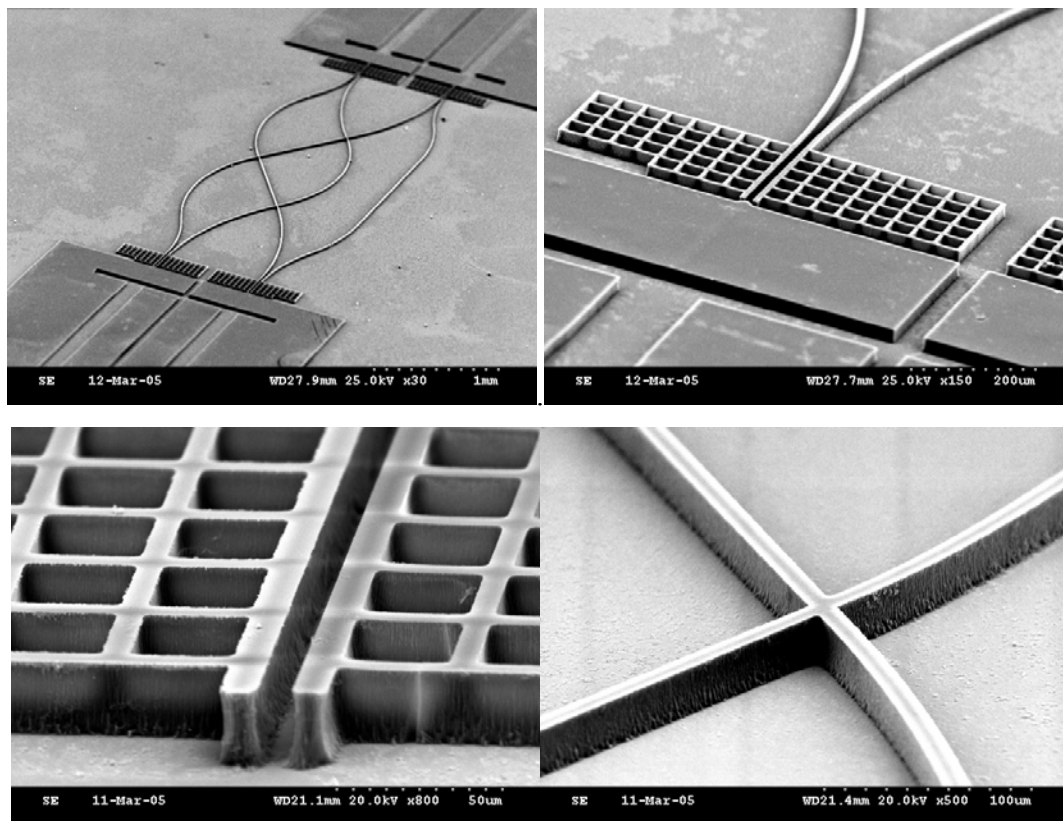
9. Apply ZP49 at 500rpm for 30secs as over-cladding layer, and then thermally cure with a hotplate. The thickness of this layer is  $14\mu\text{m}$  to cover the core. The curing process is the same as that introduced formerly.
10. E-beam of Au on the surface of ZP49 layer, as in step 4
11. Photolithography using the cladding mask. The align marks designed on the masks are used here for alignment of the core and cladding. Other lithography processes are the same as described in step 5
12. Au etching as in step 6. Figure 6.37 (A) shows the waveguide polymer film and the patterned Au layer on the quartz wafer.
13. RIE of polymer with  $\text{O}_2$  plasma at 8sccm, 80mTorr, 300W RF, for 90mins. And then etch away the Au remaining completely.

Figure 6.37 (B) shows the final shapes of the waveguides.



(A)





(B)

Figure 6.37: (A) A photo of the waveguides polymer and patterned Au layer on quartz wafer before the final dry etching step. (B) The SEM image of the cladding shape of waveguides made on the quartz wafer.

## 6.7 Silicon-Polymer Bonding and Final Steps of fabrication

As described in the last section, the waveguides can be fabricated completely on the quartz wafer. However, it is very difficult to mount the completed waveguides on the bi-stable actuator to form the SWOMS. The problem is solved by peeling off the polymer membrane and bonding it on the actuator before performing the last RIE step to etch the cladding.

Figure 6.38 illustrates the bonding process and the final etching. The steps are:

1. Peel off the polymer membrane. It is done by sinking the quartz wafer in BOE (6:1

buffered Oxide Etchant,  $\text{NH}_4\text{F}$  33.6-34.6%,  $\text{HF}$  7.08-7.38%) for about 5mins, and then DI wafer rinsing.

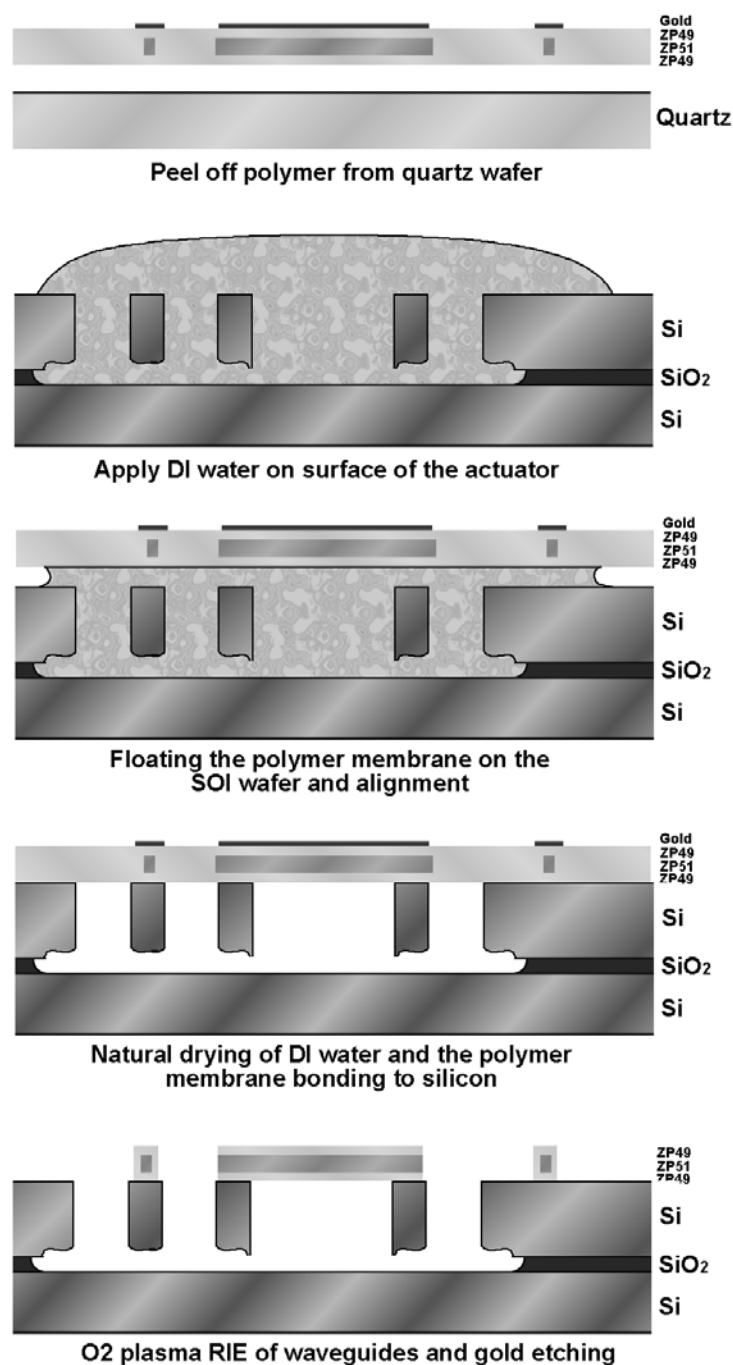


Figure 6.38: The polymer-silicon bonding & fabrication

2. Apply DI water on the surface of the bi-stable actuator.
3. Float the polymer membrane on the DI water and align it with the bi-stable actuator. The alignment is accomplished using micro probes under observation of microscope.



## Chapter 6

## Fabrication of the Optical Switch

The probes can easily push the membrane when it is floating on the water with an accuracy of  $1\mu\text{m}$ .

4. Natural drying of the DI water. The membrane is attracted to the SOI wafer because of capillary forces when the water is drying. The membrane then sticks to the wafer firmly because both the silicon and polymer surface are smooth.

5.  $\text{O}_2$  plasma etching of the polymer membrane to form the waveguide cladding shape. The etching condition is the same as described in the last section. The final polymer-silicon hybrid structure of SWOMS and a photo of a prototype with fibers attached are shown in Figure 6.39.

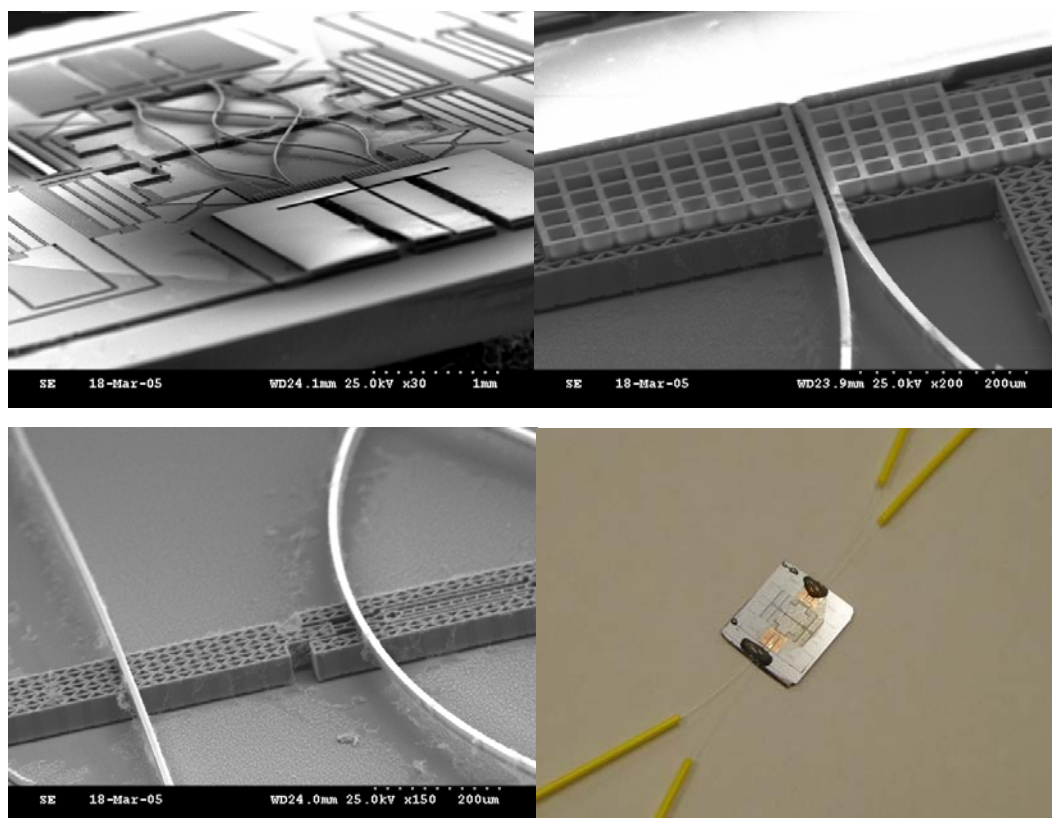


Figure 6.39: the prototype of SWOMS

## CHAPTER 7 Test of the SWOMS

We propose to test both the electro-mechanical property and the optical performance of the SWOMS. The facility for the electro-mechanical testing is a probe stage together with power supplier and sensor, and the facility for optical testing is an optical test stage with laser source, cameras, lenses, detector and computer for image analysis.

### 7.1 Electro-mechanical Test

#### 7.1.1 Assembly of the Spring Structure

The SWOMS is based on the bi-stable actuator. The spring of the actuator need to be assembled to a pre-compressed state before it can work. The actuator was designed to be assembled electrically. However, during our testing of the device, it did not work without hitches. The main reason is the fabrication process which resulted in a varying gap between the comb fingers, narrowing at the ends of the combdrives, where the etching condition is locally different with comb fingers in the middle. The gap there is only  $1\sim 1.5\mu\text{m}$  instead of  $2\mu\text{m}$  elsewhere as designed (see figure 7.1). Thus when we applied voltage above 60V, air ionization happened and the device was burnt.

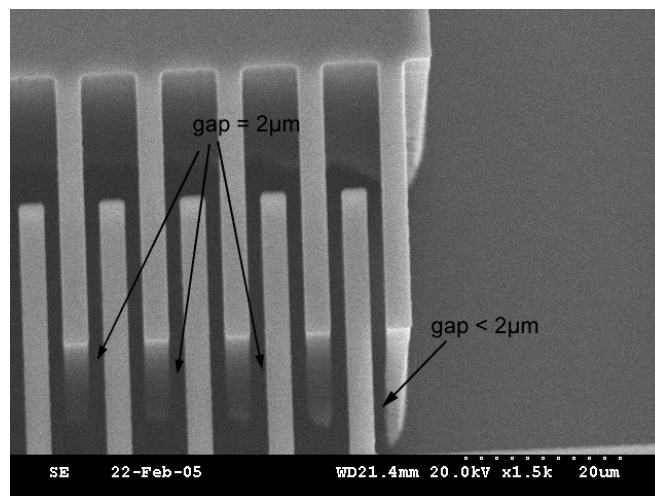


Figure 7.1: a narrower gap between the fingers at the end of a combdrive.

Although this problem can be solved by compensation in the mask design, we found that mechanical assembly is also easy. The device was fixed on a probe station and the assembly was accomplished by using two probes to push the left and right part of the actuator under microscope. The process is quick and simple. Figure 7.2 compares the SEM photo of the lock structure and the fork hinge before and after the assembly.

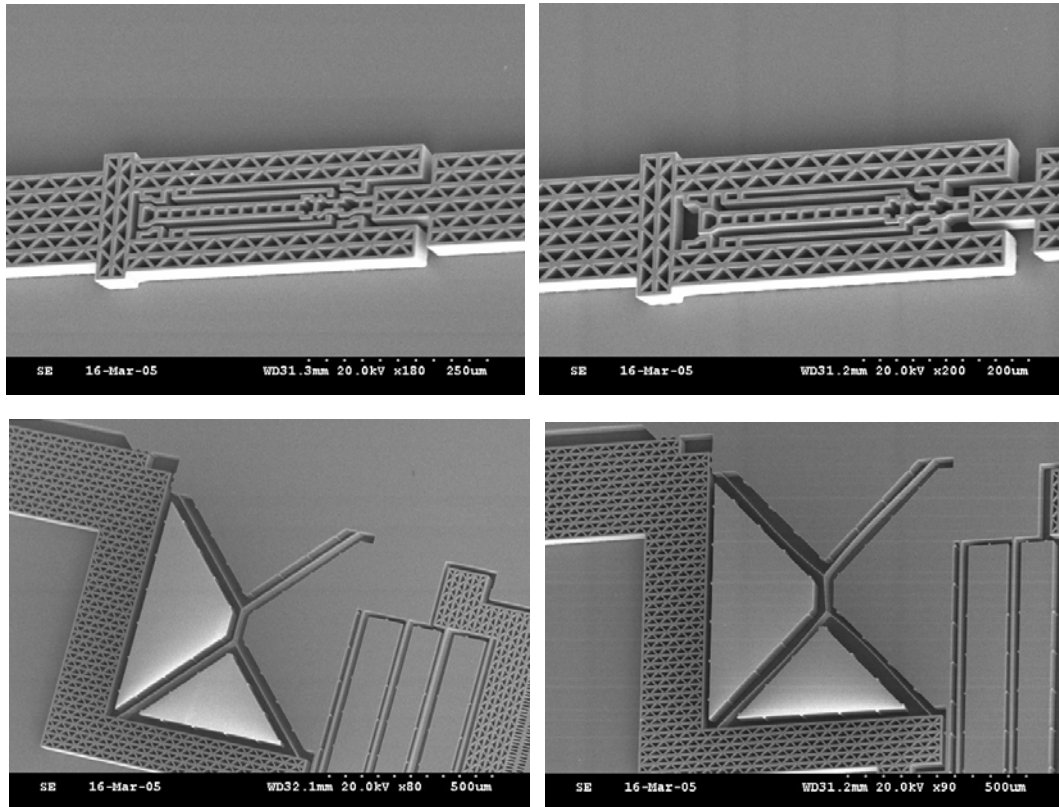


Figure 7.2: The lock structure and the fork hinge before (left) and after assembly (right).

### 7.1.2 Bi-stable Latching Functionality

After the assembly, the actuator is self-latched at one stable position, as predicted in chapter 4. Applying voltage above 36V on the combdrives, the actuator can move left and right. Removing the voltage, the actuator keeps its position. The measured switching voltage is higher than the designed voltage (25V, see chapter 4). One of the main reasons found is that during the DRIE, the under notching of the comb fingers is more significant than the main beams of the structure, which reduced the force provided by the combdrive. This can be considered as a side effect of the layout

controlled one-step dry etch & release process presented in Chapter 6.

Because the moving range of the actuator is only  $20\mu\text{m}$ , it is difficult to see the deformation of the structure from a general view of the complete device. Figure 7.3 shows enlarged SEM photos comparing the deformation of a combdrive when the actuator is at its left and right latching positions, and images captured from a video clip showing the deformation of the fork hinge during switching recorded by a camera mounted on a microscope. The deformation behavior of the fork hinge agrees well with our design and simulation.

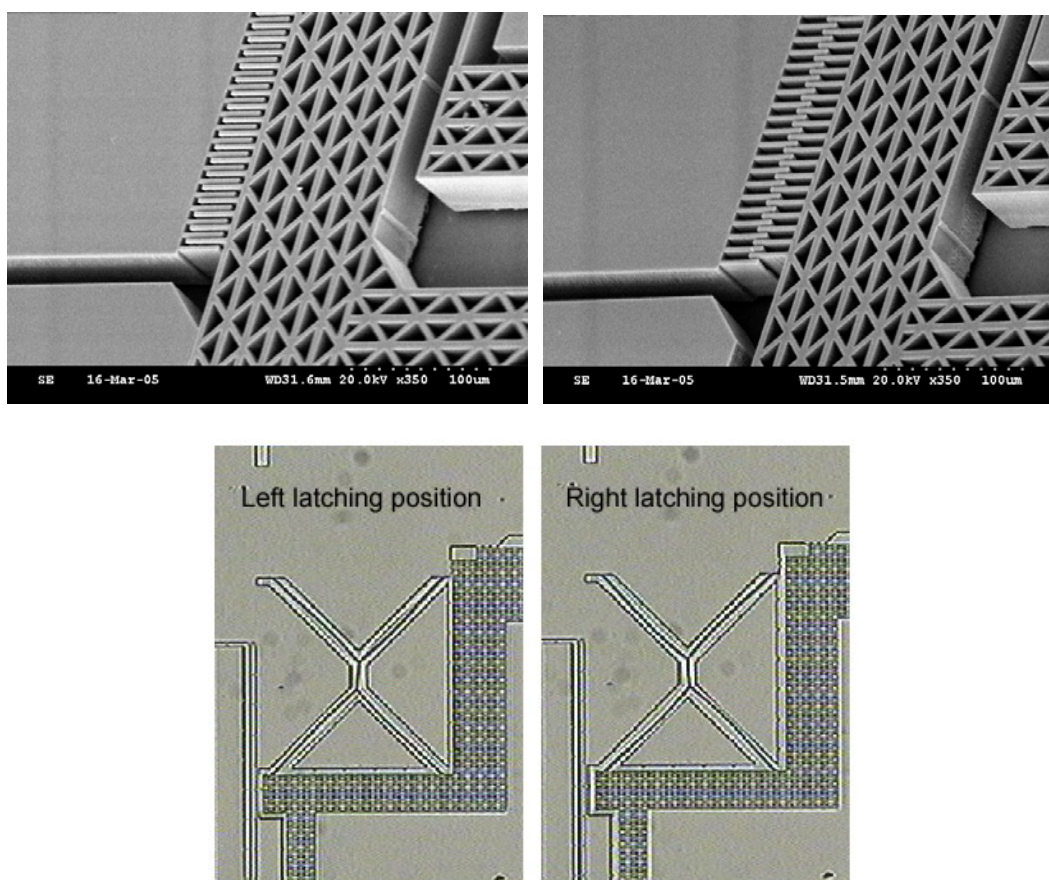


Figure 7.3: Photos of a combdrive and a fork hinge when the actuator at its left (left) and right latching position (right).

### 7.1.3 Switching Speed and Natural Frequency Test

Voltage from a wave generator and amplified is applied on the switch on a probe station. An optical vibrometer (photonics sensor) is placed  $0.5\text{mm}$  above the movable structure of the actuator to record its displacement. Both the voltage input and output



of the vibrometer are displayed by an oscilloscope (see Figure 7.4). Different input voltages and frequencies have been used for the test. The device shows a switching speed below 0.5ms. Fig. 7.5 is a screen shot of the measurement with a 100Hz square wave of amplitude 32V (voltage just below latching).

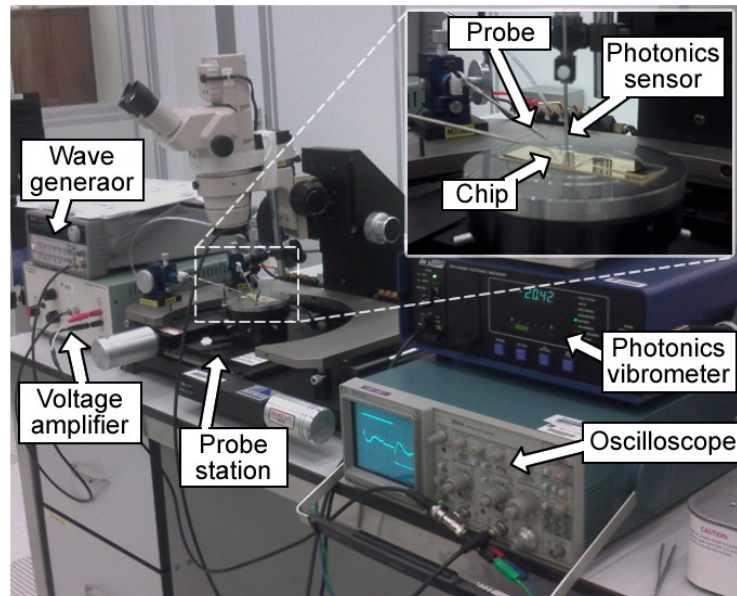


Figure 7.4: The configuration for the electro-mechanical test of the actuator.

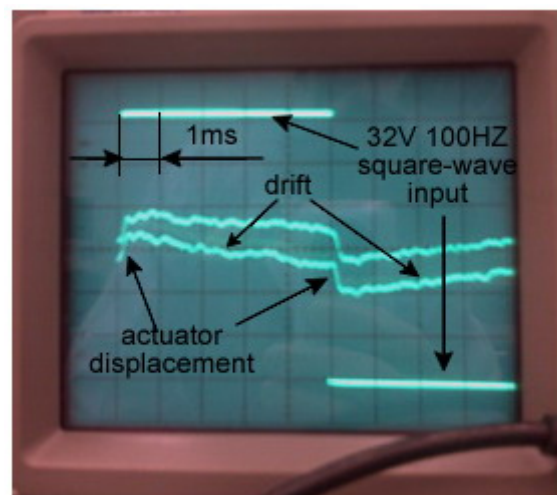


Figure 7.5: Electro-mechanical response of the actuator (the drift after the signal edge is due to the capacitive coupling with a low frequency cut-off of 20Hz).

## 7.2 Test of the Waveguides and Optical switching

The facilities for the waveguide testing are shown in Figure 7.6. We have tested the waveguides in both visible wavelength (632nm from a He-Ne laser), for easier illustration of the switching, and infrared wavelength, for which we designed it. The infrared wavelength (1550nm) comes from a Newport LD-1550-21B laser diode with fiber pigtail, which is driven by a Newport 505B laser driver. The pigtail of the laser diode was cut, stripped and cleaved to expose its single mode fiber for coupling with the waveguides. The waveguides are mounted on a stage (from Newport) that can move in 3 dimensions with a resolution of 0.1 $\mu$ m. The output of the infrared light is focused by a Newport M-20X lens, detected by a Thorlabs PDA 400 InGaAs detector, and finally the output voltage is measured by a Fluke 76 multimeter. A Carl Zeiss Stemi 2000–C microscope is used to observe the fiber and the waveguides from the top. Cameras mounted on the microscope and connected with a PC are used to capture photos. The camera for visible wavelength is a Firewire/(1394) Pixelink PL-A741, and the camera for infrared is an analog Micro Viewer 7290A from Electrophysics Corp.

In order to easily handle and test different parts of the waveguides, the polymer waveguide film was sandwiched in between two pieces of acrylic plastic and glued using epoxy. Both ends of the waveguides were then polished using 1 $\mu$ m diamond abrasive for effective coupling of light. And during the testing, immersion oil with refractive index of 1.51 was applied between the fiber and the waveguides to further reduce the loss. A photo of such waveguide sample is shown in Figure 7.7.

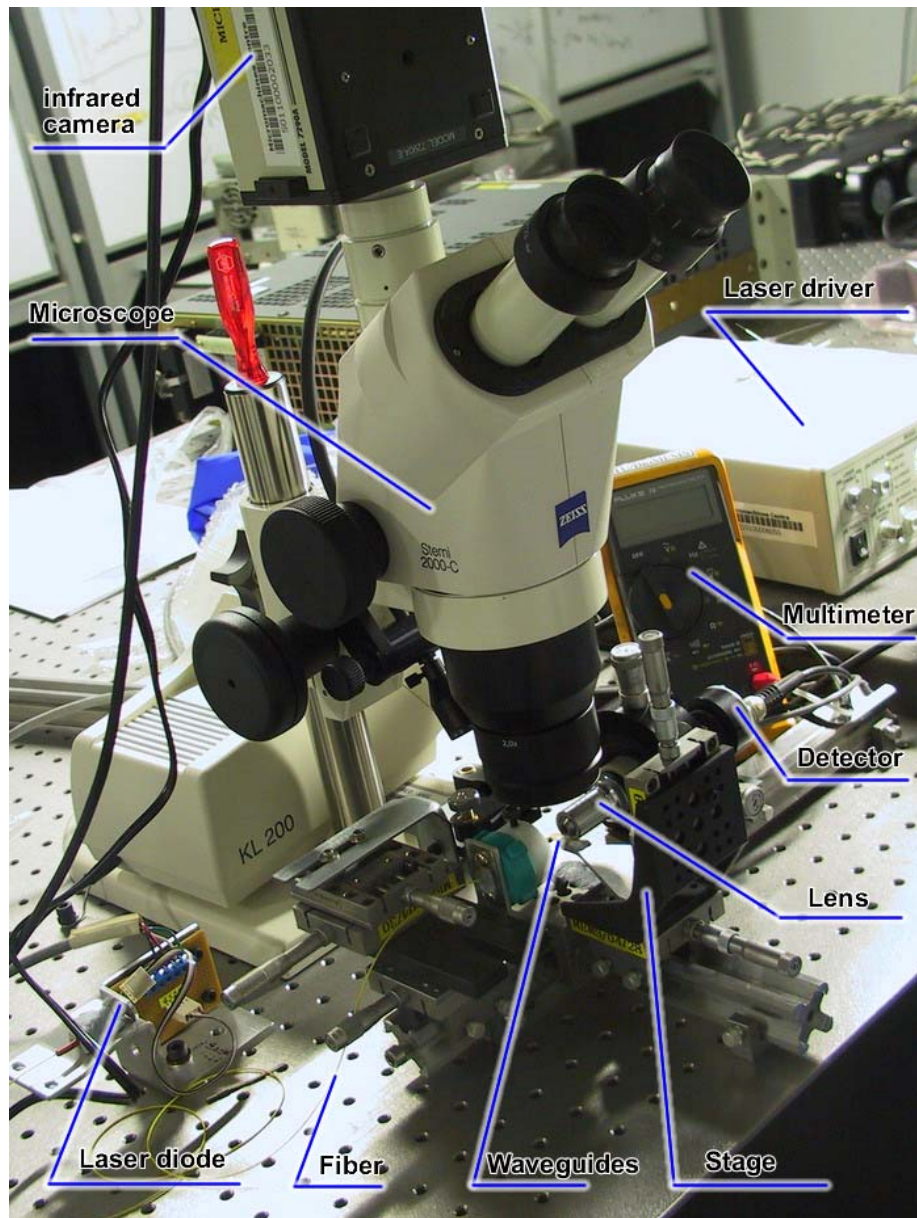


Figure 7.6: Facilities for waveguide testing

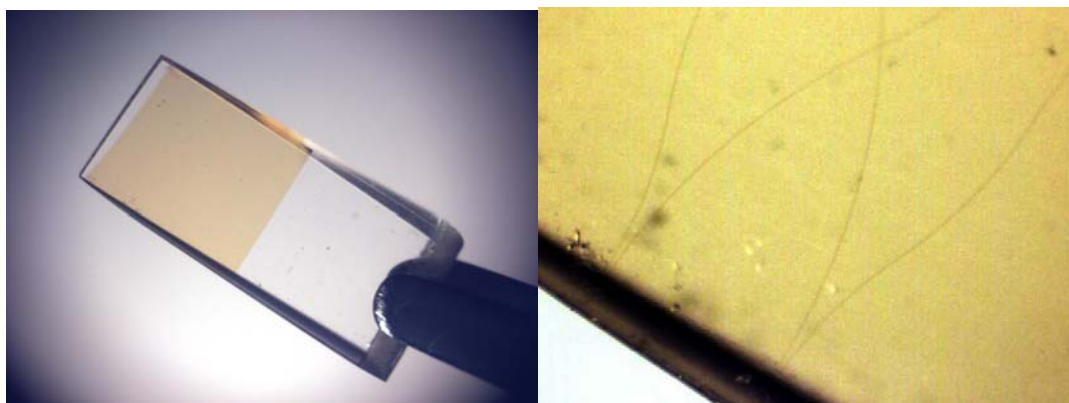


Figure 7.7: Photos of a sandwiched waveguide sample.

## 7.2.1 2x2 Optical Switching functionality of the Waveguides

### 7.2.1.1 Test Using Visible Light

For this experiment, a 632nm laser beam from a He-Ne laser is focused by a Newport M-20X lens and coupled into the waveguides. The scattering of the light is observed using a Carl Zeiss Stemi 2000–C microscope and is recorded by a Pixelink PL-A741 camera. Such a setting is sketched in Figure 7.8. When we move the waveguides, the light couples into different waveguides and the recorded images are shown in Figure 7.9.

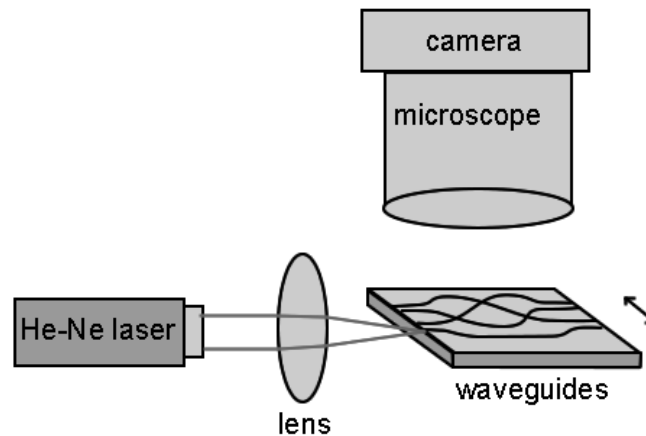


Figure 7.8: Observation setting for switching function using visible laser.

From the measurement of the light intensity decay in the waveguide, we observed high propagation loss of about 15dB/cm. High loss exists here because the core size and bending are not designed for this visible wavelength, the polymer absorbs more visible wavelength, and the scattering of a shorter wavelength (0.6 $\mu$ m) is more sensitive to surface roughness of the waveguide core than the longer infrared wavelength (1.5 $\mu$ m). However, this high scattering makes it possible for us to observe the light propagation in the waveguides directly, and visualize easily the optical switching function of the moving waveguides.



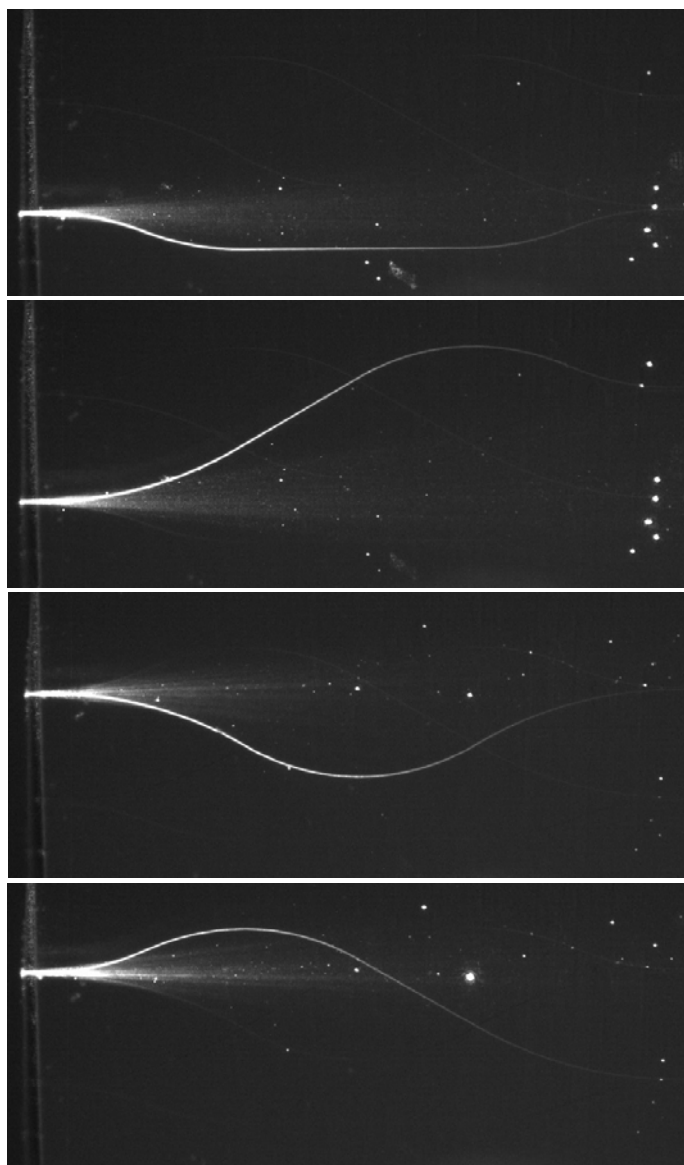


Figure 7.9: Visible laser couples into different waveguides when moving the waveguides.

#### 7.2.1.2 Optical Switching Function Test of the Polymer Waveguides Using Infrared Light

For this experiment, a 1550nm infrared laser beam from a laser diode is coupled into a single mode fiber and then coupled into the waveguides. The output light of the waveguides was reflected by a white board and is observed by the Micro Viewer 7290A infrared camera. The setting and the recorded images of the infrared camera are shown in Figure 7.10. An extra illumination is added to show the position of the fiber when taking the photos. Because there is no detectable light scattering when infrared light propagates through the waveguides, some dashed lines were sketched on

the image to indicate the location of the waveguides.

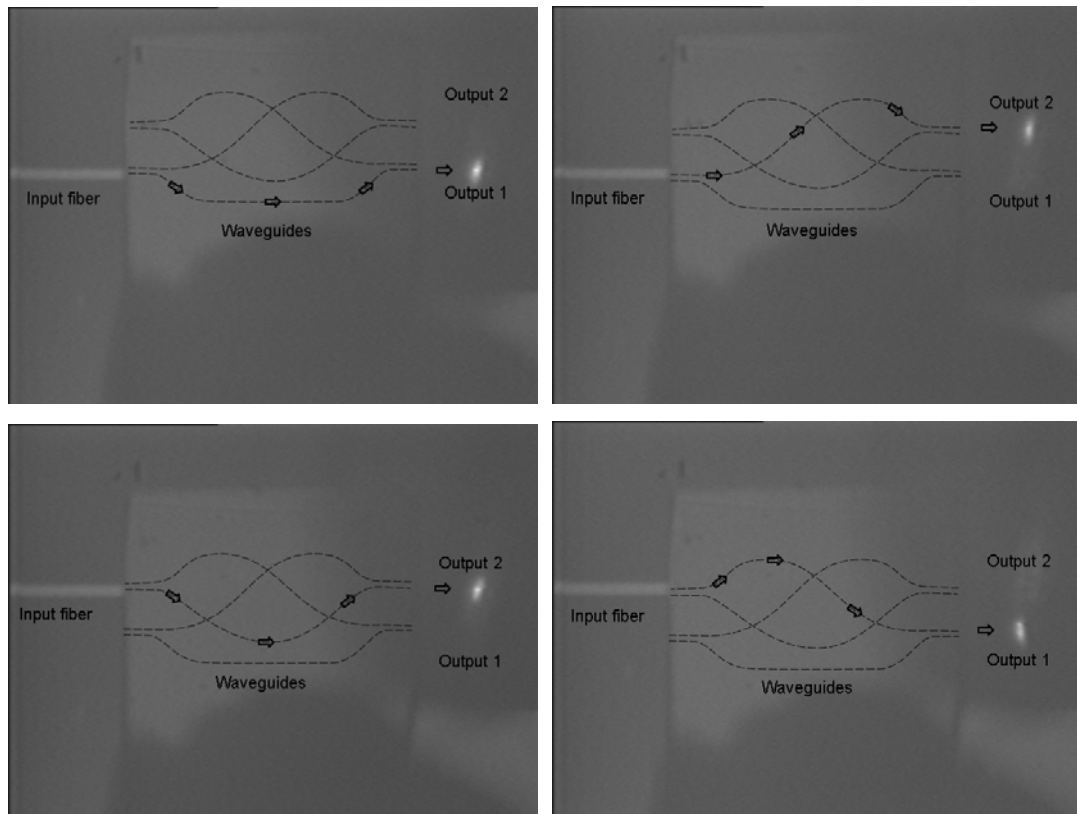
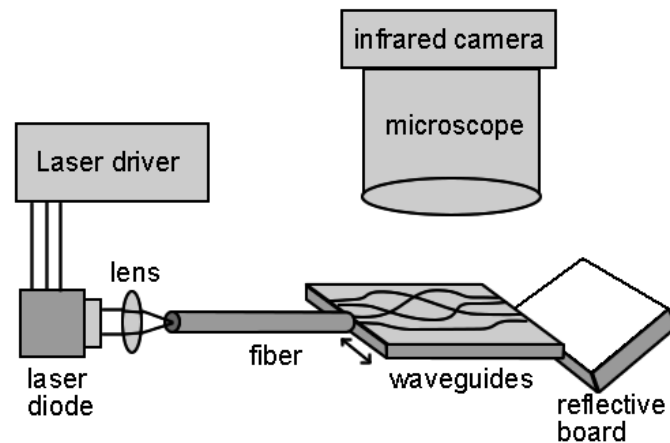


Figure 7.10: Infrared laser input from the fiber switches to the two outputs by moving the waveguides. The dashed lines were plotted on the images to indicate the locations of waveguide cores.

These infrared images are verification of the switching function of the waveguides we designed. Unlike the propagation of visible light in the waveguides, the scattering of the infrared light from the waveguide is undetectable by the infrared camera set on top

of the waveguides. Instead, the output is strong and shows nearly no crosstalk. In another test setting that the infrared camera is aligned with light propagation direction, the field image at the end of the waveguide with  $4 \times 9 \mu\text{m}$  core is recorded (see Figure 7.11). The field image recorded from the end of the fiber is also shown in the figure for comparison. The field images agree well with our 3D BPM simulation in Chapter 5. These results confirm smaller scattering loss and bending loss of the waveguides at 1550 nm infrared wavelength than at visible wavelength, and imply that our waveguide design and fabrication are qualitatively successful. We will try to give quantitative evaluation of the waveguides in the following sections.

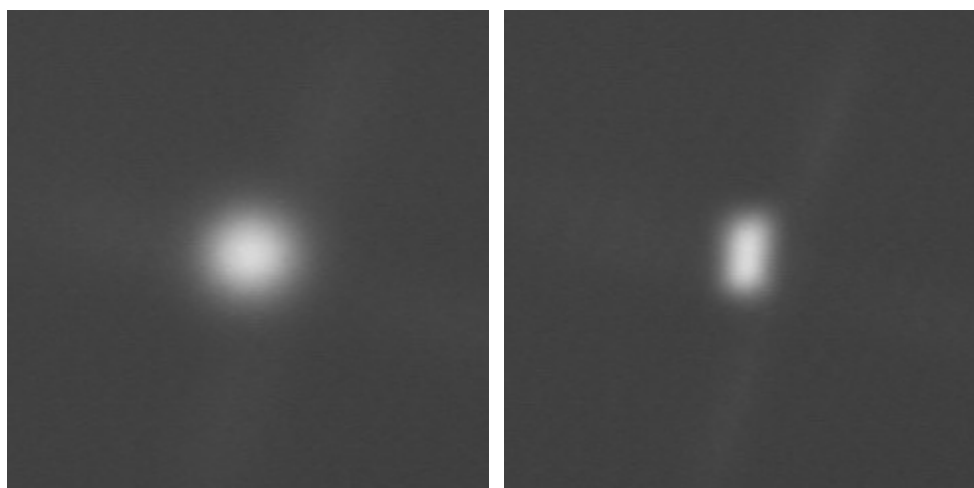
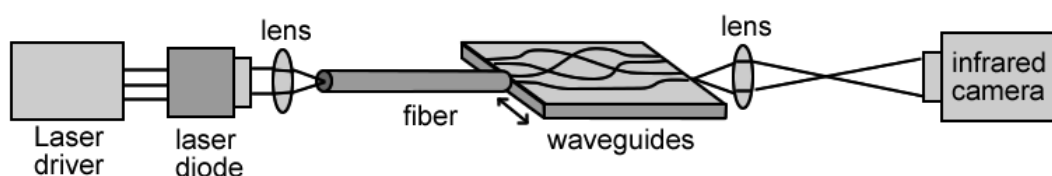


Figure 7.11: Field images recorded from the end of the single mode fiber (left) and the waveguide with  $4 \times 9 \mu\text{m}$  core (right).

## 7.2.2 Characterization of the Polymer Waveguides Using Infrared Light

The Thorlabs PDA400 InGaAs infrared light detector has a sensitivity of 0.9A/W at a

wavelength of 1550nm. At its gain switch position 1, it has a trans-impedance gain of  $1.5 \times 10^4 \text{ V/A}$ . The output voltage of the detector is measured by a Fluke 76 digital multimeter. With these instruments, we can measure infrared light powers and compare them to characterize the waveguides. The basic setting for the characterization experiments is shown in Figure 7.12. The Newport M-20X lens is mounted on an adjustable stage and used to focus the output light to the  $0.5 \text{ mm}^2$  detecting area of the PDA400 detector. The microscope used here is to allow observation when we align the waveguide and the fiber. And for all the tests, immersion oil was applied to fill the air gap in the fiber-waveguide and/or waveguide-waveguide coupling.

We set the laser diode driver at constant current 19.7mA for infrared laser emission. We measure the fiber output power as a reference, and then we insert waveguides between the fiber and detector and measured the coupling loss, the influence of the waveguide taper structure for coupling, the bending loss, the intersection loss, and the loss uniformity.

The setting for measurement of the fiber output is shown in Figure 7.13. It is a simplified plot as all other parts of the setting are the same as in Figure 7.12.

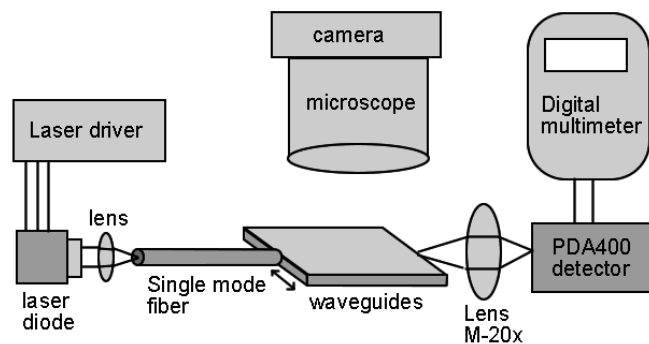


Figure 7.12: Setting for characterization of the polymer waveguides with infrared laser.

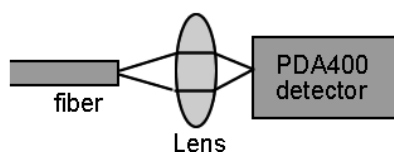


Figure 7.13: Setting to measure the reference fiber output power.

After careful adjustment of the lens focus, the measured voltage by the multimeter is 8.36V. Thus the reference power can be calculated as,

$$P_r = 8.36V \div (1.5 \times 10^4 V/A) \div 0.9 A/W = 6.19 \times 10^{-4} W = 619 \mu W$$

This power is the power reaching the detector instead of the power coming from the fiber because the lens introduces about 0.8dB of infrared power loss. However, because all our later measurements use the same lens and detector, this  $P_r$  can be used as the reference power.

### 7.2.2.1 The Propagation Loss of 4x9 $\mu$ m Core Straight Waveguide and Its Coupling Loss with Single Mode Fiber.

Except very short (0.3mm long) ends of the tapers, the rest of the waveguides used on the SWOMS (5~5.5mm long) have a core size of 4 $\mu$ m wide and 9 $\mu$ m deep. The propagation loss in such core thus represents the propagation loss of the waveguide of the switch. In this test, four segments of straight waveguides with lengths of 0.49cm, 0.91cm, 1.81cm and 2.83cm cut from longer waveguides with 4x9 $\mu$ m core fabricated together with the waveguides used on the SWOMS are coupled with the fiber and the outputs are measured. For each length, 3 samples are tested. The setting for the measurement of the output is shown in Figure 7.14.

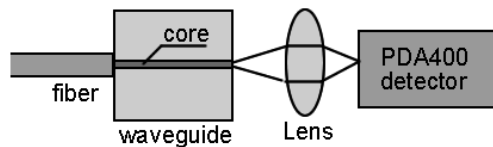


Figure 7.14: Setting for straight waveguide coupling with fiber.

After adjusting the positions of the waveguides for best coupling, the voltage outputs are measured and the losses are calculated. The results are listed in Table 7.1. The calculation process for sample 1 as an example is as following:

The voltage by the multimeter is 5.40V. Thus the output power is,

$$P_1 = 5.40V \div (1.5 \times 10^4 V/A) \div 0.9 A/W = 400 \mu W$$

## Chapter 7

## Test of the SWOMS

Consequently the loss is,

$$\text{Loss}_1 = 10 \times \log (P_r / P_1) = 10 \times \log (619\mu\text{W}/400\mu\text{W}) = 1.90\text{dB}$$

Sample NO	Sample length	Voltage measured	Average voltage	Optical power	Loss* (dB)	Average loss
1	0.49cm	5.40 V	5.32 V	400 $\mu$ W	1.90	1.96 dB
2		5.30 V		393 $\mu$ W	1.97	
3		5.26 V		390 $\mu$ W	2.01	
4	0.91cm	3.93 V	3.71 V	291 $\mu$ W	3.28	3.53 dB
5		3.79 V		281 $\mu$ W	3.43	
6		3.42 V		253 $\mu$ W	3.89	
7	1.81cm	1.96 V	1.87 V	145 $\mu$ W	6.30	6.51 dB
8		1.93 V		143 $\mu$ W	6.36	
9		1.71 V		127 $\mu$ W	6.88	
10	2.83cm	1.28 V	1.13 V	94.8 $\mu$ W	8.15	8.70 dB
11		1.10 V		81.5 $\mu$ W	8.81	
12		1.02 V		75.6 $\mu$ W	9.13	

\* Reference Power: 619 $\mu$ W

Table 7.1: Losses measured coupling single mode fiber with different lengths of straight waveguides with core size of 4x9 $\mu$ m.

Figure 7.15 compares the losses of samples with their lengths. The slope of the linear fit of the points represents the propagation loss, which is:

$$\text{Loss}_p = 2.88\text{dB}/\mu\text{m}$$

Comparing this value with the specified propagation loss of 0.3dB/cm of the polymer material when measured from slab waveguide at 1.55 $\mu$ m wavelength (see table 5.1), the main propagation loss we measured are attributed to the scattering loss due to sidewall roughness of the waveguides core formed during RIE process. A group using similar process and same material have measure the sidewall roughness to be 40~70nm. And by tweaking the RIE process, such as changing pressure and using N<sub>2</sub>/O<sub>2</sub> plasma instead of pure O<sub>2</sub> plasma, the side wall roughness can be reduced [108]. Thus it is possible to reduce the propagation loss in our waveguides, and this issue need to be further investigated.

In the figure where the sloppy line intersecting with the vertical axis, the value there is the coupling loss between the single mode fiber and the  $4 \times 9 \mu\text{m}$  core waveguide:

$$\text{Loss}_{\text{cl}} = 0.83 \text{ dB}$$

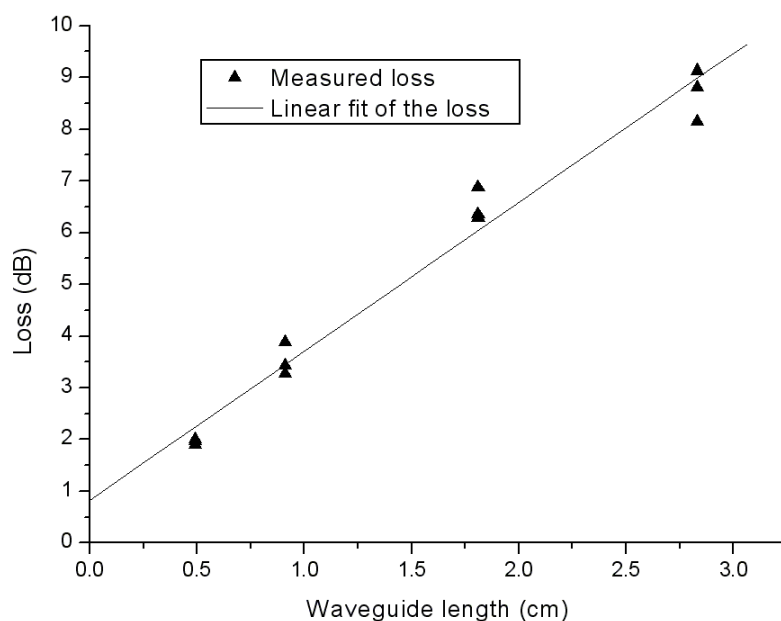


Figure 7.15: Measured Loss VS Waveguide length when coupling single mode fiber with straight waveguides with core size of  $4 \times 9 \mu\text{m}$ .

### 7.2.2.2 Effect of the Taper on Fiber Coupling

In the simulation of the waveguides, we found that using larger waveguide core to couple light with the fiber and a taper to shrink the core size when a bend is needed can significantly reduce the total loss of the waveguide. Here we use the fabricated tapered core to verify if it couples better with the fiber. The larger end of the taper has a width of  $11 \mu\text{m}$  while thinner end has a width of  $4 \mu\text{m}$ . The depth of the core is  $9 \mu\text{m}$  and length is about  $0.3 \text{ mm}$ . The setting for this measurement is shown in Figure 7.16.

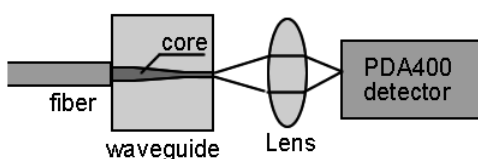


Figure 7.16: Setting for tapered core waveguide coupling with fiber.

After adjusting the position of the waveguide for best coupling, the voltage measured by the multimeter is 8.06V. Thus the output power is,

$$P_2 = 8.06V \div (1.5 \times 10^4 V/A) \div 0.9 A/W = 597 \mu W$$

And the loss is,

$$\text{Loss}_2 = 10 \times \log (P_r / P_2) = 10 \times \log (619 \mu W / 597 \mu W) = 0.16 \text{ dB}$$

Considering the existence of some propagation loss of the 0.03cm long waveguide, the coupling loss is smaller than 0.16dB. If using the value of 2.88dB/cm to calculate, the coupling loss of the fiber with 11x9 $\mu$ m core waveguide is:

$$\text{Loss}_{\text{cfw}} = 0.16 - 2.88 \times 0.03 = 0.07 \text{ dB/coupling}$$

Such a loss is much less than the 0.83dB that the 4x9 $\mu$ m straight core coupling with the fiber, indicating that the improvement brought by the taper is significant. The improvement verified the conclusion we formerly made using computer simulation. In both the 4 $\mu$ m straight core and the tapered core cases, the coupling losses measured include the Fresnel loss and loss due to field mismatch of fiber and waveguide. As the immersion oil was applied in the tests the Fresnel loss should be nearly the same zero in both cases, the reduction of the coupling loss with tapered core is certainly because of the reduction of field mismatch.

### 7.2.2.3 Loss Due to Intersections

60° intersections are used in the waveguides of the SWOMS. Three samples are used to measure the loss due to such intersections. One sample is a 0.49cm long straight waveguide with five 60° intersections on it, as shown in Figure 7.17. The second sample has a length of 0.91cm with seven intersections on it, and the third sample has a length of 2.83cm with ten intersections. The core size of all the waveguides are 4x9 $\mu$ m. Comparing their loss with the same lengths straight waveguides without intersections, we can have the value of the loss due to the intersection. The results are listed in Table 7.2.



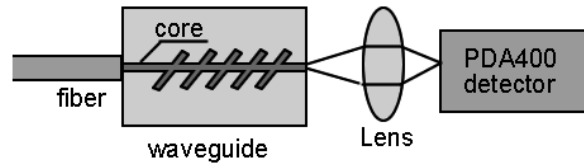


Figure 7.17: Setting for measurement of the intersection loss.

NO	length (cm)	Intersection number	Measured voltage (V)	Reference voltage (V)	Loss per intersection (dB)	Average Loss per intersection
1	0.49	5	4.87	5.32	0.077	0.10 dB
2	0.91	7	3.34	3.71	0.084	
3	2.83	10	0.84	1.13	0.129	

Table 7.2: Loss measurement of 60° intersections.

As an example of the calculation, for sample 1 the measured voltage is 4.87 V. Comparing this with the average voltage 5.32V measured for 0.49 cm long straight waveguides as listed in table 7.1, the loss per intersection is calculated as:

$$\text{Loss}_{i1} = 1/5 \times 10 \times \log (5.32/ 4.87) = 0.077\text{dB}$$

The losses per intersection calculated from the three samples are close to each other. And their average value is adopted as loss per 60° intersection:

$$\text{Loss}_i = 1/3 (\text{Loss}_{i1} + \text{Loss}_{i2} + \text{Loss}_{i3}) = 0.10\text{dB/intersection}$$

With similar processes, losses due to 30°, 45°, and 90° intersections are also measured. The results are illustrated in Figure 7.18. The BPM simulated results from Chapter 5 are also listed in the figure for comparison. The measured losses are higher than the simulated values, which might caused by the round corners formed during fabrication process, especially for shape angles like 30° and 45°. More over the relative large variation of propagation loss may result in an overestimation of the actual loss due to the intersections.

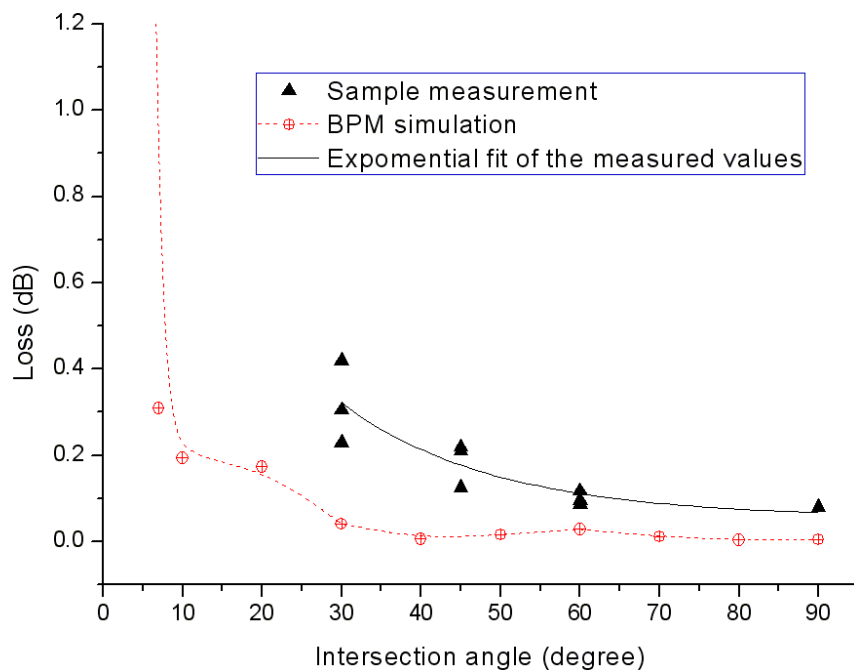


Figure 7.18: Loss measured per intersection at different angles.

#### 7.2.2.4 Bending Loss of the Polymer Waveguides

A series of 90° bends with radius from 500μm to 3000μm were fabricated together with the waveguides used on the SWOMS and have the same core size of 4x9μm. The setting for loss measurement is shown in Figure 7.19. After the measurement, the total loss for each bend was calculated. Then the bending loss was calculated by subtracting the coupling loss and the propagation loss according to its length. The resulting measured bending losses for all the radii are illustrated in Figure 7.20.

The measured values fit with an exponential decay curve although the measurement has a limited precision (as evidenced with the non-physical “negative” loss values obtained for some radii) due to the higher scattering loss. The bending losses are well below 0.5dB when the radii are above 1200μm. And the measured results agree with our analytical calculation and BPM simulation, as also shown in the figure.

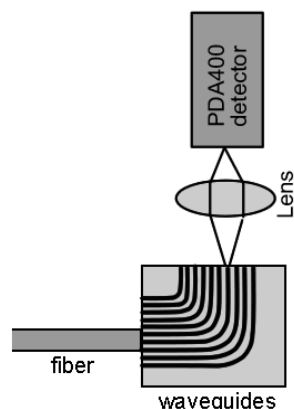


Figure 7.19: Setting for the bending loss measurement.

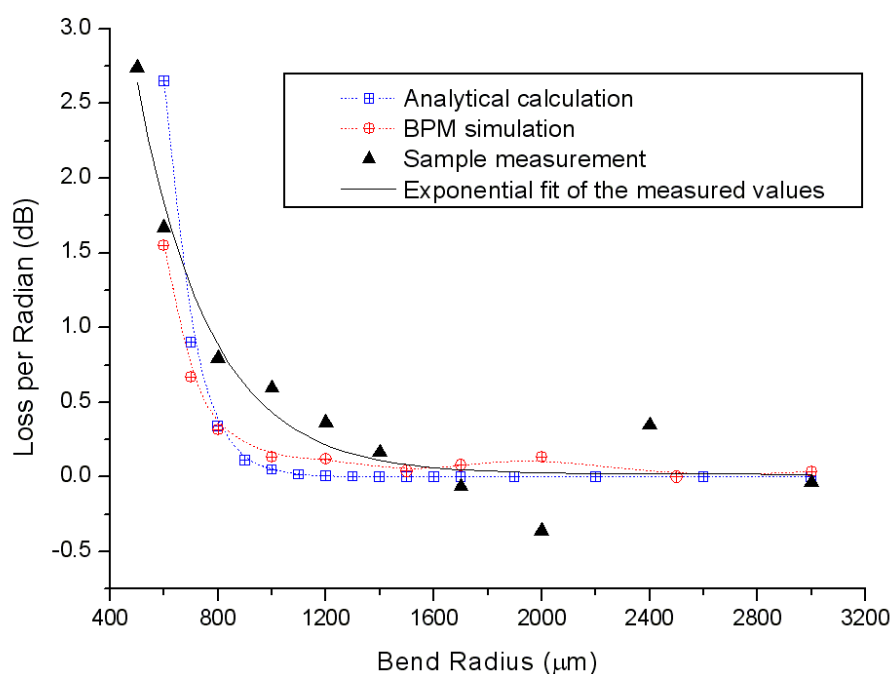


Figure 7.20: The bending loss measured for the polymer waveguide bends with different radii.

### 7.2.2.5 Coupling Loss Between $4 \times 9 \mu\text{m}$ core Waveguides

In this test, two pieces of waveguides mounted on two 3 axis stage are coupled to measure the coupling loss, as shown in Figure 7.20. The length of the waveguide 1 is 0.91cm, while the length of the waveguide 2 is 0.49cm. Firstly the waveguide 1 is adjusted to best coupling with the fiber, and the current of the laser diode is adjusted

until the output from the waveguide 1 is measured as 8.00V. Then the waveguide 2 is moved to couple with waveguide 1. Three samples of the waveguide 2 are measured. After adjusting to best coupling, the output voltages from the three samples are recorded as in Table 7.3. Considering the propagation loss using 2.88dB/cm for the waveguides, for sample 1 the coupling loss between the 4x9 $\mu$ m core waveguides can be calculated as:

$$\text{Loss}_{\text{cww1}} = 10 \times \log (8.00 \div 5.56) - 0.49 \times 2.88 = 0.17 \text{ dB}$$

And the average coupling loss of the three samples is

$$\text{Loss}_{\text{cww}} = 0.19 \text{ dB/coupling}$$

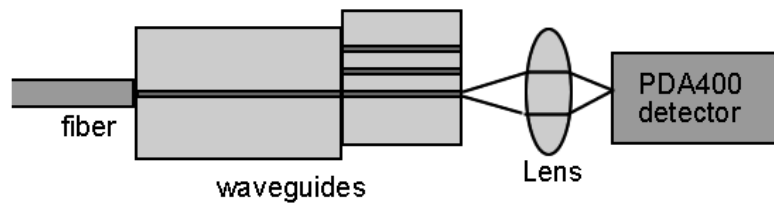


Figure 7.20: Setting for measurement of waveguide/waveguide coupling loss.

NO	Sample length (cm)	Reference voltage (V)	Measured voltage (V)	Coupling loss (dB)	Average coupling loss
1	0.49	8.00	5.56	0.17	0.19 dB
2			5.67	0.08	
3			5.38	0.31	

Table 7.3: Coupling loss measured between waveguides with core size of 4x9 $\mu$ m

#### 7.2.2.6 Propagation Loss and Crosstalk of the Waveguides Used on the SWOMS

Two waveguide samples are used in this test, and each sample contains the four waveguides used on the SWOMS, numbered as waveguide 1, 2, 3, and 4, as illustrated in Figure 7.21. Coupling these waveguides with the single mode fiber, the

outputs are recorded in Table 7.4.

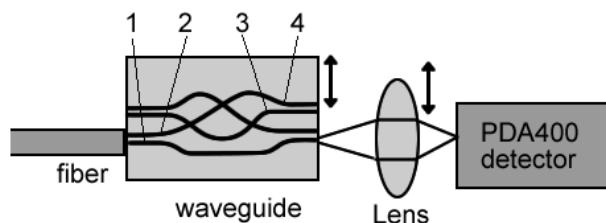


Figure 2.21: Setting for the test of waveguides used on the SWOMS

Wave-guide NO	Length (cm)	Bend (rad)	Inter-section amount	Sample NO	Measured voltage* (V)	Loss (dB)	Average loss (dB)	Propagation loss (dB)
1	0.47	1.61	0	1	5.05	2.19	2.21	1.38
				2	5.02	2.22		
2	0.49	1.85	2	1	4.37	2.82	2.72	1.89
				2	4.58	2.61		
3	0.48	2.09	2	1	4.71	2.49	2.43	1.60
				2	4.84	2.37		
4	0.49	1.85	2	1	4.14	3.05	2.86	2.03
				2	4.53	2.66		

\*Reference input voltage: 8.36V

Table 7.4: Loss measurement of the waveguides used on the SWOMS

Comparing the average losses in the table and also with the average loss (1.96dB) of 0.49cm long straight waveguides, their differences can be well explained with our former characterizations of the waveguides. For instance, waveguide 1 has  $2.21 - 1.96 = 0.25\text{dB}$  more loss than the straight waveguide, which is mainly attribute to the 1.61rad bend in waveguide 1. Waveguide 3 has  $2.43 - 2.21 = 0.22\text{dB}$  more loss than waveguide 1, which is because waveguides 3 has two  $60^\circ$  intersections and more total bending angle.

In Section 7.2.2.4 we've roughly measured the bending losses at different radii. Using the results here we can characterize the bends used on the SWOMS more precisely. All the bends used on the SWOMS have radius between  $1600 \sim 2500\mu\text{m}$ . From our former characterization the bends with radius in this range have similar low bending loss. Here we treat them as have same loss per radian. The results are listed in Table

7.5. An example calculation process for waveguide No 3 is as following,

$$\begin{aligned} \text{Loss}_3 &= ((2.43\text{dB}-1.96\text{dB}) - (0.48-0.49)\times 2.88\text{dB/cm} - 2\times 0.1\text{dB/intersection})\div 2.09\text{rad} \\ &= 0.14 \text{ dB/rad} \end{aligned}$$

The average bending loss per radian is:

$$\text{Loss}_{\text{bpr}} = 0.25 \text{ dB/rad}$$

Wave-guide NO	Length (cm)	Bend (rad)	Inter-section amount	Loss (dB)	Bending loss (dB)	Bending loss per radian (dB/rad)	Average bending loss per radian
0	0.49	0	0	1.96			0.25
1	0.47	1.61	0	2.21	0.31	0.19	
2	0.49	1.85	2	2.72	0.56	0.30	
3	0.48	2.09	2	2.43	0.30	0.14	
4	0.49	1.85	2	2.86	0.70	0.38	

Table 7.5: Characterization of bending loss of the waveguides used in the SWOMS

The same test setting is also used to measure the crosstalk of the waveguides. When one waveguide is coupled with the fiber, the lens is moved to measure the output from other waveguides. As far as we've tried, the maximum crosstalk voltage measured is 0.001V which is the minimum resolution of our sensor, and thus only allowed us to find the upper limit of the crosstalk. Comparing to an (e.g. 4.84V) output from waveguide 3, we have:

$$\text{Crosstalk} < 10\times\log(0.001\div 4.84) = -36.8\text{dB}$$

### 7.2.3 Estimation and Analysis of Total Insertion Loss of the SWOMS

The loss in waveguide devices is generally attributable to three different factors: scattering loss, radiation loss, and coupling loss. Scattering loss is caused by imperfections of the waveguide material and waveguide surface irregularities and

roughness. In our case, the polymer waveguides has a characterized scattering loss of 2.88dB/cm which mainly due to side wall roughness of the core.

The radiation loss mainly comes from the bending loss and the loss at waveguide intersection. Using bends with radius of 1600~2500 $\mu$ m, the bending loss has measured to be about 0.25 dB/rad. The loss due to the 60° intersection used is characterized to be 0.10dB/intersection.

The other loss of the device comes from the coupling loss. There are four couplings in the 2×2 SWOMS: two fiber/waveguide couplings and two waveguide/waveguide coupling. The two main source of coupling loss are reflection (called Fresnel loss) and the loss caused by the mismatch between fiber and waveguide modes. The Fresnel loss can be calculated by [70]:

$$L_F = -10 \log(1 - (\frac{n_1 - n_2}{n_1 + n_2})^2)$$

If air gap exists between the coupling waveguides, the Fresnel loss from waveguide to air is 0.18dB as calculated. However, the Fresnel loss is greatly reduced by using index matching oil. By using tapers to couple with fiber, the field mismatch is also significantly reduced. A fiber/waveguide coupling loss of 0.07dB/coupling and waveguide/waveguide coupling loss of 0.19dB/coupling have been measured.

With the above characterization of the waveguides, the total inserting loss of the SWOMS is estimated in Table 7.6 to be 2.45~2.82dB, which is comparable to the 2D MEMS switches (1.7dB to 3.1dB) [71].

In our former 3D-BPM simulation, we obtained a total loss of 0.428dB. However, the simulation hasn't included the scattering loss, and the coupling loss caused by the imperfection of the coupling surfaces and the alignment error because of the fabrication process.

From the table we can see that currently the loss of the device is mainly due to scattering loss caused by side wall roughness. By fine tune the fabrication process or

design shorter waveguides, this part of loss can be reduced.

Loss components	Loss characterized	Parameters of the SWOMS	Estimated loss of the SWOMS
Scattering loss	2.88dB/cm	0.53~0.55cm	1.53~1.58dB
Bending loss	0.25dB/rad	1.61~2.09rad	0.40~0.52dB
Intersection loss	0.10/intersection	0~2intersections	0~0.20dB
Fiber/waveguide Coupling loss	0.07dB/coupling	2 couplings	0.14dB
Waveguide/waveguide coupling loss	0.19dB/coupling	2 coupling	0.38dB
<b>Total</b>			<b>2.45~2.82dB</b>

Table 7.6: Loss components and the estimated values

So far the losses of the four waveguides are not uniform (15~20% difference), which is attribute to design differences of these waveguides, e.g. different total length, different bending angle, without or without intersections. With more optimized design, the loss uniformity can be further improved.

### 7.3 Summary of the Tests

In this chapter we tested the electro-mechanical properties of the bi-stable actuator and optical properties of the polymer waveguides. The spring structure was manually assembled using probe stage. The latching mechanism works well and the Fork Hinge behaves as predicted. The actuator has an operating voltage of 36V, and a switching speed below 0.5ms.

The 2x2 optical switching functionality by moving waveguides was finally established. The waveguides was characterized to have an attenuation of 2.88dB/cm. The bending losses with different radii were measured and the result agrees with our former calculation and simulation. For the bends of 1600~2500 $\mu$ m used on the switch the bending loss was measured as 0.25dB/rad. The losses due to intersections with



different angles were measured, and the  $60^\circ$  intersections used on the switch was characterized to have a loss of 0.10dB/intersection. The tapered waveguide structure was proved to be effective for reducing the fiber/waveguide coupling loss from 0.83dB to 0.07dB. And a waveguide/waveguide coupling loss of 0.19dB/coupling was reached in the test. Finally, the waveguide switch can obtain a total inserting loss of 2.45~2.82dB and a crosstalk below -36.8dB.

The characterization of the waveguide also provided useful information for further improvement of the performance. E.g. the scattering loss plays a key role in the total loss, which can be reduced by fine-tuning the fabrication process to reduce sidewall roughness or design shorter waveguides.

## Chapter 8 Conclusions

### 8.1 Summary of the Report

In this report, we introduced a new bi-stable self-latching MEMS actuator after studying the current existing ones. Combining this device with moving polymer waveguide technology, we introduce a new  $2 \times 2$  all-optical switch named SWOMS, and compared the SWOMS with other optical switching technologies. We designed the MEMS actuator using analytical calculation and FEA simulation methods, especially focused on two novel MEMS structures: the Fork Hinge and the self-assembly spring. Using BPM method, we simulated and optimized the polymer waveguide design. Then we fabricated the device using micro machining, and invented some new technologies for micro fabrication, such as Layout controlled one-step dry etch and release of MEMS using deep RIE on SOI wafer, and a polymer-silicon structure assembly technique. Finally, we tested the device electro-mechanically and optically, characterized the polymer waveguides, and proved that the design and fabrication of SWOMS are successful.

### 8.2 Contributions

- Developed a novel bi-stable, self-latching MEMS actuator with a moveable stage that can be widely used in different applications. And studied the features of such device.
- Developed a novel micro Fork Hinge structure that can rotate a relatively large angle with no fiction. Such structure can be used in many MEMS applications where a quasi-hinge is needed.

- Developed a novel spring structure for MEMS applications. Such a spring can reach a pre-compressed status by a simple micro assembly step using a lock structure.
- Introduced the Gap-reduction concept to the MOEMS optical switches based on moving waveguides by really moving the waveguides instead of only bend them as in former approaches. This feature decreased the insertion loss and improved the loss uniformity of such devices.
- Developed a novel all-optical switch named SWOMS based on above technologies. The switch broke through the limitation that switches with moving waveguides can only build  $1 \times N$  unit. A  $2 \times 2$  SWOMS unit was designed that greatly increased the scalability of this kind of switch.
- Polymer waveguides are used for the switch. With the process of simulation, optimization, fabrication, and testing the polymer waveguides, precious experience has been gained for using polymer waveguide on optical telecommunication system.
- Developed a layout controlled one-step dry etch and release technology for MEMS devices using deep RIE on SOI wafer. By removing the stiction problem, this technology allowed to design complicated micro devices with relatively large size on SOI wafer.
- Introduced a polymer to silicon structure assembly technique which allows the silicon structure and polymer structure to be fabricated using their own optimized process separately before assembly and a final dry etch step.
- Successfully designed, fabricated, and tested the  $2 \times 2$  optical switch based on the bi-stable actuator and polymer waveguides. With further developing, the switch can find a role in optical communication applications such as small scale OXCs, add-drop switch, or for protection, restoration, and provisioning.

### 8.3 Directions for Further Developing

Although a lot of hard tasks have been accomplished for the research on the topic of self-latching MEMS devices with moving polymer waveguides for optical telecommunication, the end of this report is no more than the beginning of a journey. We list here some directions for further development,

- Improve the design of the actuator, increase its fabrication tolerance and yield.
- Try different material and fabrication process to ease the fabrication and reduce the cost.
- Further improve the design, fabrication and assembly of the polymer waveguides
- Develop different sizes of switch. For example  $1 \times 2$ ,  $2 \times 2$ ,  $1 \times 4$ ,  $4 \times 4$ ,  $1 \times N$ , and  $N \times N$  to verify the scalability of the SWOMS.
- Design suitable electrical circuit to work with SWOMS and integrate them together.
- Develop suitable packaging method for the switch, thoroughly test the switch, and further more, commercialize it.
- Use the bi-stable self-latching device on other applications. The self-latching device can find many other promising applications such as switches, valves, sensors, memory cells, logic elements, or configuration elements.

## Appendix A: Calculation Programs for Maple 7

### Calculation of the Fork Hinge

> **restart;**

give s=10um

> **s:=10e-6;**

$s := .000010$

> **del:= diff(w(x),x,x)=(m1-fla\*(L1-x)+flb\*(-w(x)))/(E45\*i);**

$$\text{del} := \frac{\partial^2}{\partial x^2} w(x) = \frac{m1 - fla(L1 - x) - flb w(x)}{E45 i}$$

>

> **dsolve({del, w(0)=0,D(w)(0)=0},w(x));**

$$w(x) = -\frac{\sin\left(\frac{\sqrt{flb} x}{\sqrt{E45} \sqrt{i}}\right) fla \sqrt{E45} \sqrt{i} - \cos\left(\frac{\sqrt{flb} x}{\sqrt{E45} \sqrt{i}}\right) (-fla L1 + m1)}{flb^{(3/2)}} - \frac{\cos\left(\frac{\sqrt{flb} x}{\sqrt{E45} \sqrt{i}}\right) (-fla L1 + m1)}{flb} + \frac{(-L1 + x) fla + m1}{flb}$$

>

**ww:=-sin(1/E45^(1/2)/i^(1/2)\*flb^(1/2)\*x)\*fla\*E45^(1/2)\*i^(1/2)/flb^(3/2)-cos(1/E45^(1/2)/i^(1/2)\*flb^(1/2)\*x)\*(-fla\*L1+m1)/flb+((-L1+x)\*fla+m1)/flb;**

$$ww := -\frac{\sin\left(\frac{\sqrt{flb} x}{\sqrt{E45} \sqrt{i}}\right) fla \sqrt{E45} \sqrt{i} - \cos\left(\frac{\sqrt{flb} x}{\sqrt{E45} \sqrt{i}}\right) (-fla L1 + m1)}{flb^{(3/2)}} - \frac{\cos\left(\frac{\sqrt{flb} x}{\sqrt{E45} \sqrt{i}}\right) (-fla L1 + m1)}{flb} + \frac{(-L1 + x) fla + m1}{flb}$$

> **diff(%,x);**

$$-\frac{\cos\left(\frac{\sqrt{flb} x}{\sqrt{E45} \sqrt{i}}\right) fla}{flb} + \frac{\sin\left(\frac{\sqrt{flb} x}{\sqrt{E45} \sqrt{i}}\right) (-fla L1 + m1)}{\sqrt{E45} \sqrt{i} \sqrt{flb}} + \frac{fla}{flb}$$

>

**thetatheta:=-cos(1/E45^(1/2)/i^(1/2)\*flb^(1/2)\*x)/flb\*fla+sin(1/E45^(1/2)/i^(1/2)\*flb^(1/2)\*x)/E45^(1/2)/i^(1/2)/flb^(1/2)\*(-fla\*L1+m1)+1/flb\*fla;**

$$\text{thetatheta} := -\frac{\cos\left(\frac{\sqrt{flb} x}{\sqrt{E45} \sqrt{i}}\right) fla}{flb} + \frac{\sin\left(\frac{\sqrt{flb} x}{\sqrt{E45} \sqrt{i}}\right) (-fla L1 + m1)}{\sqrt{E45} \sqrt{i} \sqrt{flb}} + \frac{fla}{flb}$$

## Appendix

&gt;

```
eq1:=omega=-sin(1/E45^(1/2)/i^(1/2)*f1b^(1/2)*x)*f1a*E45^(1/2)*i^(1/2)/f1b^(3/2)-cos(1/E45^(1/2)/i^(1/2)*f1b^(1/2)*x)*(-f1a*L1+m1)/f1b+((-L1+x)*f1a+m1)/f1b;
```

$$eq1 := omega = -\frac{\sin\left(\frac{\sqrt{f1b} x}{\sqrt{E45} \sqrt{i}}\right) f1a \sqrt{E45} \sqrt{i}}{f1b^{(3/2)}} - \frac{\cos\left(\frac{\sqrt{f1b} x}{\sqrt{E45} \sqrt{i}}\right) (-f1a L1 + m1)}{f1b} + \frac{(-L1 + x) f1a + m1}{f1b}$$

&gt;

```
eq2:=theta=-cos(1/E45^(1/2)/i^(1/2)*f1b^(1/2)*x)/f1b*f1a+sin(1/E45^(1/2)/i^(1/2)*f1b^(1/2)*x)/E45^(1/2)/i^(1/2)/f1b^(1/2)*(-f1a*L1+m1)+1/f1b*f1a;
```

$$eq2 := \theta = -\frac{\cos\left(\frac{\sqrt{f1b} x}{\sqrt{E45} \sqrt{i}}\right) f1a}{f1b} + \frac{\sin\left(\frac{\sqrt{f1b} x}{\sqrt{E45} \sqrt{i}}\right) (-f1a L1 + m1)}{\sqrt{E45} \sqrt{i} \sqrt{f1b}} + \frac{f1a}{f1b}$$

&gt; eq3:=E45=129.5e9;

$$eq3 := E45 = .1295 \cdot 10^{12}$$

&gt; eq4:=f1b=2\*sqrt(2)\*m1/s;

$$eq4 := f1b = 200000.0000 \sqrt{2} \cdot m1$$

&gt;

```
eq5:=0=-sin(1/E45^(1/2)/i^(1/2)*f1b^(1/2)*L1)*f1a*E45^(1/2)*i^(1/2)/f1b^(3/2)-cos(1/E45^(1/2)/i^(1/2)*f1b^(1/2)*L1)*(-f1a*L1+m1)/f1b+(m1)/f1b;
```

$$eq5 := 0 = -\frac{\sin\left(\frac{\sqrt{f1b} L1}{\sqrt{E45} \sqrt{i}}\right) f1a \sqrt{E45} \sqrt{i}}{f1b^{(3/2)}} - \frac{\cos\left(\frac{\sqrt{f1b} L1}{\sqrt{E45} \sqrt{i}}\right) (-f1a L1 + m1)}{f1b} + \frac{m1}{f1b}$$

&gt; eq6:=i=1/12\*30e-6\*2.0e-6^3;

$$eq6 := i = .2000000000 \cdot 10^{-22}$$

&gt; solve(eq5,f1a);

$$-\frac{m1 f1b^{(3/2)} \left( \cos\left(\frac{\sqrt{f1b} L1}{\sqrt{E45} \sqrt{i}}\right) - 1 \right)}{\sin\left(\frac{\sqrt{f1b} L1}{\sqrt{E45} \sqrt{i}}\right) \sqrt{E45} \sqrt{i} f1b - \cos\left(\frac{\sqrt{f1b} L1}{\sqrt{E45} \sqrt{i}}\right) f1b^{(3/2)} L1}$$

&gt; eq7:=f1a=eval(solve(eq5,f1a),[eq4,eq3,eq6]);

## Appendix

$$eq7 := f1a = -.8944271910 \cdot 10^8 \cdot mI (\sqrt{2} \cdot mI)^{(3/2)} (\cos(.2778850071 \cdot 10^9 \sqrt{\sqrt{2} \cdot mI} \cdot LI) - 1) \\ / (.3218695388 \sin(.2778850071 \cdot 10^9 \sqrt{\sqrt{2} \cdot mI} \cdot LI) \sqrt{2} \cdot mI \\ - .8944271910 \cdot 10^8 \cos(.2778850071 \cdot 10^9 \sqrt{\sqrt{2} \cdot mI} \cdot LI) (\sqrt{2} \cdot mI)^{(3/2)} LI)$$

&gt;

```
eval(-cos(1/E45^(1/2)/i^(1/2)*f1b^(1/2)*x)/f1b*f1a+sin(1/E45^(1/2)
)/i^(1/2)*f1b^(1/2)*x/E45^(1/2)/i^(1/2)/f1b^(1/2)*(-f1a*L1+m1)+1
/f1b*f1a,[eq7,eq4,x=L1]);
```

$$223.6067978 \cos\left(447.2135955 \frac{\sqrt{\sqrt{2} \cdot mI} \cdot LI}{\sqrt{E45} \sqrt{i}}\right) \sqrt{2} (\sqrt{2} \cdot mI)^{(3/2)} \\ (\cos(.2778850071 \cdot 10^9 \sqrt{\sqrt{2} \cdot mI} \cdot LI) - 1) / ( \\ .3218695388 \sin(.2778850071 \cdot 10^9 \sqrt{\sqrt{2} \cdot mI} \cdot LI) \sqrt{2} \cdot mI \\ - .8944271910 \cdot 10^8 \cos(.2778850071 \cdot 10^9 \sqrt{\sqrt{2} \cdot mI} \cdot LI) (\sqrt{2} \cdot mI)^{(3/2)} LI) + \\ .002236067977 \sin\left(447.2135955 \frac{\sqrt{\sqrt{2} \cdot mI} \cdot LI}{\sqrt{E45} \sqrt{i}}\right) (.8944271910 \cdot 10^8 \cdot mI (\sqrt{2} \cdot mI)^{(3/2)} \\ (\cos(.2778850071 \cdot 10^9 \sqrt{\sqrt{2} \cdot mI} \cdot LI) - 1) LI / ( \\ .3218695388 \sin(.2778850071 \cdot 10^9 \sqrt{\sqrt{2} \cdot mI} \cdot LI) \sqrt{2} \cdot mI \\ - .8944271910 \cdot 10^8 \cos(.2778850071 \cdot 10^9 \sqrt{\sqrt{2} \cdot mI} \cdot LI) (\sqrt{2} \cdot mI)^{(3/2)} LI) + mI) / ( \\ \sqrt{E45} \sqrt{i} \sqrt{\sqrt{2} \cdot mI}) - 223.6067978 (\sqrt{2} \cdot mI)^{(3/2)} \\ (\cos(.2778850071 \cdot 10^9 \sqrt{\sqrt{2} \cdot mI} \cdot LI) - 1) \sqrt{2} / ( \\ .3218695388 \sin(.2778850071 \cdot 10^9 \sqrt{\sqrt{2} \cdot mI} \cdot LI) \sqrt{2} \cdot mI \\ - .8944271910 \cdot 10^8 \cos(.2778850071 \cdot 10^9 \sqrt{\sqrt{2} \cdot mI} \cdot LI) (\sqrt{2} \cdot mI)^{(3/2)} LI)$$

&gt;

```
thetab:=eval(-cos(1/E45^(1/2)/i^(1/2)*f1b^(1/2)*x)/f1b*f1a+sin(1/
E45^(1/2)/i^(1/2)*f1b^(1/2)*x)/E45^(1/2)/i^(1/2)/f1b^(1/2)*(-f1a*
L1+m1)+1/f1b*f1a,[eq7,eq6,eq3,eq4,x=L1]);
```

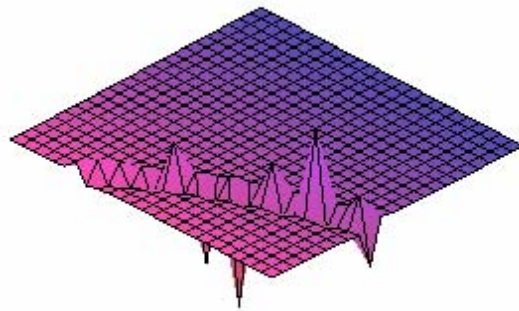
$$thetab := 223.6067978 \cos(.2778850071 \cdot 10^9 \sqrt{\sqrt{2} \cdot mI} \cdot LI) \sqrt{2} (\sqrt{2} \cdot mI)^{(3/2)} \\ (\cos(.2778850071 \cdot 10^9 \sqrt{\sqrt{2} \cdot mI} \cdot LI) - 1) / ( \\ .3218695388 \sin(.2778850071 \cdot 10^9 \sqrt{\sqrt{2} \cdot mI} \cdot LI) \sqrt{2} \cdot mI \\ - .8944271910 \cdot 10^8 \cos(.2778850071 \cdot 10^9 \sqrt{\sqrt{2} \cdot mI} \cdot LI) (\sqrt{2} \cdot mI)^{(3/2)} LI) + \\ 1389.425035 \sin(.2778850071 \cdot 10^9 \sqrt{\sqrt{2} \cdot mI} \cdot LI) (.8944271910 \cdot 10^8 \cdot mI (\sqrt{2} \cdot mI)^{(3/2)} \\ (\cos(.2778850071 \cdot 10^9 \sqrt{\sqrt{2} \cdot mI} \cdot LI) - 1) LI / ($$

## Appendix

```

.3218695388 sin(.2778850071 109 √√2 ml Ll) √2 ml
- .8944271910 108 cos(.2778850071 109 √√2 ml Ll) (√2 ml)(3/2) Ll + ml) /
√√2 ml - 223.6067978 (√2 ml)(3/2) (cos(.2778850071 109 √√2 ml Ll) - 1) √2
/ (.3218695388 sin(.2778850071 109 √√2 ml Ll) √2 ml
- .8944271910 108 cos(.2778850071 109 √√2 ml Ll) (√2 ml)(3/2) Ll)
>
> plot3d(thetab,L1=0..400e-6,m1=5e-10..3e-9);

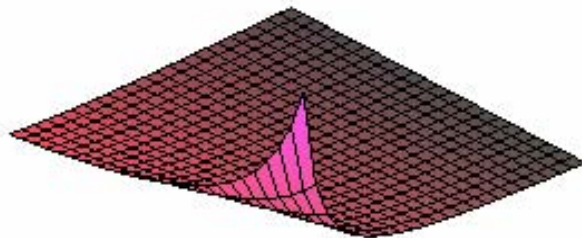
```



```

> plot3d(thetab,L1=0..410e-6,m1=5e-10..1.0e-9);

```

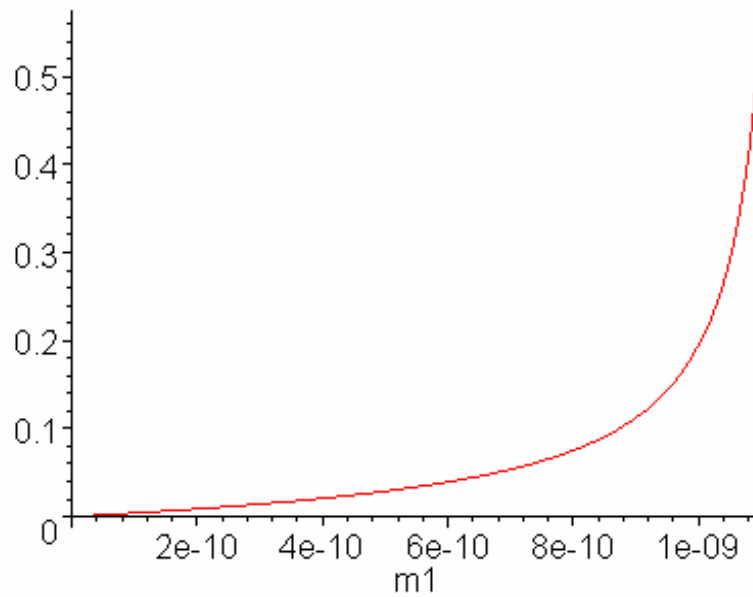


```

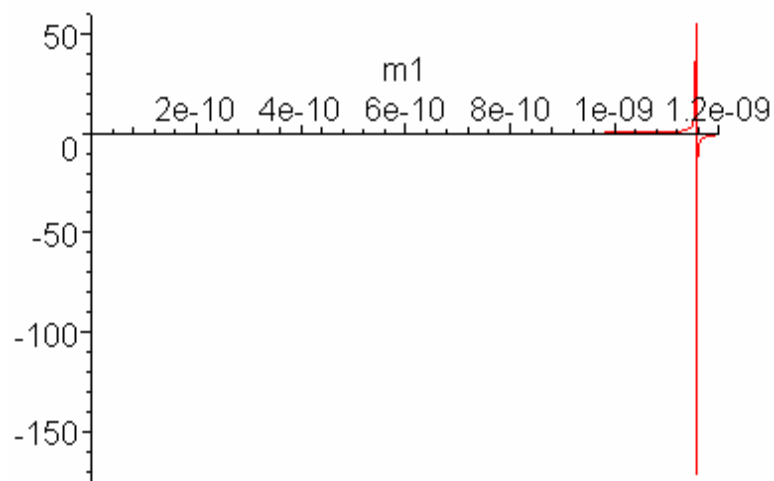
>
Fit L1
> plot(eval(thetab,L1=400e-6), m1=0..1.10e-9);

```

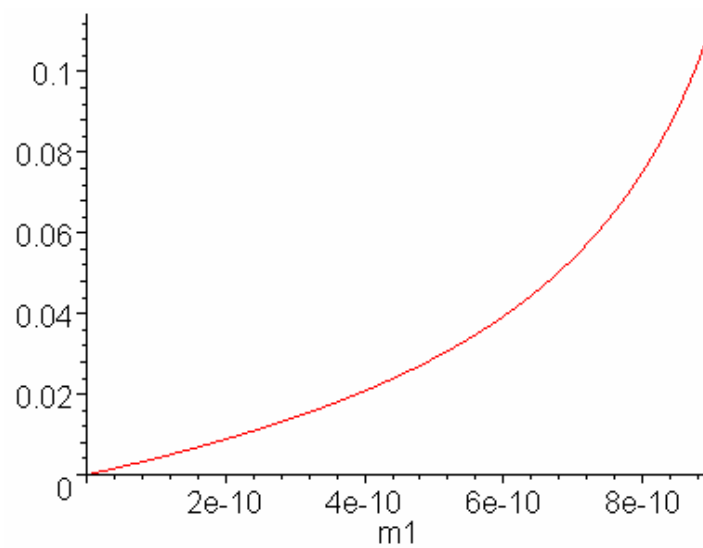




```
> plot(eval(thetab,L1=400e-6), m1=0..1.20e-9);
```

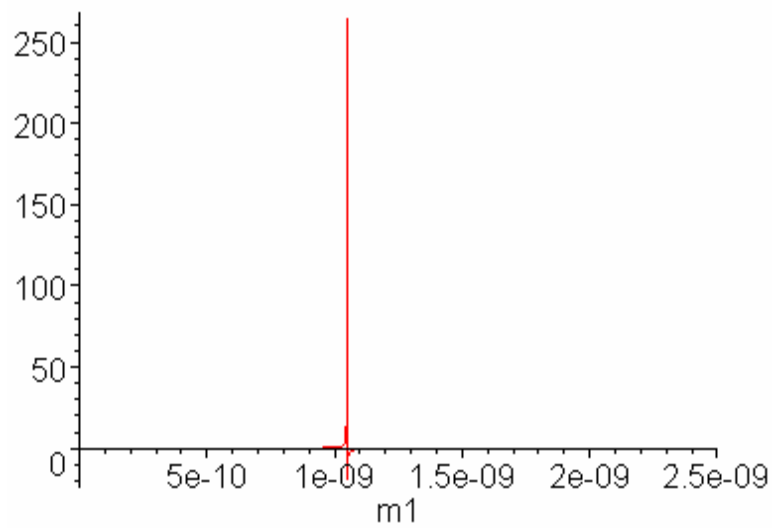


```
> plot(eval(thetab,L1=400e-6), m1=0..0.9e-9);
```

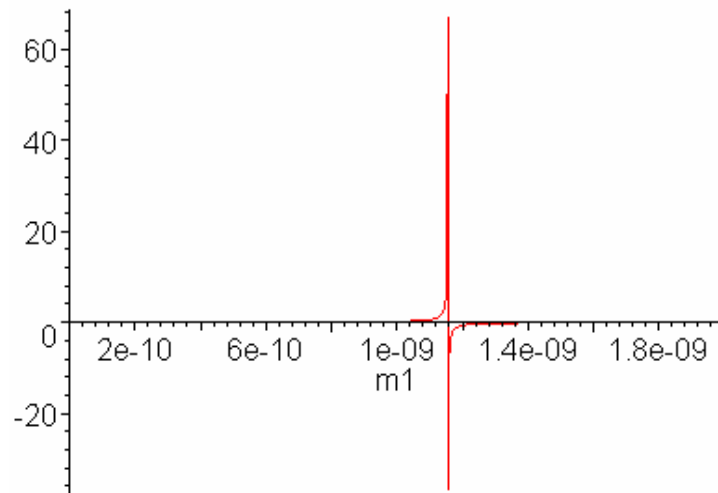


## Appendix

```
> plot(eval(thetab,L1=420e-6), m1=0..2.5e-9);
```



```
> plot(eval(thetab,L1=400e-6), m1=0..2.0e-9);
```



Fit L1=400e-6, thetab=0.10, get m1.      m1=

```
> L11:=400e-6;
```

$L11 := .000400$

```
> m11:=0.88e-9;
```

$m11 := .88 \cdot 10^{-9}$

```
> evalf(eval(thetab,[L1=L11,m1=m11]));
```

```
>
```

$.1026863968$

```
> thetab1:=0.1027;
```

$thetab1 := .1027$

```
> evalf(eval(eq7,[L1=L11,m1=m11]));
```

$f1a = .7077944429 \cdot 10^{-5}$

## Appendix

```
> flaa:=.7077944429e-5;
```

$$flaa := .7077944429 \cdot 10^{-5}$$

```
> pp:=4*m11/s;
```

$$pp := .0003520000000$$

```
> flbb:=evalf(2^(1/2)/2*pp);
```

$$flbb := .0002489015869$$

calculation the maximum moment on branch

```
>
```

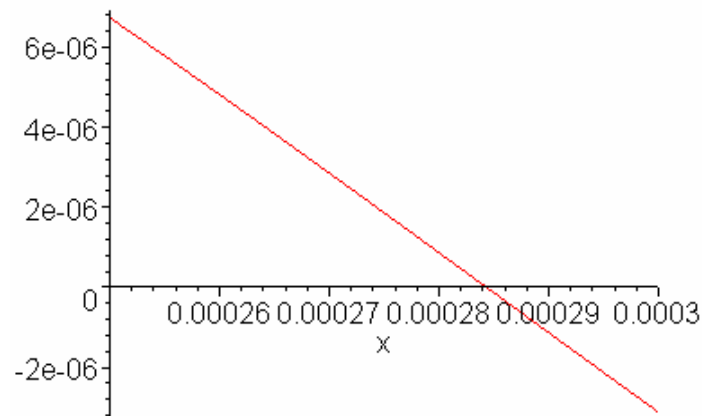
```
eq14:=fla-flb*(-cos(1/E45^(1/2)/i^(1/2)*flb^(1/2)*x)/flb*fla+sin(
1/E45^(1/2)/i^(1/2)*flb^(1/2)*x)/E45^(1/2)/i^(1/2)/flb^(1/2)*(-fl
a*L1+m1)+1/flb*fla);
```

$$eq14 := fla - flb \left( -\frac{\cos\left(\frac{\sqrt{flb} x}{\sqrt{E45} \sqrt{i}}\right) fla}{flb} + \frac{\sin\left(\frac{\sqrt{flb} x}{\sqrt{E45} \sqrt{i}}\right) (-fla L1 + m1)}{\sqrt{E45} \sqrt{i} \sqrt{flb}} + \frac{fla}{flb} \right)$$

```
> kk:=eval(eq14,[fla=flaa,flb=flbb,m1=m11,L1=L11,eq6,eq3]);
```

$$kk := .1 \cdot 10^{-14} + .7077944428 \cdot 10^{-5} \cos(9803.111687 x) \\ + .00001912761362 \sin(9803.111687 x)$$

```
> plot(kk,x=.00025..0.0003);
```



so that moment get maximum value when  $x=284\mu\text{m}$ .

```
> xmm:=284e-6;
```

$$xmm := .000284$$

```
>
```

```
wmm:=evalf(eval(wv,[fla=flaa,flb=flbb,m1=m11,L1=L11,eq6,eq3,x=xmm
]));
```

$$wmm := -.8121726612 \cdot 10^{-5}$$

## Appendix

```

>
>
mmax1:=evalf(eval(m1-f1a*(L1-xmm)-f1b*wmm,[f1a=f1aa,f1b=f1bb,m1=m
11,L1=L11,eq6,eq3]));

mmax1 := .2080469088 10-8

> h:=2.0e-6;

h := .20 10-5

> ii:=.2e-22;

ii := .2 10-22

> stressmax1:=mmax1*h/ii/2;

stressmax1 := .1040234544 109

calculate theta and R
> thetabb:=0.1027;

thetabb := .1027

> p:=pp;

p := .0003520000000

> E0:=168e9;

E0 := .168 1012

> i1:=ii;;

i1 := .2 10-22

> eqn1:=r*sin(theta)=s/2;

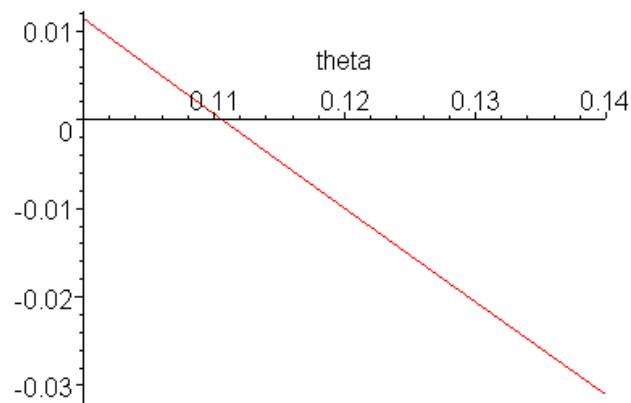
eqn1 :=  $r \sin(\theta) = .5000000000 10^{-5}$ 

>
curve1:=p*sin(theta)*((s/2)/sin(theta))^2/(3*E0*i1)+thetabb-theta
;

curve1 := .0008730158733  $\frac{1}{\sin(\theta)} + .1027 - \theta$ 

> plot(curve1,theta=0.1..0.14);

```



```
> theta1:=0.1106;
```

```
theta1 := .1106
```

```
> eval(curve1,theta=theta1);
```

```
.95683 10-5
```

```
> solve({eqn1,theta=theta1});
```

```
{r = .00004530025497, theta = .1106000000}
```

```
>
```

```
>
```

```
calculate gap
```

```
>
```

```
> EE45:=129.5e9;
```

```
EE45 := .1295 1012
```

```
>
```

```
eqg1:=0=eval(theta,theta,[f1a=f1aa,f1b=f1bb,m1=m11,L1=L11,eq6,eq3])
```

```
eqg1 := 0 = -.02843671877 cos(9803.111687 x) - .07684809832 sin(9803.111687 x) + .02843671877
```

```
> solve(eqg1,{x});
```

```
{x = 0.}, {x = .0002481626239}
```

```
> xm:=.2481626239e-3;
```

```
xm := .0002481626239
```

```
>
```

```
wm:=evalf(eval(ww,[f1a=f1aa,f1b=f1bb,m1=m11,L1=L11,eq6,eq3,x=xm]))
```

```
wm := -.8621376463 10-5
```

```
> xm2:=L11-xm;
```

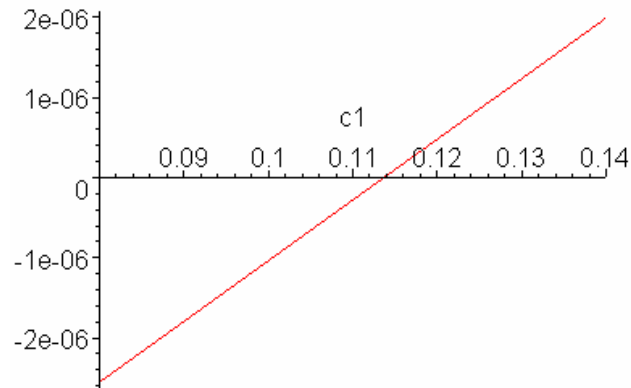
```
xm2 := .0001518373761
```

## Appendix

```
> eqq1:=xm2/c1*(1-cos(c1))+wm;
```

$$eqq1 := .0001518373761 \frac{1 - \cos(c1)}{c1} - .8621376463 \cdot 10^{-5}$$

```
> plot(eqq1, c1=0.08..0.14);
```



```
> c1:=0.114;
```

$$c1 := .114$$

```
> p1:=xm2/c1;
```

$$p1 := .001331906808$$

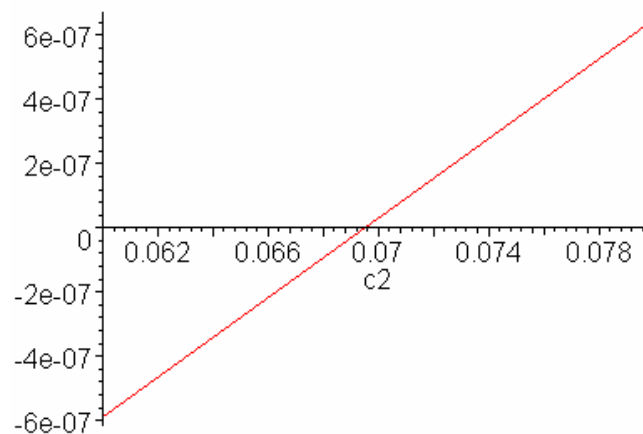
```
> dL1:=xm2-p1*sin(c1);
```

$$dL1 := .3286661 \cdot 10^{-6}$$

```
> eqq2:=xm/2/c2*(1-cos(c2))+wm/2;
```

$$eqq2 := .0001240813120 \frac{1 - \cos(c2)}{c2} - .4310688232 \cdot 10^{-5}$$

```
> plot(eqq2, c2=0.06..0.08);
```



```
> c2:=0.0695;
```

$$c2 := .0695$$

```
> p2:=xm/2/c2;
```

$$p2 := .001785342618$$

```

> dL2:=xm/2-p2*sin(c2);
                                      $dL2 := .998665 \cdot 10^{-7}$ 

> dL:=dL1+2*dL2;
                                      $dL := .5283991 \cdot 10^{-6}$ 

> rr:=".453e-4";
                                      $rr := .0000453$ 

> gap:=evalf(2*rr*(1-cos(theta1))+2*dL*sqrt(2));
                                      $gap := .2048099627 \cdot 10^{-5}$ 

>
>
>
>

```

## Latching force calculation

Latching force calculation

```

> restart;
> g:=2.0e-6;
                                      $g := .20 \cdot 10^{-5}$ 

> s0:=10e-6;
                                      $s0 := .000010$ 

> thetaa:=2*g/s0;
                                      $thetaa := .4000000000$ 

> ss:=s0/sin(thetaa);
                                      $ss := .00002567932456$ 

> theta:=s/ss;
                                      $\theta := 38941.83422 \text{ s}$ 

> ddy:=ss-(ss-g)/cos(theta);
                                      $ddy := .00002567932456 - \frac{.00002367932456}{\cos(38941.83422 \text{ s})}$ 

> Ks:=75;
                                      $Ks := 75$ 

> Y0:=6e-6;
                                      $Y0 := .6 \cdot 10^{-5}$ 

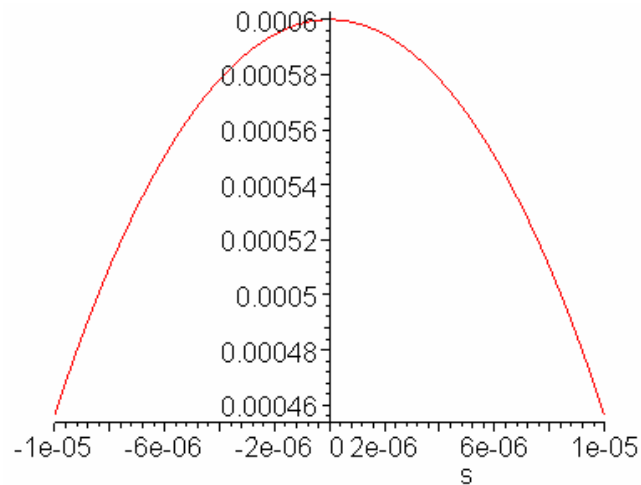
```

## Appendix

> **Fy:=Ks\*(Y0+ddy);**

$$Fy := .002375949342 - \frac{.001775949342}{\cos(38941.83422 s)}$$

> **plot(Fy,s=-10e-6..10e-6);**



calculate the moment of latching

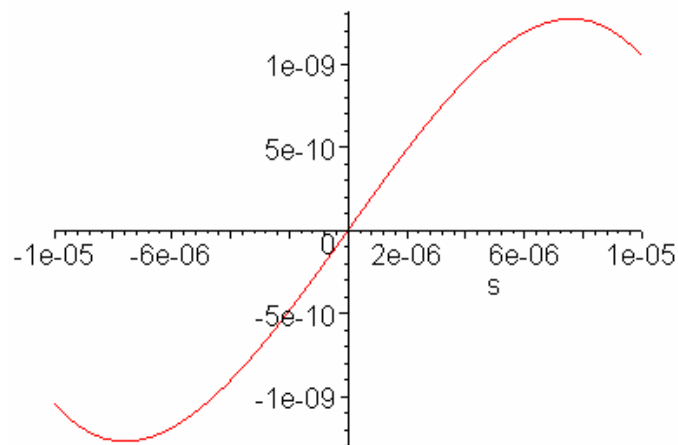
> **Ps:=352e-6;**

$$Ps := .000352$$

> **Ms:=(Fy-Ps)\*s;**

$$Ms := \left( .002023949342 - \frac{.001775949342}{\cos(38941.83422 s)} \right) s$$

> **plot(Ms,s=-10e-6..10e-6);**



The force needed

> **RR:=91e-6;**

$$RR := .000091$$

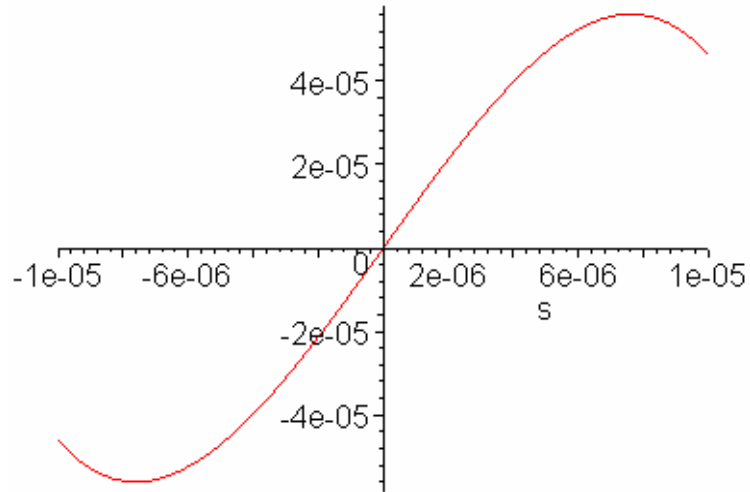
> **Fc:=4\*Ms/(RR\*cos(s/RR));**

$$Fc := 43956.04396 \frac{\left( .002023949342 - \frac{.001775949342}{\cos(38941.83422 s)} \right) s}{\cos(10989.01099 s)}$$



## Appendix

```
> plot(Fc, s=-10e-6..10e-6);
```



```
>  
>  
>  
>
```

## Appendix B: Steps and Options of the ANSYS FEA Simulation

### 1. Preference.

Individual disciplines to show in the GUI:     Structure.

Discipline Options:                             h-Method.

### 2. Preprocessor.

1). Element Type:             PLANE82.

Element behavior:     Plane stress with thickness.

2). Real Constants:     Thickness:     3e-005.

3). Material Props:

Material Models:

Density:             2330

Linear Isotropic:     Ex: 1.3e+011

PRXY: 0.17

4). Modeling:

Create:             Keypoints → Lines → Areas.

Operate:           Booleans:     Add.

5). Meshing:

Meshing Tool:     Mesh:             Areas.

Size Control:       0.5e-006

Shape:             Quad.

### 3. Solution.

1). Analysis Type:

Sol'n Controls:     Basic:

Analysis options: Large Displacement Static.

Time Control:             Numbers of Substeps:     10

2). Define Loads:

Apply:             Structural:             Displacement.

Force/Moment.

3). Solve:             Current LS.

### 4. General Postproc.

---

## Appendix

1). Plot Results: Contour Plot:

Nodal Solu: Von Mises Stress.

DOF Solution Translation UY.

2). Result Viewer: Query Results.

## Publication list

- 1 H. -B. Liu, F. Chollet, "Characterization of Latching 2x2 Optical Switch with Movable Polymer Waveguide", Transducers' 07.
- 2 H. Liu, F. Chollet, "Design and Fabrication of Latching Micro-opto-mechanical 2x2 Switch with Movable Polymer Waveguide", Asia Pacific Conference on Transducers, Nano Micro Technology (APCOT), 26-28 June 2006 (2006).
- 3 Liu Haobing, Franck Chollet, "Layout Controlled One-Step Dry Etch and Release of MEMS Using Deep RIE on SOI Wafer", IEEE/ASME Journal of MEMS, vol. 15, no. 3 (2006): 541- 547.
- 4 H. Liu, F. Chollet, "Micro Fork Hinge for MEMS Devices", Journal of Experimental Mechanics (special issue: 'Advance in Experimental Mechanics in Asia'), vol. 21, no. 1 (2006): 61-70.
- 5 HB. Liu, F. Chollet, "Design, Simulation and Fabrication of Polymer Waveguide Device for Micro Optical Switch", ICMAT conference, July 3-5, Singapore (2005).
- 6 H. Liu, F. Chollet, "Layout Design Rules for One-step Dry release and Non-stiction Wet Release of MEMS Using DRIE/SOI technology", International Conference on Solid State Sensors, Actuators and Microsystems (Transducers' 05), June 5-9, Seoul, Korea, vol. 2 (2005) : 1384-1387.
- 7 HB. Liu, F. Chollet, "Optical Switch Based on Moving Polymer Waveguides and Self-latching Structure", Int. J. of Computation. Eng. Sci., vol. 4, n. 3 (2003): 447-450.

## References

- [1] M. Fuller, All-optical-switch market revives...again, *Lightwave*, June, 2005.
- [2] S. Nagaoka, Compact latching type PANDA fiber switch, *IEEE photonics technology letters*, vol. 10, No. 2, Feb. 1998.
- [3] H. Toshiyoshi, H. Fujita, "Electrostatic Micro Torsion Mirrors for an Optical Switch Matrix", *IEEE J. Microelectromechanical Systems*, Vol. 5, pp. 231-237, (1996)
- [4] D. J. Bishop, C. R. Giles, G. P. Austin, The Lucent LambdaRouter: MEMS technology of the future here today, *IEEE Communications Magazine*, volume: 40, Issue: 3, March 2002, Page(s): 75 -79.
- [5] J. E. Frouquet, Compact optical cross-connect switch based on total internal reflection in a fluid-containing planar circuit, in *OFC 2000*, Baltimore, MD, Mar. 7-10, 2000.
- [6] E. Ollier and P. Mottier, Integrated electrostatic micro-switch for optical fiber networks driven by low voltage, *Electronics Letters*, Vol. 32, No. 21, 10<sup>th</sup>, October 1996.
- [7] K. Hattori, M. Fukui, M. Jinno, M. Oguma, K. Oguchi, PLC-based optical add/drop switch with automatic level control, *Journal of Lightwave Technology*, Volume: 17, Issue: 12, Dec. 1999, Page(s): 2562 –2571
- [8] H. Uetsuka, WDM optical components using PLCs, *Lasers and Electro-Optics*, 1999, CLEO/Pacific Rim '99. The Pacific Rim Conference on, Volume: 3, 1999, Page(s): 585 -586.
- [9] S. Sumriddetchkajorn, D. K. Sengupta, N. A. Riza, Self-aligning 2×2 fiber-optic switch using liquid crystals, *LEOS '99. IEEE Lasers and Electro-Optics Society 1999 12th Annual Meeting*, Volume: 1, 1999 Page(s): 135 -136.
- [10] W. A. Crossland, I. G. Manolis, M. M. Redmond, K. L. Tan, T. D. Wilkinson, M. J. Holmes, T. R. Parker, H. H. Chu, J. Croucher, V. A. Handerek, S. T. Warr, B. Robertson, I. G. Bonas, R. Franklin, C. Stace, H.J. White, R. A. Woolley, G. Henshall, Holographic optical switching: the "ROSES" demonstrator, *Journal of Lightwave Technology*, Volume: 18 Issue: 12, Dec 2000, Page(s): 1845 -1854.
- [11] R. Cooper, All-optical and OEO switching will unleash real network capacity, *WDM Solutions*, March 2001, pp.31-33.
- [12] P. F. Van Kessel, L. J. Hornbeck, R. E. Meier, M. R. Douglass, A MEMS-based projection display, *Proceedings of IEEE*, Vol. 85, No. 8, Aug. 1998.
- [13] M. Ruan, J. Shen, C.B. Wheeler, Latching micro magnetic relays with multistrip permalloy cantilevers, *Micro Electro Mechanical Systems*, 2001. The 14th IEEE International Conference on, 2001. Page(s): 224 –227.
- [14] S. Nagaoka, Y. Suzuki, Compact optomechanical switches and their applications in optical communication and testing systems, *Micro Electro Mechanical Systems*, 1997. MEMS '97, Proceedings, IEEE. Tenth Annual International Workshop on, 1997. Page(s): 366 –371.

## References

- [15] H. Hosaka, H. Kuwano, Design and fabrication of miniature relay matrix and investigation of electromechanical interference in multi-actuator systems, Micro Electro Mechanical Systems, 1994, MEMS '94, Page(s): 313 -318.
- [16] X-Q. Sun; K. R. Farmer, W. N. Carr, A bistable microrelay based on two-segment multimorph cantilever actuators, Micro Electro Mechanical Systems, 1998. Proceedings, The Eleventh Annual International Workshop on, 1998. Page(s): 154 –159.
- [17] H. Matoba, T. Ishikawa, C.-J. Kim, R. S. Muller, A bistable snapping microactuator, Micro Electro Mechanical Systems, 1994, Proceedings, IEEE Workshop on , 1994. Page(s): 45 –50.
- [18] B. Halg, On a nonvolatile memory cell based on micro-electro-mechanics Micro Electro Mechanical Systems, 1990. Proceedings, An Investigation of Micro Structures, Sensors, Actuators, Machines and Robots. IEEE , 1990. Page(s): 172 –176.
- [19] P. L. Bergstrom, T. Tamagawa, D. L. Polla, Design and fabrication of micromechanical logic elements, Micro Electro Mechanical Systems, 1990. Proceedings, An Investigation of Micro Structures, Sensors, Actuators, Machines and Robots. IEEE , 1990. Page(s): 15 –20.
- [20] J. E. Ford, J. A. Walker, Dynamic spectral equalization using micro-opto-mechanics, Broadband Optical Networks and Technologies: An Emerging Reality/Optical MEMS/Smart Pixels/Organic Optics and Optoelectronics. 1998 IEEE/LEOS Summer Topical Meetings, 1998. Page(s): I/9 -I10.
- [21] C. Marxer, M. A. Gretillat, N.F. de Rooij, R. Batig, O. Anthamatten, B. Valk, and P. Vogel, Reflective duplexer based on silicon micromechanics for fiber-optic communication, J. Lightwave Technol., Vol. 17, Jan. 1999.
- [22] P. Tayebati, P. Wang, M. Azimi, L. Malflah, and D. Vakhshoori, Microelectromechanical tunable filter with stable half symmetric cavity, Electron. Lett. Vol. 34, Oct. 1998.
- [23] T. Weyrauch, M. A. Vorontsov, T. G. Bifano, A. Tuantranont, V. M. Bright, J. Karpinsky, and J. Hammer, Performance evaluation of micromachined mirror arrays for adaptive optics, Proc. SPIE, Vol. 4124, 2000.
- [24] L.J. Hornbeck, Current status of the digital micromirror device (DMD) for projection television applications, Electron Devices Meeting, 1993. Technical Digest., International, 1993. Page(s): 381 -384.
- [25] L. Y. Lin, and E. L. Goldstein, Optical-layer networking: opportunities for and progress in lightwave micromachines, in OFC 2000, Baltimore, MD, Mar, 7-10, 2000.
- [26] C. Marxer, N. F. de Rooij, Micro-opto-mechanical 2×2 switch for single-mode fibers based on plasma-etched silicon mirror and electrostatic actuation, Journal of Lightwave Technology, Volume: 17 Issue: 1 , Jan. 1999. Page(s): 2 –6.
- [27] J-P. Faure, L. Noirie, E. Ollier, A 8x8 all optical space-switch based on a novel 8x1 MOEMS switching module, OFC'01
- [28] Y. W. Kim, M. G. Allen and N. F. Hartman, Proc. SPIE 1793, 183 (1992).
- [29] W. Lukosz, Proc. SPIE 1793, 214 (1992).
- [30] K. Fischer, J. Muller, R. Hoffmann, F. Wasse, D. Salle, Elastooptical properties of SiON layers in an integrated optical interferometer used as a

## References

- pressure sensor, *Journal of Lightwave Technology*, Volume: 12 Issue: 1, Jan. 1994. Page(s): 163 -169.
- [31] E. Ollier, p. Ohiippe, C. Chabrol, and P. Mottier, Micro-opto-mechanical vibration sensor integrated on silicon, *J. Lightwave Technology – Special Selection on MOEMS*, vol. 14, Jan. 1999.
- [32] S. Valette, *J. Modern Opt.* 35, 993, 1005, 1988
- [33] A. A. Boiarski, J. R. Bush, B. S. Bhullar, R. W. Ridgway, and V. E. wood, *Proc. SPIE* 1793,199 (1992).
- [34] M. Abraham, W. Ehferld, M. Lacher, O. Marti, K. Mayr, W. Noell, P. Gunther and J. Barrenz, *Proc. SPIE* 30999, 248 (1997).
- [35] K. Petroz, E. Ollier, H. Grateau, P. Mottier. Integrated silica micro-opto-mechanical steering device for laser beam scanning, *Sensors and Actuators*, Vol. 73, 1999.
- [36] M. Horino, K. Sato, T. Akashi, N. Komatsu, D. Kobayashi, Development of prototype micromechanical optical switch, in *JSME Int. J.*, ser. C, 1998, vol. 41, no. 4.
- [37] As recounted by A. Pisano in the foreword of N. Maluf, *An introduction to microelectromechanical systems engineering*. Boston: Artech House, 2000.
- [38] <http://www.mems-exchange.org/MEMS/what-is.html>, 21<sup>st</sup> August, 2002.
- [39] E. Ollier, Optical MEMS devices based on moving waveguides, *IEEE J. on selected topics in quantum electronics*, Vol. 8, No. 1, Jan./Feb. 2002.
- [40] <http://www.darpa.mil/MTO/MOEMS/index.html>, 21<sup>st</sup> August, 2002.
- [41] Jeff Hecht, *An introduction to optical networking*, WDM Solutions, January, 2002.
- [42] Tellium, *Optical Switches: Making Optical Networks a Brilliant Reality*, [http://www.iec.org/online/tutorials/opt\\_switch/](http://www.iec.org/online/tutorials/opt_switch/), 21st August, 2002.
- [43] B. Halg, On a micro-electro-mechanical nonvolatile memory cell, *Electron Devices*, *IEEE Transactions on*, Volume: 37 Issue: 10, Oct. 1990. Page(s): 2230 –2236.
- [44] D. J. Bishop, C. R. Giles, G. P. Austin, The Lucent LambdaRouter: MEMS technology of the future here today, *IEEE Communications Magazine*, Volume: 40 Issue: 3, March 2002. Page(s): 75 -79.
- [45] M. Hoffmann, P. Kopka, E. Voges, Bistable micromechanical fiber-optic switches on silicon *Broadband Optical Networks and Technologies: An Emerging Reality/Optical MEMS/Smart Pixels/Organic Optics and Optoelectronics*. 1998 IEEE/LEOS Summer Topical Meetings, 1998. Page(s): II/31 -II/32 .
- [46] B Jensen et al, Design of two-link, in plane, bistable compliant micro-mechanisms, *J Mech Design*, 121:3, 416-423, 1999.
- [47] E Kruglick et al, Bistable MEMS relays and contact characterization, *Proc SSSA Workshop*, 333-337, 1998.
- [48] T-W. Yoew, K. L. Eddie Law, A. Goldenberg, MEMS optical switches, *IEEE Communication Magazine*, November, 2001.
- [49] L. Y. Lin, E. L. Goldstein, MEMS for free-space optical switching, *LEOS '99. IEEE Lasers and Electro-Optics Society 1999 12th Annual Meeting*, Volume: 2, 1999. Page(s): 483 -484 vol.2.
- [50] M. Makihara, Microelectromechanical intersecting waveguide optical switch based on thermo-capillarity, *Optical MEMS*, 2000 IEEE/LEOS International

## References

- Conference on, 2000. Page(s): 33 –34.
- [51] M. Makihara, F. Shimokawa, K. Kaneko, Strictly nonblocking  $N \times N$  thermo-capillarity optical matrix switch using silica-based waveguide, in Tech. Dig. OFC2000, 2000, TuM2, pp. 207–209.
- [52] J. E. Fouquet, Technical Digest of OFC2000, PP. 204-206, 2000.
- [53] S. Nagaoka, Compact latching-type single-mode-fiber switches fabricated by a fiber-micromachining technique and their practical applications, Selected Topics in Quantum Electronics, IEEE Journal on, Volume: 5 Issue: 1, Jan.-Feb. 1999. Page(s): 36 -45.
- [54] S. Sohma, T. Goh, H. Okazaki, M. Okuno, A. Sugita, Low switching power silica-based super high delta thermo-optic switch with heat insulating grooves, Electronics Letters, Volume: 38 Issue: 3, 31 Jan. 2002. Page(s): 127 –128.
- [55] J.-C. Eloy, Status of the MEMS industry, Yole Développement (2002).
- [56] M. Zdeblick, Design variables prevent a single industry standard. Laser Focus World, March 2001.
- [57] J. R. Palmer, All-optical and OEO switches will share the load, WDM Solutions, March 2001.
- [58] Waterloo Maple Inc, Maple 7 help files. 2001.
- [59] Coventor Inc, CoventorWare Analyzer reference guide, page R1-1, march, 2001.
- [60] Fan Qinsan, Textbook for material mechanics (in Chinese), Higher education press. Beijing, China, 1995.
- [61] S. D. Senturia, Microsystem Design, Kluwer academic publishers, US, 2001.
- [62] G. Kovacs, Micromachined Transducers Sourcebook, WCB/McGraw-Hill, 1998.
- [63] M. Madou, Fundamentals of Microfabrication, Pg59, Pg412, CRC Press, 1997.
- [64] R. Legtenberg, A.W. Groeneveld, M. Elwenspoek, Comb-drive actuators for large displacements, J. Micromech. Microeng. P320-329, 6, 1996.
- [65] P. Pai-Choudhury, MEMS and MOEMS Technology and Applications. Pg268, SPIE Press, 2001.
- [66] T. Bakke, C. P. Tigges, J. J. Lean, C. T. Sullivan, O. B. Spahn, Planer Microoptomechanical Waveguide Switches, IEEE Journal on Selected Topics In Quantum Electronics, Vol. 8, No. 1, Jan/Feb, 2002.
- [67] F. Ladouceur, J. D. Love, Silica-based Buried Channel Waveguides and Devices, Chapman & Hall press, 1996.
- [68] [www.zolotech.com/sub/photonics/dwdm.php](http://www.zolotech.com/sub/photonics/dwdm.php), 2006
- [69] H. G. Bukkems, C. G. P. Herben, M. K. Smit, F. H. Groen, I. Moerman, Minimization of the Loss of Intersecting Waveguides in InP-Based Photonic Integrated Circuits, IEEE Photonics Technology Letters, Vol. 11, No. 11, November, 1999.
- [70] T. S. Barry, D. L. Rode, R. R. Krchnavek, High Efficient Coupling Between Single-Mode Fiber and Polymer Optical Waveguides, IEEE Transactions on Components, Packaging, and Manufacturing Technology-Part B, Vol. 20, NO. 3, August, 1997.
- [71] P. De Dobbelaere, K. Falta, L. Fan, S. Gloechner, S. Patra, Digital MEMS for Optical Switching, IEEE Communication Magazine, March, 2002.
- [72] NTU website, <http://mmc.mpe.ntu.edu.sg/equipment.asp>, 10<sup>th</sup> October, 2002.



## References

- [73] Ansys Inc, Ansys Operations Guide, 2001.
- [74] C2V (Concept to Volume b.v.), Introduction to Olympos, Version 5.1, 2003.
- [75] [http://www.zenphotonics.com/products/thermal\\_polymer.html](http://www.zenphotonics.com/products/thermal_polymer.html), Website of ZEN Photonics Co. Ltd, May, 2004.
- [76] E. A. J. Marcatili, Bends in Optical Guides, The Bell System Technical Journal, September, 1969.
- [77] F. Chollet, HB. Liu, A (not so) short introduction to MEMS, <http://memscyclopedia.org/IntroMEMS.html>
- [78] Silicon Temperature-Dependent Refractive Index Dispersion Profile. [http://www.irfilters.reading.ac.uk/library/technical\\_data/infrared\\_materials/si3.htm](http://www.irfilters.reading.ac.uk/library/technical_data/infrared_materials/si3.htm)
- [79] K. Petersen, Silicon as a Mechanical Material, Proceedings of the IEEE, vol. 70, pp. 420-457, 1982.
- [80] L. Chen, J. Miao, L. Guo, and R. Lin, Control of stress in highly doped polysilicon multi-layer diaphragm structure, Surface and Coatings Technology, vol. 141, pp. 96-102, 2001.
- [81] F. Chollet, The SU-8 photoresist for MEMS, 2004. <http://memscyclopedia.org/su8.html>
- [82] C. Marxer, C. Thio, M. A. Grétilat, O. Anthamatten, R. Baettig, B. Valk, P. Vogel, and N. F. de Rooij, Vertical mirrors fabricated by deep reactive ion etching for fiber optic switching applications, IEEE J. Micro Electro Mech. Syst., vol. 6, pp. 277-285, 1997.
- [83] K. Pister, M. Judy, S. Burgett, R. Fearing, Microfabricated hinges, Sensors & Actuators A, vol. 33, pp. 249-256, 1992.
- [84] N.-T. Nguyen and S. T. Wereley, Fundamentals and Applications of Microfluidics. Boston: Artech House, 2002.
- [85] H. Zhang, F. Chollet, E. Burdet, A. N. Poo, D. Hutmacher, Fabrication of 3-D microparts for the assembly of scaffold/cell constructs in tissue engineering, Int. J. of Computation. Eng. Sci., vol. 4, pp. 281-284, 2003.
- [86] T. Hsu, MEMS packaging. London: Inspec IEE, 2004.
- [87] A. M. Receveur, C. R. Marxer, R. Woering, V. C. M. H. Larik, N. F. de Rooij, Laterally moving bistable MEMS DC switch for biomedical applications, J. MEMS, v 14, n 5, October, pp. 1089-1098, 2005
- [88] H. Toshiyoshi, M. Mita, H. Fujita, A MEMS piggyback actuator for hard-disk drives, Journal of Microelectromechanical Systems, v 11, n 6, Dec. 2002, p 648-54.
- [89] O. Gigan, H. Chen; O. Robert, S. Renard, F. Marty, Fabrication and characterization of resonant SOI micromechanical silicon sensors based on DRIE micromachining, freestanding release process and silicon direct bonding, Proceedings of the SPIE - The International Society for Optical Engineering, v 4936, 2002, p 194-204.
- [90] H. B. Liu, F. Chollet, Optical switch based on moving polymer waveguides and self-latching structure, International Journal of Computational Engineering Science. Vol. 4, No. 3, Sept. 2003, p 447-450.
- [91] C. H. Mastrangelo, C. H. Hsu, Mechanical stability and adhesion of microstructure under capillary forces – part I: basic theory, J. Microelectromechanical Systems, Vol. 2, No.1, March 1993, p 33-43.
- [92] M. Madou, Fundamentals of Microfabrication, Pg235~236, CRC Press, 1997.

## References

- [93] J.Y. Kim, C.-J. Kim, Comparative study of various release methods for polysilicon surface micromachining, Proceedings IEEE, The Tenth Annual International Workshop on Micro Electro Mechanical Systems: An Investigation of Micro Structures, Sensors, Actuators, Machines and Robots (Cat. No.97CH36021), 1997, p 442-7.
- [94] T. Abe, W. C. Messner, M. L. Reed, Effective methods to prevent stiction during post-release-etch processing, Proceedings: IEEE Micro Electro mechanical Systems (MEMS '95), Amsterdam, Netherland, 1995, p. 94-99.
- [95] G. K. Fedder, J. C. Chang, R. T. Howe, Thermal assembly of polysilicon microactuators with narrow-gap electrostatic combdrive, Technical Digest: 1992 Solid State Sensor and Actuator Workshop, Hilton Head Island, S.C., 1992, p. 63-68.
- [96] C. H. Mastrangelo, G. S. Saloca, A dry-release method based on polymer columns for microstructures fabrication, Proceedings: Micro Electro Mechanical Systems (MEMS '93), Ft. Lauderdale, Fla., 1993, p. 77-81.
- [97] T. A. Lober, R. T. Howe, Surface micromachining for electrostatic microactuator fabrication, Technical Digest: 1988 Solid State Sensor and Actuator Workshop, Hilton Head Island, S.C., 1988.
- [98] M. R. Houston, R. Maboudian, R. T. Howe, Ammonium fluoride anti-Stiction treatments for polysilicon microstructure, Int. conf. Solid State Sensors and Actuators, Stockholm, Sweden, 1995, p. 210-213.
- [99] G. T. Mulhern, D. S. Soane, R. T. Howe, Supercritical carbon dioxide drying of microstructures, Int. Conf. Solid-State Sensors and Actuators, Yokohama, Japan, 1993, p. 296-299.
- [100] P. T. Docker, P. K. Kinnell, M. C. L. Ward, Development of the one-step DRIE dry process for unconstrained fabrication of released MEMS devices, Journal of Micromechanics and Microengineering, v 14, n 7, July 2004, p 941-4.
- [101] G. S. Hwang, K. P. Giapis, On the origin of the notching effect during etching in uniform high density plasmas, Journal of Vacuum Science & Technology B: Microelectronics Processing and Phenomena, v 15, n 1, Jan-Feb, 1997, p 70.
- [102] M. Chabloz, J. Jiao, Y. Yoshida, T. Matsuura, K. Tsutsumi, Method to evade microloading effect in deep reactive ion etching for anodically bonded glass-silicon structures, Proceedings of the IEEE Micro Electro Mechanical Systems (MEMS), 2000, p 283-287.
- [103] K. P. Giapis, G. S. Hwang, Pattern-dependent charging and the role of electron tunneling, Japanese Journal of Applied Physics, Part 1: Regular Papers & Short Notes & Review Papers, v 37, n 4B, Apr, 1998, p 2281-2290.
- [104] F. Lärmer, A. Schilp, Method of anisotropically etching silicon, US Patent Specification 5501893 German Patent Specification DE4241045.
- [105] A. A. Ayon, X. Zhang, R. Khanna, Ultra Deep Anisotropic Silicon Trenches Using Deep Reactive Ion Etching (DRIE), in Solid-State Sensor and Actuator Workshop. Hilton Head Island, S.C.: Transducers Research Foundation, Inc, 2000, p 339-42.
- [106] P.T. Docker, P. Kinnell, M. C. L. Ward, A dry single-step process for the manufacture of released MEMS structures, Journal of Micromechanics and Microengineering, v 13, n 5, Sept. 2003, p 790-4.
- [107] B. E. Volland, Profile simulations of gas chopping etching process, Ph.D Thesis Report, Institute of Physics, University of Kassel, 2004.

## References

---

- [108] S. K. Pani, C. C. Wang, K. Sudharsanam, C. S. Premachandran, and M. K. Iyer, "Evolution of variation of sidewall roughness of polymeric waveguides during reactive ion etching", J. Vac. Sci. Technol. B 24 (2006) P. 163.